JPL Quarterly Technical Review

Volume 2 July 1972 Number 2

Contents

Bibliography of Current Reporting

Index: atmospheric entry, planetary atmospheres

Models for the Atmospheres of Jupiter and Saturn

N. Divine and F. D. Palluconi

Project Engineering Division

Numerical models of the atmospheres of Jupiter and Saturn have been created for use in the development of design criteria for space vehicles intended to investigate these planets. These models contribute to spacecraft design by providing a basis for the assessment of entry heating, the transmission and emission of radiation, and structural and aerodynamic interactions. The model atmospheres are based on data and analyses published in the literature through 1970. The composition is discussed, and the relative amounts of each molecular species are tabulated for nominal and extreme cases. The structure of the atmospheric regions is discussed, and the principal features of one nominal and two limiting models for each planet are indicated. The models are illustrated by pressure-temperature profiles which also display the major cloud layers. Reference is made to complete descriptions of altitude, pressure, temperature, density, scale height, and cloud relationships for these models which are specified in appropriate NASA publications.

Introduction

Models of the atmospheres of Jupiter and Saturn have been created for the purpose of developing space vehicle design criteria. Such models provide a means of estimating entry heating, atmospheric transmission and emission, spacecraft structural and aerodynamic interactions, and other effects.

Present evidence suggests that the atmospheres of Jupiter and Saturn display basic similarity in composition and structure, the major differences being related to Saturn's smaller mass and radius and greater distance from the Sun. The similarity permits a common approach to the development of model atmospheres for these two planets. In particular, hydrostatic equilibrium and the perfect gas law applied to a mixture of primarily molecular hydrogen and helium are appropriate in the entire pressure range encompassed by the models, namely 10^{-2} to 10^{8} N/m^2. Further details common to the atmospheres of both planets are treated in the following three sections.

Composition

Abundance values deduced from the analysis of photographic spectra of Jupiter and Saturn have suggested that the elemental composition of their atmospheres resembles that of the Sun. This conclusion is somewhat stronger for Jupiter (in whose spectra, lines of H_2, CH_4, and NH_3 have been measured) than for Saturn (only H_2 and CH_4). Reviews of the measurements are provided by McElroy (Reference 1) and Owen (Reference 2) in which the emphasis is placed on relative rather than absolute abundances because of the difficulties involved in the interpretation of the data. Notably absent from the measurements are the presumably abundant gases He and H_2O, explained respectively by spectroscopic inactivity and condensation processes (Reference 3). The most likely composition for the atmospheres thus includes solar element ratios formed into simple hydrogen-bearing molecules, completely mixed at great depths and modified by condensation at and above cloud-bearing levels (see following section).

Lower Atmosphere

Observations of Jupiter and Saturn at wavelengths greater than 10 μm imply that these planets radiate more energy than they receive from the Sun (Reference 4). The power thus radiated is expected to control the temperature structure of the lower atmosphere, which would show spherical symmetry, independent of latitude and time of day. This conclusion is supported by the latitude independence of the 8- to 14-μm brightness temperatures for Jupiter (Reference 5). Both theoretical considerations and observations of variable features on the planets suggest that convection is responsible for the energy transport in the lower atmosphere, in which case an adiabatic temperature gradient (appropriate to the local composition and gravity) is expected. In order to complete the specification of lower atmospheric structure, a correspondence between pressure and temperature at some level is required. Unfortunately, attempts to obtain such a correspondence from quantitative analysis of the many absorption lines in the photographic infrared have led to important difficulties in interpretation, so the correspondence has been computed using infrared temperatures and hydrogen opacities near 14 μm (Reference 6).

Within a convective lower atmosphere, condensation processes may be important. For Jupiter, the observational aspects of clouds are discussed by Peek (Reference 7) and others, whereas the theory is discussed by Lewis (Reference 3). For both planets the major clouds will contain NH_3 and H_2O. Because the pressure level at which these species condense depends strongly on their mixing ratios and on local conditions, it is probably not appropriate to use an altitude reference level associated with the clouds, particularly as it could not be directly associated with abundances inferred from absorption line data and analysis in any case. Thus an arbitrary association of zero altitude with the pressure level 101,325 N/m^2 (1 atm) has been made.

According to planetary atmosphere theory, the convection will extend upward only as far as it is needed for energy transport, radiative processes

being dominant at greater altitudes. The simple approximation that the convective lower atmosphere is bounded by a tropopause at which the temperature is close to $(0.5)^{1/4}$ times the effective temperature has been adopted.

Upper Atmosphere

For upper atmosphere strata (above the tropopause and the regions of significant radiation reflection, absorption, and emission), observational data are meager for Jupiter and absent for Saturn. In Jupiter's case, Wrixon (Reference 8) attributes some characteristics of the microwave spectrum to a temperature inversion near 145 K and 650 N/m^2. However, several theoretical studies (References 9, 10, 11, and others) apply to both Jupiter and Saturn, with the conclusion that upper atmosphere models may be isothermal at the tropopause temperature or include temperature inversions (up to 500 K). Because H_2 will dominate the composition up to very low pressures, little error is made by assuming the same composition for the upper and lower atmospheres (modified by condensation of some minor constituents).

Jupiter

Three new models for Jupiter's atmosphere have been created, which cover a range broad enough to include both uncertainties and latitude and time-of-day variations. The range of compositions is given in Table 1, in which the element abundance ratios are taken from Torres-Peimbert et al. (Reference 12) and Lambert (Reference 13) for the nominal case. The extreme cases are formed by assuming the mass fractions of all molecules other than hydrogen to be uncertain by a factor of two.

The nominal model has been constructed with an effective temperature of 134 K (Reference 4), an acceleration of gravity of 2500 cm/s^2, and a mean molecular weight of 2.30 g/mol, which corresponds to the nominal composition. The convective troposphere has a temperature-dependent adiabatic lapse rate (corresponding to the nominal composition) near −2 K/km, extends indefinitely downward from the tropopause temperature of 113 K, and includes the correspondence level at a temperature of 125 K and a pressure of 30,400 N/m^2 (a partial H_2 pressure near 25,331 N/m^2 (¼ atm), Reference 6). Above the tropopause, an isothermal stratosphere extends upward one scale height (16.3 km). Above the stratosphere an inversion layer of constant lapse rate is limited by an uppermost level at which the pressure and temperature are 650 N/m^2 and 145 K (Reference 8). An isothermal region extends indefinitely upward from the latter level.

The limiting models are "cool" and "warm" in the sense that for a given pressure of the nominal model they provide extremes of temperature and density which are thought to bracket the range of possible values. The pressure–temperature profiles are shown in Figure 1. In order that the cool models also be the most condensed, the largest mean molecular weight (2.70 g/mol), the largest gravity (2700 cm/s^2), and the smallest effective

Table 1. Compositions for model atmospheres of Jupiter and Saturn

Parameter		Jupiter			Saturn		
		Cool	Nominal	Warm	Cool	Nominal	Warm
Fraction by mass (or weight)	H_2	0.50696	0.75348	0.87674	0.55279	0.73514	0.89550
	He	0.46000	0.23000	0.11500	0.39474	0.19737	0.09868
	CH_4	0.00857	0.00429	0.00214	0.01332	0.00444	0.00148
	NH_3	0.00219	0.00109	0.00055	0.00339	0.00113	0.00037
	H_2O	0.01601	0.00800	0.00400	0.02484	0.00828	0.00276
	Ne	0.00229	0.00115	0.00057	0.00360	0.00120	0.00040
	Others	0.00398	0.00199	0.00100	0.00732	0.00244	0.00081
Fraction by number (or volume)	H_2	0.68454	0.86578	0.93754	0.72996	0.88572	0.94679
	He	0.31057	0.13214	0.06149	0.26251	0.11213	0.05254
	CH_4	0.00145	0.00062	0.00028	0.00221	0.00063	0.00020
	NH_3	0.00035	0.00015	0.00007	0.00053	0.00015	0.00005
	H_2O	0.00240	0.00102	0.00048	0.00367	0.00105	0.00033
	Ne	0.00031	0.00013	0.00006	0.00047	0.00013	0.00004
	Others	0.00038	0.00016	0.00008	0.00065	0.00019	0.00005
Mean molecular weight, g/mol		2.70	2.30	2.14	2.66	2.27	2.13

temperature (128 K) have been applied to it, even though the specific heat for the corresponding composition is not appropriate to the limiting tropospheric adiabatic lapse rate (-1.9 K/km). Thus the compositions and structure of the models contribute independent limits.

Sample cloud levels, corresponding to the lowest saturation levels for the compositions and structures associated above, are also schematically indicated in Figure 1. These H_2O and NH_3 clouds resemble those suggested by Lewis (Reference 3), who includes NH_4SH clouds as well; CH_4 is not expected to condense in Jupiter's atmosphere.

Saturn

A nominal and two limiting models for Saturn's atmosphere have been created. The limiting models span a range which includes uncertainties and variations expected with latitude and time of day. The specific composition for each model is given in Table 1. Where condensation occurs, the amount of condensable gas present should be determined by the saturation vapor pressure–temperature relation. The composition for the nominal model shown in Table 1 assumes solar element ratios from the tabulation provided by Lewis (Reference 14). The limiting model compositions are obtained from that of the nominal model by considering the mass fraction of He to be uncertain by a factor of two and the mass fraction of constituents other than H_2 and He to be uncertain by a factor of three.

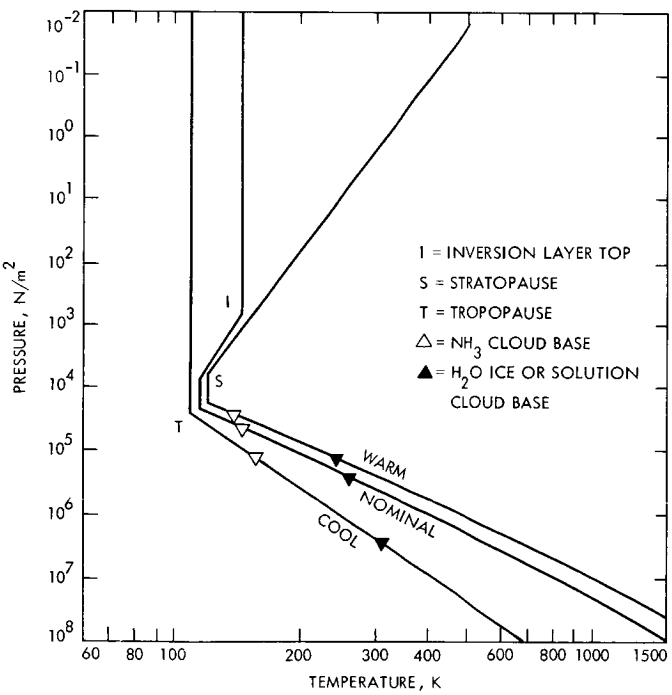

Figure 1. Pressure–temperature profiles for model atmospheres of Jupiter

The nominal model has been developed using an effective temperature of 97 K (Reference 4), an acceleration of gravity of 1050 cm/s^2, and a mean molecular weight of 2.27 g/mol. The convective troposphere has a temperature-dependent adiabatic lapse rate near -1 K/km consistent with the nominal model composition. The correspondence level temperature of 95 K is paired with a pressure of 30,400 N/m^2 (0.3 atm). An isothermal (77 K) stratosphere extends upward from the tropopause two pressure scale heights (H_p = 26.9 km). Above the stratosphere the temperature is assumed to slowly increase with a constant lapse rate until the low pressure limit of the model is reached at a temperature of 119 K and a pressure of 0.01 N/m^2.

The limiting models are "cool" and "warm" in the same sense used for Jupiter. The choices made for the composition, acceleration of gravity, and effective temperature were combined to produce the limiting character of these models whose pressure-temperature profiles are shown in Figure 2. Unlike the nominal model, the tropospheric lapse rate for the limiting models was chosen independently of the model composition. In this sense the composition and pressure-temperature structure of the limiting models can be considered as independent limits.

Figure 2 also indicates the principal cloud regions for each model. Additional cloud-forming constituents are possible as has been suggested for Jupiter by Lewis (Reference 3). All three models exhibit NH_3 ice clouds. The presence of NH_3 has not been established from photographic spectra (Reference 15) but is inferred from the analysis of radio brightness

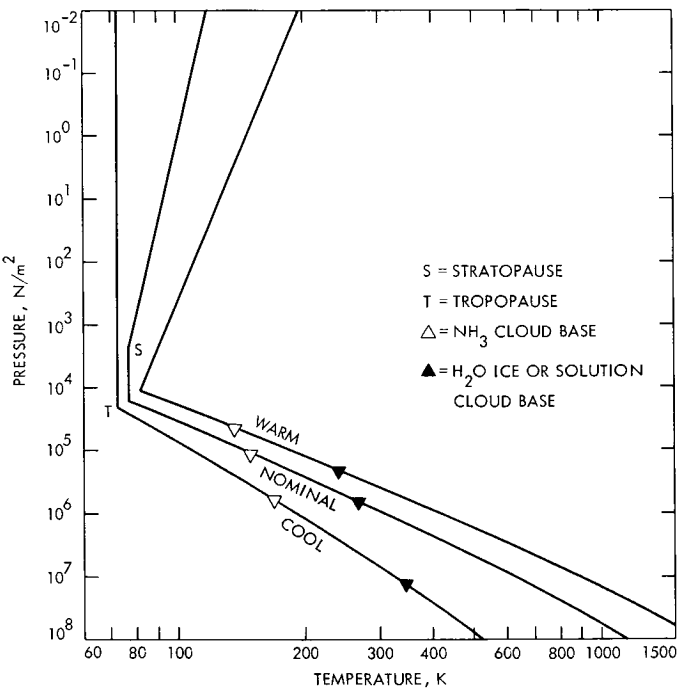

Figure 2. Pressure-temperature profiles for model atmospheres of Saturn

temperature observations (References 16 and 17). The amount of NH_3 present above the base of the NH_3 ice clouds in the nominal model would be difficult to detect by photographic means. No CH_4 clouds exist in any of these models, and none are expected unless temperatures are lower than postulated here or the CH_4 mixing ratio is much larger than that shown in Table 1 for the "cool" model.

Conclusions

The numerical models described have been used in analyses of Jupiter's spectra in the photographic infrared (Reference 18), the region at several microns wavelength (Reference 19), and the microwave region (Reference 20); in each case the nominal model yields substantial agreement with observed data. The models have further been used in studies of Jupiter atmospheric entry probes, strongly impacting the heat shield, structural, communications, and mission operations analyses (Reference 21 and others).

Because condensation of NH_3 and H_2O occurs in all models, direct sampling of the six most abundant atoms and molecules (H_2, He, H_2O, CH_4, Ne, and NH_3) will require penetration to a pressure of 2×10^5 N/m^2 (2 atm) or greater. Complete model construction details and a tabulation of atmospheric properties for Jupiter and Saturn can be found in NASA SP-8069 (Reference 22) and NASA SP-8091 (Reference 23).

References

1. McElroy, M. B., "Atmospheric Composition of the Jovian Planets," *J. Atmos. Sci.*, Vol. 26, No. 5, pp. 798–812, 1969.

2. Owen, T., "The Atmosphere of Jupiter," *Science*, Vol. 167, No. 3926, pp. 1675–1681, 1970.

3. Lewis, J. S., "The Clouds of Jupiter and the NH_3-H_2O and NH_3-H_2S Systems," *Icarus*, Vol. 10, No. 3, pp. 365–378, 1969.

4. Aumann, H. H., Gillespie, C. M., Jr., and Low, F. J., "The Internal Powers and Effective Temperatures of Jupiter and Saturn," *Astrophys. J.*, Vol. 157, No. 1, pp. L69–72, 1969.

5. Wildey, R. L., "Structure of the Jovian Disk in the ν_2-band of Ammonia at 100,000 Å," *Astrophys. J.*, Vol. 154, No. 2, pp. 761–770, 1968.

6. Gillett, F. C., Low, F. J., and Stein, W. A., "The 2.8-14-Micron Spectrum of Jupiter," *Astrophys. J.*, Vol. 157, No. 2, pp. 925–934, 1969.

7. Peek, B. M., *The Planet Jupiter*. Faber & Faber, London, 1958.

8. Wrixon, G. T., *Microwave Absorption in the Jovian Atmosphere*, Space Sci. Lab. Series 10, Issue 26. University of California, Berkeley, 1969.

9. Hogan, J. S., Rasool, S. I., and Encrenaz, T., "The Thermal Structure of the Jovian Atmosphere," *J. Atmos. Sci.*, Vol. 26, No. 5, pp. 898–905, 1969.

10. Hunten, D. M., "The Upper Atmosphere of Jupiter," *J. Atmos. Sci.*, Vol. 26, No. 5, pp. 826–834, 1969.

11. McGovern, W. E., "Exospheric Temperatures of Jupiter and Saturn," *J. Geophys. Res.*, Vol. 73, No. 19, pp. 6361–6363, 1968, and Vol. 74, No. 14, p. 3750, 1969.

12. Torres-Peimbert, S., Simpson, E., and Ulrich, R. K., "Studies in Stellar Evolution: VII. Solar Models," *Astrophys. J.*, Vol. 155, No. 3, pp. 957–964, 1969.

13. Lambert, D. L., "The Abundances of the Elements in the Solar Photosphere: I. Carbon, Nitrogen and Oxygen," *Royal Astron. Soc. Monthly Notices*, Vol. 138, No. 2, pp. 143–179, 1968.

14. Lewis, J. S., "Observability of Spectroscopically Active Compounds in the Atmosphere of Jupiter," *Icarus*, Vol. 10, No. 3, pp. 393–409, 1969.

15. Cruikshank, D. P., "A Search for Ammonia in the Atmosphere of Saturn," *Am. Astron. Soc. Bull.*, Vol. 3, No. 2, Pt. II, p. 282, 1971 (abstract).

16. Wrixon, G. T., and Welch, W. J., "The Millimeter Wave Spectrum of Saturn," *Icarus*, Vol. 13, pp. 163–172, 1970.

17. Gulkis, S., McDonough, T. R., and Craft, H., "The Microwave Spectrum of Saturn," *Icarus*, Vol. 10, No. 3, pp. 421–427, 1969.

18. Margolis, J. S., "Studies of Methane Absorption in the Jovian Atmosphere: III. The Reflecting-Layer Model," *Astrophys. J.*, Vol. 167, No. 3, pp. 553–558, 1971.

19. Taylor, F. W., and Hunt, G. E., "The Infrared Spectrum of Jupiter and Radiative Properties of the Clouds," abstract to be published in *Am. Astron. Soc. Bull.*

20. Poynter, R., and Gulkis, S., "Thermal Radio Emission from Jupiter and Saturn," abstract to be published in *Am. Astron. Soc. Bull.*

21. DeWolf, D. A., and Kaplan, G. S., *Investigation of Line-of-Sight Propagation in Dense Atmosphere: Phase III, Part I*, NASA CR-114416, National Aeronautics and Space Administration, Washington, 1971.

22. *The Planet Jupiter (1970)*, NASA SP-8069. National Aeronautics and Space Administration, Washington, 1971.

23. *The Planet Saturn (1970)*, NASA SP-8091. National Aeronautics and Space Adminstration, Washington (in press).

Index: orbits and trajectories, planetary quarantine

Aiming Strategies for Quarantined Multi-Planet Missions

N. P. Dwivedi

Mission Analysis Division

An important flight path constraint for current and future interplanetary missions arises from planetary quarantine restrictions. Each planet is assigned a maximum allowable probability of contamination which must not be violated. A portion of this probability is suballocated among the trajectory correction maneuvers. The remaining portion is allocated to the small ejecta/efflux sources released from the spacecraft that could possibly reach the planetary atmosphere and surface. For each maneuver, the suballocation is translated into an allowable probability of planetary impact. At the time of making a maneuver, the allowable probability of impact may dictate biasing the aim point. This study describes the technique of determining preferred biased aim points, given the suballocated probability of contamination for each maneuver.

Introduction

One important flight path constraint for interplanetary missions is that due to planetary quarantine (PQ). For each NASA flight project, a probability of contamination is specified for each target planet and then suballocated among the pre-encounter maneuvers. At the time a trajectory correction is to be applied, the PQ constraint may prohibit aiming the spacecraft directly at the otherwise desired target point, in which case the aim point must be biased away. This article discusses the maneuver reliability and aim point strategies for multi-planet missions. The work reported here is based on Reference 1 and further research on the subject conducted at JPL.

Maneuver Reliability Model and Probability of Impact

Maneuver reliability is defined to be the *a priori* probability of the maneuver being successful. The time variation of maneuver reliability is modeled by an exponential function as follows:

$$P_m = P_0 e^{-\alpha t} \tag{1}$$

where P_m is the maneuver reliability, P_0 is the maneuver reliability at spacecraft injection, α is a positive constant, and t denotes the time past injection. The relationship between the allocated probability of contamination (P_c) and the allowable probability of impact (P) for the maneuver is given by

$$P = \frac{P_c}{1 - P_0 e^{-\alpha t}} \tag{2}$$

Equation 2 is based upon two important assumptions. First, "contamination" is defined to occur if the planet is impacted by a large object such as an unsterile spacecraft. Second, if a scheduled maneuver places the spacecraft on an impact trajectory, a removal maneuver will be performed *as soon as* the knowledge of the impact situation exists.

Impact Probability Approximation

The capture zone of the target planet is a circular area centered at the target. The circle lies in the B-plane (which is defined to be the plane perpendicular to the asymptote of the incoming hyperbolic trajectory and passing through the center of the target planet). The actual trajectory dispersion is modeled by a gaussian density function in the B-plane. Therefore, the probability of impacting the target planet can be calculated by the surface integral of the density function over the capture area. However, this computation is quite complex and does not lend itself to the inverse problem of finding the aim point, given the probability of impact, the density function, and the capture radius. In order to overcome these difficulties, the probability of impact is approximated by a simple formula, described below:

Given a two-dimensional gaussian probability density function, the probability over an offset capture circle is approximated by

$$P_{\text{approx}} = \frac{1}{\pi} \tan^{-1}\left(\frac{\pi R_c^2}{2\sigma_1\sigma_2}\right) \exp\left(-\left[\frac{\lambda_0^2}{2}\right]\right) \tag{3}$$

where R_c is the radius of the offset capture circle, σ_1 is the semi-major axis of the probability density ellipse, σ_2 is the semi-minor axis of the probability density ellipse, and λ_0 is a measure of the distance between the centers of the ellipse and the offset circle that is illustrated in Figure 1 and defined as follows: Find the intersection of the circumference of the offset circle with the straight line joining the centers. Then λ_0 is the scale factor by which the

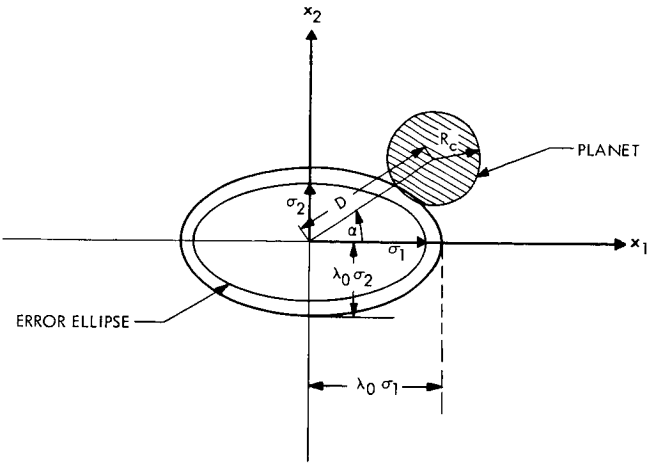

Figure 1. Notation for numerical evaluation

dimension of the one-sigma ellipse must be multiplied to cause the scaled ellipse to pass through the intersection point. More specifically,

$$\lambda_0 = \frac{(D - R_c)}{\sigma_1 \sigma_2} \sqrt{\sigma_1^2 \sin^2 \alpha + \sigma_2^2 \cos^2 \alpha} \tag{4}$$

where D is the distance between the centers, and α is the angle between the line joining the centers and the major axis.

The comparison between the exact and approximate probabilities is illustrated in Figure 2, which is based on 500 different samples involving a large dynamic range for the parameters of Equation 3. In most cases, the approximate probability of impact is less than or equal to the exact one. It will be shown later that such an approximation results in a conservative biasing of the aim point.

A navigation problem of considerable interest is to find an aim point for which the probability of impact is smaller than (or equal to) the suballotted value. This is facilitated by finding a closed contour on which the probability of impact is a given value. Then all the points interior to this contour represent a probability of impact higher than that given. Similarly, all the points exterior to the contour represent a probability of impact lower than that given. The minimally biased aim point, therefore, must lie on the contour.

It may be observed that, for a particular target planet and asymptotic approach velocity, R_c is constant. And, for a particular navigation system and maneuver time, σ_1 and σ_2 are constant. Therefore, to obtain the locus of constant P_{approx}, α is varied keeping λ_0 constant. This results in an ellipse with semi-major axis a and semi-minor axis b, given by

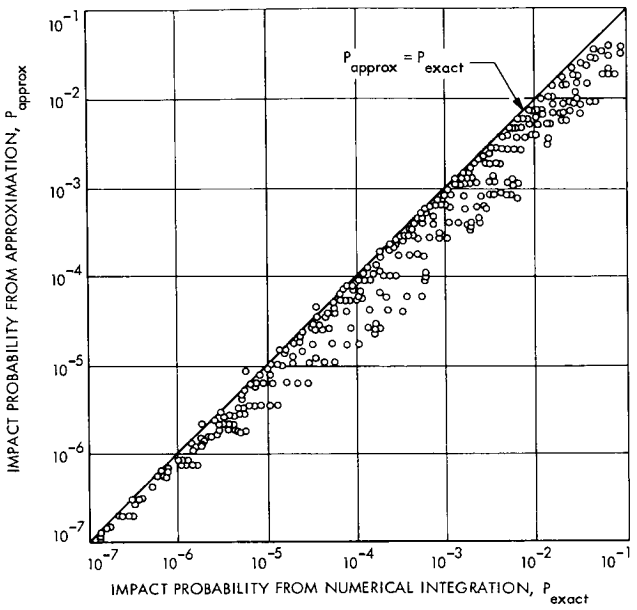

Figure 2. Comparison between approximate and exact probabilities

$$a = \lambda_0 \sigma_1 + R_c \tag{5}$$

$$b = \lambda_0 \sigma_2 + R_c \tag{6}$$

where

$$\lambda_0 = \sqrt{2 \ln \left[\frac{\tan^{-1}\left(\frac{\pi R_c^{\,2}}{2\sigma_1\sigma_2}\right)}{\pi P_{approx}} \right]} \tag{7}$$

The orientation of this ellipse is the same as the error ellipse, and its center is at the center of the capture circle.

It may be observed that the smaller the probability of impact the larger the size of the constraint ellipse. Therefore, P_{approx} results in a conservative biasing of the aim point.

Figure 3 gives an illustration of the error ellipse and the constraint contour (constant P_{approx} probability contour).

Optimum Aiming Strategies for a Single Target

A practical navigation problem is to find an aim point such that PQ is not violated subject to an additional constraint which may be minimization of miss, propellant, etc. In general, one has

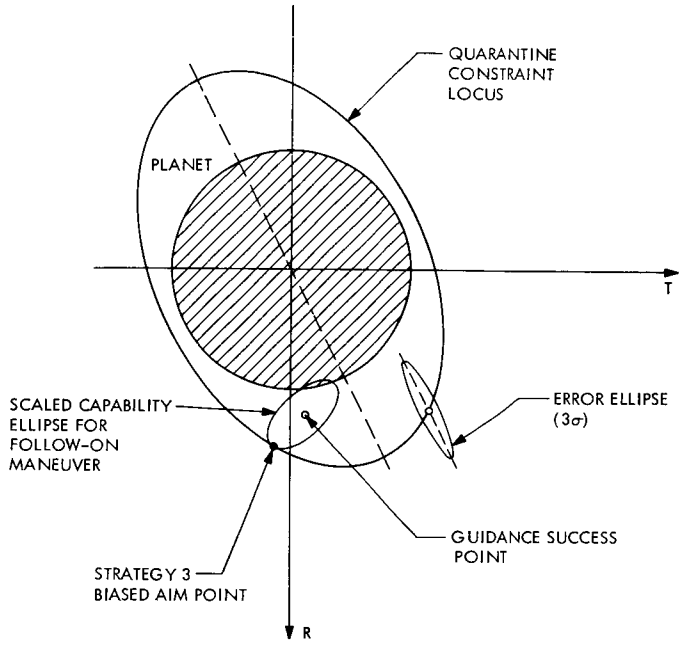

Figure 3. Constraint ellipse and biased aim point for strategy 3

$$\mu = \mathrm{f}(P, \Lambda, R_c, C) \tag{8}$$

where f is a vector function, μ is the aim point, P is the probability of impact after correction, Λ is the covariance matrix of the miss vector after correction, R_c is the capture radius of the target planet, and C is the specified constraint.

Of these parameters only R_c is constant, and the rest are complicated functions, sometimes of each other. A general solution is impossible unless simplifying assumptions are made. These assumptions are the following:

(1) Trajectory B-plane variations are within the region of linear perturbation theory.

(2) The size of the dispersion ellipse does not change between maneuvering to the final or to the biased aim points.

Additional assumptions may be necessitated by the specified constraint. Reference 1 derives optimum strategies for several types of constraints. Before stating the strategies of Reference 1, it is desirable to define a few frequently used terms. These are:

Guidance Success Point. An ideal point in the B-plane such that if the spacecraft trajectory asymptote passes through it, the resulting trajectory will permit maximum mission success to be achieved.

Guidance Success Zone. An area surrounding the guidance success point such that if the spacecraft trajectory asymptote passes through it, the resulting trajectory will permit an acceptable mission to be performed.

Guidance Success. The event of the spacecraft passing through the guidance success zone.

Capability Ellipse. An ellipse in the B-plane bounding the area achievable by a trajectory correction of unit velocity magnitude.

Strategy Curve. A closed curve in the B-plane centered at the guidance success point and scaled to be tangent to the constraint ellipse. The point of tangency yields the biased aim point. The shape of the curve is determined by the strategy used.

The constraints and their associated strategies are:

Strategy 1: Maximizing the Probability of Guidance Success. Here the specified constraint is the maximization of the probability of guidance success following the correction. If $\sigma_1\sigma_2 >> R_c^2$, then the optimum aiming point lies on the vector from the planet center to the guidance success point. The exact location is found by evaluating the probability integral. Otherwise, the optimum aiming point is the point of tangency of the constraint ellipse with the minimally scaled error ellipse centered at the guidance success point.

Strategy 2: Minimizing the Norm of the Miss. Here the constraint is the minimization of the distance from the guidance success point. The optimum aiming point is the point of tangency of the constraint ellipse with a circle of minimum radius centered at the guidance success point.

Strategy 3: Minimizing the Propellant. This strategy is found to be equivalent to minimizing the magnitude of the next correction. An example of the optimum aiming point is shown in Figure 3 as the point of tangency of the constraint ellipse with the minimally scaled capability ellipse corresponding to the next maneuver centered at the guidance success point.

Consideration of Additional Targets

If there are additional targets, it is required that the selected aim point for any maneuver not violate the PQ constraint at any of the subsequent targets.

An efficient approach is to map the capture area at the next target to an equivalent capture area at the immediate target, and to find a constraint contour corresponding to this area. The search for an aim point satisfying PQ constraints at both targets is then restricted to one plane.

Let J be the immediate target and $J + 1$ be the subsequent target. Let us consider a maneuver before the encounter of target J for which an aim point

is desired. It is assumed that the matrix for mapping the miss vector from target $J + 1$ to J is available. Let[1]

$$\mathbf{m} = \begin{bmatrix} \mathbf{B} \cdot \mathbf{R} \\ \mathbf{B} \cdot \mathbf{T} \end{bmatrix} \tag{9}$$

Subscripts J, $J + 1$, etc., will be used to denote the appropriate targets. Let

$$A = \frac{\partial \mathbf{m}_J}{\partial \mathbf{m}_{J+1}} \tag{10}$$

Let

R_{c_J} and $R_{c_{J+1}}$ be the capture radii for targets J and $J + 1$

The problem is to map the capture circle at target $J + 1$ to an equivalent capture area at target J. Figure 4 shows a sketch of the mappings involved.

The vectors to the nominal aim points on the standard trajectory at the targets J and $J + 1$ from the respective centers of the B-plane are

$$\boldsymbol{\mu}_{0_J} \text{ and } \boldsymbol{\mu}_{0_{J+1}}$$

Then the center of the B-plane at target $J + 1$ maps into a point $\boldsymbol{\mu}_c'$ given by

$$\boldsymbol{\mu}_c' = \boldsymbol{\mu}_{0_J} - A\boldsymbol{\mu}_{0_{J+1}} \tag{11}$$

The capture circle at $J + 1$ will generally map into an ellipse centered at $\boldsymbol{\mu}_c'$. This ellipse will be within two concentric circles (centered at $\boldsymbol{\mu}_c'$) of radii $R_{\max}$ and $R_{\min}$, given by

$$R_{\max} = \sqrt{\lambda_{\max}}\, R_{c_{J+1}} \tag{12}$$

$$R_{\min} = \sqrt{\lambda_{\min}}\, R_{c_{J+1}} \tag{13}$$

where $\lambda_{\max}$ and $\lambda_{\min}$ are, respectively, the maximum and the minimum eigenvalues of the matrix A^TA.

[1] A planet-centered **RST** coordinate system is defined such that **S** is along the incoming hyperbolic velocity vector, **T** lies in the B-plane and is parallel to the ecliptic plane, and **R** completes the right-handed system. **B** is defined to be the vector perpendicular to the incoming asymptote. From the definition of the B-plane, it follows that **R** and **B** lie in it. **B·R** and **B·T** denote dot products and yield the projections of **B** along the **R** and **T** axes, respectively. For a fuller description and explanatory figure, see pages 33–34 of Reference 1.

Physically, there is no reason to suspect that the ratio R_{max}/R_{min} will be much greater than 1. Therefore, under area equivalence, the capture ellipse at target J may be approximated by a circle of radius R_c' given by

$$R_c' = \sqrt{R_{max} \cdot R_{min}}$$

or

$$R_c' = \left[\lambda_{max} \cdot \lambda_{min} \right]^{1/4} R_{c_{J+1}} \tag{14}$$

which is the geometric mean. This value may now be used in Equation 3 to compute the probability of impact or else directly in Equation 7 to compute λ_0 and hence the semi-major and semi-minor axes of the constraint ellipse using Equations 5 and 6. Thus, effectively one obtains an additional constraint ellipse at the target J corresponding to the PQ constraint at the target $J + 1$.

If there are additional targets $J + 2$, $J + 3$, $\cdots$, etc., the method outlined above may be repeated. At any maneuver time, therefore, there could be as many constraint ellipses as the number of remaining targets. After obtaining the constraint ellipses, one can use the results of Reference 1 to obtain the aim point. However, there are four possible points of tangency for each constraint ellipse with any strategy curve. The test of appropriateness of the selected aim point (i.e., the minimum magnification of the strategy curve) has to be done now simultaneously for $4n$ candidate aim points if n is the number of targets. Some computational advantage may be gained by finding a constraint ellipse containing the guidance success point and finding the total number of intersecting ellipses. Let this number be $m \leq n$. Then only $4m$ aim points need be found and tested for the minimum magnification of the strategy curve to yield the optimum aim point.

Examination of Assumptions

The extension of the aim point strategies for multi-planet missions carried out here is subject to two assumptions.

(1) The geometric mean of the semi-major and semi-minor axes of the mapped ellipse is taken to be the radius of an equivalent capture circle. For an Earth-Jupiter-Saturn mission recently studied, the ratio R_{max}/R_{min} was found to be 1.17. Therefore, this assumption seems reasonable. Also, R_c is eventually used in finding λ_0. It can be shown that λ_0 is very insensitive.

(2) Linearity is assumed in the mapping from one target to another.

Conclusions

A technique has been presented which enables the satisfaction of the PQ constraint for multi-planet missions, using what are essentially extensions of

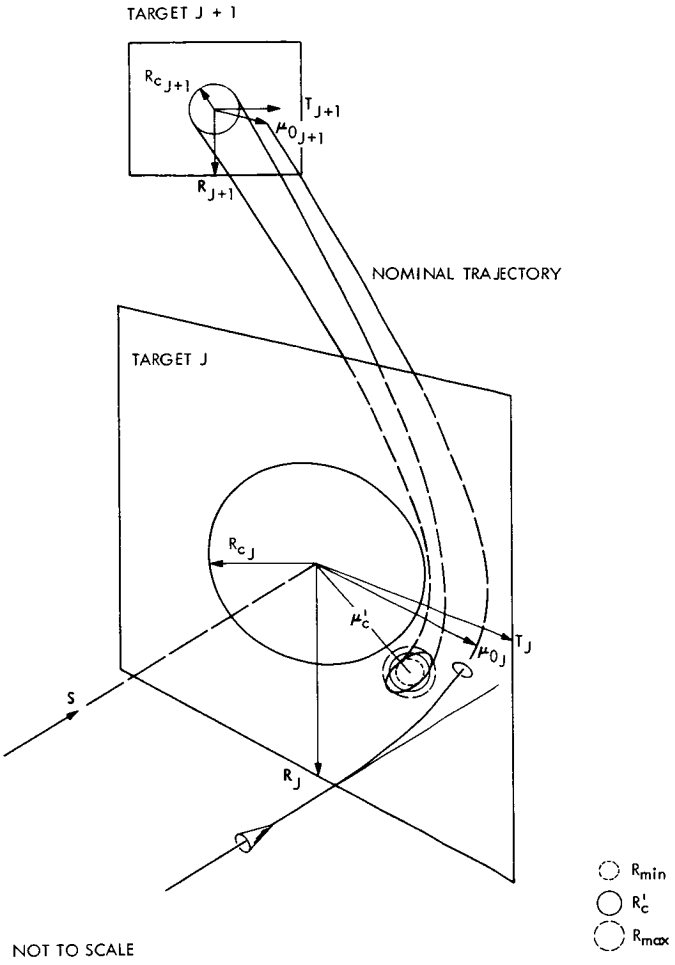

Figure 4. Mappings between target aiming planes

aim point strategies for quarantined single target missions. The technique is based on obtaining as many PQ constraint ellipses at the immediate target as the total number of targets. Determination of the optimum aim point based on a certain strategy is accomplished from among the $4m$ candidate aim points where m is the number of intersecting ellipses of constraints. The selection criterion is the minimum magnification factor of the strategy curve such that the aim point is not inside any constraint ellipse.

Reference

1. Thornton, T. H., Jr., *Aim Point Strategies for Quarantined Interplanetary Navigation*, Ph.D. Dissertation, Aerospace Engineering, University of Southern California, Los Angeles, Calif., Jan. 1970.

Index: wave propagation

Precision Signal Power Measurement

R. Winkelstein

Telecommunications Division

Accurate estimation of signal power is an important Deep Space Network (DSN) consideration. Ultimately, spacecraft power and weight is saved if no reserve transmitter power is needed to compensate for inaccurate measurements. Spectral measurement of the received signal has proved to be an effective method of estimating signal power over a wide dynamic range. Furthermore, on-line spectral measurements provide an important diagnostic tool for examining spacecraft anomalies. Prototype equipment installed at the DSN 64-m-diameter antenna site, the Mars Deep Space Station of the Goldstone Deep Space Communications Complex, has been successfully used to make measurements of carrier power and sideband symmetry of telemetry signals received from the Mariner Mars 1971 spacecraft.

Introduction

The following describes a technique for the accurate measurement of received spacecraft signal power currently being developed at the Jet Propulsion Laboratory. Knowledge of received spacecraft power is critical to many command decisions, such as the selection of suitable telemetry rates for data transmission. Spacecraft anomalies can be diagnosed and examined by observing changes in power level from predicted performance. In addition, measurement of received signal power serves to validate individual DSN station performance by comparison of station-to-station readings as each station is brought into view of the spacecraft by the Earth's rotation.

Currently, measurement of received signal power at the DSN stations is performed by calibrating the automatic gain control (AGC) receiver voltage as an indicator of signal power level. Improvements in this AGC method in the past few years have resulted in an accuracy increase from a few decibels down to a few tenths of a decibel at strong signal levels. However, the AGC method still contains certain limitations. Measurement of weak signals close to receiver threshold becomes very inaccurate. Moreover, the AGC method indicates only carrier power and cannot be used directly to measure sideband power needed to determine modulation symmetry and index.

The measurement technique described here overcomes the stated limitations of the AGC method. It is adapted from the Planetary Radar Program, where the signals are so weak that the receiver is operated in an open-loop mode, tuned to correct for doppler frequency shifts by a computer-controlled oscillator according to ephemeris predictions. The technique for power measurement consists first of measuring the power spectrum of the received signal in a bandwidth just wide enough to observe the background noise. Suitable manipulation of the power spectrum yields the signal-to-noise power ratio. An absolute value of signal power is then obtained from the precalibration or on-line measurements of system noise temperature. A prototype equipment using this method has been constructed and installed at the Mars Deep Space Station, where it has been used to measure carrier and sideband power of telemetry signals from the Mariner Mars 1971 spacecraft.

Equipment

A simplified block diagram of equipment used to implement the precision signal power measurement (PSPM) technique is shown in Figure 1. Input to the equipment is the 50-MHz intermediate frequency (IF) signal from a receiver channel not controlled by the AGC voltage. The output of such a fixed-gain channel is used because measurement accuracy depends on receiver gain stability. A mixer translates the IF signals to baseband, near zero frequency. The frequency synthesizer permits the selection of not only the carrier frequency, but alternately, any desired sideband frequency.

An amplifier with a low-pass filter is required by the PSPM technique. Its response should be extremely flat in the passband, followed by a sharp cutoff characteristic. In the prototype equipment, a 6-pole active Chebyshev filter with a 0.1-dB ripple and a bandwidth of 22 Hz is used. Its output through a dc blocking capacitor is sampled at a rate of 50-Hz by the analog-to-digital

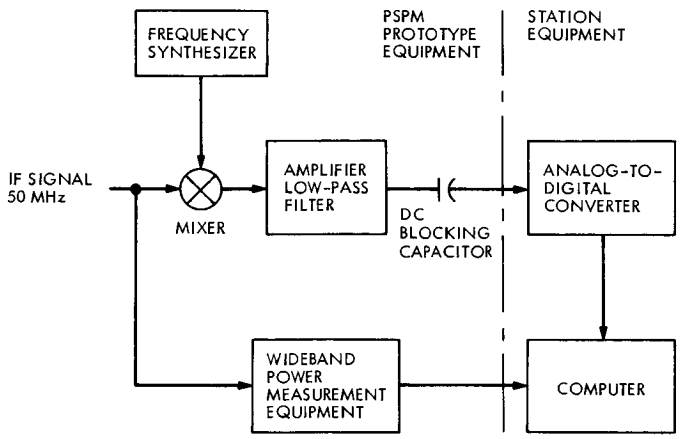

Figure 1. PSPM block diagram

(A/D) converter as shown. The derived spectrum width (which is half the sampling frequency) is therefore 25 Hz. The wideband power measurement equipment measures the total power in the IF bandwidth (several megahertz). At this bandwidth, the contribution of the signal power is negligible, and the measurement is proportional to the receiver system temperature. Determination of the proportionality constant is made by receiver precalibration measurements.

After accumulating the power spectrum of the sampled data for a predetermined measurement time, the computer inputs a value of system temperature from the wideband power measurement equipment and calculates an estimate of the observed signal power.

Theory of Operation

A typical power spectrum accumulated by the computer is shown in Figure 2. The frequency range of the spectrum extends from zero to $f_s/2$, where f_s is the sampling frequency (50 Hz). Spectrum roll-off at the low end is caused by the DC blocking capacitor, and at the high end, by the filter characteristic. In the region labeled I, it is assumed that no signal is present and that the spectrum is flat due to the flat passband characteristic of the filter. Effects on the spectrum caused by the receiver frequency characteristic are negligible because of the narrow frequency band being considered. Region II contains all the signal power in addition to the noise power density shown in region I. The frequencies limiting regions I and II are preset into the computer program. In the prototype equipment, f_1, the sum of the frequency ranges f_{1a} and f_{1b} of regions I, is 10 Hz. The frequency range of region II, f_2, is also 10 Hz. 5 Hz is split among the end bands of the spectrum.

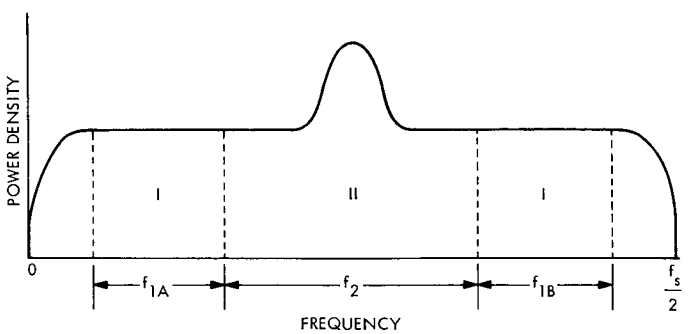

Figure 2. Power spectrum

When the spectrum has been accumulated, the computer then calculates the areas A_1 of region I and A_2 of region II by summing the individual spectral points in those regions. From the assumptions of Figure 2, these areas are equivalent to

$$A_1 = G_n f_1 N \tag{1}$$

$$A_2 = G_n(S_i + f_2 N) \tag{2}$$

where G_n is a normalizing computer gain constant, N is the noise spectral density, and S_i is the signal power. Both N and S_i are the values as referred to the input of the A/D converter. Next, the computer forms the ratio R

$$R = \frac{f_1 A_2 - f_2 A_1}{A_1} \tag{3}$$

Substituting the values of A_1 and A_2 from Equations 1 and 2 into Equation 3 shows that

$$R = \frac{S_i}{N} \tag{4}$$

Signal strength S and noise, kT, referred to the input of the receiver are related to S_i and N by

$$S_i = G_r S \tag{5}$$

$$N = G_r 2kT \tag{6}$$

where G_r is the receiver gain constant, k is Boltzman's constant (1.3806×10^{-23} W-s/K) and T is the receiver system noise temperature in kelvins.

The factor of 2 in Equation 6 accounts for the doubling of the noise spectrum caused by the mixing operation shown in Figure 1. From Equations 4, 5, and 6, the computer can calculate the received signal power as

$$S = 2kTR \tag{7}$$

Observation Time and Variance Considerations

Since R in Equation 3 is calculated from measurements made of a stochastic process, namely the signal plus noise, the value of R found is only a statistical estimate of the true value of the signal-to-noise ratio. As the

measurement time t is increased, the variance of R, viz., σ_R^2, is proportionately decreased. The measured value of R can be considered to have an accuracy of $\pm\sigma_R$. It is necessary to determine the relationship between the spectrum measurement time t and σ_R in order to ensure that t is sufficient to obtain a desired accuracy.

Considering the methods of power spectrum measurement (Reference 1) it can be shown that A_1, the area of regions I in Figure 2, and the standard deviation, σ_{A1} are related by

$$\frac{\sigma_{A1}}{A1} = \frac{1}{\sqrt{tf_1}} \tag{8}$$

or, by Equations 1 and 8,

$$\sigma_{A1} = G_n N \sqrt{\frac{f_1}{t}} \tag{9}$$

The standard deviation of A_2, σ_{A2}, is caused only by the noise portion of the signal and thus similar to Equation 9.

$$\sigma_{A2} = G_n N \sqrt{\frac{f_2}{t}} \tag{10}$$

The standard deviation σ_{R1} due to σ_{A1} can be approximated by multiplying σ_{A1} by the magnitude of the partial derivative of R with respect to A_1.

Similarly, σ_{R2} the standard deviation in R due to σ_{A2} can be approximated by multiplying σ_{A2} by the magnitude of the partial derivative of R with respect to A_2. Since deviations in A_1 and A_2 are independent of each other, the variance of R is

$$\sigma_R{}^2 = \sigma_{R1}{}^2 + \sigma_{R2}{}^2 \tag{11}$$

Carrying out the above operations, produces

$$t = \left(\frac{\left(\frac{S}{2kT} + f_2 \right)^2}{f_1} + f_2 \right) \left(\frac{2kT}{S} \right)^2 \frac{R^2}{\sigma_R{}^2} \tag{12}$$

where t is expressed in seconds and S is expressed in watts. In receiver applications, signal power is more commonly expressed in decibels below a milliwatt (dBmW), and

$$S_{(\mathrm{dBmW})} = 30 + \log_{10} S_{(\mathrm{W})} \tag{13}$$

Because the estimate of S is a random variable, so is $S_{(\mathrm{dBmW})}$, and the rms error in $S_{(\mathrm{dBm})}$ may be approximated by

$$\Delta S_{(\mathrm{dB})} = 10 \log_{10}(1 + \sigma_R/R) \tag{14}$$

Equation 12 is shown in Figure 3 as a plot of t in minutes versus $S_{(\mathrm{dBmW})}$ and $\Delta S_{(\mathrm{dB})}$ where T is 25 K and f_1 and f_2 are both 10 Hz. These values are typical for the Mars Deep Space Station and the prototype PSPM equipment installed there.

Test Results

A prototype PSPM equipment containing the functions shown in Figure 1 with the exception of the computer and A/D converter has been installed and used at the Mars Deep Space Station to measure characteristics of the telemetry signal received from the Mariner Mars 1971 spacecraft. In August of 1971 measurements were made of the ranging sidebands of the received signal as the ranging frequency was varied from 0.25 to 2.0 MHz. Observation times of 4, 8, and 16 min were used in order to keep the

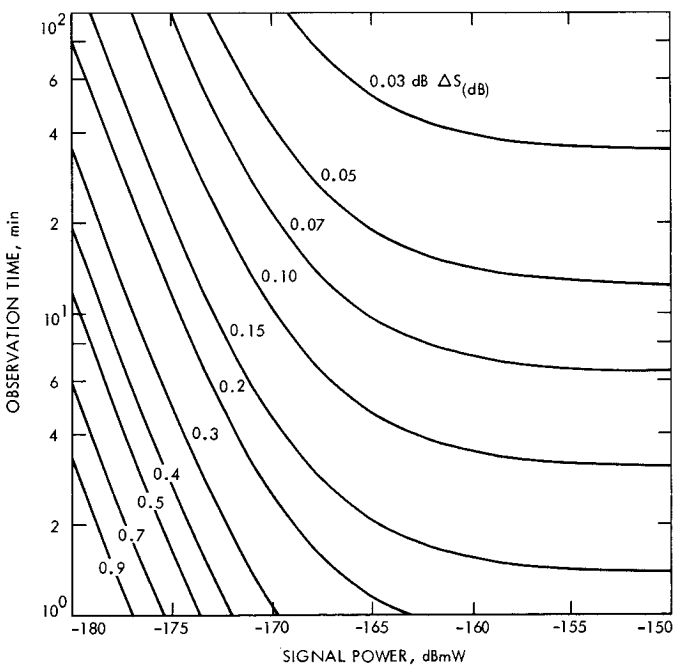

Figure 3. Required observation time

measurement deviation within 0.2 dB for signals stronger than −176 dBmW. Computations were performed in the digital instrumentation system computer which is part of the normal complement of equipment in a DSN station. These measurements indicated that the sidebands were indeed symmetrical to within 0.5 dB at ranging frequencies to 1.25 MHz. Beyond this to 2.0-MHz ranging frequency, the sideband power level dropped to −180 dBmW. Accordingly, as shown in Figure 3, the measurement accuracy dropped from 0.2 dB to 0.45 dB for an observation time of 16 min.

In January 1972, the PSPM equipment was used to demonstrate remote real-time processing of PSPM data on the IBM 360/75 computer at the Space Flight Operations Facility (SFOF) in Pasadena. The DIS computer at the Mars Deep Space Station was used to sample and format the Mariner Mars 1971 signal at the output of the PSPM low-pass filter. Formatted data was sent over a high-speed-data line to the SFOF. There the monitor program in the IBM 360/75 automatically called the PSPM processing software to calculate the power spectrum and resulting signal carrier-power levels. The 3σ-deviations in a series of signal-power measurements were found to be 0.25 dB as opposed to 0.5 dB for the normal station AGC method. However, comparison between the station method and the PSPM method showed a consistent 1-dB difference, with the PSPM method indicating a weaker signal.

Conclusion

The PSPM technique has been shown to be a convenient and repeatable method of measuring signal power characteristics not normally accessible to current DSN station instrumentation. The 1-dB discrepancy noted between AGC and PSPM carrier power measurements is currently being investigated. Future development of the PSPM technique includes utilization of a self-contained minicomputer to perform the spectral calculations and to provide feedback control to station test equipment being developed for automated station calibration procedures.

Reference

1. Winkelstein, R., "Spectral Estimate Variance Reduction by Averaging Fast Fourier Transform Spectra of Overlapped Time Series Data," in *The Deep Space Network*, Technical Report 32-1526, Vol. VII, pp. 74–80. Jet Propulsion Laboratory, Pasadena, Calif., Feb. 15, 1972.

Index: computer programs, mathematical sciences, particle physics, power sources, scientific instruments, shielding

The Response of a 0.03-cm Silicon Detector to a Mixed Neutron and Gamma Field as a Function of Shield Material and Thickness

M. Taherzadeh

Guidance and Control Division

The neutron and gamma radiation from a MHW-RTG was used to evaluate the total response of a shielded 0.3-mm silicon detector. The generator employs a 2200-W(th) PuO_2 heat source concept known as the HELIPAK. The total integrated neutron and gamma ray fluxes at 100 cm away from the source along the radial direction were 1.67×10^3 n/cm^2/s and 1.49×10^4 γ/cm^2/s, respectively. Experimental values of the response function of the shielded silicon detector were used to determine the total counting rates due to photons at bias energies ranging from 50 to 200 keV. For neutrons, analytically computed response functions were used to determine the total counting rates at the same bias energies.

It was found that for an aluminum shield the neutrons are not significant, regardless of the thickness of the shield. However, the magnitude of the total counting rate due to neutrons increases with increased atomic number of the shield and become comparable to the counting rate due to photons for a platinum shield thickness of 5 cm.

Introduction

Nuclear radiation from a radioisotope thermoelectric generator (RTG) used as the prime source of electrical power in space science missions can severely affect the scientific instruments and detectors aboard the spacecraft. This nuclear radiation consists mainly of neutrons and gamma rays, and the interference caused in the detectors in the science package by these particles is of primary concern. Generally, it is recognized that most of these detectors are a great deal more sensitive to gamma rays than they are to neutrons. However, to reduce the response of these detectors to the primary gamma rays, local shields may be employed. If a significant shield thickness is required to reduce the gamma levels, it is possible that the neutrons may become the dominating source of interaction, either directly or through the generation of secondary radiation. The purpose of this study is to determine the shield thickness at which neutrons become important.

In the case of gamma rays, experimental values of the response function have been determined; however, in the case of neutrons an analytical approach was necessary to estimate the magnitude of the response functions. The total response of a detector to a mixed field of gamma rays and neutrons can be found by folding the above response functions with the energy distributions of the photon and neutron fluxes. The individual contributions can be compared and the ratio of neutron-to-gamma response can be determined as a function of shield thickness.

Knowing the interaction processes of photons and neutrons in the shield elements and having a knowledge of the total cross sections of these reactions allows one to easily calculate the detector response due to neutron and photon interactions. The solution to the problem is simple because the range of the charged particles created in the shield due to the interaction of neutrons is limited and is independent of the shield thickness. In addition, the response function of the detector to these secondary particles is very small in comparison to the response due to elastic scattering of neutrons.

Source Radiation Characteristics

The radiation environment outside an RTG is generally determined by the neutron and gamma ray spectrum and the attenuation or scattering of the radiation within the source itself and surrounding media, such as the spacecraft.

The nuclear radiation source selected for this analysis is the multi-hundred-watt (MHW) thermoelectric generator employing a fuel capsule of the HELIPAK concept. The design details of the HELIPAK fuel capsule are reported elsewhere (Reference 1). They will not be discussed here other than to state that the design consists of 24 PuO_2 fuel spheres embedded in a graphite matrix and has a total dimension of approximately 15 cm in diameter by 42 cm in height and weighs about 18 kg.

Since the thermal power per sphere is 92 W, the total power of the radiation source is 2200 W for the 24 spheres. The HELIPAK fuel form was assumed to be the plutonium-molybdenum cermet (PMC) type having a fuel age of 18 years. In addition, it was assumed that the radiation yield of the fuel had the spectral characteristics given in Figure 1.

The integrated value of the neutron yield is equal to 1.4×10^4 neutrons/s/g PuO_2 and the average energy is about 2 MeV. The total yield for the source photons is 5.16×10^{10} gammas/s/g PuO_2; the average energy is rather meaningless, because most of the photons are emitted with a very low energy (about the 44-keV line) and they are immediately absorbed.

The effect of induced fission neutrons was incorporated into the total neutron yield by utilizing a value of 1.25 for the multiplication factor of the fuel and was calculated by the ANISN Code.

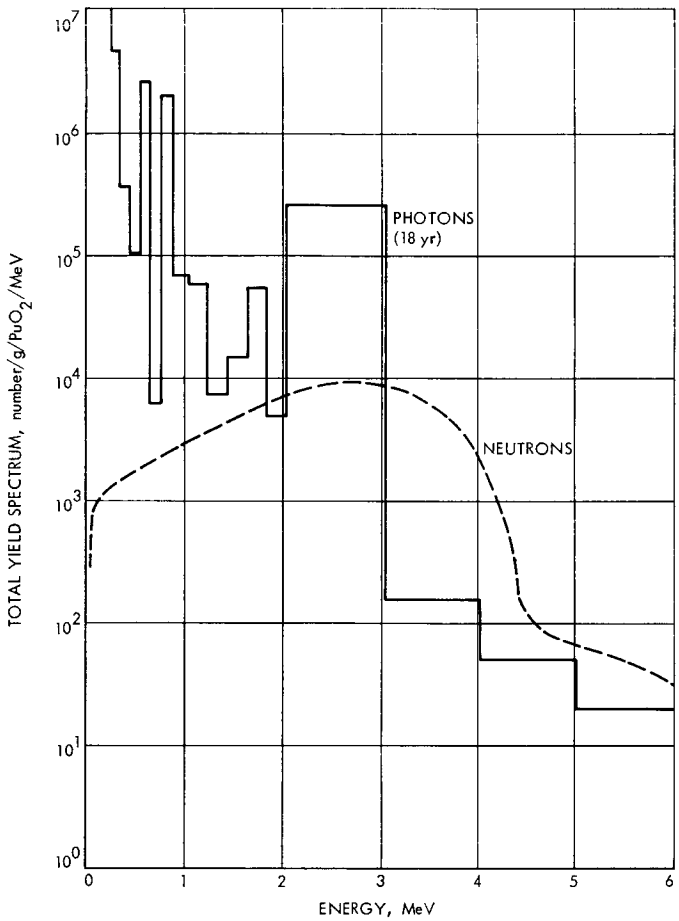

Figure 1. Neutron and gamma radiation from a PuO_2 fuel power source

Neutron and Gamma Ray Flux Spectra

A detector point was assumed to be 100 cm from the center of the source and at 90 deg with respect to the long axis of the fuel capsule. A Monte Carlo computer program (FASTER CODE, Reference 2) was used to calculate the radiation flux spectra of the neutrons and gamma rays (Figure 2). These calculations were performed with the assumption that there exists a surface source envelope which comprises the outer periphery of the thermoelectric converter. This outer surface was divided into a number of sections, and each section was used as a source of radiation. Once the 24 individual sphere surfaces are folded into a surface source, the entire fuel

region was homogenized in order to reduce the size of the required computer memory and the computer running time.

The shape of these spectra (Figure 2) can be easily explained by examination of the original source radiation characteristics and considering shielding properties of the source. The rise of the neutron flux spectrum below a 100-keV neutron energy is due to the existence of a large amount of graphite inside and outside of the source envelope which causes slowing down of neutrons via multiple neutron scatterings. The rapid fall of the neutron flux spectrum at about 4.5-MeV neutron energy is basically due to the neutron yield spectrum (Figure 1).

In the case of photon flux spectrum, the peaks and valleys are due to the gamma ray source lines and the absorption of the low-energy photons by graphite.

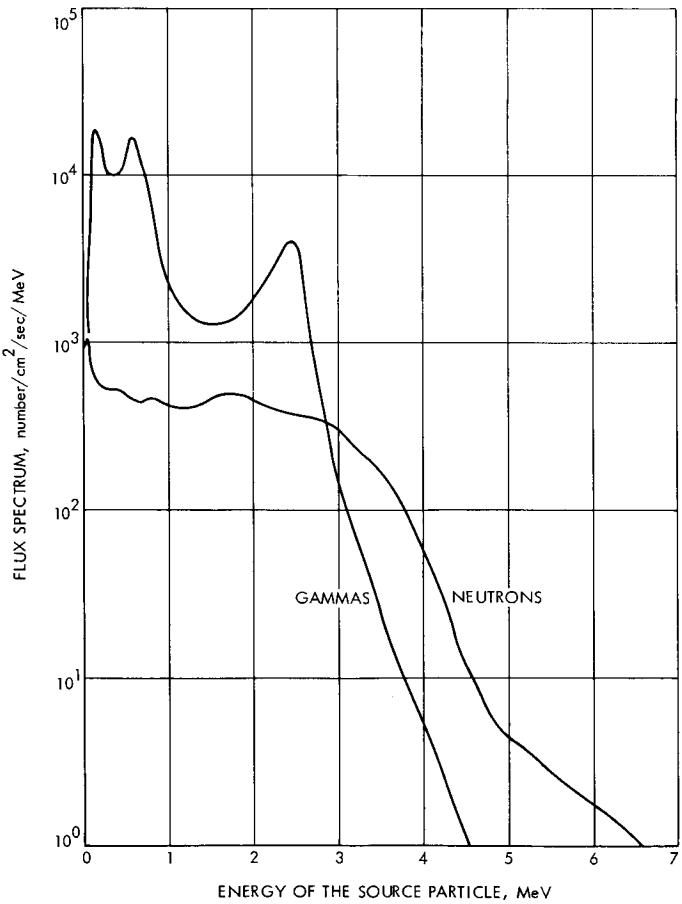

Figure 2. Source particle flux spectrum at 100 cm

Response Function of the Detector

The response of a 300-μm silicon detector to a flux of gamma rays and neutrons was obtained for the HELIPAK source using the results of previous experiment and calculations (References 3 and 4).

Response Functions to Gamma Rays

In the case of gamma rays, the experimental values of the response functions measured by M. Reier (Reference 3) were interpolated so that one could integrate the response over the entire photon energy range. These experimental data were obtained with five gamma ray standard sources at 279, 662, 835, 1250, and 2754 keV, and in each case an appropriately thick aluminum shield was used to shield against the source electrons. The absorber was thicker than the maximum range of the electrons emitted from the source or generated from surrounding objects by the Compton scattering process. Thus, one would assume that the detector is effectively shielded against this source of radiation. However, such an electron shield by itself must be considered as a new source of secondary radiations generated within the shield and interacting with the detector. Thus, the response of the detector was unavoidably enhanced by these secondary radiations (mainly electrons). The response is, therefore, due to the combination of shield and detector. From a practical point of view this is really what is necessary. In any application of a silicon detector it will always be surrounded very closely by a containment structure. The shield-detector system should behave very similarly to a detector within the boundaries of the structure.

The measured response functions were given (Reference 3) for five different bias energies (50, 75, 100, 150, and 200 keV). These functions were interpolated linearly to obtain the corresponding functions for different gamma ray energies (Figure 3). The minimum gamma energy is obtained by assuming that the detector response was generated by the Compton scattering.

Neutron Response

The silicon detector response to neutrons given in counts/neutron at a given detector bias energy E_B, was computed (Reference 4) by using the following equation:

$$r(E_n,E_B) = \epsilon_D\,(E_n)\,p\,(E_n,E_B) \qquad (1)$$

where ϵ_D is the detector zero-bias efficiency function and depends only on the neutron energy and the relaxation length of the detector. The probability that the deposited energy in the sensitive medium of the detector is greater than the detector bias energy is given by the expression

$$p(E_n, E_B) = \int_{E_B}^{E_{n,\,\max}} \frac{2dE}{(E_{\max})^{Si}} \sum_{l=0}^{\infty} \left(\frac{2l+1}{2}\right) f_l(E) \times$$

$$P_l \left(1 - 2\frac{E_{Si}}{(E_{max})^{Si}}\right)\left(1 - \frac{\langle \Delta E \rangle}{(E_{max})^{Si}}\right) \qquad (2)$$

(For more detailed discussion of Equation 3, see Reference 4.)

Both the efficiency function and the probability function are defined for the $^{28}Si(n,n)$ ^{28}Si reaction which can be considered as the most significant and the major contributor to the response of a thin detector. Other reactions, such as (n,α) and (n,p), can take place in the detector, but their contribution is very small, i.e., about 2%, because of the low number of high-energy neutrons in the spectrum. The radiative reactions such as the (n,γ) and $(n,n'\gamma)$ reactions deposit even less energy in the detector, basically because the detector is very thin (0.3 mm).

Figure 4 presents the response functions of the 0.3-mm silicon detector to monoenergetic neutrons emitted from a 2200-W(th) HELIPAK source. The source-detector distance is assumed to be 100 cm and in radial direction. The bias energies are 50, 75, 100, 150, and 200 keV, the same bias energies selected for the gamma response (Figure 3). The combined response of the protons and α particles created in the detector is also presented in Figure 4. However, the contribution from these secondary particles to the total counting rate of the detector is very small due to the sharp drop of the neutron flux spectrum at about 4.5 MeV neutron energy (Figure 2).

Total Counting Rates

The total counting rate of a detector to a neutron or a gamma flux can be obtained by folding its respective response functions into the radiation flux spectrum and integrating it over all possible energies, i.e.,

$$c(E,E_B) = A \int_{E_{min}}^{E_{max}} r(E,E_B)\,[d\phi(E)/dE]\,dE \qquad (3)$$

where c is the counting rate, A is the cross-sectional area of the detector, and $d\phi(E)dE$ (defined by $\phi'(E)$) is the particle flux spectrum given in number/cm^2/s/MeV.

The counting rate for a given reaction with a detector response of $r(E,E_B)$ can be calculated for the gamma and the neutron radiations emanated from a 2200-W PuO_2 fuel power source (HELIPAK design) by using the

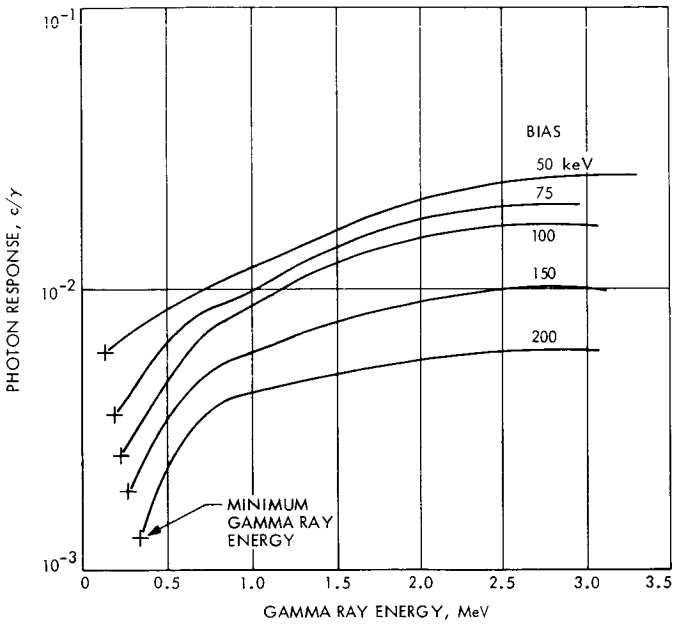

Figure 3. Response of silicon detector to source photons (zero absorption)

corresponding response function (Figures 3, 4) and the flux spectra (Figure 2). The source-to-detector separation was assumed to be 100 cm.

The result of this folding technique is presented in Figure 5. The counting rate of the detector for neutrons is scaled upward (× 100) so that it can be compared with the counting rate due to gamma rays on the same plot. The ratio of the counting rate from the source neutrons over the counting rate due to the source photons emitted from a single HELIPAK source is also presented in Figure 5.

As one can observe, the response of the 0.3-mm silicon detector to neutrons is less than 1% of the response due to gamma rays. It should be emphasized that the response functions were calculated for a bare detector in the case of neutrons and a "zero-absorption" aluminum-shielded detector in the case of gamma rays. Thus, a large fraction of the counts generated by the photons are due to the electrons emitted from the shield.

From the result of the Monte Carlo studies it was observed that the responses of the detector alone were about 36, 15, and 10% of the total response of the system (Si + Al) for gamma ray energies of 662, 835, and 1250 keV, respectively. Using these fractions one can obtain the approximate values for the neutron/gamma counting rate ratio for a bare silicon detector of 0.3 mm thick.

Since the magnitude of the error on the neutron counting rate is rather large (about 25%) one can obtain an average value for the counting rate ratio

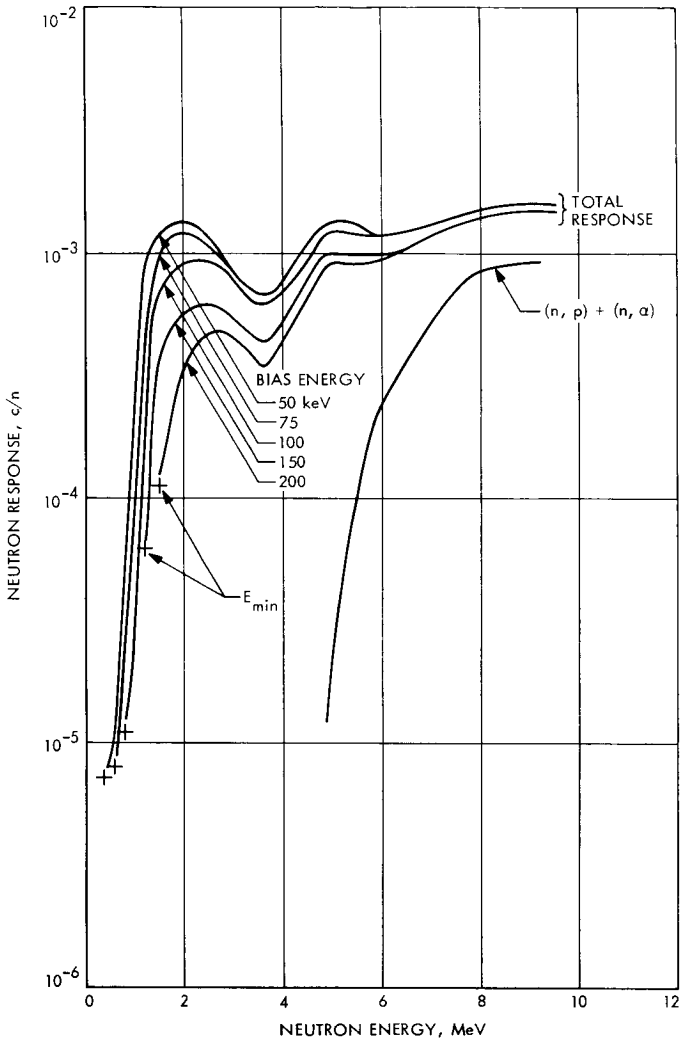

Figure 4. Response of silicon detector to monoenergetic neutrons

from Figure 5. This value can be estimated to be about (0.45 ± 0.10%) regardless of bias energy.

In order to obtain the exact counting rate ratio, one has to know the exact fraction of the gamma ray response that is due to the silicon detector alone. The Monte Carlo program was utilized only for three gamma ray energies and since this fraction ($f = r_{Si}^{\gamma}/[r_{Si}^{\gamma} + r_{Al}^{\gamma}]$, is highly energy dependent, the actual average counting rate ratio is much higher than 0.45%. If one uses an approximate average value of 20% for the response of the bare silicon detector to photons (f = 0.20), the average counting rate ratio $((c/s)_n/(c/s)_{\gamma})$ can be as high as (2.5 ± 0.5)%. However, this estimation is not important in the shielding analysis because one usually deals with a shielded detector and

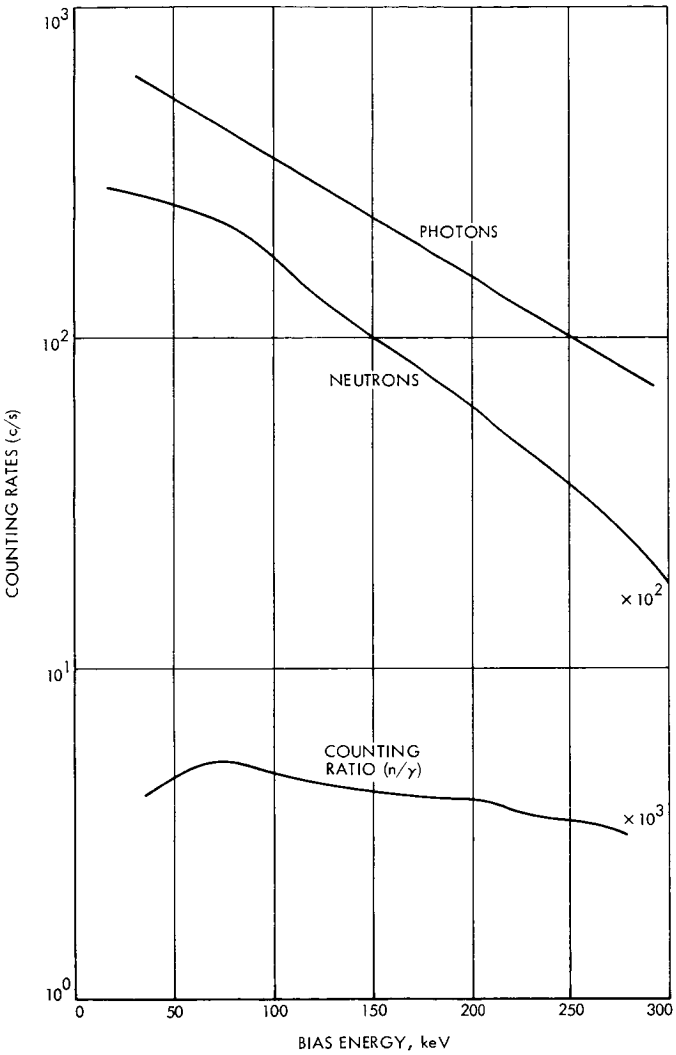

Figure 5. Counting rate ratio for a 300-μm silicon detector at 100 cm and 2200 W

would like to know the magnitude of the counting rate ratio with regard to the thickness of the shield. Consequently, the relative effects of the neutrons and photons have to be investigated for various dimensions of the absorber.

Total Counting Rate Ratio of a Shielded Silicon Detector

The total counting rate of a detector to photons and neutrons is based on the flux spectra of these particles and the respective response of the detector. In this analysis use has been made of the calculated neutron response (Reference 4) interacting with a bare silicon detector and the measured photon response (Reference 3) interacting with a shielded silicon detector.

In the case of the response of the bare detector to neutrons, the interactions considered (Reference 4) were (n,n), (n,p) and (n,α), thus

$$c_t^{n,D} = c_p^{n,D} + c_a^{n,D} + c_n^{n,D} \tag{4}$$

When the neutrons are allowed to interact in the absorber first and then in the detector, additional radiations will be generated from the shield; thus symbolically one can write:

$$c_t^{n,s} = c_p^{n,s} + c_a^{n,s} + c_n^{n,s} + c_\gamma^{n,s} + c_{\gamma e}^{n,s} \tag{5}$$

where D stands for detector and s stands for shield (Reference 5).

The protons, α particles, and recoil nuclei of the shield can be included in the total response function provided they can pass through their own path lengths in the shield and reach the detector. In order to investigate this problem, the maximum path length ($L_{i,\max}$) for these particles should be determined.

Since the maximum neutron energy ($E_{n,\max}$) is about 6 MeV, the maximum energy of the first three particles in the aluminum shield will be 3.8, 2.3 and 0.828 MeV for protons, α particles and Al nuclei. The corresponding maximum path lengths are 66 μm for protons, 7.2 μm for α particles and 0.044 μm for Al nuclei. From these results one can conclude that the contribution from Al nuclei is extremely small because only those Al nuclei which are generated in the last 0.044 μm of the shield can deposit their energy in the detector (which is subject to the largest pulse height defect) and the number of these nuclei are, of course, small.

In the case of protons and α particles, one would conclude that, since they have small path lengths, their combined contribution is also small. In addition, the response of these charged particles would remain constant as the thickness of the shield is increased (beam attenuation is not included at this time). After the dimension of the shield exceeds one path length, one expects no more contribution from protons and α particles.

In order to estimate the magnitude of the response of the silicon detector to photons generated by the source neutrons in the shield and the Compton electrons created by these gamma rays (also in the shield), an experimental set-up was hypothesized so that this problem could be simulated by a Monte Carlo computer program. This experiment was performed for a 0.218-cm aluminum shield. The result of this calculation indicates that the response of a 0.3-mm silicon detector to the photons emitted from the interaction of neutrons in the 0.218-cm aluminum shield for a typical neutron energy of 1.49 MeV and a typical bias energy of 100 keV is about 7.5×10^{-8} c/n for the $(n,n'\gamma)$ reaction and 2.3×10^{-7} c/n for the (n,γ) reaction, for a total response of 3.05×10^{-7} c/n for both reactions. At almost the same neutron energy and at 100 keV bias energy the response of the silicon detector to the elastically scattered neutrons (i.e., energy deposition due to the moving silicon nuclei in silicon) is about 7×10^{-4} c/n. This means the response of the silicon detector due to the photons emanated from the shield is less than 0.05% at a 100 keV bias energy and 1.49 MeV neutron energy. Thus, the ejected photons from the shield have an insignificant effect on the total response in this case.

The situation for Compton electrons emitted from the shield is even worse, because these electrons are created via the interaction of photons and the bound electron in the medium. In the first place the flux of these electrons is very low due to the fact that they are produced by the *secondary* particles (i.e., secondary photons). In the second place, the shield is much too thick to allow these electrons to get out. Therefore, one can neglect these electrons completely. As the shield thickness is increased, more photons are generated and they may have some contribution to the total counting rate, as will be demonstrated later.

As the thickness of the shield is increased, both the counting rates due to the source photons and source neutrons will be reduced because of the attenuation of the flux in the shield.

In order to calculate the counting rates at different bias energies and for various thicknesses, one should use techniques of numerical calculations, but due to the fact that the net effect of these secondary particles is small, one can introduce certain valid approximations so that the problem is significantly simplified:

(1) The radiation length of photons generated in the shield is equal to half the shield thickness.

(2) The response of the ith secondary particle (P and α) due to the interaction of neutrons in the shield is the same as the response of the same particle in the detector with the detector thickness enhanced.

(3) One may pull out the attenuation factors from the integral signs without changing the results significantly. This basically is because of the small variations in the total cross sections of neutrons and photons in the shield. The photon cross section varies from 3.75 to 1.57 barns for the energy range of 0.1 to 2.5 MeV. Similarly, the cross section

for neutrons varies between 3 and 2 barns for the energy range of 0.3 to 6 MeV.

(4) The path length of the charged particles (protons and particles) may be replaced by their maximum values.

(5) The cross-sectional area of the shield is assumed to be the same as the detector (namely 2 cm^2); therefore, the effect of buildup factor will be small and can be neglected.

(6) The secondary particles generated in the shield can leave the shield without entering into the detector. In the real case a Monte Carlo type of program is needed to follow each particle. In this calculation it is assumed that secondary particles can escape from the shield only in a forward direction. This assumption clearly will cause an overestimation of the total counting rate due to neutrons.

Therefore, one can now write a simple relationship for counting rate due to photons or neutrons (Reference 5):

$$C_t^{\gamma,A}(E_B) = \exp\left[-\mu_s^{\gamma}(\bar{E}_\gamma)\, t_s\right] C_t^{\gamma,D} \tag{6}$$

$$C_t^{n,A}(E_B) = \exp\left[-\mu_s^{n}(\bar{E}_n)\, t_s\right] C_t^{n,D} \times \left[1 + \left(1 + \frac{t_s}{2t_D}\right)\frac{C_\gamma^{n,D}}{C_t^{n,D}} \exp\left(+\Delta\mu_s \frac{t_s}{2}\right)\right] \tag{7}$$

The last term in this equation is a function of the thickness of the shield, t_s, and therefore will increase as t_s increases.

The counting rate ratio, then, can be obtained easily:

$$R(E_B, t_D) \equiv \frac{C_t^{n,A}}{C_t^{\gamma,A}} = K(E_B, t_D, t_s) \exp(-\mu_s t_s)\left[\frac{C_t^{n,D}}{C_t^{\gamma,D}}\right] \tag{8}$$

where $\mu_s^{\gamma}(\bar{E}_\gamma)$ means the photon attenuation cross section in the shield at average photon energy $\bar{E}_\gamma$ and where

$$\Delta\mu_s \equiv \mu_s^{n}(\bar{E}_n) - \mu_s^{\gamma}(\bar{E}_\gamma)$$

and K is the only function involved with the secondary particle ejected from the shield and is given by (Reference 5):

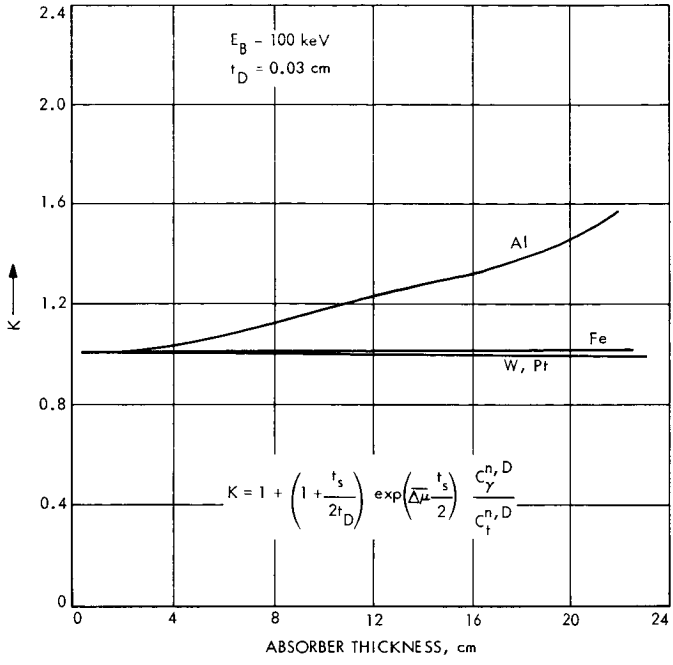

Figure 6. Function *K* versus absorber thickness

$$K(E_B, t_D, t_s) \equiv 1 + \left(1 + \frac{t_s}{2t_D}\right)\left(\frac{C_\gamma^{n,D}}{C_t^{n,D}}\right) \exp\left(+\Delta\mu_s \frac{t_s}{2}\right) \qquad (9)$$

In Figure 6 different values of K are plotted against the thickness of four different absorbers—aluminum, platinum, iron, and tungsten—with a 100-keV bias energy. From the result of this computation one can conclude that K is approximately equal to unity except for aluminum, for which K can have a value of 1.47 at the unlikely thickness of 20 cm. Even at this large thickness the value of 1.47 is not a large number considering the magnitude of the

$$C_t^{n,D} / C_t^{\gamma,D}$$

ratio at the 100-keV bias energy (~0.001).

The reason that K is so close to unity is that the

$$(C_\gamma)^{n,D} / (C_t)^{n,D}$$

ratio is small (Reference 5) (at 100-keV bias energy this ratio is less than 0.1%) and the $(1 + t_s/2t_D)$ term or the exponential term cannot compensate

for the small value of this ratio. The exponential term in K is not a great contributor because $\Delta\mu_s$ is a negative parameter for all elements considered here except for aluminum. This is why K is larger for aluminum than the other three elements; i.e., $\Delta\mu_s$ = -0.7, -0.244, -0.935 and +0.042 for W, Fe, Pt, and Al, respectively. As t_s increases, the exponential term decreases rapidly, while the $(1 + t_s/2t_D)$ term increases very slowly; thus K approaches unity very quickly for three of the four elements.

What all this mean is that K can be effectively assumed to be equal to one, and thus the magnitude of R depends upon the attenuation term only (Equation 9); for all practical purposes it is independent of the responses that the secondary charged particles (generated by neutrons in the shield) may produce in the detector. The effect of the electrons generated in the shield due to the photon interactions is included in the parameter $C_t^{\gamma,s}$ and thus the counting rate ratio is sensitive only to this secondary radiation. As the thickness of the detector, t_D, increases, the magnitude of counting rate due to photons generated in the shield, $C_\gamma^{n,D}$, will increase and the value of K increases also.

The average energy of the source photons is about 1.11 MeV, while the average energy of the photons created in the shield via $(n,n'\gamma)$ reaction is about 1.07 MeV; these are very close and one can neglect the difference between these two sources of gamma rays as far as their attenuations in the shield are concerned.

In Figure 7, the total counting rate of a 0.3-mm silicon detector exposed to a single HELIPAK source is plotted against various thicknesses of a plutonium absorber at a bias energy of 100 keV. The total counting rate due to the combined radiation is also plotted. One can notice that for shield thicknesses of under 2 to 3 cm neutrons have a very small effect in comparison with photons. This situation reverses itself above 6 cm.

The counting rate due to the neutrons becomes important at about 5 cm and becomes a dominant term at higher thicknesses. The fundamental cause of this effect is the fact that $(\Delta\mu)_{Pt} = \mu^n(\overline{E}_n) - \mu^\gamma(\overline{E}_\gamma)$ is a negative number ($\sim$ -0.935 cm^{-1}) and as t_s increases, the photons attenuate much faster than the neutrons. The same effect can be shown in a different manner by plotting the count rate *ratio* as a function of the thickness of the absorber. This plot is shown in Figure 8. In addition to platinum, the counting rate ratios for tungsten, iron, and aluminum are also shown.

The counting rate due to neutrons is less important for Al than other absorbers. Actually, the counting rate due to neutrons for aluminum always remains much smaller than the counting rate due to photons. The question: "At what point is the response due to neutrons comparable with photons?" is answered easily by setting the counting rate ratio equal to unity (i.e., R = 1). This situation occurs at about 5 cm for $_{78}$Pt, 8 cm for $_{74}$W and 22 cm for $_{26}$Fe. The reason for this difference has to do with the magnitude of $\Delta\mu_s$, which was discussed previously.

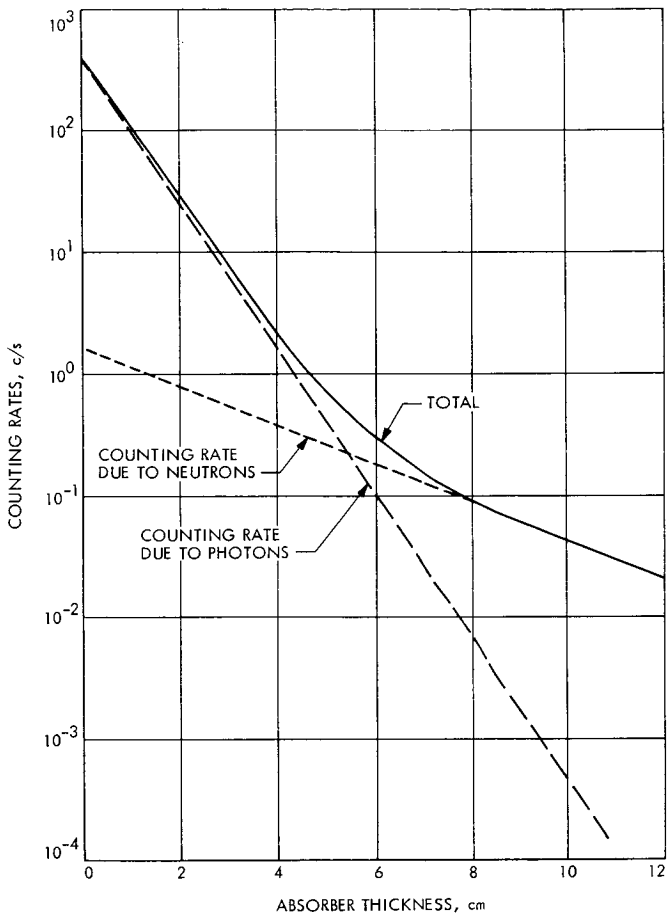

Figure 7. Total counting rate for a 300-μm silicon detector covered by platinum

Error Calculation

The magnitude of the uncertainties is estimated to about 28% when no absorber is considered. However, when various shields are used, the magnitude of the error increases rapidly, depending upon the thickness of the detector. Since the major cause of error is the error in the neutron response function (Reference 4), one can account for at least a 25% error for the counting rates due to neutrons. As the absorber thickness increases, the magnitude of error increases in accordance with the thickness of the detector because the error in the cross section doubles the error on the exponential factor for every relaxation length. Thus, at higher thicknesses the magnitude of the errors will increase.

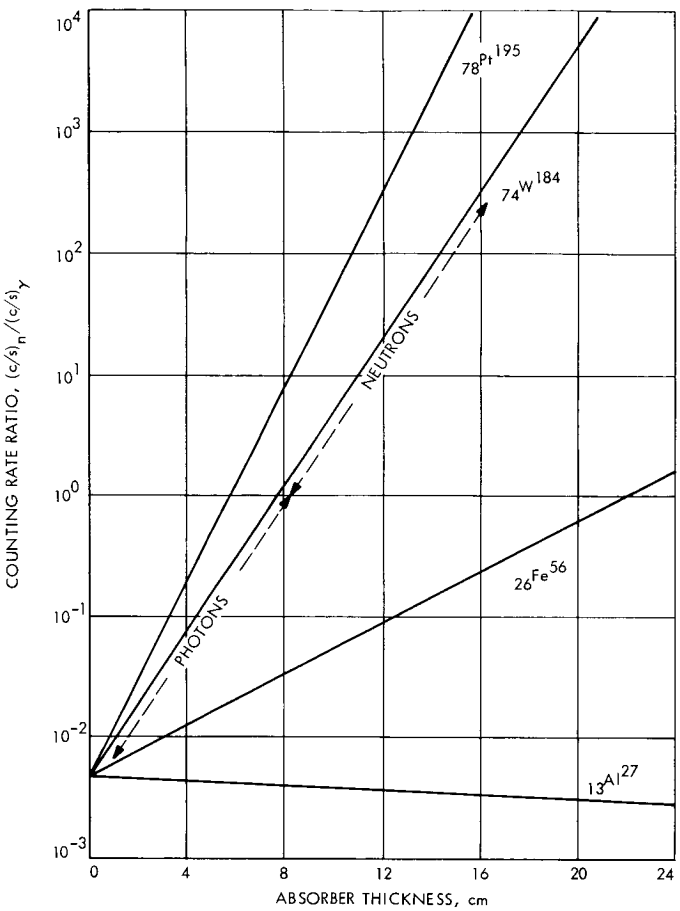

Figure 8. Total counting rate ratio for Pt, W, Fe, and Al

Conclusions

The most significant conclusions determined by this study are as follows:

The counting rate of a shielded 0.3-mm silicon detector to neutrons is practically independent of the secondary charged particles emitted from the shield (Figure 6).

The counting rate ratio of neutrons to photons for a shielded but thin detector is directly related to the ratio of the attenuation factors of these radiations (Equations 6, 7).

The effect of neutrons becomes comparable to that of photons at about 5 cm of platinum, 8 cm of tungsten and 22 cm of iron. For the aluminum shields the neutrons should never be significant (Figure 8).

For a 0.3-mm thick silicon detector positioned 100 cm away (radially) from a 2200 W(th) HELIPAK source within the MHW thermoelectric converter, the total neutron and gamma ray counting rate at a 100-keV bias energy is equal to 1.7 and 350 c/s, respectively. Therefore, the counting rate ratio can be estimated to be equal to (0.48 ± 0.10)% under the above assumptions. About 80% of the counting rate for the photons is due to the Compton electrons emitted from the shield and therefore the counting rate ratio for a 0.3-mm *bare* silicon detector is about 2.4%.

References

1. Anno, G. H. et al., "Analytical Radiation Transport Services in Support of JPL's Nuclear Power Sources Group," Progress Report No. 12. ART Associates, Santa Monica, Calif., February 1, 1971.

2. Jordan, T. M., "FASTER, a Fortran Analytical Solution of the Transport Equation by Random Sampling, Synthesis of Calculational Methods for the Design and Analysis of Radiation Shields for Nuclear Rocket Systems," Westinghouse Report WANL-PR-(LL)-010, June 1967.

3. Reier, M., "The Response of a Shielded 300-Micron Silicon Detector to Monoenergetic Gamma Rays From 0.279 to 2.75 MeV," EM 342-118, September 1970 (JPL internal document).

4. Taherzadeh, M., "The Analytically Determined Response of a 300-Micron Silicon Detector to a Polyenergetic Neutron Beam," EM 342-140, May 1970 (JPL internal document).

5. Taherzadeh, M., "The Response of a 300-Micron Silicon Detector to a Mixed Neutron and Gamma Field as a Function of Shield Material and Thickness," EM 342-147, Nov. 1971 (JPL internal document).

Index: antennas and transmission lines, structural engineering

Large Spacecraft Antennas: Conical Ring-Membrane Reflectors

R. E. Oliver and M. R. Trubert

Engineering Mechanics Division

A. H. Wilson

Environmental Sciences Division

A 1.83-m (6-ft)-diameter furlable conical Gregorian antenna based on a novel spoke-supported ring-membrane concept has been successfully demonstrated. Mechanical measurements of the conical reflecting surface, as well as RF gain measurements at Ku-band, show an rms surface deviation from the proper conical surface of 0.3 mm (0.012 in.),[1] and a repeatability after multiple furling–unfurling cycles of ±0.05 mm (0.002 in.). Design features and performance characteristics of this antenna indicate that the spoke-supported ring-membrane concept is a promising approach for producing large, furlable, lightweight, conical reflectors for spacecraft high-gain antennas.

Efforts directed toward the development of lightweight furlable conical reflectors for spacecraft high-gain antennas recently culminated in the successful demonstration of a 1.83-m (6-ft)-diameter conical Gregorian antenna based on the spoke-supported ring-membrane concept. Mechanical measurements of the main reflecting surface, as well as Ku-band RF tests of the entire antenna, show an rms surface of 0.3 mm (0.012 in.) from the desired cone. Repeatability of rms surface deviations after multiple furling–unfurling cycles is about ±0.05 mm (0.002 in.). This surface accuracy and repeatability compare very favorably with that previously achieved with a sheet metal design, namely, 0.2 mm ± 0.04 mm (0.008 in. ± 0.0015 in.).

RF performance tests at Ku-band, as measured by the Telecommunications Division, showed a gain of 47.55 dB, which corresponds to an efficiency of 58%.

[1] Values in customary units are included in parentheses after values in SI (International System) units if the customary units were used in the measurements or calculations.

The novelty of this spoke-supported ring-membrane concept is threefold:

(1) The conical reflecting surface is formed by a very thin lightweight membrane stretched between two circular rings.

(2) The outer registration ring is formed by a flat circular annulus that can be elastically deformed into a multi-lobed serpentine configuration.

(3) The outer ring is supported at a large number of points by pretensioned spokes. These spokes provide high out-of-plane bending stiffness to the ring, as well as a large number of adjustment points for the axial position of the ring, and are still compatible with the simple furling scheme.

The successfully demonstrated antenna is shown in its unfurled and furled configurations in Figures 1 and 2, respectively. The conical reflecting surface is formed by 0.025-mm (0.001-in.)-thick aluminized Mylar membrane. The spokes on the illuminated side of the main reflector are made of relatively RF-transparent fiberglass tapes; those on the nonilluminated side are steel wires. The outer ring is made of aluminum and is designed with section properties that permit elastic deformation into the serpentine configuration shown in Figure 2 when furled.

The reflecting surface was formed by nine separate gores. This approach was found to be more desirable than using a single continuous sheet to form

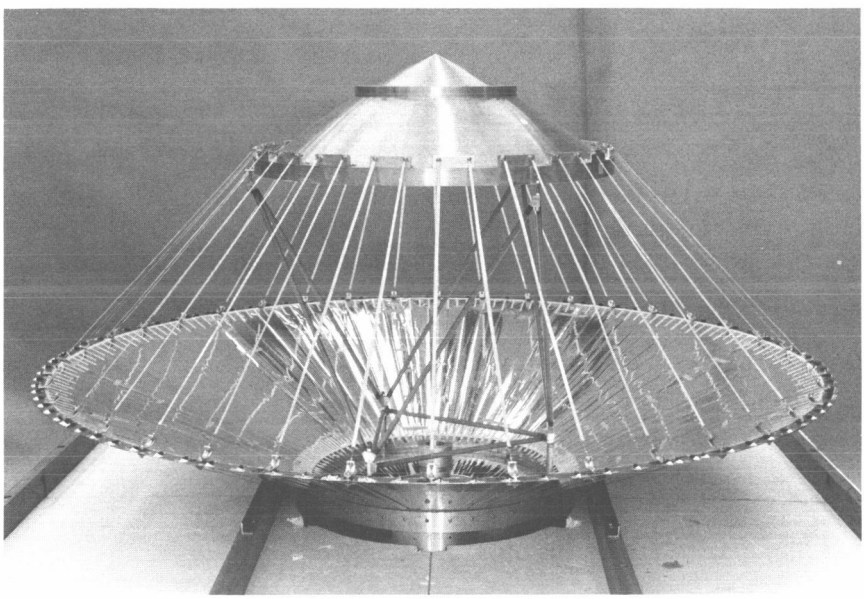

Figure 1. Unfurled 1.83-m (6-ft)-diameter spoke-supported ring-membrane conical Gregorian antenna

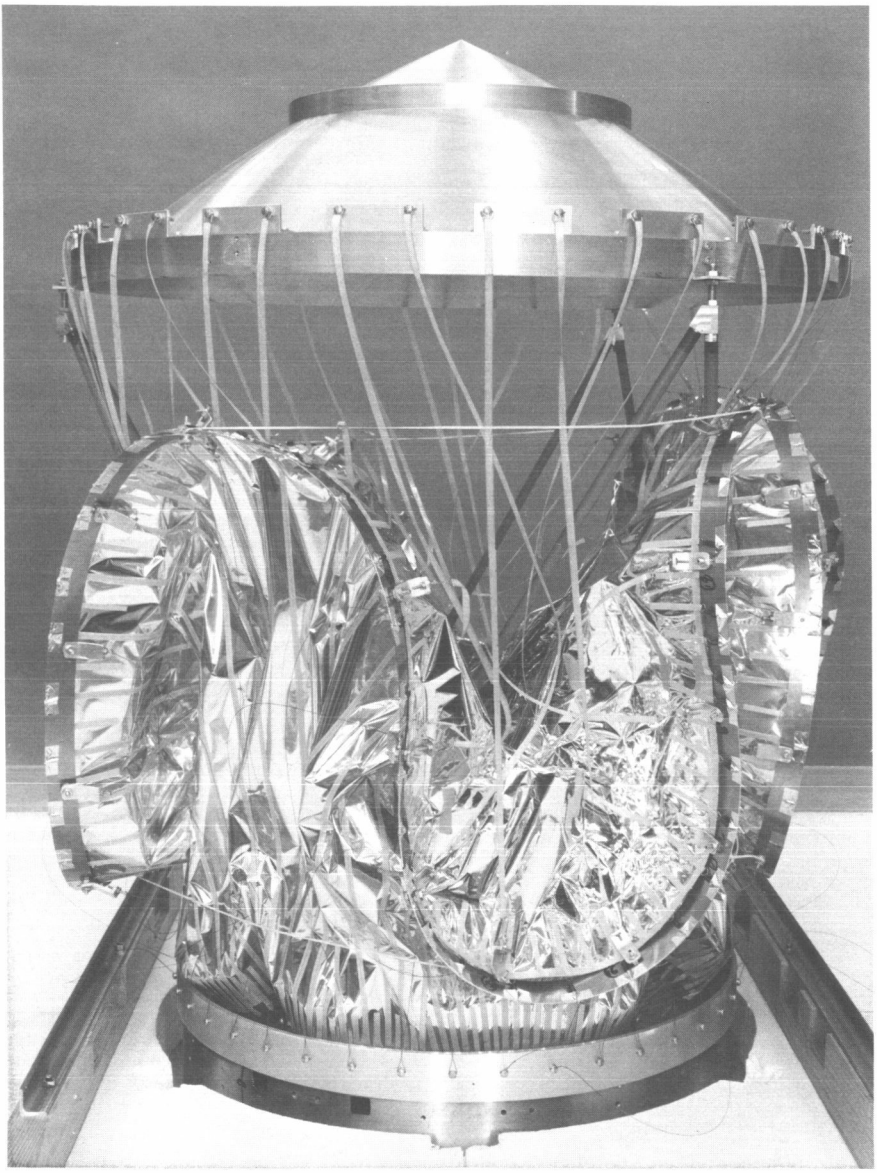

Figure 2. Furled 1.83-m (6-ft)-diameter spoke-supported ring-membrane conical Gregorian antenna

the conical surface. In the single sheet approach, deviations of the surface from the proper cone due to tolerance buildup can be compensated for only by applying radial tension to force the outer edge of the surface to coincide with the proper circle. Poisson's effect then produces circumferential tension which, in turn, produces adverse inward bulging of the membrane surface. In the multiple-gore approach, however, the individual gores can be adjusted radially to produce a close approximation to the desired conical surface.

Another significant feature of the membrane gore construction is shown in Figure 3. The membrane gores are supported by radial fiberglass tapes cemented to the backside (nonilluminated) of the Mylar. These tapes are attached to coil springs at each end. The springs are then stretched and attached to the inner and outer rings. Radial tension in the fiberglass tapes then tends to produce straight line elements between the inner and outer rings.

The weight of the conical reflector shown in Figure 1 (including the outer ring, spokes, Mylar sheet, and fittings) is about 17.8 N (4 lb). This is about one-third the weight of a comparable reflector based on the rib-supported sheet metal design concept (Reference 1).

The technique used for obtaining mechanical measurements of locations of points on the Mylar reflecting surface is illustrated in Figure 3. The antenna was mounted on a bearing with a vertical axis coincident with the

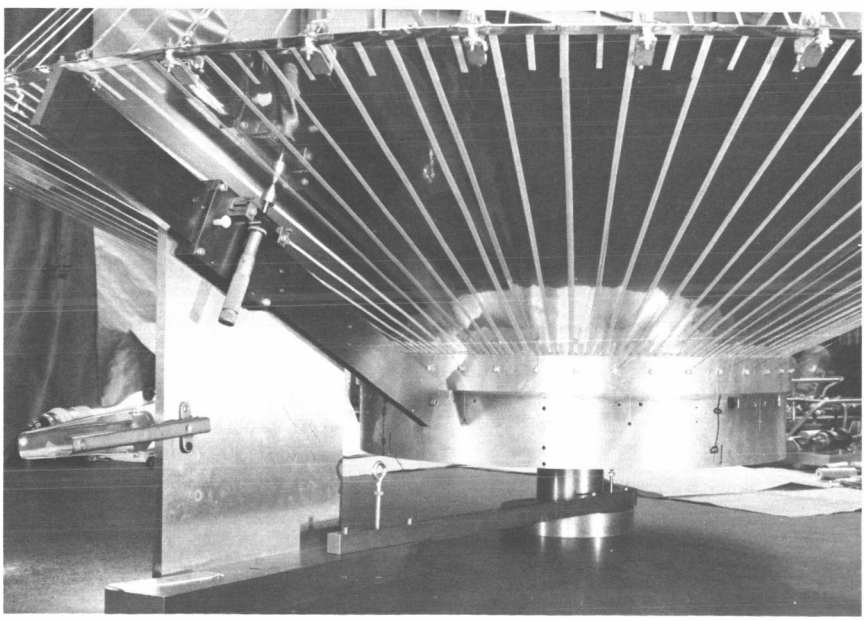

Figure 3. Mechanical surface measurement device

antenna feed axis. The fixture shown in Figure 3 provided measurements, by means of the micrometer screw, of the deviation of the backside of the Mylar membrane from the proper conical surface. Measurements at 160 points distributed over the Mylar surface were used to obtain estimates of the area-weighted rms surface deviation from the proper cone.

The mechanical measurement device shown in Figure 3 was also used in an adjustment procedure for decreasing the rms surface deviation. The lengths of the spokes supporting the outer ring are individually adjustable. This feature provides 40 equally spaced adjustment points (there are 40 pairs of spokes) on the outer ring. In practice, each of these 40 adjustment points was moved until the Mylar surface at a point near the adjustment point was on a cone of the proper half-angle and passing through the best-fit circle through the Mylar surface near the inner fixed ring.

The thin Mylar reflecting surface of this antenna is, of course, very sensitive to wind loads. In order to obtain meaningful RF test results on the outdoor antenna test range, it was necessary to protect the antenna from even slight air currents. The required protection was provided by a styrofoam box as shown in Figure 4. RF tests indicate that RF losses due to the styrofoam face of this box are negligible.

The technology development demonstrated by this antenna configuration is directly applicable to several new antenna concepts requiring furlable conical main reflectors (References 1–5). A more detailed description of the

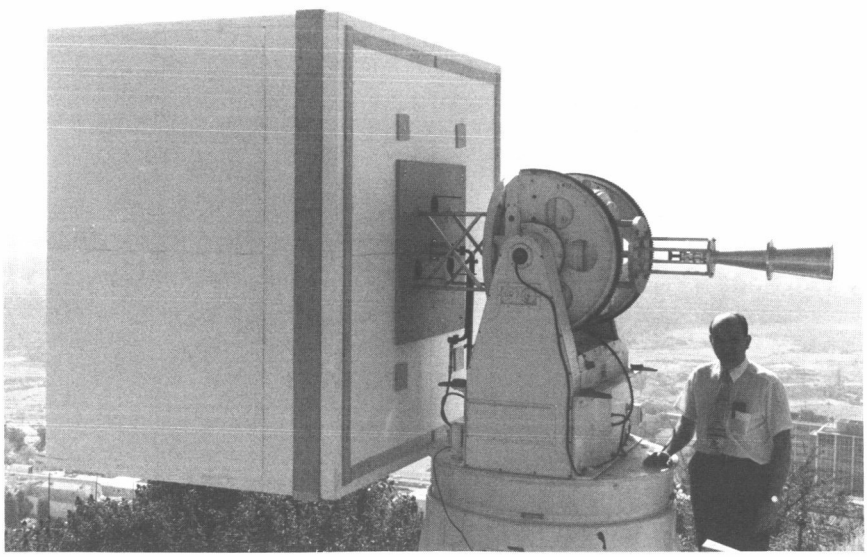

Figure 4. Styrofoam wind-protection cover for the 1.83-m conical Gregorian antenna

conical Gregorian antenna concept is presented in References 1, 2, and 5. Reference 6 describes development activities carried out during the past 1½ years and the evolution of concepts leading to the successful demonstration of a furlable spoke-supported ring-membrane conical antenna.

References

1. Ludwig, A. C., "Conical Reflector Antennas," *IEEE Trans.*, Vol. AP-20, No. 2, Mar. 1972.

2. Ludwig, A., "Spacecraft Antenna Research: Large Spacecraft Antennas (Non-Paraboloidal Reflector)," in *Supporting Research and Advanced Development*, Space Programs Summary 37-59, Vol. III, pp. 55–57. Jet Propulsion Laboratory, Pasadena, Calif., Oct. 31, 1969.

3. Oliver, R. E., "Large Spacecraft Antennas: New Geometric Configuration Design Concepts," in *JPL Quarterly Technical Review*, Vol. 1, No. 1, pp. 78–85. Jet Propulsion Laboratory, Pasadena, Calif., Apr. 1971.

4. Bright, T., Every, R., Sheppard, R., and Manson, R., "Systems Impact of a Conical Antenna for Planetary Communications," Preprint No. AAS-71-151, presented at the American Astronautical Society 17th Annual Meeting, Seattle, Washington, June 29-30, 1971.

5. Ludwig, A. C., and Hardy, J., "Spacecraft Antenna Research: Preliminary RF Test of Conical Gregorian Antenna," in *Supporting Research and Advanced Development*, Space Programs Summary 37-63, Vol. III, pp. 42–46. Jet Propulsion Laboratory, Pasadena, Calif., June 30, 1970.

6. Oliver, R. E., and Wilson, A. H., *Furlable Spacecraft Antenna Development: An Interim Report*, Technical Memorandum 33-537. Jet Propulsion Laboratory, Pasadena, Calif., Apr. 15, 1972.

Index: nonmetallic materials, solid-state physics, structural engineering

On the Elastic Properties of Fiber Composite Laminates With Statistically Dispersed Ply Orientations

E. Y. Robinson

Engineering Mechanics Division

Structural application of advanced composite filamentary materials requires lamination of the basic orthotropic plies into "angle-ply" laminates. The resulting elastic and strength properties depend on the pattern of orientation and are influenced by inevitable errors and inaccuracy in placement of the angle plies. Misorientation results also from irregular displacements following processing at elevated temperatures.

This article reviews the effect on elastic properties of orientation dispersion. The conventional constitutive relations are recast in a homologous form to account for orientation dispersion by addition of a single parameter. Graphical results are presented to show the behavior of the most important advanced composite materials. The results are directly useful for estimating effects of manufacturing inaccuracy and for design of partially oriented reinforced structures.

Introduction

JPL interest in structural application of advanced composites stems from the potential weight saving and better performance of these materials in spacecraft structure. The work described here provides insight into the effect of accuracy limits in fabricating laminates, and gives a readily usable design technique for partially oriented material systems.

Dispersion of orientation in a fiber composite is necessary (and usually unavoidable) in molded structures made with short segments, and provides useful mechanical properties at various directions. Sometimes a uniform orientation distribution is desired to yield in-plane isotropic behavior in a molded fiber-reinforced component. More often the required properties exceed the strength and stiffness of the laminate isotropic limits, and partial orientation of the material is introduced to up-grade properties in selected directions, but at the expense of certain properties in other directions. Alternatively, precisely oriented material may be added to the uniformly

distributed random phase to form another type of partially oriented laminated material. The analysis of such structures applies to inaccurately fabricated angle-ply laminates in which inevitable errors cause a dispersion of ply orientation about the intended nominal directions. The method also applies to elastic analysis of fittings, truss joints, and similar components where selective reinforcement is combined with random phases. Essential analytical results are presented here without detailed derivation.

Analytical Background

Lamination theory is covered in the Air Force Design Guide for Advanced Composites and other sources (References 1, 2, and 3). Some elements of laminate analysis are given here to provide a useful description of the equations appropriate to randomly oriented layers.

A generalized Hooke's Law is used, with the stiffness elements $Q(ij)$ defined by the matrix equation:

$$\sigma(i) = [Q(ij)]\,[\epsilon(j)]$$

(See Table 1 for a glossary of terms used in this article.)

The elements of $Q(ij)$ depend on the orientation of the ply principle elastic axes (natural directions) in the loading coordinate system. When

Table 1. Glossary of terms

$\sigma(i)$	stresses
$\epsilon(i)$	strains
E_1	principle Young's modulus
E_2	secondary Young's modulus
ξ	$=E_2/E_1$
ν_1	primary Poisson ratio
G_1	shear modulus in 1–2 direction; elastic constants without subscripts denote the isotropic asymptotes
$Q(ij)$	stress–strain stiffness element
U_k	coefficients of the multiple-angle formulation for coordinate transformation of $Q(ij)$
θ	angle of *orientation* of the natural longitudinal direction measured positive counter-clockwise from the reference coordinate axis
$f(\theta)$	frequency distribution function of orientation angle
$\overline{Q}(ij)$	properties of the multi-layer laminate, analogous to the single layer properties defined above
α	intended orientation
$\pm\delta$	bounds of orientation dispersion

these directions coincide (i.e., $\theta = 0$), the matrix elements are the natural direction orthotropic properties given by

$$Q(11) = \frac{E_1}{1 - \xi\nu_1^2} \qquad Q(22) = \frac{E_2}{1 - \xi\nu_1^2}$$

$$Q(12) = \frac{\nu_1 E_1}{1 - \xi\nu_1^2} \qquad Q(66) = G_1$$

When the natural direction is oriented at θ, the stiffness coefficients $Q(ij)$ are given by

$$\left.\begin{aligned} Q(11) &= U_1 + U_2 \cos(2\theta) + U_3 \cos(4\theta) \\ Q(22) &= U_1 - U_2 \cos(2\theta) + U_3 \cos(4\theta) \\ Q(12) &= U_4 - U_3 \cos(4\theta) \\ Q(66) &= U_5 - U_3 \cos(4\theta) \\ Q(16) &= +\frac{1}{2} U_2 \sin(2\theta) + U_3 \sin(4\theta) \\ Q(26) &= +\frac{1}{2} U_2 \sin(2\theta) - U_3 \sin(4\theta) \end{aligned}\right\} \quad (1)$$

U_1, U_4, and U_5 are invariants, unaffected by rotation. The coefficients $U(i)$ are defined in References 1 and 3.

Now consider a large number n of similar plies in a laminate of unit thickness, with orientations distributed from $-\delta$ to $+\delta$. The laminate stiffness elements are obtained by summing the stiffness contributions from each ply. For large n and small angular interval, we can pass from the sum to the integral:

$$\overline{Q}(ij) = \int_{-\delta}^{\delta} Q(ij)\, f(\theta)\, d\theta \quad (2)$$

where $f(\theta)$ is the normalized frequency distribution of orientation, and $Q(ij)$ are given by Equation 1.

Quasi-Isotropic Limits

The in-plane isotropic elastic limits of a composite result when the orientation distribution is uniform, $f(\theta) = 1/(2\delta)$, and unbounded:

$$\overline{Q}(ij) = \frac{1}{\pi} \int_{-\frac{\pi}{2}}^{\frac{\pi}{2}} Q(ij)\, d\theta$$

This equation shows that the "invariant" terms U_1, U_4, and U_5 are the unbounded θ averages of the $Q(ij)$ for symmetrical probability distributions.

The quasi-isotropic engineering parameters are

$$\nu = \frac{U_4}{U_1} \qquad G = U_5 \qquad E = U_1\,(1 - \nu^2)$$

It is instructive to examine the invariants as given in terms of the engineering constants of the individual layers:

$$\left.\begin{aligned} U_1 &= \frac{E_1}{8}\left[\frac{3 + 4\frac{G_1}{E_1} + \xi\left(3 + 2\nu_1 - 4\nu_1{}^2\,\frac{G_1}{E_1}\right)}{1 - \xi\nu_1{}^2}\right] \\ U_4 &= \frac{E_1}{8}\left[\frac{1 - 4\frac{G_1}{E_1} + \xi\left(1 + 6\nu_1 + 4\nu_1{}^2\,\frac{G_1}{E_1}\right)}{1 - \xi\nu_1{}^2}\right] \\ U_5 &= \frac{E_1}{8}\left[\frac{1 + 4\frac{G_1}{E_1} + \xi\left(1 - 2\nu_1 - 4\nu_1{}^2\,\frac{G_1}{E_1}\right)}{1 - \xi\nu_1{}^2}\right] \end{aligned}\right\} \qquad (3)$$

This form exhibits the contribution of element Poisson ratio and anisotropy to the invariant parameters. The theoretical value for the isotropic Poisson ratio, given by U_4/U_1, shows a fundamental trend to values around ⅓ which is only slightly altered by varying the anisotropy parameters. This tendency to Poisson ratios around ⅓ is seen to be a structural consequence of combining a large number of randomly oriented orthotropic layers into a quasi-isotropic laminate. For random layers of unbonded filaments ($E_2 = G_{12} = 0$) Equation 3 predicts $\nu = ⅓$. This result sheds light on the well

known fact that nearly all macroscopically isotropic materials exhibit Poisson ratios in the vicinity of 0.3. The isotropic sheet may therefore be modeled as an ensemble of random orthotropic layers. The isotropic Poisson ratio is plotted in Figure 1 for the case

$$\frac{G_1}{E_1} = \frac{\xi}{2(1+\nu_1)} \tag{4}$$

and several values of ν_1.

For highly anisotropic constituent layers, the quasi-isotropic parameters can be estimated by $E = E_1/3$; $G = E_1/8$; $\nu = 1/3$. These should be lower bounds for properly made laminates.

The isotropic limits for several important types of advanced composites are collected in Table 2. Observed data (References 4, 5 and 6) are also included.

Angle-Ply Laminates With Dispersed Orientation

In angle-ply laminates the concern is with random partial orientation distributed about an intended nominal direction. The orientations are assumed to be distributed in the interval $-\delta$ to $+\delta$ about the nominal

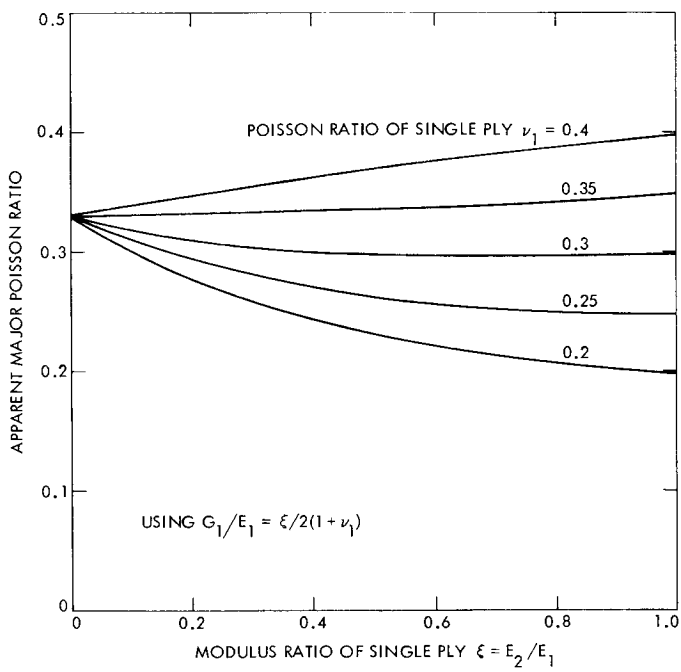

Figure 1. Poisson ratio of quasi-isotropic laminates

Table 2. Quasi-isotropic values for advanced composites

Material	Single-ply elastic parameters				Predicted isotropic limits			Observed E for quasi-isotropic specimens, 10^9 N/m^2 (10^6 psi)
	E_1, 10^9 N/m^2 (10^6 psi)	E_2, 10^9 N/m^2 (10^6 psi)	G_1, 10^9 N/m^2 (10^6 psi)	ν_1	E, 10^9 N/m^2 (10^6 psi)	G, 10^9 N/m^2 (10^6 psi)	ν	
High-modulus graphite/epoxy	275.8 (40)	8.3 (1.2)	5.5 (0.8)	0.25	99.3 (14.4)	37.9 (5.5)	0.31	96.5 (14.0)
Intermediate graphite/epoxy	206.8 (30)	6.9 (1)	6.9 (1)	0.25	76.5 (11.1)	29.6 (4.3)	0.29	
High-strength graphite/epoxy	137.9 (20)	6.9 (1)	5.2 (0.75)	0.25	52.4 (7.6)	20.0 (2.9)	0.29	82.7 (12.0)
Type 1002 glass/epoxy	39.3 (5.7)	9.6 (1.4)	6.9 (1)	0.25	21.4 (3.1)	9.0 (1.3)	0.20	20.7 (3.0)
S-glass/epoxy	55.8 (8.1)	13.1 (1.9)	6.9 (1)	0.23	28.3 (4.1)	11.0 (1.6)	0.25	
Boron/epoxy	206.8 (30)	20.7 (3)	6.9 (1)	0.35	81.4 (11.8)	30.3 (4.4)	0.34	
Boron-glass/ epoxy (1:2)	103.4 (15)	15.8 (2.3)	6.9 (1)	0.29	45.5 (6.6)	17.2 (2.5)	0.3	69.0 (10)
Boron/ aluminum	206.8 (30)	117.2 (17)	62.0 (9)	0.3	148.2 (21.5)	57.2 (8.3)	0.29	

direction angle α. The stiffness elements for unit thickness laminate are given by

$$\bar{Q}(ij) = \int_{\alpha-\delta}^{\alpha+\delta} Q(ij)\, f(\theta)\, d\theta \tag{5}$$

For a uniform distribution, $f(\theta) = 1/(2\delta)$, the integration gives:

$$\left.\begin{aligned}
Q(11) &= U_1 + U_2 \cos(2\alpha)\left(\frac{\sin 2\delta}{2\delta}\right) + U_3 \cos(4\alpha)\left(\frac{\sin 4\delta}{4\delta}\right) \\
Q(22) &= U_1 - U_2 \cos(2\alpha)\left(\frac{\sin 2\delta}{2\delta}\right) + U_3 \cos(4\alpha)\left(\frac{\sin 4\delta}{4\delta}\right) \\
Q(12) &= U_4 - U_3 \cos(4\alpha)\left(\frac{\sin 4\delta}{4\delta}\right) \\
Q(66) &= U_5 - U_3 \cos(4\alpha)\left(\frac{\sin 4\delta}{4\delta}\right) \\
Q(16) &= \frac{U_2}{2} \sin(2\alpha)\left(\frac{\sin 2\delta}{2\delta}\right) + U_3 \sin(4\alpha)\left(\frac{\sin 4\delta}{4\delta}\right) \\
Q(26) &= \frac{U_2}{2} \sin(2\alpha)\left(\frac{\sin 2\delta}{2\delta}\right) - U_3 \sin(4\alpha)\left(\frac{\sin 4\delta}{4\delta}\right)
\end{aligned}\right\} \tag{6}$$

As the dispersion limit δ approaches zero, the ideal anisotropic results of Equation 1 are obtained. When δ reaches $\pi/2$, the isotropic limits result. Equation 6 is identical in form (homologous) to Equation 1 if modified values are used for U_2 and U_3:

$$\bar{U}_2 = U_2 \frac{\sin(2\delta)}{2\delta}$$

$$\bar{U}_3 = U_3 \frac{\sin(4\delta)}{4\delta}$$

Equation 6 provides a new generalized form of the constitutive elements given by Equation 1. The homologous formulation allows simple alteration of existing computation procedures to incorporate effects of uniform, bounded dispersion, and for analysis of partially oriented composites.

The engineering properties of certain angle-ply laminates with dispersed orientation were calculated and are plotted on Figures 2 and 3. Most engineering applications utilize orthotropic laminates in which orientations

at $+\alpha$ and $-\alpha$ are balanced. For such laminates the orthotropic engineering parameters are calculated by

$$\left.\begin{aligned} \bar{\nu}_1 &= \frac{\bar{Q}(12)}{\bar{Q}(11)} \qquad \bar{\xi} = \frac{\bar{Q}(22)}{\bar{Q}(11)} \\ \bar{E}_1 &= \bar{Q}(11)\left[1 - \bar{\xi}\bar{\nu}_1^{\,2}\right] \qquad \bar{E}_2 = \bar{\xi}\bar{E}_1 \qquad \bar{G} = \bar{Q}(66) \end{aligned}\right\} \tag{7}$$

The effects of various dispersed orientations are shown in Figure 2 for the $\pm\theta$ class of orthotropic laminates. Ultra-high modulus and high-strength graphite/epoxy advanced composites were used for Figure 2. Figure 2c shows the profound effect of dispersion on shear modulus. The orthotropic properties of partially oriented composites (uniform dispersion from $-\delta$ to $+\delta$ with $\alpha = 0$) are shown in Figure 3 for the same materials. These plots demonstrate the utility of the reformulation given by Equation 6 to analyze more realistic laminate systems.

The laminate analysis assumes that all layers are acting contiguously and are mutually restrained by interlaminar shears, caused by differences in the Poisson ratio and layer stresses. This assumption probably leads to an upper bound. The lower bound condition occurs when layers contract independently of one another and the laminate Young's modulus is simply the weighted average of the layer moduli values (Reference 5).

Experimental data on some molded partially oriented composite (Reference 6) were compared to the prediction of these equations. The partially oriented material was made by molding short strips [2.54 by 0.32 cm (1 by ⅛ in.)] of composite in a 1.27-cm (½-in.)-wide mold. The resulting coupon is assumed to have a uniform dispersion of orientation of ±22 deg to the major axis. The observed values and predictions are collected in Table 3.

Random Phase Laminated With Partially Oriented Material

The problem of an isotropic phase laminated with either unidirectional material or partially oriented material is very conveniently analyzed by the methods presented.

If r is the volume ratio of isotropic-to-oriented material in a unit thickness laminate, the stiffness-matrix elements are given again by a form homologous to Equation 1, provided the U_2 and U_3 terms are modified. The modifications of the U_2 and U_3 terms, to include effects of dispersion and the type of lamination considered in this section, are

$$\left.\begin{aligned} \bar{U}_2 &= U_2\left(\frac{1}{1+r}\right)\frac{\sin(2\delta)}{2\delta} \\ \bar{U}_3 &= U_3\left(\frac{1}{1+r}\right)\frac{\sin(4\delta)}{4\delta} \end{aligned}\right\} \tag{8}$$

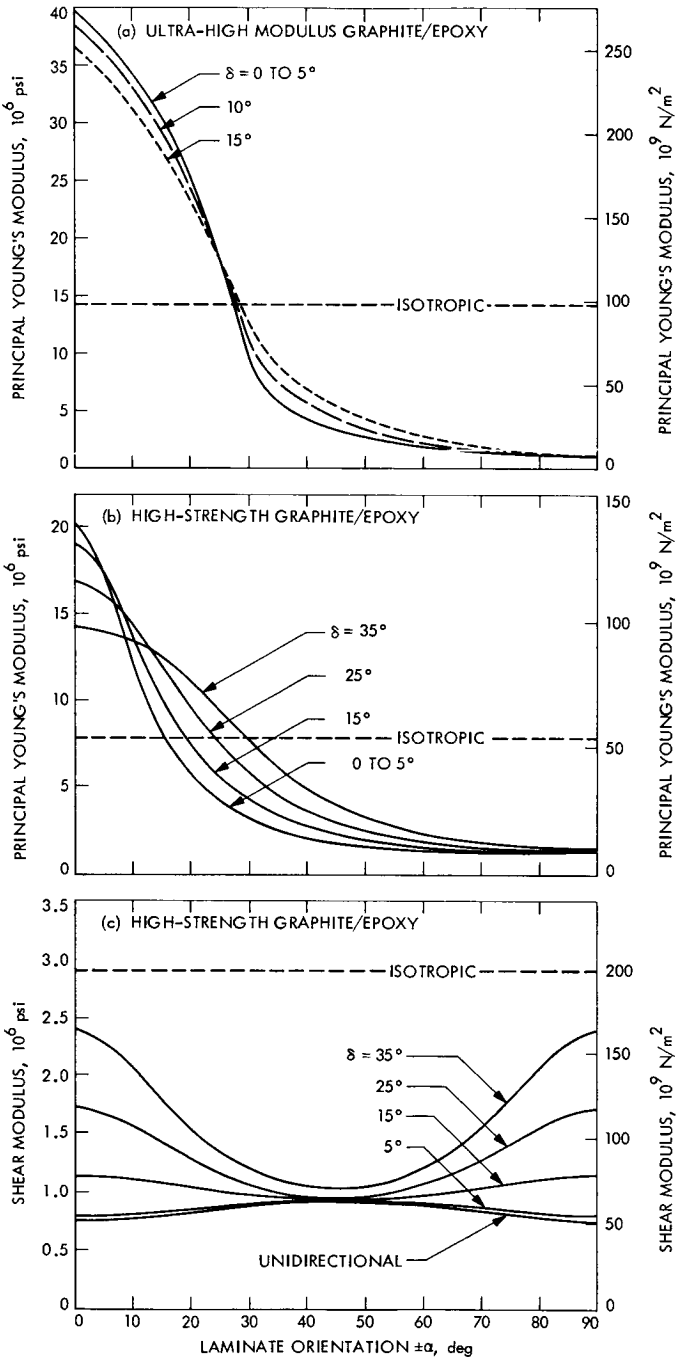

Figure 2. Principal elastic modulus for $\pm\theta$ laminates with dispersed orientation

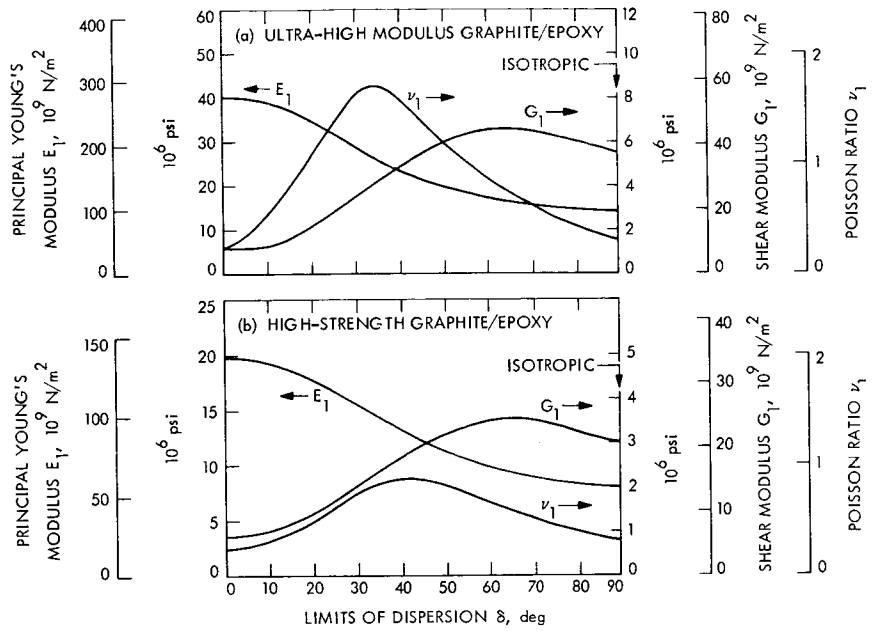

Figure 3. Principal orthotropic properties of partially oriented advanced composites

The engineering parameters of this laminate may be calculated using these modified values in Equation 7, provided the oriented reinforcing phase is of the $\pm\theta$ type.

A few results for graphite/epoxy systems are shown in Table 4.

Conclusions

The preceding analytical approach provides useful predictions on the elastic behavior of laminated partially oriented composites. The following conclusions are noted:

(1) Real orientation errors in a laminate may be conveniently approximated by the methods presented to indicate expected variation of engineering parameters.

(2) The analytical results demonstrate the utility of the multiple-angle formulation of the stiffness coordinate transformation. Results are obtained directly in a clear and concise form.

(3) The constitutive relation of Equation 6 modified by Equation 8 is a useful homologous relation allowing direct analysis for angular dispersion as well as multi-phase lamination.

(4) Calculated results are in reasonable agreement with the limited experimental data available.

Table 3. Orthotropic elastic properties of partially oriented composites[a]

Material	Predicted orthotropic properties				Observed Young's modulus E_1, 10^9 N/m^2 (10^6 psi)
	E_1, 10^9 N/m^2 (10^6 psi)	E_2, 10^9 N/m^2 (10^6 psi)	G_1, 10^9 N/m^2 (10^6 psi)	ν_1	
Intermediate graphite/epoxy	172.4 (25)	7.58 (1.1)	14.5 (2.1)	1.1	118.6 (17.2)
High-strength graphite/epoxy	117.2 (17)	7.58 (1.1)	10.3 (1.5)	0.89	107.6 (15.6)
Boron-glass/epoxy (1:2)	89.8 (13)	15.86 (2.3)	10.3 (1.5)	0.5	93.1 (13.5)

[a]Uniform orientation dispersion from −22 deg to +22 deg.

Table 4. Elastic properties of graphite/epoxy isotropic phase reinforced with oriented phase

Material	r	δ, deg	E_1, 10^9 N/m^2 (10^6 psi)	E_2, 10^9 N/m^2 (10^6 psi)	G_1, 10^9 N/m^2 (10^6 psi)	ν_1	Isotropic part of laminate, %
High-strength graphite/epoxy	0	0	137.9 (20)	6.9 (1)	6.9 (1)	0.25	0
	0.11	0	129.6 (18.8)	11.9 (1.73)	8.3 (1.2)	0.26	10
	0.5	15	103.4 (15)	23.4 (3.4)	13.1 (1.9)	0.33	33
	1	15	92.4 (13.4)	31.8 (4.61)	15.2 (2.2)	0.31	50
	1	25	86.9 (12.6)	31.9 (4.63)	17.2 (2.5)	0.32	50
	3	25	69.0 (10.0)	42.1 (6.1)	17.9 (2.6)	0.29	75
Ultra-high modulus graphite/epoxy	0	0	275.8 (40)	8.3 (1.2)	6.2 (0.9)	0.25	0
	0.11	0	258.6 (37.5)	17.9 (2.6)	9.0 (1.3)	0.29	10
	0.5	15	206.9 (30)	41.4 (6)	20.0 (2.9)	0.38	33
	1	15	180.0 (26.1)	57.2 (8.3)	24.8 (3.6)	0.35	50
	1	25	167.5 (26.1)	57.0 (8.27)	29.0 (4.2)	0.41	50
	3	25	133.8 (19.4)	79.3 (11.5)	33.8 (4.9)	0.34	75

(5) The method is readily extended to questions of thermal expansion and stability, which are of primary importance in space-antenna programs.

(6) Similar analytical approaches, based on the compliance (strain–stress) elements, may be used to evaluate the effect of irregular orientation along the length of a ply or tape (so-called fiber washing, or "wavy orientation"). This applies to tape-wound structures such as rocket motor cases, wherein nongeodesic winding and high-temperature curing cause irregular orientation along the tape length as well as between layers.

References

1. *Structural Design Guide for Advanced Composite Materials*, Second Edition. Prepared under AF Material Laboratory Contract No. F33615-69-C-1368 by Los Angeles Division of North American Rockwell Corp., Los Angeles, Calif., Jan. 71.

2. Ashton, J. E., Halpin, J. C., and Petit, P. H., *Primer on Composite Materials*, p. 21. Technomic Publishing Co., Stamford, Conn., 1969.

3. Tsai, S. W., and Pagano, N. J., "Invariant Properties of Composite Materials," in *Composite Materials Workshop*, p. 233. Technomic Publishing Co., Stamford, Conn., 1968.

4. "Non-Metallic News," *Materials Engineering*, Jan. 1970.

5. Nielsen, L. E., and Chen, P. E., "Young's Modulus of Composites with Randomly Oriented Fibers," *J. Composite Materials*, Vol. 3, No. 2, p. 352, June 1969.

6. *Goodyear Aerospace Data Sheets*, Goodyear Aerospace Co., Akron, Ohio.

JPL Quarterly Technical Review Volume 2, Number 2 July 1972

Index: antennas and transmission lines, electric propulsion, plasma physics, wave propagation

Spacecraft Ion Beam Noise Effects

G. L. Anenberg

Telecommunications Division

An estimate of the antenna noise temperature and the uplink signal-to-noise ratio (S/N) has been made for Bremsstrahlung radiation emitted by a spacecraft ion beam; a worst-case situation in which the spacecraft antenna is located in the exit plane of the ion beam and directed at varying angles into the ion beam is assumed. Numerical results of the antenna noise temperature versus antenna pointing angle are given for a typical set of ion-beam and antenna-pattern parameters. The uplink signal-to-noise ratio due to the ion-beam noise alone is given in terms of a critical range in AU at which a typical ranging transmission is received with S/N = 0 dB. The effects of the ion-beam divergence angle and antenna distance on the ion beam are also presented. Results of the study show typical increases in the antenna noise temperature of about 0.2 K and critical ranges of the order of 3–5 AU. An ion engine thus generally introduces an undetectable level of noise into a spacecraft receiver.

Introduction

This article examines the magnitude of the noise interference in an uplink signal reception due to the operation of an ion engine onboard a spacecraft. The discussion is limited to noise generated by the exhaust beam as a result of ion–electron collisions, or "Bremsstrahlung radiation." Degradation is estimated in terms of the uplink received signal-to-noise ratio and the increase in antenna noise temperature. This activity represents one phase of the SEPSIT (Solar Electric Propulsion System Integration Technology) program to determine the interaction of a solar electric propulsion system with other spacecraft subsystems.

Under ideal conditions, the spacecraft antenna is pointing away from the ion-beam axis; thus there is little chance for ion-noise interference. If the antenna is steerable, however, there is a possibility that the antenna might point into the exhaust beam during certain portions of its mission. This article thus assumes a worst-case spacecraft antenna/ion-beam configuration in which the antenna is located in the exit plane of the ion engine exhaust, at a distance R_a from the beam axis, and pointing in the direction $\phi = \pi/2$, $\theta = \psi$ (see Figure 1). R_0 is the beam exit radius and α is the beam divergence

angle. The geometry of this worst-case configuration simplifies the mathematics and provides an upper limit to other, perhaps more realistic, cases.

The incident noise power to the antenna from the ion beam is obtained by integrating the Bremsstrahlung radiation, weighted by the antenna gain pattern, over the volume of the exhaust plume. We first discuss the radiative properties of the exhaust-beam model.

Radiative Properties of the Exhaust Beam

The exhaust of an ion-propulsion engine consists of a diverging beam of ions, which are neutralized outside of the engine by injected electrons. These electrons have a certain thermal velocity, and thus suffer Coulomb

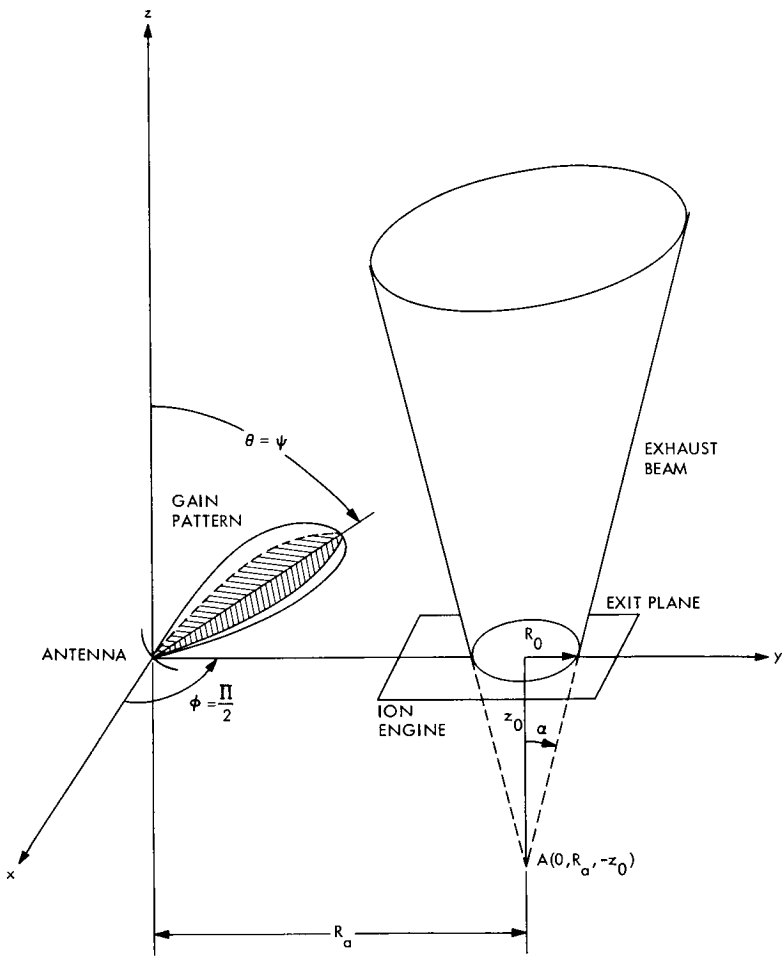

Figure 1. Spacecraft antenna/exhaust beam configuration

collisions with neighboring ions which produces Bremsstrahlung radiation. A numerical expression for the radiated spectral power density is given by Heald (Reference 1):

$$S_b = \frac{3.2 \times 10^{-47} G_a n^2 \exp(-h\omega/eT)}{\sqrt{T}} \text{ watts/cm}^3\text{/Hz} \qquad (1)$$

where n is the electron density in particles/cm^3, T is the electron temperature in electron volts and G_a is the "Gaunt factor" (typically between 1 and 10), which accounts for the collective effects of ion–electron interactions for varying collision impact parameters. At microwave frequencies, the noise spectrum is essentially "white" and independent of frequency.

To find the power radiated by the ion beam, spatial variations of the electron density and temperature must be assumed throughout the volume of the beam. A truncated conical beam with a uniform core (i.e., no transverse variation) and a decreasing axial dependence is assumed in the work that follows. Approximate variations for $n(z)$ and $T(z)$ have been investigated by Sellen (Reference 2) for a constant current, conservative energy flow; the normalized dependence is

$$\frac{n(z)}{n_0} = \frac{1}{\left(1 + \frac{z}{z_0}\right)^2}, \qquad \frac{T(z)}{T_0} = \frac{1}{\left(1 + \frac{z}{z_0}\right)^{4/3}} \qquad (2)$$

where n_0 and T_0 are the exit plane (i.e., $z = 0$) values, and z_0 is the distance from the apex of the cone to the x–y exit plane. The axial dependence of $S(z)$ is thus

$$S_b(z) = \frac{S_0}{\left(1 + \frac{z}{z_0}\right)^{10/3}} \qquad (3)$$

where S_0 is the exit plane value of S_b.

Antenna Noise Temperature

The energy radiated from a source may be expressed in terms of its brightness b in units of power/area/steradian/Hz. A brightness temperature T_b associated with this radiation is found by equating it to the equivalent

Planck radiation from a blackbody at a temperature T_b. In the limit $hf << kT_b$, the radiation from a blackbody is

$$b = \frac{2kT_b}{\lambda^2} \tag{4}$$

For the case considered here, which assumes isotropic radiation, the brightness of the ion beam is given by $S_b(r,\theta,\phi)/4\pi$, where r, θ, and ϕ are the spherical coordinates shown in Figure 2. A single integration over the line of sight produces the brightness temperature $T_b(\theta,\phi)$:

$$T_b(\theta,\phi) = \frac{\lambda^2}{2k} \int_{r_1(\theta,\phi)}^{r_2(\theta,\phi)} \frac{S_b(\theta,\phi)\, dr}{4\pi} \tag{5}$$

The above expression neglects absorption since the optical depth is much larger than the beam dimension. The limits $r_1(\theta,\phi)$ and $r_2(\theta,\phi)$ in the integral

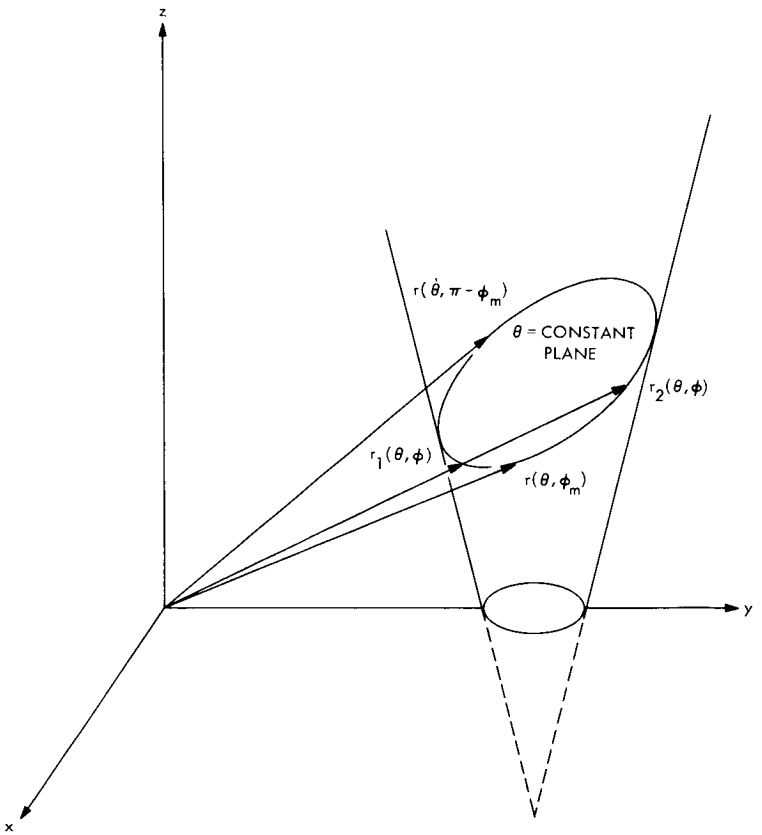

Figure 2. Integration limits of conical beam

are determined in the next section. Note, however, that $S_b(z)$ may be expressed in spherical coordinates, since $z = r \cos \theta$:

$$S_b(r,\theta,\phi) = \frac{S_0}{\left(1 + \frac{r \cos \theta}{z_0}\right)^{10/3}} \tag{6}$$

The brightness temperature can then be integrated directly to give

$$T_b(\theta,\phi) = \frac{3S_0 \lambda^2 z_0}{56\pi k \cos \theta} \left[t_1(\theta,\phi) - t_2(\theta,\phi)\right] \tag{7}$$

where

$$t_i(\theta,\phi) = \left[1 + \frac{r_i(\theta,\phi) \cos \theta}{z_0}\right]^{-7/3}, \qquad i = 1, 2 \tag{8}$$

The antenna noise temperature is a measure of the total received power from the radiating source. To obtain this power, we integrate the Bremsstrahlung radiation, or its equivalent brightness temperature, weighted by the antenna gain pattern. The general form of the antenna noise temperature T_a is therefore given by the equation

$$T_a = \frac{\iint T_b(\theta,\phi) G(\theta,\phi)\, d\Omega}{\iint G(\theta,\phi)\, d\Omega} \tag{9}$$

where $G(\theta,\phi)$ is the gain pattern, and $d\Omega$ is an element of solid angle. The received noise power then is $N = kT_aB$, where B is the bandwidth of the receiver.

Conical Beam Limits of Integration

In the preceding section, an expression for the brightness temperature $T_b(\theta,\phi)$ was derived, in which the limits of integration $r_1(\theta,\phi)$ and $r_2(\theta,\phi)$ were left undetermined. These limits are found by writing the equation of the cone in spherical coordinates.

The equation, in rectangular coordinates, of a right cylindrical cone with half-angle α, axis parallel to the z direction, and apex located at $(0, R_a, -z_0)$ is

$$x^2 + (y - R_a)^2 = m^2(z + z_0)^2 \tag{10}$$

where $m = \tan \alpha = R_0/z_0$ (see Figure 1). The equation of the cone transformed into spherical coordinates, and solved explicitly for $r(\theta,\phi)$ is

$$r(\theta,\phi) = \frac{R_a \sin\theta \sin\phi + m^2 z_0 \cos\theta}{\sin^2\theta - m^2\cos^2\theta} \pm \frac{\sqrt{(R_a \sin\theta \sin\phi + m^2 z_0 \cos\theta)^2 - (\sin^2\theta - m^2\cos^2\theta)\,(R_a^2 - R_0^2)}}{\sin^2\theta - m^2\cos^2\theta} \tag{11}$$

The limits of integration are $r_1(\theta,\phi)$ and $r_2(\theta,\phi)$, with the plus and minus sign, respectively, are shown in Figure 2.

The domain of ϕ for a given value of θ in the range $\alpha < \theta < \pi/2$ is $\phi_m < \phi < \pi - \phi_m$, where ϕ_m is determined by setting the square-root expression in $r(\theta,\phi)$ equal to zero:

$$\sin\phi_m = \frac{\sqrt{(\sin^2\theta - m^2\cos^2\theta)\,(R_a^2 - R_0^2) - m^2 z_0 \cos^2\theta}}{R_a \cos\theta} \tag{12}$$

The source of radiation is now defined by $T_b(\theta,\phi)$ everywhere in the volume of the ion beam, and zero outside this volume.

Antenna Gain Pattern

The antenna gain pattern $G(\theta,\phi)$ is assumed in this treatment to be symmetric and pointing in the $\theta = \psi$, $\phi = \pi/2$ direction. For simplicity, the pattern is assumed to have no sidelobes. The shape of the pattern is taken to be a simple cosine distribution with a half-power beamwidth of θ_3 as given below:

$$G(\theta,\phi) = \cos\left[\frac{\pi}{3}\frac{(\psi - \theta)}{\theta_3}\right]\cos\left[\frac{\pi}{3}\frac{\left(\frac{\pi}{2} - \phi\right)}{\theta_3}\right] \tag{13}$$

if

$$\left|\frac{\psi - \theta}{\theta_3}\right| \leq 1.5 \quad \text{and} \quad \left|\frac{\pi - \phi}{\theta_3}\right| \leq 1.5$$

and $G(\theta,\phi) = 0$ otherwise.

The limits of integration for the antenna-noise-temperature integral are given by the intersection of the domains given by the cone boundary and the antenna gain pattern.

Noise generated by the exhaust beam may then be compared to the received uplink signal level to obtain the signal-to-noise ratio. The received signal power is

$$S = P_{\text{inc}} A_{\text{eff}} \tag{14}$$

where A_{eff} is the effective aperture area of the antenna, and P_{inc} is the incident power density. For an antenna that is always pointing toward the point of transmission, perfectly matched and lossless, the maximum effective area is given by

$$A_{\text{eff}} = \frac{\lambda^2}{\iint G(\theta,\phi)\, d\Omega} \tag{15}$$

The signal-to-noise ratio is thus

$$\frac{S}{N} = \frac{P_{\text{inc}} \lambda^2}{kB \iint T_b(\theta,\phi) G(\theta,\phi)\, d\Omega} \tag{16}$$

where B is the receiver bandwidth.

Discussion of Results

Two effects of ion-beam-induced noise may be calculated: the increase in antenna noise temperature caused by the exhaust beam, and the uplink signal-to-noise ratio, when all other noise contributions are zero.

The expression for the antenna noise temperature was evaluated on the UNIVAC 1108 computer. Results of the antenna noise temperature versus antenna pointing angle are shown in Figure 3 for several half-power beamwidths. The brightness temperature $T_b(\psi,\pi/2)$ is also plotted for reference. The peak in T_a for each value of θ_3 corresponds to pointing angles ψ in which the gain pattern is partially blocked by the engine, which is exterior to the beam volume. A case with an assumed isotropic pattern, i.e., $G(\theta,\phi) = 1$, is also shown; the low value of T_a for this case is due to the large field of view and thus lower gain of the antenna in the direction of the plume. A peak antenna noise temperature of about 0.2 K (about −200 dBm/Hz) was found. A spacecraft receiver might typically have a noise temperature of 500 K (or −170 dBm/Hz), a margin of 30 dB above the ion noise.

Although the ion-noise signal increases for narrow antenna beam patterns, the effective aperture area is also larger so that received signals are greater than for broader patterns. Thus, to find the signal-to-noise ratio for the worst case, comparisons of S/N for various antenna beamwidths must be made.

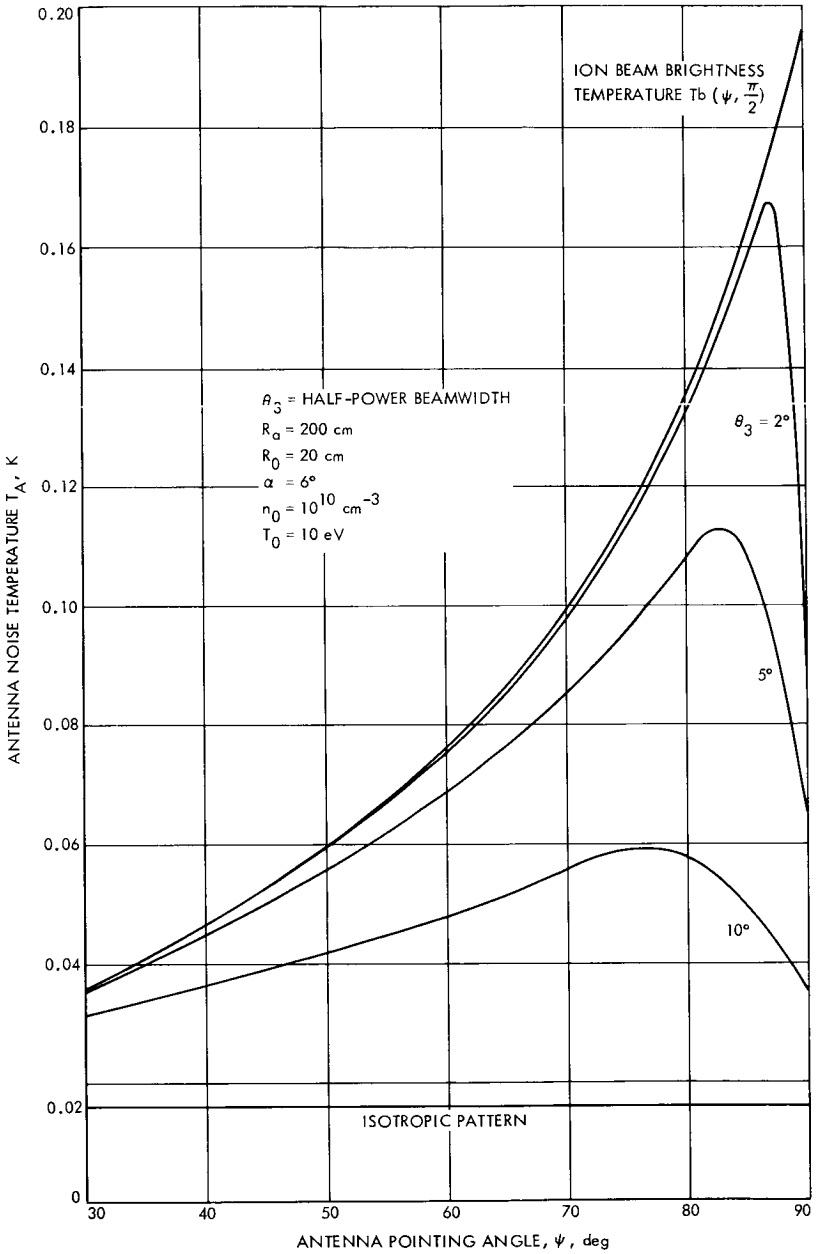

Figure 3. Antenna noise temperature vs pointing angle

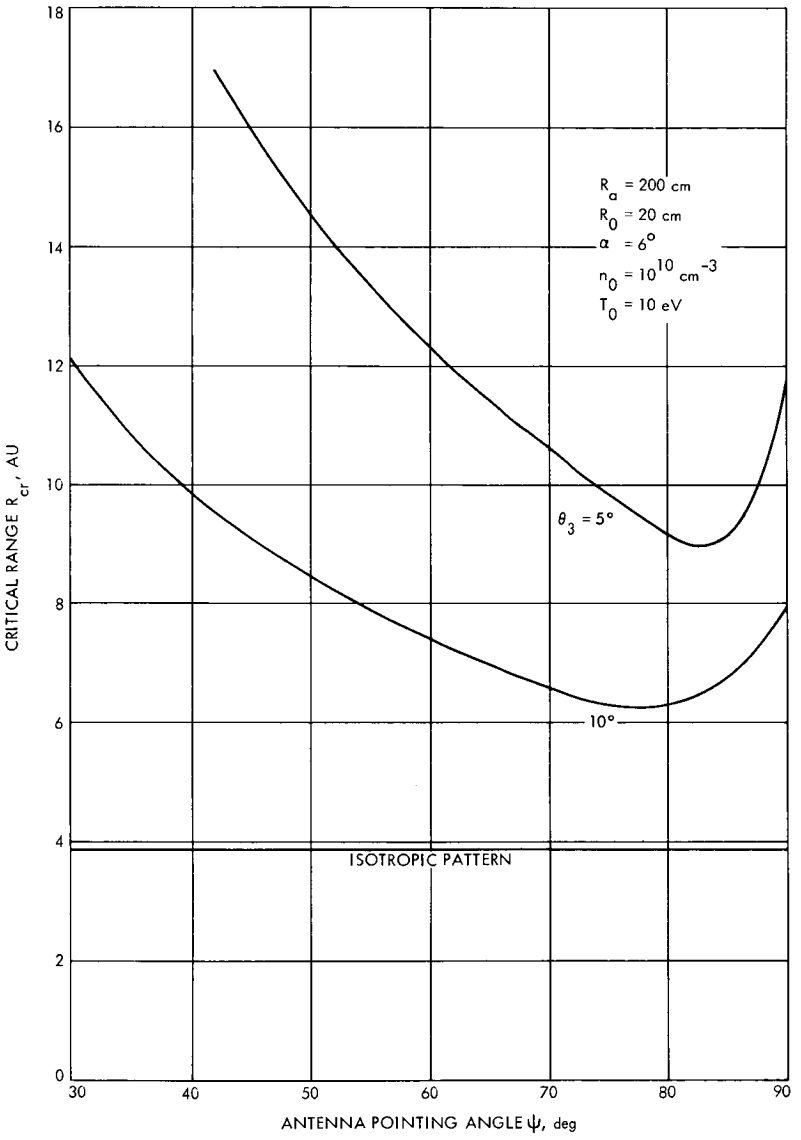

Figure 4. Critical range versus pointing angle

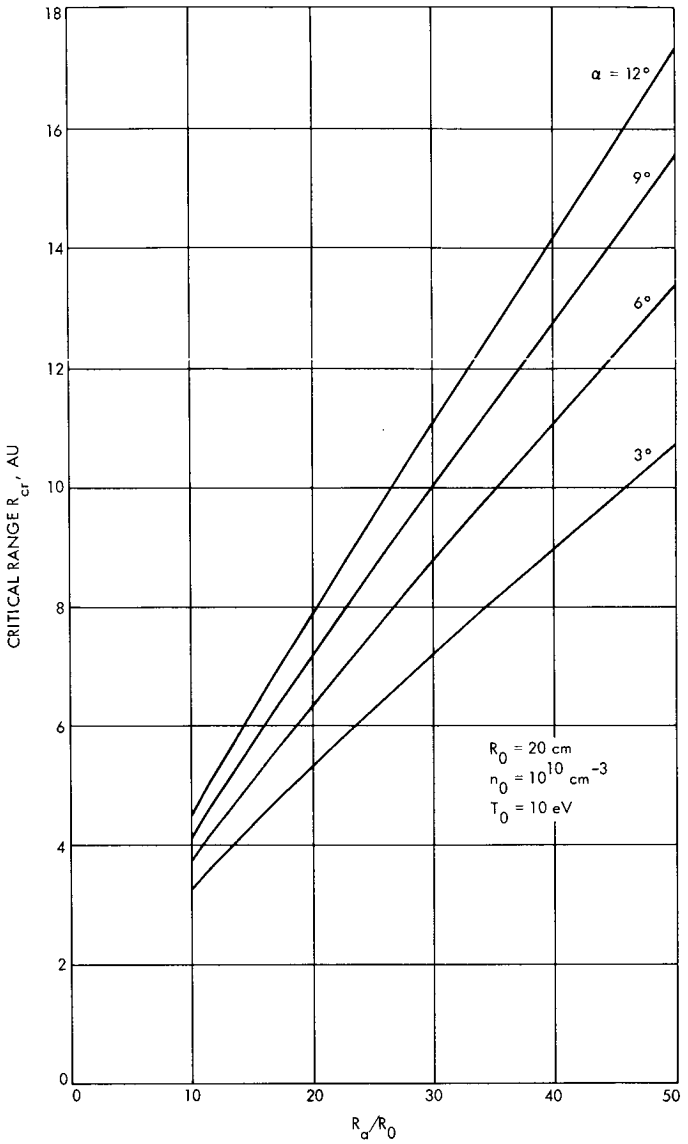

Figure 5. Critical range versus normalized spacecraft antenna distance to beam radius

Consider a typical uplink ranging signal transmitted by a 26-meter-diameter antenna (52-dB gain) at 10 kW with 12-dB ranging suppression, at 2 GHz with a 1-MHz bandwidth. Rather than determining the S/N at various distances, we will determine that critical distance R_{cr} (in AU) at which the uplink signal equals the exhaust beam noise.

The critical range is shown in Figure 4 for several beamwidths and the isotropic case. The shortest critical range occurs for an isotropic or low-gain antenna, which for the spacecraft parameters indicated on the figure is 4 AU.

The effect of the exhaust beam divergence angle α and the antenna distance to the beam axis is shown in Figure 5 for an isotropic antenna. As the exhaust beam divergence angle decreases, the characteristic length z_0 increases, indicating a decreased ion density and temperature drop-off and thus larger noise contributions.

We may thus conclude that operating an ion engine ordinarily introduces much less degradation than receiver noise.

References

1. Heald, M. A., and Wharton, C. B., *Plasma Diagnostics with Microwaves*, p. 254, John Wiley & Sons, Inc., New York, 1965.

2. Sellen, G. M., Jr., Ogawa, H. S., and Cole, R. K., "Factors in the Electrostatic Equilibrium Between a Plasma Thrust Beam and Ambient Space Plasma," AIAA Paper 70-1142, presented at the AIAA 8th Electric Propulsion Conference, Stanford, California, August 31–September 2, 1970.

Index: solid-state physics

Thermal Noise in Space-Charge-Limited Hole Current in Silicon

A. Shumka

Astrionics Division

J. Golder and M-A. Nicolet

California Institute of Technology

Present theories on noise in single-carrier space-charge-limited currents in solids have not been quantitatively substantiated by experimental evidence. To obtain such experimental verification, the noise in specially fabricated silicon structures is being measured and analyzed. The first results of this verification effort are reported in this article.

Noise in single-carrier space-charge-limited currents (SCLC) in solids has been extensively treated theoretically. The more recent rigorous analyses all yield similar results (References 1–4). So far, experimental evidence has been unable to quantitatively substantiate these models or theories (References 5–7). In order to obtain an experimental verification of the theories we have proceeded to fabricate special silicon structures and to measure and analyze noise in these structures, the status of the latter being presented in this report.

Specifically, the theoretical prediction for the spectral intensity $S_i(\omega)$ of the equivalent current noise source (References 1–4) is

$$S_i(\omega) \equiv \langle i^2 \rangle / \Delta f = 4\alpha kTg(\omega), \tag{1}$$

where α is known to have the value of 2 for pure SCLC and $g(\omega)$ is the incremental conductance at the operating point considered. We confine our attention to the range of low frequencies where transit-time effects can be neglected. The conductance is then independent of the frequency (Reference 8) and assumes the value

$$g_0 = dI/dV \tag{2}$$

Thus, at low frequencies

$$S_i = 4\alpha kTg_0 \tag{3}$$

with $\alpha = 2$ for pure SCLC.

Van der Ziel proposes an ad hoc formula for the spectral intensity of the equivalent noise voltage of injection devices known as "van der Ziel's rule" (Reference 9):

$$S_v \equiv \langle v^2 \rangle / \Delta f = 4kT(V/I) \tag{4}$$

In this case, therefore,

$$S_i = 4kT(V/I)\, g_0^{\,2} = 4\,(V/I)\,(dI/dV)\,kTg_0 \tag{5}$$

A comparison with Equation 3 thus shows that van der Ziel's rule predicts a general low-frequency form for α of

$$\alpha = (V/I)\,(dI/dV) \tag{6}$$

This reduces to $\alpha = 2$ for pure SCLC and agrees with the more rigorous derivations available in this particular case.

Devices required for the experiments described have been manufactured from very-high-purity near-intrinsic n-type silicon (~65 kΩ-cm, ν-type). The hole injecting and collecting contacts were obtained by alloying Al to both faces and have an area of 2.42×10^{-2} cm^2. The separation distance between the two contacts is 98 μm. Figure 1 shows the I–V characteristic of such a device at room temperature. The solid line, $I \sim V^2$, is a theoretical curve expected for pure SCLC due to holes, and the solid line $I \sim V$ is for an ohmic type of conduction. This latter component was subsequently found to be partly attributable to leakage.

Conductance measurements were carried out in the frequency range 0.5 MHz to 22 MHz. In Table 1 the experimental values of the conductance g_0 are given, as well as the bias current I and voltage V of the corresponding operating point. By using the experimental values of I and V we can compute the spectral intensity S_i of the current noise according to Equation 5. These values appear in Table 1, expressed as $I_{eq} = S_i/2q$.

Figure 2 gives current noise spectra obtained from the same device for five different operation points. Limiting noise is very clearly shown in all cases. For comparison with the experiment the corresponding calculated values of I_{eq} for the limiting noise listed in Table 1 are shown in Figure 2 as dashed lines. These noise levels as predicted by Equation 5 agree very well

Table 1. Parameters for silicon solid-state diode

Experimental values			Calculated values	
I, mA	V, V	g_0, $\mu\Omega^{-1}$	I_{eq},[a] μA	α[b]
0.2	3.1	109	9.4	1.69
0.5	5.4	171	16.2	1.85
1.0	7.9	238	22.9	1.88
1.5	9.9	286	27.7	1.89
2.0	11.6	329	32.2	1.91
2.5	13.2	362	35.4	1.91

[a] I_{eq} calculated by using Equation 5.

[b] α calculated by using Equation 6.

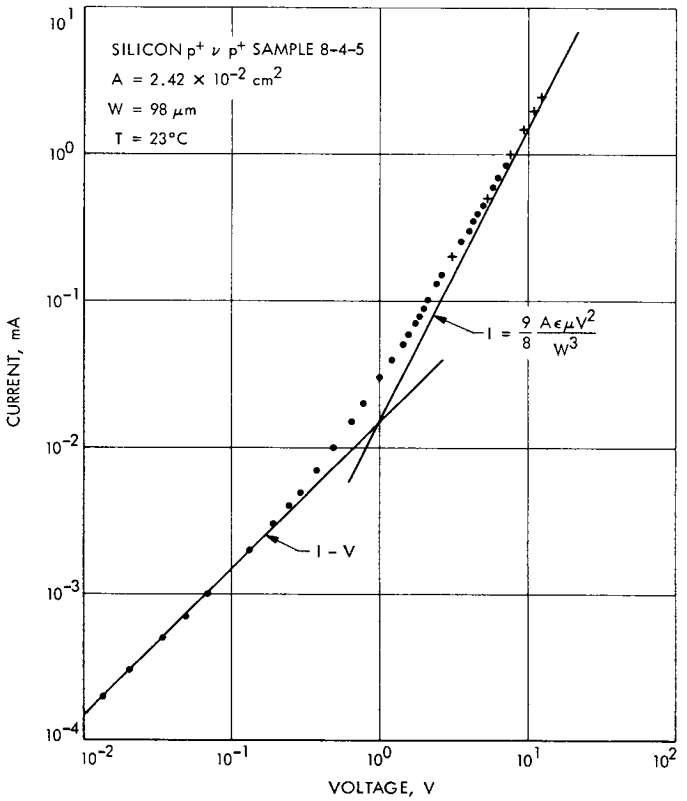

Figure 1. I–V characteristics for a silicon $p^+\nu p^+$ structure. The I–V^2 line is the theoretical curve for pure SCLC due to holes and the I–V line is fitted to the data

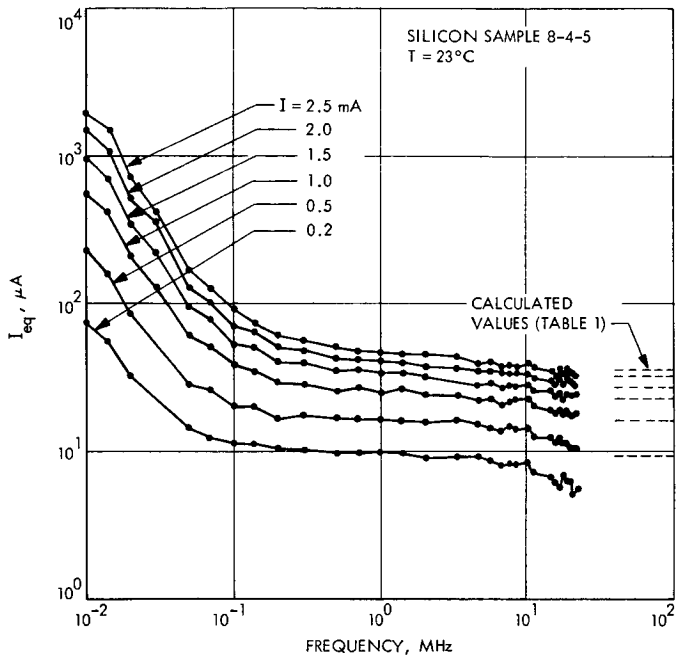

Figure 2. Noise spectra for silicon sample 8-4-5

with the observed values. Fall-off in the flat region of the noise spectra observed at the higher frequencies and lower current operating points can be attributed to transit-time effects. An analysis not presented here has shown that this fall-off is in good agreement with the theoretical frequency dependences $g(\omega)$ as given by Shao and Wright (Reference 8).

The crucial test parameter is α, and it is listed in Table 1. At higher current biases α is equal to 2 within 5%. This is in very good agreement with theory which predicts an α equal to 2 for pure SCLC. At lower current biases α appreciably differs from 2, and this difference can in part be attributed to leakage effects present in our samples.

At present various silicon and germanium solid-state diodes will be used to make noise measurements for SCLC at various temperatures. These results will greatly add to the experimental verification of the existing theories. Further extensions in this effort will lead to the investigation of the effects of transit-time and hot-carriers (Reference 10) on noise.

References

1. van der Ziel, A., *Solid St. Electron.* Vol. 9, p. 1139, 1966.
2. Shumka, A., *Solid St. Electron.* Vol. 13, p. 751, 1970.
3. Nicolet, M-A., *Solid St. Electron.* Vol. 14, p. 377, 1971.

4. Riguad, A., *Proceedings of the International Conference on the Noise in Active Semiconductor Devices*, held at Toulouse, France, September 21–23, 1971.
5. Yamamoto, S., et al., *Solid St. Electron.* Vol. 11, p. 707, 1968.
6. Liu, S. T., et al., *Physica*, Vol. 38, p. 279, 1968.
7. Nicolet, M-A., et al., *Solid St. Electron.* Vol. 14, p. 667, 1971.
8. Shao, J., and Wright, G. T., *Solid St. Electron.* Vol. 3, p. 291 1961.
9. van der Ziel, A., *Solid St. Electron.* Vol. 9, p. 899, 1966.
10. Shumka, A., *Solid St. Electron.* Vol. 13, p. 751, 1970.

Index: solid propulsion

Long-Term Storage Test of a SYNCOM Solid Rocket Motor

R. L. Ray

Propulsion Division

After 7.5 years of storage at ambient temperature, a solid propellant apogee motor was tested successfully at the Air Force Rocket Propulsion Laboratory. The performance of the motor did not deteriorate as a result of prolonged storage. Tabular performance data and graphic thrust and pressure variations are given.

Introduction

A solid rocket motor cast in May of 1964 during the SYNCOM satellite program was recently test fired at the Air Force Rocket Propulsion Laboratory, (AFRPL) under simulated space conditions. The motor had been stored for 7.5 years at the JPL Edwards Test Station. The average temperature of the storage magazine was 72°F, but the motor experienced temperature extremes between +20 and +110°F on several occasions when the temperature control equipment was out of service.

Figure 1 shows the motor being installed in the test cell at AFRPL. The motor configuration is shown in Figure 2.

Test Results

Table 1 shows a comparison between motor P-43 physical data and typical flight motor data. Motor P-43 differed from the flight motors only to the extent that the ignitor had pressure taps and used a Holex P/N 1345 squib in order to permit the motor pressure to be recorded.

Table 2 compares the vacuum performance of motor P-43 with the typical flight motor operation. There appear to be no significant changes in the performance as a result of the 7.5-year storage. There were three chuffs after the normal motor burn out, apparently caused by residual propellant slivers.

Figure 1. JPL motor P-43 at AFRPL cell 1-42A

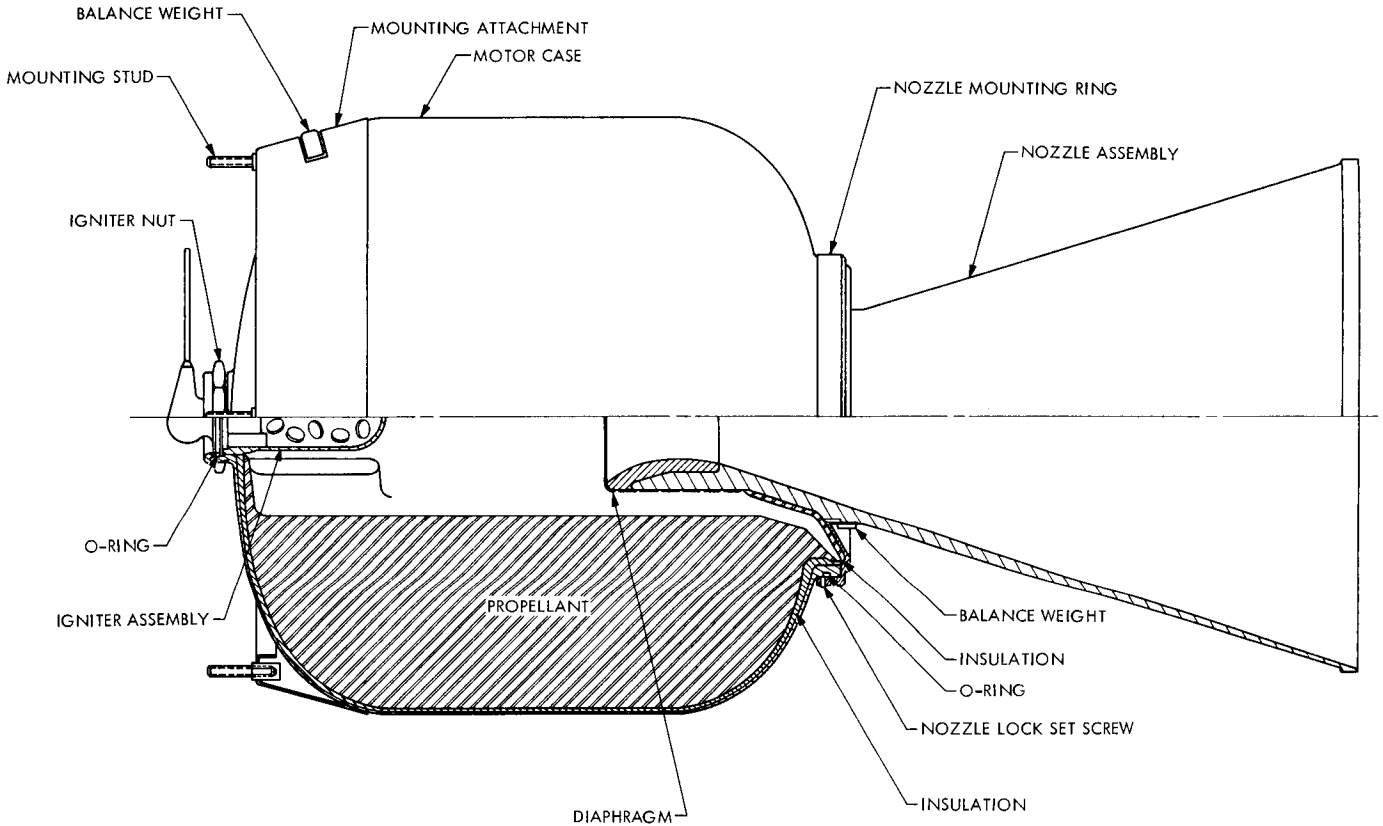

Figure 2. Motor assembly

Table 1. Comparison of motor physical data with standard flight motor data

Weight data (pretest)	Standard[a]	Motor P-43
Inert		
Chamber, kg	1.79	1.74
Insulation, kg	0.85	0.83
Nozzle, kg	1.90	1.96[b]
Igniter, kg	0.19	0.19
Igniter nut, O-ring, g	27.22	31.75
Attachment studs, g	22.68	N.A.
Balance weights, g	18.14	[b]
Total inerts (prefire), kg	4.79	4.76
Propellant		
Propellant (maximum), kg	27.56	27.68
Total assembly, kg	32.35	32.44
Motor mass fraction	0.852	0.853

[a] From Reference 1.

[b] Nozzle weight includes diaphragm and balance weights.

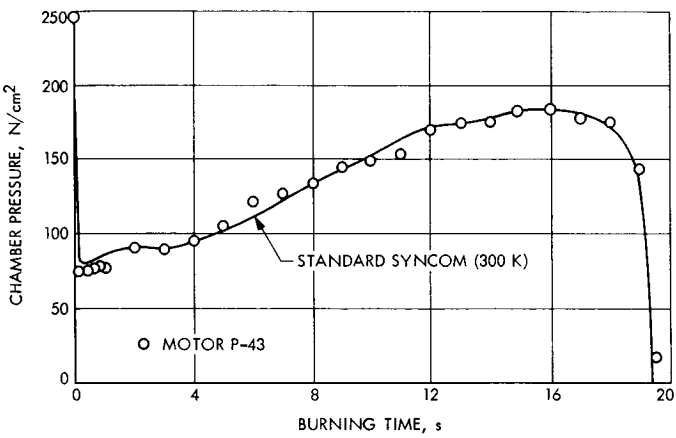

Figure 3. Motor thrust variation with time

Table 2. Motor performance (vacuum)

Parameter	Nominal flight motor performance[a]		Motor P-43 performance	
	300 K	(80°F)	294 K	(70°F)
Action time, s		19.55		19.46
Maximum chamber pressure, N/cm^2 (psia)	177.8	(258)	178.4	(259)
Average chamber pressure, N/cm^2 (psia)	135.8	(197)	137.2	(199)
Maximum thrust, N (lbf)	4893	(1100)	4933	(1109)
Average thrust, N (lbf)	3803	(855)	3830	(861)
Total delivered impulse, N-s (lbf-s)	74226	(16680)	74586	(16761)
Propellant specific impulse, N-s/kg (lbf-sec/lbm)	2688.8	(274.2)	2693.7	(274.7)
Nozzle				
Initial throat diameter, cm (in.)			4.448	(1.751)
Final throat diameter, cm (in.)			4.470	(1.760)
Initial exit diameter, cm (in.)			26.294	(10.352)
Final exit diameter, cm (in.)			26.238	(10.330)
Throat area increase		0.5–1.5%		1.03%

[a]From Reference 1.

[b]Post-burnout chuffing data not included.

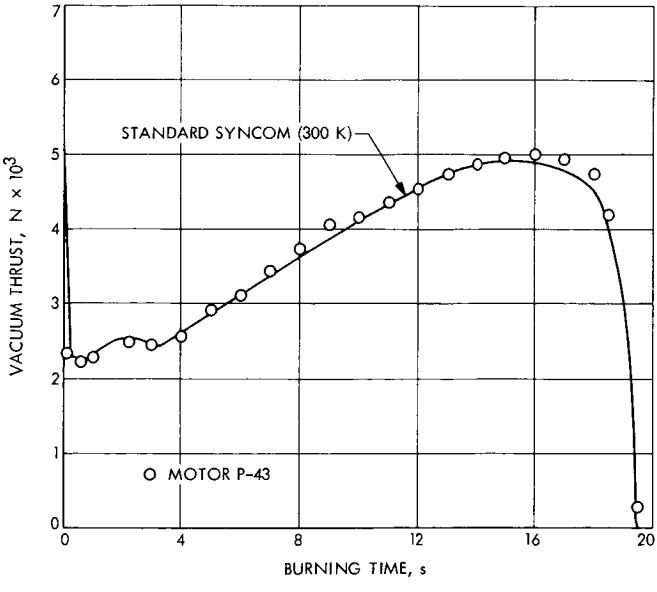

Figure 4. Motor pressure variation with time

Figure 3 shows the P_c versus time trace of motor P-43 compared to the typical SYNCOM motor performance. Figure 4 shows the vacuum thrust of motor P-43 compared to the typical SYNCOM motor thrust.

Conclusion

Since the motor performance and the post-firing physical condition of the motor were both very typical of the SYNCOM motors, it must be concluded that there were no adverse effects resulting from the 7.5-year storage period.

Reference

1. Haserot, R. L., *SYNCOM Apogee Rocket Motor (Description and Performance Characteristics)*, Technical Memorandum No. 33-176. Jet Propulsion Laboratory, Pasadena, Calif., July 1, 1964.

Index: chemistry, electricity and magnetism, solid-state physics

Superconductivity in the Alkali Metal Intercalates of Molybdenum Disulphide

R. B. Somoano, V. Hadek, and A. Rembaum

Propulsion Division

The complete series of alkali metals, lithium through cesium, have been intercalated into molybdenum disulphide, using both the liquid ammonia and vapor techniques. All the intercalates with the exception of lithium yielded full superconducting transitions with onset temperatures of 6 K for A_xMoS_2 (A_x=K,Rb,Cs) and 4 K for B_xMoS_2 (B_x=Li,Na). The superconducting transition for lithium was incomplete down to 1.5 K. Stoichiometries and unit cell parameters have been determined for the intercalation compounds. Both rhombohedral and hexagonal polymorphs of MoS_2 have been intercalated and found to exhibit the same superconductivity behavior. The nature of the extraneous superconducting transition of some intercalated samples on exposure to air was elucidated.

Introduction

The onset of superconductivity in sodium and potassium intercalated molybdenum disulphide (MoS_2) has been previously described (References 1 and 2). This article reports on (1) the intercalation of the entire alkali metal series, lithium through cesium; (2) stoichiometries of the intercalated compounds; (3) X-ray data on all compounds as well as complete indexing of the potassium and rubidium intercalates; and (4) superconductivity data for all intercalation compounds. The onset of superconductivity for the potassium, rubidium, and cesium compounds was at ~6 K, i.e., 2 K higher than for the lithium and sodium compounds. Identical superconducting behavior was observed in both the intercalated hexagonal and rhombohedral polymorphs. The superconductivity was also independent of the intercalation technique, i.e., the use of metals dissolved in liquid ammonia or alkali metal vapors resulted in a similar superconducting behavior.

Experimental Procedures

The structural, optical, and transport properties of MoS_2 are well known (Reference 3). The intercalation of alkali metals by the liquid ammonia

technique has been previously described as well as the X-ray, chemical, and low-temperature methods used to study these compounds (Reference 4).

The MoS_2 samples consisted of either purified powdered molybdenite or of well-shaped polycrystals cleaved from a large natural crystal of molybdenite. Both types of samples had the hexagonal polymorph structure as ascertained by X-ray analysis. The alkali metals lithium, sodium, potassium, rubidium, and cesium were intercalated by means of liquid ammonia, or vapor (potassium only). An additional synthetic sample of rhombohedral MoS_2 was also intercalated with potassium.

Results

The stoichiometries of the intercalated compounds as determined by X-ray and chemical analysis (Reference 4) are shown in Table 1. The differences between our data and those in the literature (Reference 5) are probably due to the fact that in our chemical analysis it is possible to distinguish alkali metal amide and sulphide from the pure metal. An important result of the chemical analysis is that the compounds are characterized by a definite stoichiometry and the alkali metal content cannot be varied arbitrarily.

The stoichiometry of the potassium vapor intercalated sample (3 days at 200°C) was not determined, although chemical analysis also indicated, apart from the metal, the presence of a considerable amount of K_2S, most probably resulting from the reduction of MoS_2 by the hot potassium vapor.

X-ray data obtained in absence of air on all intercalated compounds are shown in Table 1. The X-ray analysis of the potassium and rubidium intercalates has been completed and all the observed lines indexed (Table 2).

Table 2 shows little change in the a_0 axis but a considerable expansion of the c_0 axis. This, therefore, indicates that the alkali metal occupies the octahedral holes in the Van der Waals gap which separates the MoS_2 layers. The values of the unit cell expansions, Δc_0, are shown in Table 1. The expansions increase in the order Na < K < Rb < Cs.

The intercalation of lithium metal is still in the preliminary stage. The stiochiometry appears to be in the range $0.5 < x < 1.0$, and the X-ray data indicate a possible large expansion of the c_0 axis. This large expansion has previously been attributed to the intercalation of NH_3, in addition to lithium (Reference 5), but such a conclusion based on our chemical and X-ray data, at this point, would be premature. The investigation of lithium compounds as well as the intercalation of lithium from the vapor state is presently in progress.

All intercalated compounds, including the vapor intercalated sample and the intercalated rhombohedral polymorph, showed a superconducting transition. The intercalated powders exhibited a wide (several degrees) and incomplete transition at the lowest temperature investigated (~0.5 K). The onset of superconductivity was ~6.2 K for the potassium and ribidium

Table 1. X-ray, chemical, and superconductivity data for intercalated MoS_2

Compound	c_0, 10^{-10}m	Δc_0, 10^{-10}m	Δd_0, 10^{-10}m[a]	T_{ONSET}, K	IP, eV[b]
Na_xMoS_2 ($0.3 < x < 0.6$)	14.998	2.698	1.349	4.15 ± 0.4	5.138
$K_{0.4}MoS_2$(2H)[c]	16.5804	4.2804	2.1402	6.10 ± 0.2	4.339
$K_{0.4}MoS_2$(3R)[d]	24.810	6.360	2.180	5.5 ± 0.1	4.339
$Rb_{0.3}MoS_2$	17.1937	4.8937	2.4469	6.25 ± 0.1	4.176
$Cs_{0.3}MoS_2$	19.606	7.306	3.653	6.30 ± 0.15	3.893
MoS_2(2H)	12.30				

[a]Change in interplanar spacing, d_0.

[b]IP = ionization potential of the isolated alkali metal.

[c]2H represents the hexagonal polymorph.

[d]3R represents the rhombohedral polymorph.

Table 2. Observed and calculated powder diffraction data for intercalated MoS_2 with potassium and radium[a]

$K_{0.4}MoS_2$				$Rb_{0.3}MoS_2$			
hkℓ	I	$10^5 \sin^2 \Theta_{obs}$	$10^5 \sin^2 \Theta_{calc}$	hkℓ	I	$10^5 \sin^2 \Theta_{obs}$	$10^5 \sin^2 \Theta_{calc}$
002	S	867	865	002	S	809	804
004	W	3478	3459	004	W	3233	3216
100	W	7741	7721	100	W	7743	7719
101	S	7917	7936	101	S	7895	7920
102	W	8602	8586	102	W	8518	8523
103	W	9646	9666	103	W	9517	9528
104	S	11165	11179	104	S	10917	10935
105	W	13104	13124	{105 / 008}	W	12791	12745 / 12865
008	VW	13849	13835				
106	W	15518	15503	106	M	14945	14956
107	VW	18299	18313	107	W	17566	17569
{0010 / 108}	W	21596	21617 / 21555	0010	VW	20123	20102
				108	W	20580	20584
110	S	23124	23162	110	S	23139	23157
112	M	23995	24026	112	M	23934	23962
109	VW	25218	25230	114	W	26356	26374
114	VVW	26557	26620	0012	W	28969	28947
201	VS	31064	31098	{200 / 201}	W	30967	30877 / 31077
202	VVW	31733	31746				
204	VW	34362	34341	202	VW	31777	31681
205	VVW	36304	36286	203	VW	32572	32685
118	VW	37062	36996	204	W	34114	34093
206	VW	38629	38664	118	W	35945	36023
208	W	44719	44717	1012	VVW	36511	36666
{1112 / 211}	VW	54329	54259	206	W	38072	38113
				207	VVW	40714	40726
214	VW	57495	57502	1110	W	43233	43259
2012	VW	62013	62010	208	W	43643	43742
1016	VW	63027	63060	1112	W	52183	52105
				211	W	54259	54234
				214	W	57377	57250
				1016	W	59227	59181
				216	W	61361	61271
				218	W	67106	66899
				301	W	69540	69673
				302	W	70280	70275
$a_0 = 3.2036 \pm 0.0002 \times 10^{-10}$ m				$a_0 = 3.2039 \pm 0.0002 \times 10^{-10}$ m			
$c_0 = 16.5804 \pm 0.0003 \times 10^{-10}$ m				$c_0 = 17.1937 \pm 0.0004 \times 10^{-10}$ m			
$c_0/a_0 = 5.1755$				$c_0/a_0 = 5.3665$			
$V^b = 147.37 \times 10^{-30}$ m^3				$V^b = 159.85 \times 10^{-30}$ m^3			
$\Delta c_0 = 4.2804 \times 10^{-10}$ m				$\Delta c_0 = 4.8937 \times 10^{-10}$ m			

[a] Phillips camera and CuK_α ($\lambda = 1.54178 \times 10^{-10}$ m) used.

[b] $V \equiv$ volume of intercalated unit cell

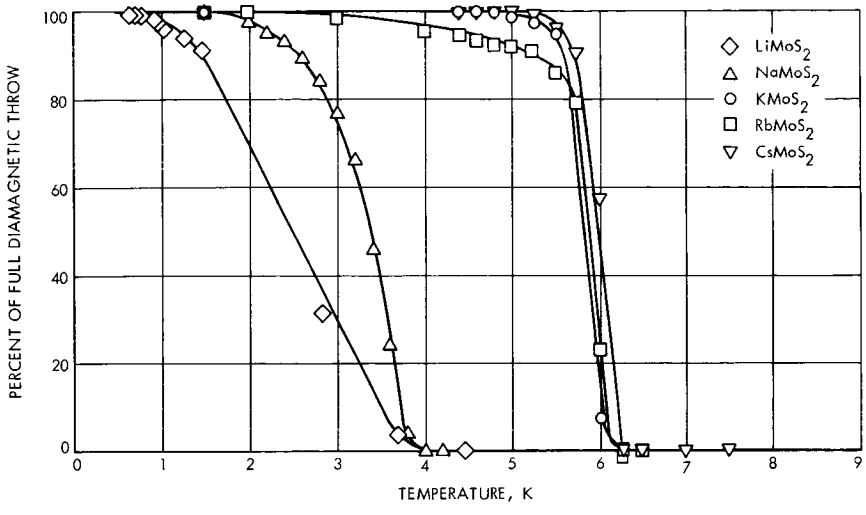

Figure 1. Superconductivity in intercalated MoS_2

intercalated powders regardless of the polymorph or the technique of intercalation (vapor or liquid ammonia). The onset of superconductivity for the sodium intercalated powders was found to be at ~4.4 K. All superconductivity disappeared upon exposure of the samples to air. The superconducting transitions observed in the intercalated natural polycrystals were complete and narrower than the transitions found in the intercalated powders. For these measurements, polycrystals were oriented in the test coil with their layers perpendicular to the alternating magnetic field, and, consequently, the shielding currents flowed parallel to the layers. When possible, transitions were also measured for the parallel orientation, although the small thickness and fragility of the crystals made this orientation unprecise. Although the polycrystals lack the regularity of single crystals, gross orientational effects were observed.

The transitions for the perpendicular orientation are shown in Figure 1. The potassium, rubidium, and cesium intercalated compounds all show an onset of superconductivity at ~6.2 K (see Table 1), whereas for the sodium compound the onset of superconductivity is ~4.0 K as in the intercalated powders. The onset of superconductivity was the same for both the perpendicular and parallel orientations, indicating that the alkali metal couples the layers together, thereby eliminating some of the anisotropy of pure MoS_2. For comparison purposes the superconductivity data for the lithium intercalation compound are also presented in Figure 1.

Conclusions

The present investigation was stimulated by a model proposed by Ginzburg (Reference 6) in which an excitonic mechanism is suggested for the achievement of high-temperature superconductivity. The model

suggests the intercalation of a metal into a layered excitonic material, and the alkali metal intercalates of MoS_2 appeared as an ideal system to test the model. However, upon intercalating the metals, the resulting compounds did not satisfy the requirements of Ginzburg's theory, and, therefore, a meaningful test of the model was not possible.

The fact that MoS_2 becomes superconducting upon intercalation of alkali metal is believed to be a result of the alkali metal donating its electron to an unfilled d-band of MoS_2. MoS_2 should become metallic, or semimetallic, with an increased free electron charge density. The existence of an unfilled d-band in MoS_2 was proposed by Wilson and Yoffe (Reference 5), and a recent band structure calculation by Bromley, Murray, and Yoffe (to be published) confirms the presence of an empty band above the Fermi level. Additional evidence of the increased electron density upon intercalation is derived from the absence of excitons in sodium intercalated MoS_2 (Reference 7). In this case the increased electron density screens the electron-hole interaction causing disruption of the excitons. The difference between the onset temperatures for the lithium and sodium compounds and the potassium, rubidium, and cesium compounds is not understood. The ionization potential of the alkali metals varies fairly uniformly (see Table 1) in contrast to the onset of superconductivity, and, therefore, there is little correlation of ionization potentials and onset temperatures. The heavier alkali metals (potassium, rubidium, and cesium) differ from the lighter ones in the importance of their d levels in their energy band structures. It is thus possible that this difference, together with the much greater expansion of the unit cell [which could result in different alkali metal coordinations as well as changes in the MoS_2 band structure since the layer–layer interactions may change considerably (Reference 8)], could result in different amounts, or degrees, of electron delocalization. This, in turn, could affect the effective free electron density and the superconducting transition temperatures. It is hoped that investigations of the X-ray structure, electrical conductivity, and magnetic susceptibility in intercalated single crystals now in progress will shed more light on the superconductivity behavior.

References

1. Somoano, R. B., and Rembaum, A., "Onset of Superconductivity in Sodium and Potassium Intercalated Molybdenum Disulphide," in *JPL Quarterly Technical Review*, Vol. 1, No. 3, pp. 33–37. Jet Propulsion Laboratory, Pasadena, Calif., Oct. 1971.

2. Somoano, R. B., and Rembaum, A., *Phys. Rev. Lett.*, Vol. 27, p. 402, 1971.

3. Wilson, J. A., and Yoffe, A. D., *Advan. Phys.*, Vol. 18, p. 193, 1970.

4. Somoano, R., Hadek, V., and Rembaum, A., "Superconductivity in d- and f-band Metals." Edited by D. H. Douglas. *AIP Conference Proceedings*, No. 4, p. 243, 1972.

5. Rudorff, W., *Chimia*, Vol. 19, p. 489, 1965.

6. Ginzburg, V. L., *Contemp. Phys.*, Vol. 9, p. 355, 1968.

7. Acrivos, J. V., Liang, W. Y., Wilson, J. A., and Yoffe, A. D., *J. Phys., Sec. C*, Vol. 4, p. 118, 1971.

8. Grant, A. J., Wilson, J. A., and Yoffe, A. D., *Phil. Mag.*, Vol. 25, p. 625, 1972.

Index: control and guidance, fluid mechanics, liquid propulsion, test facilities and equipment

Small Rocket Exhaust Plume Data

J. E. Chirivella, P. I. Moynihan, and W. Simon

Propulsion Division

During recent cryodeposit tests with an 0.18-N (0.04-lbf)[1] thruster in the JPL Molsink facility, the mass flux in the plume back field was measured for the first time for nitrogen, carbon dioxide, and a mixture of nitrogen, hydrogen, and ammonia at various inlet pressures. This mixture simulated gases that would be generated by a hydrazine plenum attitude propulsion system. The measurements furnish a base upon which to build a mathematical model of plume back flow that will be used in predicting the mass distribution in the boundary region of other plumes. The results are analyzed and compared with existing analytical predictions.

Introduction

Plumes from small attitude propulsion engines as well as from spacecraft main engines have been suspected of impinging on spacecraft surfaces and causing anomalous behavior of the instrumentation. Existing plume prediction methods fail to give a satisfactory account of the presence of plume gases in the far upstream regions (large plume turning angles) where most instrumentation is located. The problem is increased if the Reynolds number of the internal flow becomes sufficiently small that the boundary layer occupies almost the entire flow field, since it is the gas in the boundary layer which turns beyond the predicted limits. An experiment simulating these conditions has been conducted in the JPL Molsink facility and has demonstrated that a significant exhaust gas mass flux exists in regions where classical theoretical turning angle analyses predict no flow. A brief description of the facility, the simulated propulsion systems, and the instrumentation are given in subsequent sections of this article.

Facility

The Molsink is an ultra-high vacuum facility constructed of three concentric chambers. The innermost chamber is a sphere approximately 3 m

[1] Values in customary units are included in parentheses after values in SI (International System) units if the customary units were used in the measurements or calculations.

(10 ft) in diameter and, during normal operations, is maintained at a temperature between 10 and 15 K with gaseous helium. The inner walls are wedge-shaped, resembling an anechoic chamber, with a total surface area of approximately 200 m^2 (2000 ft^2). The chamber walls are coated with titanium which acts as "getter" material to trap helium and hydrogen which are not cryopumped at 10 K. [In the test with the simulated hydrazine by-products (described in a later section), hydrogen was successfully cryopumped by condensed ammonia. Both gases were present in the mixture.] Figure 1 illustrates the Molsink chamber; additional information is available in References 1, 2, and 3.

A plume in the Molsink would almost identically simulate a plume in space if the chamber walls were to behave as perfect sinks. However, some small fraction of the plume gases is reflected from the walls, and although the molecules are quickly scattered back toward the wall by collisions with the oncoming gases, these reflected plume gases perturb the concentrations of the plume gases near the surface by a factor that is an increasing function of the evaporation rate at the wall of the lightest constituent. Therefore, in order to optimize a space environment flow field simulation, it is necessary to minimize the gas returned from the wall as much as possible. The Molsink approximates space closer than any other known facility.

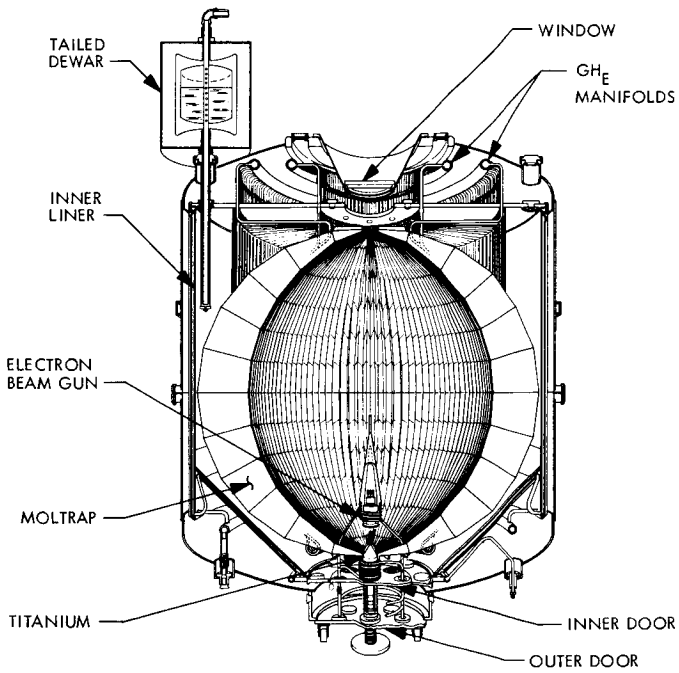

Figure 1. Molsink chamber

Propulsion and Thruster Operation

The thruster assembly utilized for this test series was a modified version of the TRW Model 35 flight assembly. It consisted of a double-seat valve which was mounted on a clustered nozzle assembly. Only one of the nozzles was used for this test. The feed tube from the valve was coiled around a 12-W heater to heat the gas prior to entering the nozzle in order to provide a higher specific impulse in-flight. The active nozzle was a 15-deg half-angle cone with a 0.106 cm-(0.042-in.)-diameter throat and an area ratio ϵ of 52. The specimen gases entered the propellant valve from a 0.6- by 0.07-cm (0.25- by 0.028-in.) wall tube. This tube was fed through a hand regulator and a flowmeter from a pressure vessel containing the desired test gas, which was located outside the vacuum chamber.

Instrumentation

Quartz crystal microbalances (QCM) were used to measure the mass flux in the plume far field, which is defined as distances greater than 50 exit diameters from the thruster. A QCM is essentially a crystal oscillator for which the quartz plate is excited in thickness shear oscillation (see Figure 2). A change of mass or temperature of the crystal is depicted by a shift in the resonant frequency. However, for each crystal cut angle there is a specific temperature range for which the temperature effect alone is negligible, and the frequency change is due totally to mass deposit. Crystals cut at an angle to make them insensitive to temperatures within the cryogenic range of interest were used for these experiments. The relationship between the frequency shift and mass deposit is linear for these conditions and is given by Equation 1 of Reference 4, which is

$$\Delta m = \frac{4.35 \times 10^{-7}}{F_c^{\,2}} \Delta F \tag{1}$$

where Δm is the mass deposit in g/cm^2, F_c is the crystal resonance frequency in MHz, and ΔF is the frequency shift in Hz. Additional information related to QCM theory can be found in Reference 4. Three sets of these crystals were located as shown in Figure 3. Figure 4 depicts a typical crystal set attached to a remote oscillator.

Tests

Table 1 summarizes the gases utilized and the various thruster valve inlet pressures at which the tests were conducted. There were one-day intervals between the tests with each different gas. However, the tests corresponding to the three inlet pressures for each individual gas were performed consecutively for a duration of approximately 5 min each. An additional 5 min was maintained between each test to monitor the physics of the QCM under a zero flow condition. It was possible to determine the evaporation

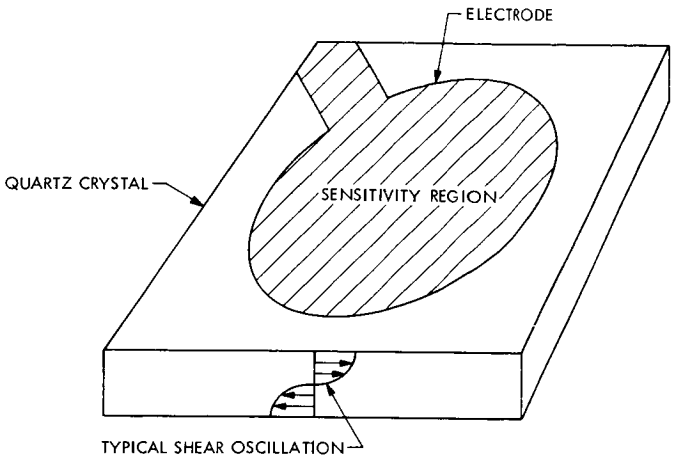

Figure 2. Schematic diagram of thickness shear oscillation mode in quartz crystal

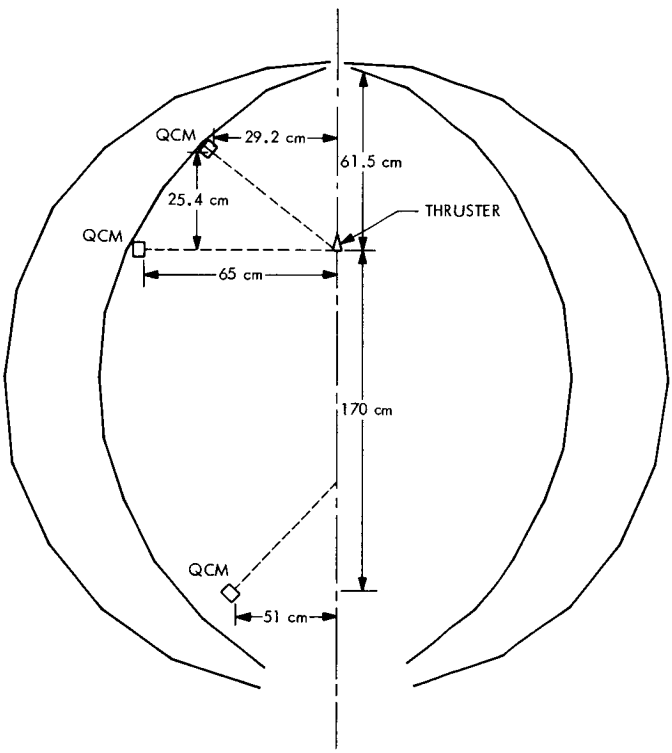

Figure 3. Quartz crystal microbalance (QCM) location in Molsink chamber

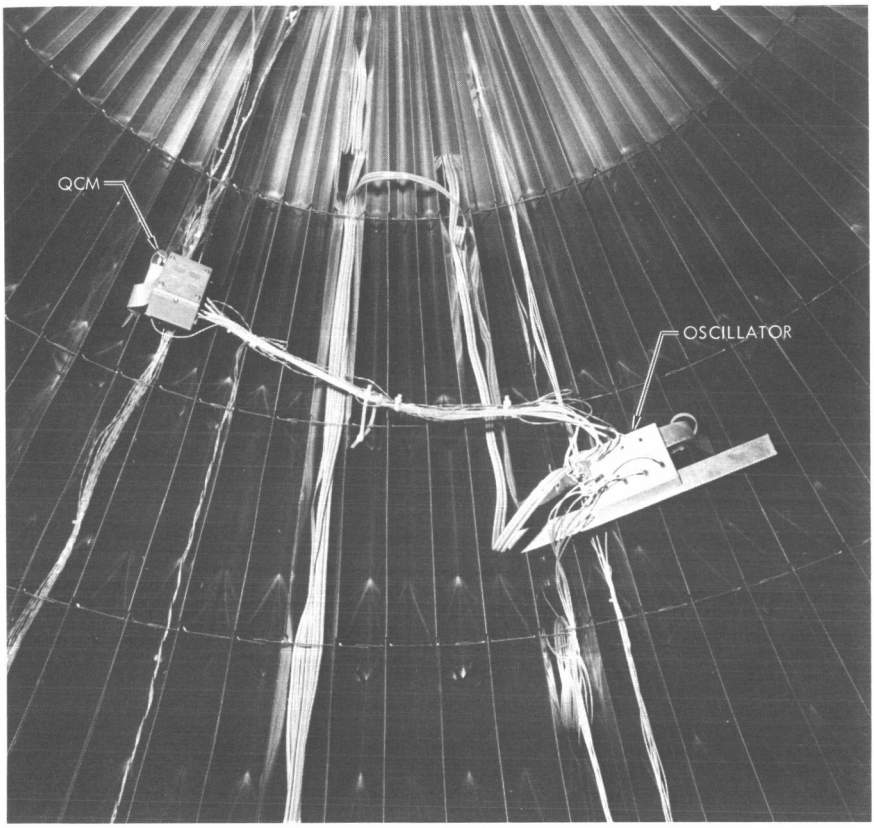

Figure 4. QCM unit and its remote oscillator in Molsink chamber

and desorption rates with this technique and thus correct the readings obtained for the flowing gas.

The simulated hydrazine by-products were analyzed and found to be composed of 19.8% hydrogen, 24.2% nitrogen, and 55.2% ammonia by volume. For this concentration, hydrogen was cryopumped satisfactorily by ammonia frost (a cryosorptive compound) in spite of the spoiling effect of nitrogen (which impedes adsorption when condensed) for thruster valve inlet pressures as high as 8.27×10^4 N/m^2 (12 psia). The test conducted at 1.17×10^5 N/m^2 (17 psia) was stopped after 45 s because of a pressure buildup due to a saturation of the cryopumping area.

The nozzle inlet pressure was not directly measured; the pressures that appear in Table 1 were calculated by subtracting the pressure drop through the thruster capillary tube from the pressure measured in the gas line outside the Molsink. The temperature of the thruster was nominally 21.1°C (70°F) for all cases.

Table 1. Matrix of test cases

Gas	Thruster valve inlet pressure, N/m^2 (psia)	
Nitrogen	3.86×10^4	(5.6)
	6.27×10^4	(9.1)
	8.96×10^4	(13.0)
Carbon dioxide	1.23×10^4	(1.79)
	1.80×10^4	(2.61)
	2.43×10^4	(3.53)
Simulated hydrazine by-products	4.76×10^4	(6.9)
	7.98×10^4	(11.58)
	1.18×10^5	(17.07)

The functional reliability of the individual QCM was low, but sufficient redundancy was incorporated to assure data from each test. The greatest cause of instrumentation failure was the lack of stability in the crystal oscillation frequency. An improvement in oscillator design for cryogenic conditions would minimize this type of failure.

Discussion of Results

Figures 5, 6, and 7 compare the radial flow mass fluxes measured by the QCM with those from the source flow theory of Hill and Draper (Reference 5) for the far field exhausting in vacuum. The vertical axis parameter is the mass flux per unit solid angle at an angle θ from the nozzle centerline, normalized by the corresponding value at $\theta = 0$. The region on the right of these curves represents the "plume free" region that is predicted by this theory which has been successfully correlated with previous experimental data in the region close to the plume axis. The raw data was obtained in the form of instantaneous crystal frequency.

Figure 8 shows a typical frequency shift as a function of time. The frequency shift curve was converted to mass deposit data by Equation 1, discussed in the *Instrumentation* section. The mass flux per unit solid angle is determined by the geometry depicted in Figure 9 from which, by assuming source flow,

$$\frac{d\dot{m}}{d\Omega} = \dot{M}r^2 \cos\varphi \tag{2}$$

is derived, where $\dot{M}$ is the mass flux per unit area of the active region of the quartz crystal as determined by Equation 1; r is the distance from the

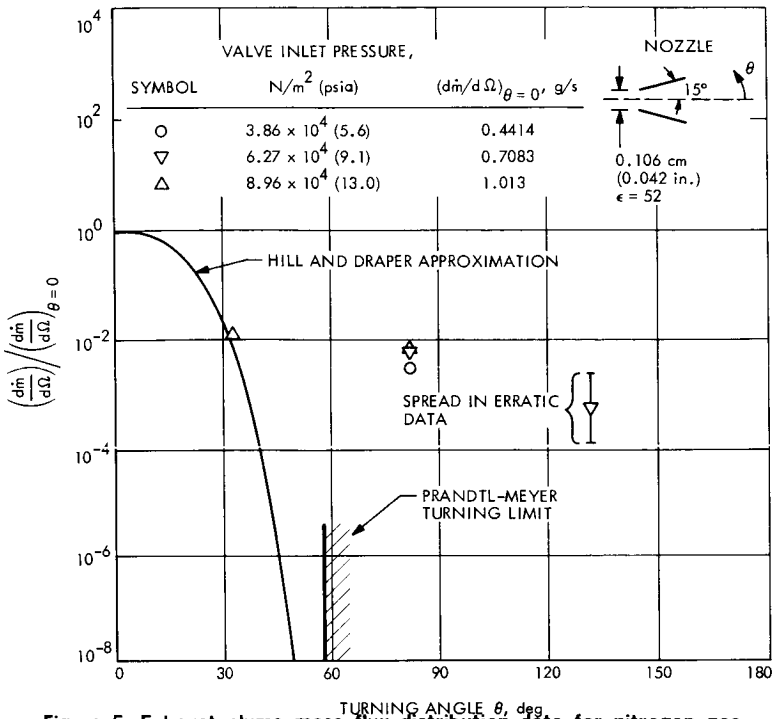

Figure 5. Exhaust plume mass flux distribution data for nitrogen gas

thruster to the QCM; and ϕ the angle between the normal to the crystal surface and its position vector **r**.

The QCM data has been normalized by the $d\dot{m}/d\Omega$ at the thruster center line as given by the Hill and Draper scheme, which is

$$\left(\frac{d\dot{m}}{d\Omega}\right)_{\theta=0} = \frac{m\lambda}{\pi^{3/2}} \tag{3}$$

where λ is a plume shape factor associated with the nozzle expansion A_t/A_e and the gas specific heat ratio γ, and $\dot{m}$ is the total mass flowrate.

The maximum plume flow turning limit used by present detailed near field computational techniques is the Prandtl-Meyer turning angle, which has been indicated in Figures 5, 6, and 7. In Figure 5, one can see that the QCM data agrees very well with both theories for values of $\theta = 33$ deg, and 9×10^4 N/m^2 (13 psia) nozzle inlet pressure when flowing nitrogen. It is from these figures that the experiment dramatically displays the existence of considerable mass flux in regions where no existing theoretical plume distribution model can as yet predict. The data obtained here, along with the

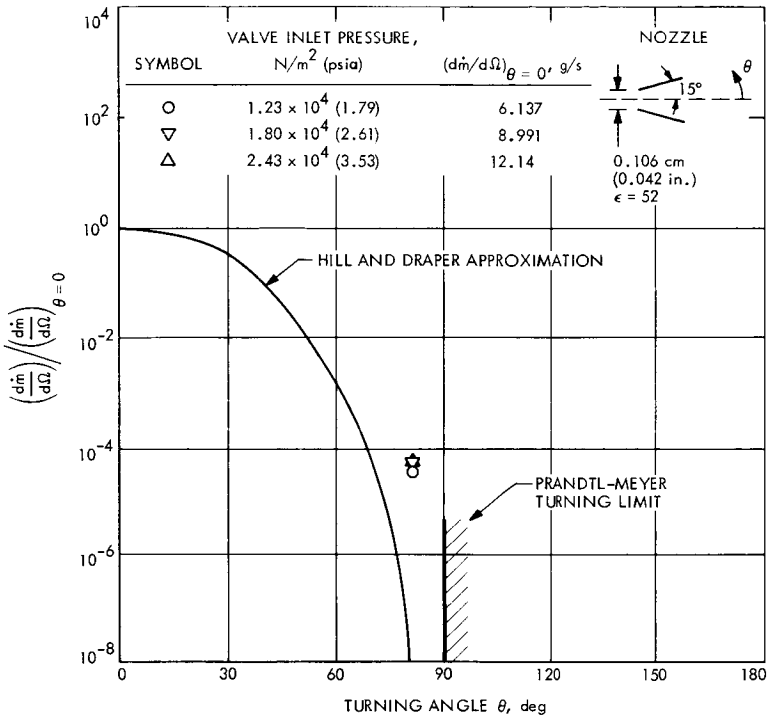

Figure 6. Exhaust plume mass flux distribution data for carbon dioxide gas

data reported in Reference 6, will constitute the basis for a model to predict the far field mass flux in the large turning angle region of the plume. The data and the model will be valuable to future spacecraft projects as a basis for predicting and minimizing plume interference problems.

Future Efforts

During future tests, data repeatability at the same QCM locations will be determined, after which the measurements will be extended to additional plumes and locations. To accomplish this, work is being conducted to improve the QCM performance and reliability. The data acquisition and reduction system is being automated for on-line monitoring of the data.

Acknowledgment

The authors wish to extend their gratitude to Mr. Ralph Bartera of the JPL Space Simulation Section for his invaluable assistance in the Molsink operations.

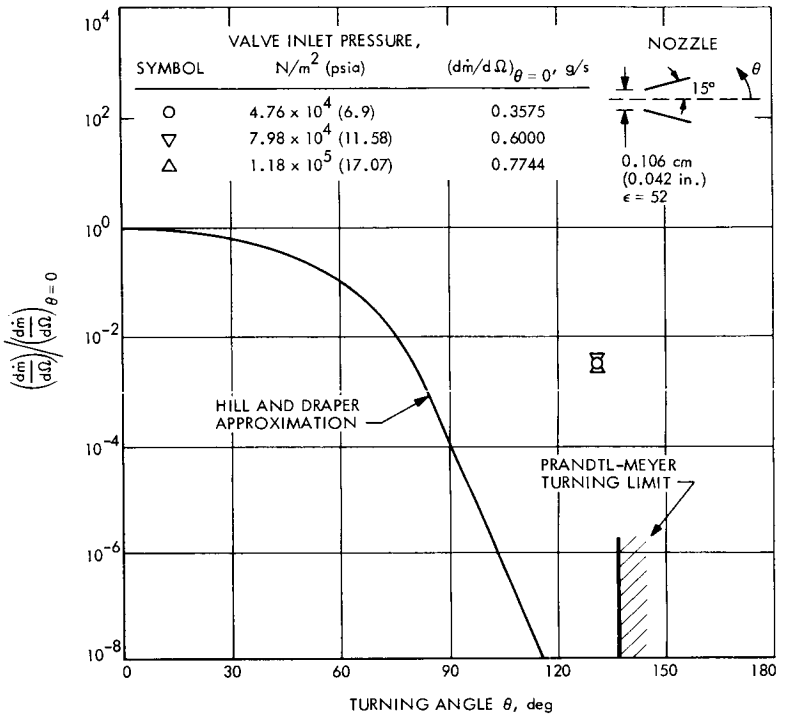

Figure 7. Exhaust plume mass flux distribution data for simulated hydrazine exhaust products

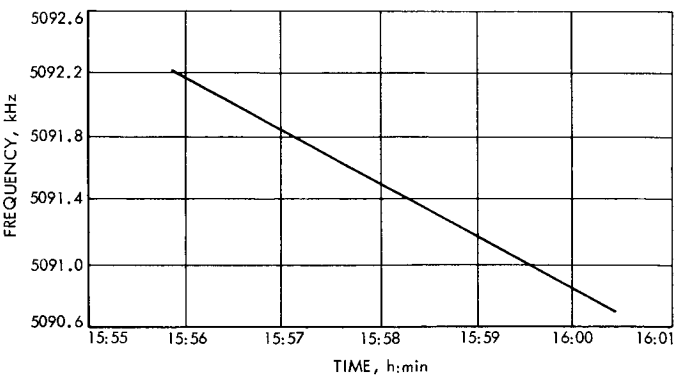

Figure 8. Typical QCM frequency change with time

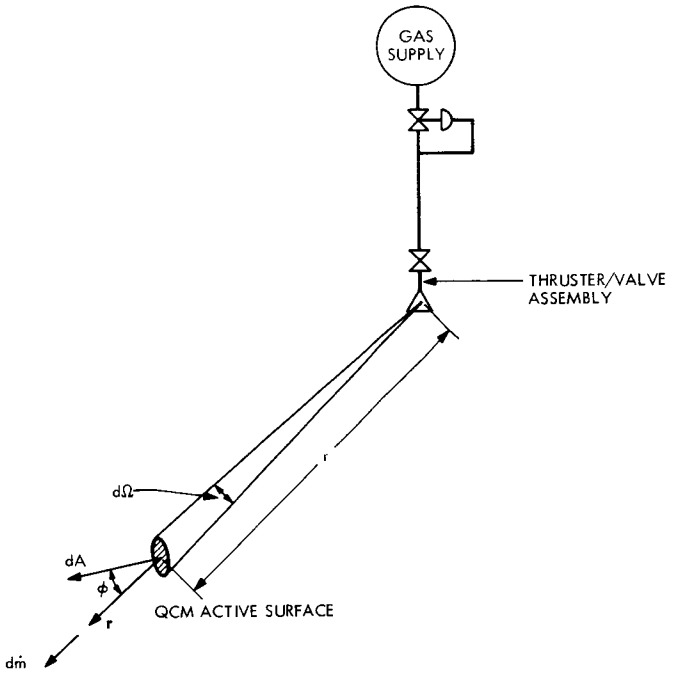

Figure 9. Solid angle subtended by the QCM active surface

References

1. Stephens, J. B., "Spacecraft Mechanism Testing in the Molsink Facility," paper presented at the 4th Aerospace Symposium, University of Santa Clara, May 22–23, 1969.

2. Stephens, J. B., "Molecular Sink," *Research/Development*, July 1967.

3. Stephens, J. B., "Space Molecular Sink Simulator Facility Design," *J. Spacecraft Rockets*, June 1966.

4. Sauerbrey, G., "Use of Oscillator Quartz Crystals for Weighing Thin Layers and Microweighing," *Ann. Physik*, Vol. 155, pp. 206–222, 1959.

5. Hill, J. A. F., and Draper, J. S., "Analytical Approximation for the Flow from a Nozzle into a Vacuum," *J. Spacecraft Rockets*, Vol. 3, No. 10, pp. 1552–1559, Oct. 1966.

6. Simon, W., *Plume Backscatter Measurements Using Quartz Crystal Microbalances in JPL Molsink (Molecular Sink)*, Technical Memorandum 33-540. Jet Propulsion Laboratory, Pasadena, Calif., May 15, 1972.

Index: control and guidance, electric propulsion, electronic components and circuits

Solar-Electric Propulsion Breadboard Thrust Subsystem

T. D. Masek

Propulsion Division

A solar-electric propulsion breadboard thrust subsystem has been designed, built, and tested. A 1500-h test was performed to demonstrate the functional capabilities of the subsystem. This report describes the subsystem functions and testing process. The results show that the ground work has been established for development of an engineering model of the thrust subsystem.

Introduction

The functional demonstration of a solar electric propulsion (SEP) thrust subsystem (TSS) has been the primary goal of the JPL Solar Electric Propulsion System Technology (SEPST) Development Program since 1966 (References 1–6). The TSS concept, upon which the SEPST experimental program is based, has been described in the referenced papers and has remained essentially unchanged during the last five years. The resulting TSS, including hardware, software, control techniques, and general operation philosophy can be considered a baseline for constructing and evaluating other TSS designs. The present TSS is a breadboard type design and is not intended to represent a flight unit. However, all functions anticipated to be required for TSS operation on a planetary spacecraft have been included.

Other reports have described the general nature of SEP missions and general TSS requirements (References 7–12). This report summarizes the results of the third phase of the SEPST program (i.e., SEPST III). The first (Reference 13) and second (Reference 5) phases of the program dealt with element and initial system testing problems, respectively. Element descriptions are presented here only as required, and detailed information is referenced wherever possible.

Subsystem testing, including element final integration and a 1500-h test, was performed over a period of six months. The tests were directed primarily toward demonstrating the basic TSS functions: (1) power

matching, with variable solar array (simulator) output voltage, (2) thrust vector control, (3) TSS automatic control, and (4) propellant storage and delivery. In addition, individual element tests were performed to evaluate specific problems and to check performance not demonstrated by subsystem operation.

Thrust Subsystem Description

General Functions

The elements used in the SEPST III test and the functional relationship of these in the TSS are presented in Figure 1. Four basic functions are illustrated: (1) conversion of electrical power to thrust, (2) thrust vector control, (3) TSS command and control, and (4) propellant supply.

The first function is the basis of electric propulsion. Solar power, simulated in this test by dc power supplies, passes through an interface box and enters the power conditioners (PC). Each PC has ten power outputs which are connected through switches to thrusters. The thruster is an electron bombardment type (References 14, 15) which uses the power to produce and accelerate mercury ions. Each of the subsystem elements is discussed later in this section.

The second function, thrust vector control (TVC), is required to maintain spacecraft three-axis attitude control. The use of multiple thrusters, to provide efficient power throttling and redundancy, results in relatively large thrust vector movements when thrusters are turned on and off. The present TVC technique translates the thruster array in two orthogonal directions for control about two axes and gimbals pairs of thrusters around the thruster array diagonals for third-axis control. The TVC drive electronics, including a closed-loop control system, is shown (Figure 1) connected to an analog computer. The computer, programmed to simulate typical spacecraft dynamic response to thrust vector and other spacecraft errors, is used to demonstrate the TVC system response and stability.

The third function illustrated in Figure 1, TSS command and control, is required to varying degrees of complexity depending upon mission requirements. The tradeoff of ground commands against automatic onboard control will depend upon communication capabilities and upon allowable inflight performance variations. The present subsystem provides automatic functions such as PC-thruster set selection, startup, power matching, failure detection, and failure evaluation by means of a PDP-11 digital computer. In addition, it provides for manual operation of the PCs (and therefore the thrusters) and the switching matrix.

The fourth function, propellant supply, provides the transfer of liquid mercury from a zero-gravity propellant tank across the TVC mechanism to the thrusters. This includes tank pressurization (using Freon 113) of a neoprene bladder and mercury transfer through flexible feedlines.

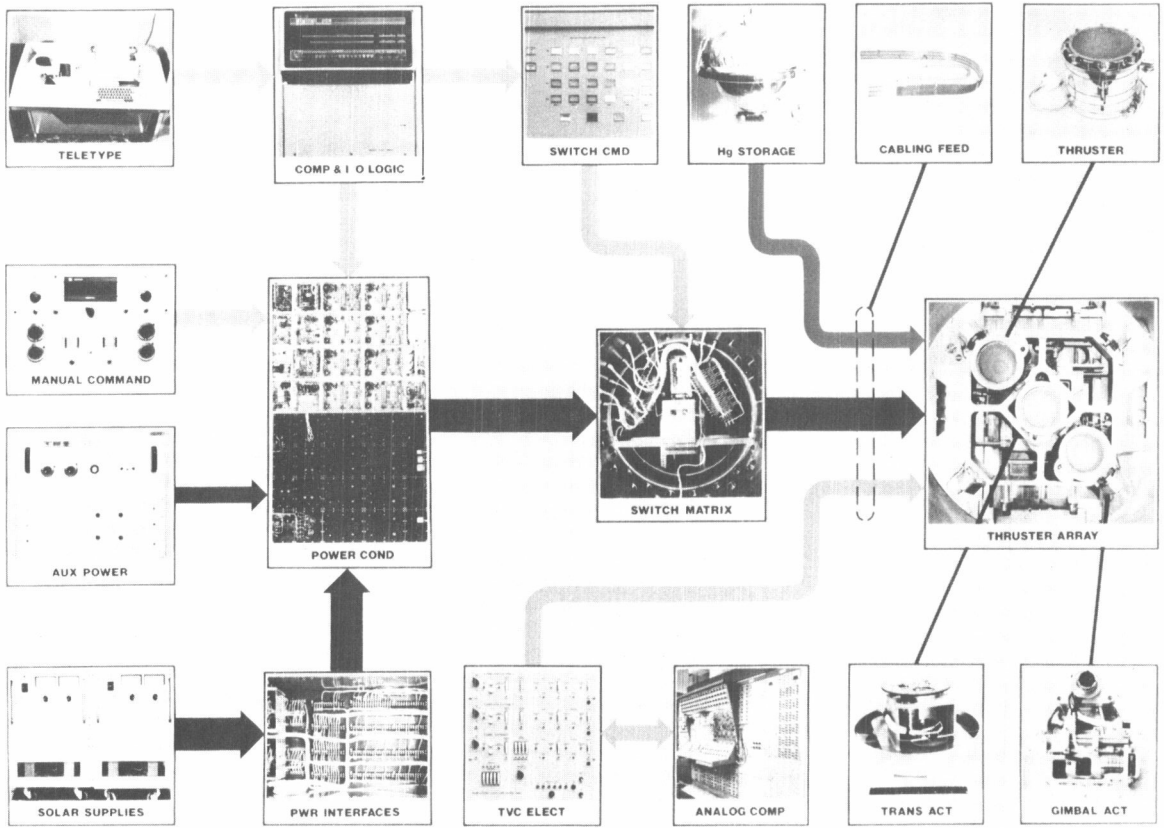

Figure 1. SEPST III system block diagram

Thruster

The thruster used in this program has been thoroughly discussed previously (References 6, 16). It is a 20-cm (beam diameter) unit which uses about 2.4 kW input with 2.0 kW output at full power. The design specific impulse is approximately 40 km/s (4000 s) at a propellant utilization efficiency of 90%. Thruster input power, control, and operational requirements are included in other sections of this report.

Power Conditioner

The present transistor PC technology has been developed in several steps as described in References 17–22. The SEPST III units (EX-1 and EX-2) were built by Hughes Aircraft Company, have dimensions of 92 × 76 × 10 cm, weigh 13.3 kg, and are 89.5 ± 0.5% efficient at full power (Reference 21). Tests, using a mass model of these units, are being conducted to evaluate the structural design for launch requirements (Reference 23). Both the EX-1 and EX-2 units were operated in thermal vacuum for the duration of the 1500-h subsystem test. Detailed thermocouple measurements were made during this test to evaluate the PC thermal design.

Details of the power supply design are described in Reference 21. PC-thruster integration, control-loop operation, recycle during thruster arcing, and the effects of control-loop gain, ripple, and regulation on thruster performance are described in Reference 22.

Switching Matrix

The SEPST III switching matrix (SMX) is composed of switches, a cabling interface, and a logic module. The switches are a commercial rotary-stepping type having two wipers, with six contact positions each, per deck. A total of eight decks, using two switches, are required per PC. PC outputs are connected to wipers, and up to five thrusters and a dummy load can be connected to the contacts. The purchased switches were repackaged for vacuum operation and minimum voltage drops. PC output cables are terminated with connectors which join to the cabling interface. The switches are hard-wired to the PC mating connector halves.

The switching logic module determines the switch position, prevents the connection of two or more thrusters to a single PC, and sends the power pulse to the switch motor. The choice of switch position is determined by the operator (manual) or by the computer (automatic). The logic module is then instructed to switch.

Since future TSS designs may use other switching philosophies (i.e., partial or no interconnections) the present design is intended only as an option. If switching is used, the switching logic function may be incorporated into the TSS command and control element.

Thrust Vector Control Mechanism

This element includes the thruster array structure, the translation and gimballing mechanisms, and the flexible cabling and propellant feedlines. A full description, including the reason for its selection, was presented in Reference 24 and no changes were required since that report.

Translation of the thruster array, ±33 cm in the horizontal and vertical directions, and gimballing of the corner thrusters, ±10 deg, is adequate to reposition the thrust vector for all operating modes, including single thruster operation. When pairs of thrusters are not available for gimballing, due to multiple failures, a conventional spacecraft reaction control system would be required for the third-axis control.

The present TVC actuators have less than one step of backlash (Reference 24). This minimizes the number of stepper motor steps required to maintain precise control of spacecraft attitude. Additional studies will be required to define actuator backlash and step size requirements for an actual spacecraft.

This TVC mechanization is one of many alternatives. Other means of controlling the thrust vector will be considered as they become available.

Thrust Vector Control Electronics

The TVC electronics (TVCE) provide the link between the spacecraft Sun and star sensors and the thrust vector position actuators (References 25, 26). The sensor outputs are resolved into three-axis error signals by the sensor electronics. These error signals are the inputs to the TVCE module. The TVCE then repositions the thrust vector to correct the spacecraft attitude error.

The demonstration of the stability and stability margin of this control scheme is a major function of the SEPST program. Both analytic (Reference 25) and experimental (Reference 27) studies have been conducted to this end. The experimental work summarized in this report as part of SEPST III, used an analog computer for simulating the spacecraft dynamics (Reference 27). The computer was programmed with the three-axis linearized flexible body equations of large area solar array spacecraft. Using the thrust vector position determined from TVC actuator position potentiometers, the spacecraft attitude errors are generated by the computer simulation program. In closed loop, the actuators are repositioned to null the simulated spacecraft attitude errors. Complete stability is demonstrated by the results discussed later.

Command and Control

It is anticipated that the SEP TSS on deep space missions will require some degree of automatic control. This control requirement results from the expected limited use of communications through the Deep Space Network (DSN) due to the time sharing of the DSN for multiple missions. During long periods (up to a week) without communications, off-normal TSS operation

could jeopardize the mission success and/or make guidance and navigation impossible.

The SEPST III command and control (CC) element (References 28, 29) was designed to automatically perform all presently known TSS control functions. This approach allows the difficulty of full automatic control to be assessed and provides a baseline for possible modifications or simplifications. The primary part of the CC element is a PDP-11 digital computer. The input and output (I/O) logic (Figure 1) is the interface for the computer with other elements. Details of programming, I/O logic design, and specifics of the subroutines used are described in Reference 29.

The computer is commanded from a teletype (Figure 1) for initial startup, interrogation, data printout, override and shutdown. Manual operation is possible through the teletype/computer or through the "manual command" and "switch command" panels (Figure 1).

Propellant Supply

Two means of mercury supply were provided in the SEPST III test setup: (1) a reservoir external to the vacuum chamber to allow flowrate measurements, and (2) a Freon-pressurized bladder-type tank (Reference 30) inside the vacuum chamber. A valve on the tank and hose clamps on the external reservoir line allowed the use of either mercury source. In addition, on the thruster array, a valve was used in the feedline to each thruster to allow individual thruster flowrate measurements. Each thruster was isolated electrically from the common feedline (Reference 6).

1500-h Test Results

The primary objective of the SEPST III testing was to demonstrate the operation of the functionally complete TSS. This demonstration took the form of a 1500-hour test during which two PC-thruster sets were operated simultaneously. A third thruster, provided for redundancy, was operated for a portion of the 1500 h. Operation was controlled by the CC computer and the TVC system was activated periodically.

The summary of testing time accumulated on the TSS (two PC-thruster sets operating simultaneously) and on the PCs is shown in Figure 2. The numbered arrows indicate system shutdowns and/or failures. A detailed discussion of these is presented in Reference 31. The PC accumulated time includes all tests performed in thermal vacuum.

The test plan followed in performing the 1500-h test is shown in Table 1. The corresponding total ion beam current history during the 1500-h test is presented in Figure 3. During the first 1100 h of the test, the beam and arc current level changes were commanded through the teletype/computer manually. This approach was used to accomplish the tasks in Table 1 and to establish mass flowrates and propellant utilization efficiencies over long intervals (12 to 72 h) with constant conditions. The "flight profile" incrementing program incorporated into the CC computer was based on

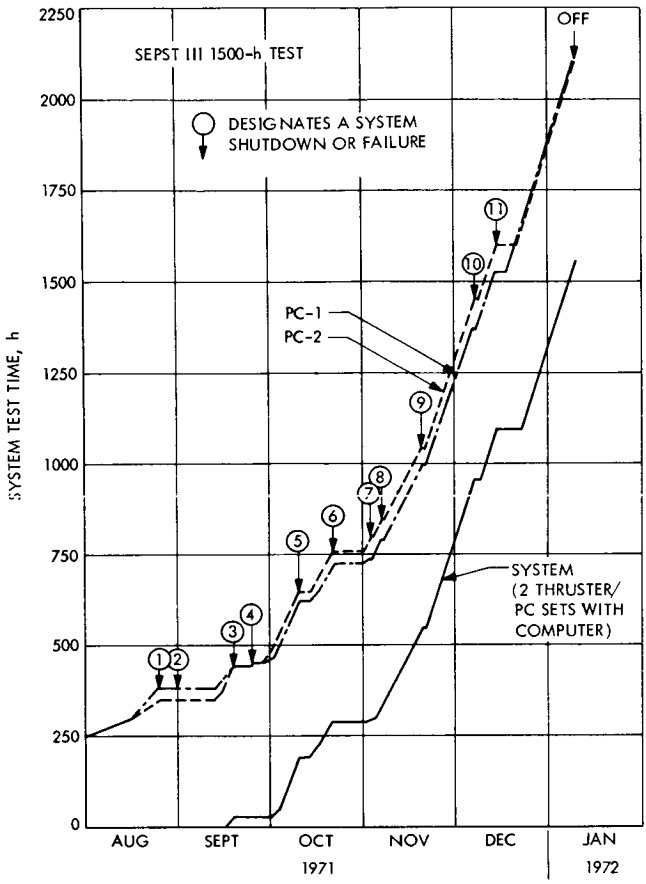

Figure 2. Summary of PC and TSS accumulated test time

operating with a propellant utilization efficiency of about 95%. In the last 400 h the computer increased and decreased the power level automatically using both 2- and 4-h intervals between increments. Both PC-thruster sets were changed simultaneously. Increment intervals as short as a minute or as long as desired were found to be acceptable.

At several times during the 1500 h, the PC input voltages were varied to demonstrate the PC regulation capabilities. Within the accuracy of the data system (± 0.5%), the PC efficiency, including input and output cabling losses, remained constant for input voltage variations over the full design range of 53 to 80 V. A more thorough discussion of PC efficiency measurements is presented in Reference 22.

Thrust Vector Control

The closed-loop TVC function was demonstrated several times during the 1500-h test. A typical result is presented in Figure 4 (from Reference 27) and

Table 1. 1500-h test plan

Time, h	Test
0 - 100	Establish system nominal operation
100 - 110	Check TVC functions
110 - 200	System operation with variable input voltage
200 - 300	PC-thruster switching
300 - 400	Power matching
400 - 1100	Check efficiencies
1100 - 1500	Accelerated flight profile

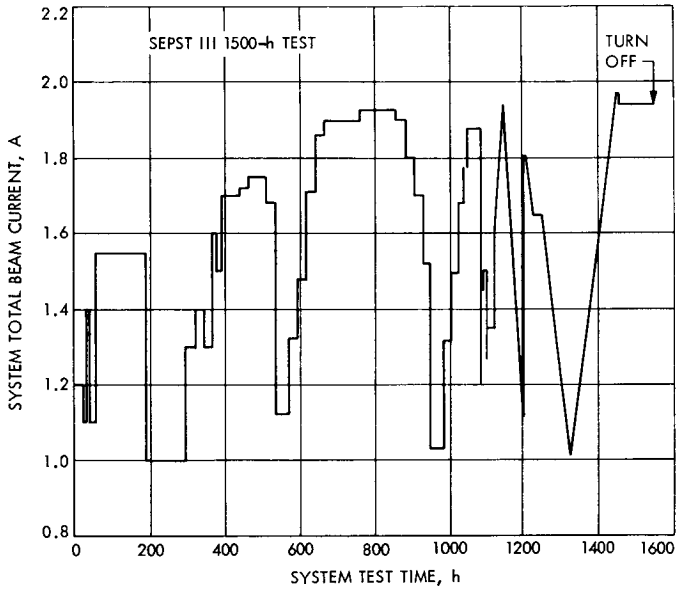

Figure 3. Ion beam-current history during 1500-h test

shows the spacecraft phase plane (angular velocity and position) response to a thrust vector position error. The fact that the curve approaches a null position at a low angular rate demonstrates the closed-loop stability. The long time-constant of the control loop and amplifier drifts in the analog computer required tests to be terminated before the damping was complete. The spacecraft dynamics model used for this work was based on a configuration proposed in Reference 31. A limitation of the present system is its sensitivity to noise at the null position. However, this difficulty is

expected to be solved by improvements in sensor electronics and increased actuator step size.

A complete discussion of the closed-loop TVC testing, including present experimental results and possible improvements in noise sensitivity, is presented in Reference 27. The background analytical results are given in References 25 and 26.

Conclusions

The completion of the 1500-h TSS functional demonstration test was the primary objective of the SEPST III program. However, in achieving this goal, substantially more than the basic functional demonstration was accomplished. The impact of each element on TSS integration, operation, and future development has been experienced. The primary conclusions drawn from this work are:

(1) Accurate and specific definition of interfaces is essential to a timely system integration program. In addition to normal operating requirements, this definition must include requirements for preflight checkout, self-protection at all interfaces, capability expansion, failure modes, maximum input power, inter-element power losses, noise and transient sensitivity and production, packaging for vacuum, thermal control, electrical grounding, cabling, mounting and handling.

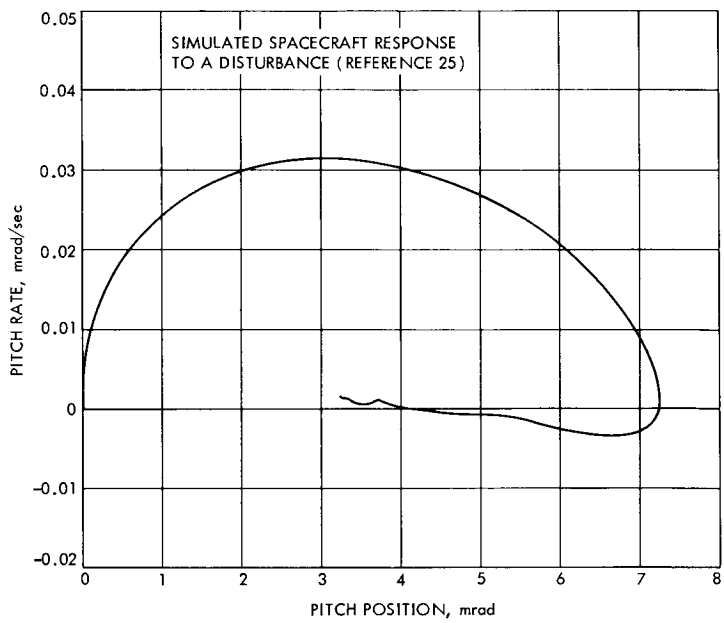

Figure 4. Phase plane plot of simulated spacecraft dynamics using SEPST III TVC

(2) In any future design, each phase of the TSS operation (e.g., startup, throttling, switching, etc.) must be considered in detail to anticipate and account for possible in-flight variations in element characteristics and performance.

(3) Several problem areas require further investigation. These areas include electromagnetic interference, computer noise sensitivity, TVC noise sensitivity, PC input power transients, and applicability of present spacecraft computers to TSS command and control requirements.

(4) This work provides a firm basis for building an engineering model TSS. No fundamental technical problems are apparent, and the TSS efficiency and weight have been shown to fall within presently identified mission constraints.

References

1. Stearns, J. W., and Kerrisk, D. J., "Solar-Powered Electric Propulsion Systems—Engineering and Applications," Paper No. 66-576, in *Proceedings of the AIAA Second Propulsion Joint Specialist Conference*, held in Colorado Springs, Colo., June 1966.

2. Kerrisk, D. J., and Kaufman, H. R., "Electric Propulsion Systems for Primary Spacecraft Propulsion," AIAA Paper No. 67-424, AIAA Third Propulsion Joint Specialists Conference, Washington, D. C., July 1967.

3. Masek, T. D., and Pawlik, E. V., "Thrust System Technology for Solar Electric Propulsion," AIAA Paper No. 68-541, presented at the 4th Propulsion Joint Specialists Conference, Cleveland, Ohio, June 1968.

4. Kerrisk, D. J., and Bartz, D. R., "Primary Electric-Propulsion Systems Technology and Applications," *Astronaut. Aeronaut.*, Vol. 6, No. 6, June 1968.

5. Pawlik, E. V., Costogue, E. N., Ferrera, J. D., and Macie, T. W., "Solar Electric Propulsion System Test," Technical Report 32-1480, Jet Propulsion Laboratory, Pasadena, Calif., August 1970.

6. Masek, T. D., and Macie, T. W., "Solar Electric Propulsion System Technology," AIAA Paper 70-1153, 8th Electric Propulsion Conference, Stanford, California, August 1970.

7. "Solar Electric Propulsion Asteroid Belt Mission Study," Final Report on JPL Contract 952566, North American Rockwell Document SD 70-21, January 1970.

8. "Study of a Solar Electric Multi-Mission Spacecraft," Final Report on JPL Contract 952394, TRW, Inc., Document 09451-6001-RO-02, January 1970.

9. Bartz, D. R., and Horsewood, J. L., "Characteristics, Capabilities, and Costs of Solar-Electric Spacecraft for Planetary Missions," AIAA

Paper No. 69-1103, AIAA Sixth Annual Meeting and Technical Display, October 1969.

10. Wrobel, J. R., and Kerrisk, D. J., "Early Exploration of the Asteroids Region by Solar Powered Electrically Propelled Spacecraft," Paper XA.4, Joint National Meeting of the American Astronautics Society (15th Annual) and the Operations Research Society (35th National), June 1969.

11. Kerrisk, D. J., "Implications of Electric Propulsion Systems for Spacecraft Designs," paper presented at the ASME Space Technology and Heat Transfer Conference, June 1970.

12. Kerrisk, D. J., and Masek, T. D., "Propulsion System Design for Solar Electric Spacecraft," in *Elektrische Antriebssysteme*, proceedings of the Berich uber das DGLR Symposium, held in Braunschweig, West Germany, June 22–23, 1971.

13 Masek, T. D., and Womack, J. R., "Experimental Studies with a Mercury Bombardment Ion Engine System," AIAA Paper No. 67-698, AIAA Electric Propulsion and Plasma Dynamics Conference, Colorado Springs, Colorado, September 1967. (Appears also as Technical Report 32-1280, Jet Propulsion Laboratory, Pasadena, California, July 15, 1968).

14. Weigand, A. J., and Nakanishi, S., "A Survey of Kaufman Thruster Cathodes," NASA TM X-67918, presented at Symposium on Ion Sources for Formation of Ion Beams, Upton, New York, October 1971.

15. Reader, P. D., and Kerslake, W. R., "Bombardment Thruster Investigations at the Lewis Research Center—1971," NASA TM X-67836, presented at Sixth Symposium on Advanced Propulsion Concepts sponsored by the Air Force Office of Scientific Research, Niagara Falls, New York, May 1971.

16. Pawlik, E. V., and Fitzgerald, D. J., "Cathode and Ion Chamber Investigations on a 20-cm Diameter Hollow Cathode Ion Thruster," AIAA Paper No. 71-158, AIAA Aerospace Sciences Meeting, New York, New York, January 1971.

17. "Development and Test of an Ion Engine System Employing Modular Power Conditioning," Final Report on JPL Contract 951144, Hughes Aircraft Company Document SSD60374R, September 1966.

18. Pawlik, E. V., Costogue, E. N., and Schaefer, W. C., "Operation of a Light-weight Power Conditioner with a Hollow Cathode Ion Thruster," AIAA Paper No. 70-648, AIAA Sixth Propulsion Joint Specialist Conference, June 1970.

19. Macie, T. W., and Masek, T. D., "Power Conditioner Evaluation—Circuit Problems and Cures—SEPST III, BB-1," in *Supporting*

Research and Advanced Development, Space Programs Summary 37-62, Vol. III, pp. 245–250. Jet Propulsion Laboratory, Pasadena, California, April 1970.

20. Muldoon, W. J., Garth, D. R., and Benson, G. C., "Functional and Physical Design of a Flight Prototype Ion Engine Power Conditioner," ASME Paper No. 70-AV/SPT-38, ASME Space Technology and Heat Transfer Conference, June 1970.

21. "Development and Test of a Flight Prototype Power Conditioner for 20-cm Mercury Bombardment Electric Thruster System," Report on JPL Contract 952297, Hughes Aircraft Company, April 1971.

22. Masek, T. D., Macie, T. W., Costogue, E. N., Muldoon, W. J., Garth, D. R., and Benson, G. C., "Integration of a Breadboard Power Conditioner with a 20-cm Ion Thruster," in *J. Space. Rock.*, Vol. 9, No. 2, pp. 71–78, February 1972.

23. Womack, J. R., and Chen, J., "Structural Evaluations and Dynamic Testing of Solar Electric Propulsion Components," presented at the 9th Electric Propulsion Conference, Washington, D.C., April 1972.

24. Perkins, G. S., Johnson, K. G., Ferrera, J. D., and Masek, T. D., "A Mechanism for Three Axis Control of an Ion Thruster Array," AIAA Paper No. 70-1156, 8th Electric Propulsion Conference, Stanford, California, August 1970.

25. Marsh, E. L., "The Attitude Control of a Flexible Solar Electric Spacecraft," AIAA Paper No. 70-1140, 8th Electric Propulsion Conference, Stanford, California, August 1970.

26. Crawford, W. E., and Fleischer, G. E., "Solar Electric Spacecraft Thrust Vector Control Mechanization," in *Supporting Research and Advanced Development*, Space Programs Summary 37-62, Vol. III, pp. 217–219. Jet Propulsion Laboratory, Pasadena, California, April 1970.

27. Fleischer, G. E., and Crawford, W. E., "A Summary of Solar Electric Thrust Vector Control System Development Efforts and Results," EM 344-376, April 25, 1972 (JPL internal document).

28. Doupe, H., and Macie, T. W., "Master Controller for an Electric Thrust Subsystem," presented at Fall Symposium of Digital Equipment Computer Users Society, San Francisco, California, November 11, 1971.

29. Macie, T. W., and Doupe, H., "Automatic Control of an Electric Thrust Subsystem," presented at AIAA 9th Electric Propulsion Conference, Washington, D. C., April 1972.

30. Womack, J. R., "Design and Evaluation of Propellant Tankage for SEPST Program, in *Supporting Research and Advanced Development*, Space Programs Summary 37-58, Vol. III, pp. 217-219. Jet Propulsion Laboratory, Pasadena, California, August 1969.

31. Masek, T. D., "Solar Electric Propulsion Breadboard Thrust Subsystem Test Results," AIAA Paper No. 72-507, presented at AIAA 9th Electric Propulsion Conference, Washington, D. C., April 1972.

32. "Solar Electric Multimission Spacecraft: (SEMMS) Phase A, Final Report 617-4," Jet Propulsion Laboratory, Pasadena, California, March 17, 1972 (JPL internal document).

Bibliography of Current Reporting

Author Index With Abstracts

ABREU, A.

A01 Transformation of Received Signal Polarization Angle to the Plane of the Ecliptic

C. T. Stelzried, T. Sato, and A. Abreu

J. Spacecraft Rockets, Vol. 9, No. 2, pp. 69–70, February 1972

For abstract, see Stelzried, C. T.

ADAMS, R. W.

A02 Ion Thruster Performance Calibration

E. V. Pawlik, R. Goldstein, D. J. Fitzgerald, and R. W. Adams

Preprint 72-475, AIAA Ninth Electric Propulsion Conference, Bethesda, Maryland, April 17–19, 1972

For abstract, see Pawlik, E. V.

ALLEN, J. E.

A03 DSN Progress Report for March–April 1972: DSN Monitor Performance Program

J. E. Allen

Technical Report 32-1526, Vol. IX, pp. 5–11, June 15, 1972

This article provides: (1) a general description of the programs used by DSN monitor analysts in the generation of the weekly and monthly performance summary reports, and (2) the format guide

used by the DSN real-time analyst to assist in interpreting the formatted data.

ANDERSON, T. O.

A04 DSN Progress Report for March–April 1972: Wide Range, Essentially Linear Control Circuit for Control of the Reference Frequency in Digital Phase-Locked Loops

T. O. Anderson

Technical Report 32-1526, Vol. IX, pp. 119–122, June 15, 1972

A simple all-digital control circuit intended for control of the frequency of the reference signal in all-digital phase-locked loops is presented. Such control circuits, of prior art, are often nonlinear and provide only narrow frequency range. The present control circuit, though very simple, provides essentially linear control for a wide frequency range. The circuit presented in this article is intended for use in all-digital phase-locked loops and is described in this context.

A05 DSN Progress Report for March–April 1972: Efficient Implementation of a Multichannel High-Speed Correlator

T. O. Anderson

Technical Report 32-1526, Vol. IX, pp. 123–127, June 15, 1972

The correlator presented in this article is an all-digital or sampled real-time signal processing system. It is intended for applications requiring wide bandwidth and high resolution, such as measurement of spacecraft spectra or the close scrutiny of a wide bandwidth for interference to validate the performance of the new dual S/X-band DSN system. The detection of signals in noise upon reception of radio astronomy signals is yet another application for which the present instrumentation would be useful.

ANDRYCZYK, R. W.

A06 A Closely Regulated TWT Converter

D. J. Hopper and R. W. Andryczyk (General Electric Company)

IEEE Trans. Aerosp. Electron. Sys., Vol. AES-7, No. 6, pp. 1147–1150 November 1971

For abstract, see Hopper, D. J.

BACK, L. H.

B01 Partially Ionized Gas Flow and Heat Transfer in the Separation, Reattachment, and Redevelopment Regions Downstream of an Abrupt Circular Channel Expansion

L. H. Back, P. F. Massier, and E. J. Roschke

Trans. ASME, Ser. C: J. Heat Transf., Vol. 94, No. 1, pp. 119–127, February 1972

Heat transfer and pressure measurements obtained in the separation, reattachment, and redevelopment regions along a tube and nozzle located downstream of an abrupt channel expansion are presented for a very high enthalpy flow of argon. The ionization energy fraction extended up to 0.6 at the tube inlet just downstream of the arc heater. Reattachment resulted from the growth of an instability in the vortex sheet-like shear layer between the central jet that discharged into the tube and the reverse flow along the wall at the lower Reynolds numbers, as indicated by water flow visualization studies which were found to dynamically model the high-temperature gas flow. A reasonably good prediction of the heat transfer in the reattachment region where the highest heat transfer occurred and in the redevelopment region downstream can be made by using existing laminar boundary layer theory for a partially ionized gas. In the experiments as much as 90% of the inlet energy was lost by heat transfer to the tube and the nozzle wall.

BARBER, T. A.

B02 Basic Parameters for Low Thrust Mission and System Analysis

T. A. Barber, J. L. Horsewood (Analytical Mechanics Associates, Inc.), and H. Meissinger (TRW Systems, Inc.)

Preprint 72-426, AIAA Ninth Electric Propulsion Conference, Bethesda, Maryland, April 17–19, 1972

Any form of mission analysis has as its basis a large number of trajectories mapping out the parameter range of the mission under study. Low thrust mission analysis has long been hampered by this requirement to generate many optimized trajectories which frequently need to be rerun to explore the effect of changes in some vehicle or mission parameters, particularly launch vehicle changes. This paper proposes a basic set of normalized parameters to represent the low thrust system characteristics and derives the conditions which must be met to obtain trajectory and performance data which are invariant with the launch vehicle characteristics, the selected power, the specific mass of the low thrust vehicle, and the efficiency of the ion propulsion system. This normal-

ized representation of mission characteristics frees the analyst from having to rerun the trajectories if any of the aforementioned parameters are varied. Examples pertaining to a low thrust Jupiter flyby and comet Encke rendezvous are given to demonstrate the utility of the method of presentation.

BARNES, G. D.

B03 DSN Progress Report for January–February 1972: Angle Tracking Analysis and Test Development for the Integrated Stations

G. D. Barnes

Technical Report 32-1526, Vol. VIII, pp. 131–140, April 15, 1972

Analysis and test development have been completed for the integrated tracking system. An antenna servo model was developed and its transfer function and gain constants are presented. The model was used to simulate the response of an antenna in the autotrack and program modes. These simulation results are compared with the data collected at the Pioneer Deep Space Station, and the differences between the two modes are shown. Antenna response data for the integrated servo system are compared with the Echo Deep Space Station response data and the Deep Space Instrumentation Facility servo specification curves. The servo specification curves are shown to be unrealistic for either the standard or integrated angle tracking systems.

BARNES, T. G.

B04 Jupiter: Observation of Deuterated Methane in the Atmosphere

R. Beer, C. B. Farmer, R. H. Norton, J. V. Martonchik (University of Texas), and T. G. Barnes (University of Texas)

Science, Vol. 172, No. 4028, pp. 1360–1361, March 24, 1972

For abstract, see Beer, R.

BARTH, C. A.

B05 Mariner 9 Science Experiments: Preliminary Results

R. H. Steinbacher, A. J. Kliore, J. Lorell, H. Hipsher (National Aeronautics and Space Administration), C. A. Barth (University of Colorado),

H. Masursky (U.S. Geological Survey), G. Münch (California Institute of Technology), J. C. Pearl (Goddard Space Flight Center), and B. A. Smith (New Mexico State University)

Science, Vol. 175, No. 4019, pp. 293–294, January 21, 1972

For abstract, see Steinbacher, R. H.

B06 Mariner 9 Ultraviolet Spectrometer Experiment: Initial Results

C. A. Barth (University of Colorado), C. W. Hord (University of Colorado), A. I. Stewart (University of Colorado), and A. L. Lane

Science, Vol. 175, No. 4019, pp. 309–312, January 21, 1972

The ultraviolet airglow spectrum of Mars has been measured from an orbiting spacecraft during a 30-day period in November–December 1971. The emission rates of the carbon monoxide Cameron and fourth positive bands, the atomic oxygen 1304-Å line and the atomic hydrogen 1216-Å line have been measured as a function of altitude. Significant variations in the scale height of the CO Cameron band airglow have been observed during a period of variable solar activity; however, the atomic oxygen and hydrogen airglow lines are present during all the observations. Measurements of the reflectance of the lower atmosphere of Mars show the spectral characteristics of particle scattering and a magnitude that is about 50% of that measured during the Mariner 6 and 7 experiments in 1969. The variation of reflectance across the planet may be represented by a model in which the dominant scatterer is dust that absorbs in the ultraviolet and has an optical depth greater than 1. The atmosphere above the polar region is clearer than over the rest of the planet.

B07 Mariner 9 Ultraviolet Spectrometer Experiment: Stellar Observations

C. F. Lillie (University of Colorado), R. C. Bohlin (University of Colorado), M. R. Molnar (University of Colorado), C. A. Barth (University of Colorado), and A. L. Lane

Science, Vol. 175, No. 4019, pp. 321–322, January 21, 1972

For abstract, see Lillie, C. F.

BATELAAN, P. D.

B08 DSN Progress Report for March–April 1972: Radio Source Calibration Program (RASCAL)—Phase 1: Antenna Gain Calibration

P. D. Batelaan

Technical Report 32-1526, Vol. IX, pp. 137–140, June 15, 1972

A new program for measuring antenna gain of the large DSN antennas is described. The gain measurement procedure is outlined. Improvements over past techniques have resulted in better knowledge of gain-standard-horn calibrations, in more compact procedure, and in changes in the precision comparison attenuator. The gain accuracy goal of the primary station is ±0.05 dB, 1 σ.

BAUMERT, L. D.

B09 DSN Progress Report for March–April 1972: A Note on the Griesmer Bound

L. D. Baumert and R. J. McEliece

Technical Report 32-1526, Vol. IX, pp. 49–52, June 15, 1972

Griesmer's lower bound for the word length n of a linear code of dimension k and minimum distance d is shown to be sharp for fixed k when d is sufficiently large. For $k \leq 6$ and all d, the minimum word length is determined.

B10 Weights of Irreducible Cyclic Codes

L. D. Baumert and R. J. McEliece

Inform. Control, Vol. 20, No. 2, pp. 158–175, March 1972

With any fixed prime number p and positive integer N, not divisible by p, there is associated an infinite sequence of cyclic codes. In a previous article, it was shown that a theorem of Davenport-Hasse reduces the calculation of the weight distributions for this whole sequence of codes to a single calculation (essentially that of calculating the weight distribution for the simplest code of the sequence). The primary object of this paper is the development of machinery which simplifies this remaining calculation. Detailed examples are given. In addition, tables are presented which essentially solve the weight distribution problem for all such binary codes with $N < 100$ and, when the block length is less than one million, give the complete weight enumerator.

BEER, R.

B11 Astronomical Infrared Spectroscopy With a Connes-Type Interferometer: III. Alpha Orionis, 2600–3450 cm^{-1}

R. Beer, R. B. Hutchison, R. H. Norton, and
D. L. Lambert (University of Texas)

Astrophys. J., Vol. 172, No. 1, Pt. 1, pp. 89–115,
February 15, 1972

Recent spectra of α Ori in the 3–4-μ region at a resolving power of about 10,000 show clear evidence of the $\Delta v = 1$ sequence of the rotation-vibration bands of OH. A detailed investigation of the rotational and vibrational populations suggests that the OH is close to being in LTE at an apparent temperature of 4100 ± 200°K. We deduce an OH abundance of 1.2×10^{20} molecules cm^{-2} and upper limits for H_2O and $H^{35}Cl$ of 8×10^{18} and 8×10^{17} molecules cm^{-2}, respectively. We further deduce that the rms turbulence velocity in the region of OH line formation is 11.5 ± 2 km s^{-1}. The implications of these data on abundances in *M* supergiant atmospheres are discussed.

B12 Jupiter: Observation of Deuterated Methane in the Atmosphere

R. Beer, C. B. Farmer, R. H. Norton,
J. V. Martonchik (University of Texas), and
T. G. Barnes (University of Texas)

Science, Vol. 172, No. 4028, pp. 1360–1361,
March 24, 1972

During May 1971, the authors obtained a number of whole-planet spectra of Jupiter in the spectral region from 1800 to 2200 cm^{-1} at a resolution of 0.55 cm^{-1}. Singly deuterated methane was positively identified in the 4- to 5-μ spectrum of Jupiter.

BEJCZY, A. K.

B13 Switched-Mode Adaptive Terminal Control for Propulsive Landing of Nonlifting Spacecraft

A. K. Bejczy

Preprint 71-903, AIAA Guidance,
Control and Flight Mechanics Conference, Hempstead,
New York, August 16–18, 1971

A combined estimation and control scheme is described for propulsive landing of a nonlifting gravity-turn ballistic vehicle under uncertain atmospheric conditions. The core of the scheme is a dual integration algorithm. One algorithm acts as a sequential filter

producing updated estimates on the *a priori* uncertain atmospheric parameters and the state variables, while the other algorithm acts in an iterative-logical mode to control the throttle setting. The filter inputs are on-board radar range and doppler velocity measurements and accelerometer data related to the vehicle's nongravitational longitudinal acceleration. Three different filter schemes are developed, utilizing different combinations of measurement inputs. The adaptive switched-mode landing control policy can handle a considerable number of errors in initial altitude and velocity, as well as 50–70% uncertainties in the atmospheric parameters, and performs the soft-landing task with a 20–35% reduction of the fuel consumption needed by a comparable control law.

B14 Approximate Nonlinear Filters and Deterministic Filter Gains

A. K. Bejczy and R. Sridhar (University of California, Los Angeles)

Trans. ASME, Ser. G: J. Dynam. Sys., Meas., Contr., Vol. 94, No. 1, pp. 57–63, March 1972

A simple nonlinear filter construction and performance evaluation method is described and illustrated on several examples by comparing it to more complex nonlinear filter schemes. In the new method, the filter gain is a precomputed, deterministic quantity (possibly a constant) and, the filter's performance is (approximately) described by deterministic differential equations which can be solved off-line.

BENSON, G. C.

B15 Integration of a Breadboard Power Conditioner With a 20-cm Ion Thruster

T. D. Masek, T. W. Macie, E. N. Costogue,
W. J. Muldoon (Hughes Aircraft Company),
D. R. Garth (Hughes Aircraft Company), and
G. C. Benson (Hughes Aircraft Company)

J. Spacecraft Rockets, Vol. 9, No. 2, pp. 71–78, February 1972

For abstract, see Masek, T. D.

BERMAN, A. L.

B16 DSN Progress Report for March–April 1972: Effects of the Pioneer 10 Antenna Polarization and Spacecraft Rotation as Seen in the Radio Metric Data

A. L. Berman

Technical Report 32-1526, Vol. IX, pp. 201–206, June 15, 1972

The Pioneer 10 antenna polarization and spacecraft rotation introduce a signature into the radio metric doppler data, which, unless otherwise noted, might be confused with a degradation of the tracking system. This signature, especially in regard to effects as seen in doppler residuals and doppler noise, is analyzed in detail in this article.

BERMAN, P. A.

B17 Considerations With Respect to the Design of Solar Photovoltaic Power Systems for Terrestrial Applications

P. A. Berman

Technical Report 32-1558, June 15, 1972

The various factors involved in the development of solar photovoltaic power systems for terrestrial application are discussed. The trade-offs, compromises, and optimization studies which must be performed in order to develop a viable terrestrial solar array system are described. It is concluded that the technology now exists for the fabrication of terrestrial solar arrays, but that the costs would be prohibitive. Various approaches to cost reduction are presented, and the general requirements for materials and processes are delineated.

B18 JPL Lithium-Doped Solar Cell Development Program

P. A. Berman

JPL Quarterly Technical Review, Vol. 2, No. 1, pp. 29–36, April 1972

One of the most significant problems encountered in the use of silicon solar cells in space has been their sensitivity to electron and proton radiation exposure. A major advancement was achieved when the P-diffused-into-N-base solar cells were replaced with the more radiation-tolerant N-diffused-into-P-base solar cells. Another advancement in achieving greater radiation tolerance was the discovery that the addition of lithium to N-base silicon resulted in what appeared to be annealing of radiation-induced defects. This

phenomenon is being exploited to develop a high-efficiency, radiation-resistant, lithium-doped solar cell. In this investigation, lithium-doped solar cells fabricated from oxygen-lean and oxygen-rich silicon have been obtained with average initial efficiencies of 11.9% at air mass zero and 28°C, as compared to state-of-the-art N/P cells fabricated from 10-Ω-cm silicon with average efficiencies of 11.3% under similar conditions. Lithium-doped cells have demonstrated the ability to withstand three to five times the fluence of 1-MeV electrons before degrading to a power equivalent to that of state-of-the-art solar cells. This article discusses the principal investigations carried out with respect to fabrication of high-efficiency, radiation-resistant, lithium-doped cells, including starting material, P/N junction diffusion, lithium source introduction, and lithium diffusion.

BIERMAN, G. J.

B19 Power Series Evaluation of Transition and Covariance Matrices

G. J. Bierman (Litton Systems)

IEEE Trans. Automat. Contr., Vol. AC-17, No. 2, pp. 228–232, April 1972

Power series solutions to the matrix covariance differential equation

$$\dot{P} = AP + (AP)' + Q$$

and the transition differential equation

$$\dot{\Phi} = A\Phi$$

are re-examined. Truncation error bounds are derived which are computationally attractive and which extend previous results. Polynomial approximations are obtained by exploiting the functional equations satisfied by the transition and covariance matrices. The series-functional equation propagation technique represents a fast and accurate alternative to the numerical integration of the time-invariant transition and covariance equations.

BILLINGSLEY, F. C.

B20 Computer-Generated Color Image Display of Lunar Spectral Reflectance Ratios

F. C. Billingsley

Photogr. Sci. Eng., Vol. 16, No. 1, pp. 51–57,
January–February 1972

Color separation pictures were taken on Apollo 12 through red, green, and blue filters on black-and-white film. Computer processing has been utilized to extract quantitative color information from these pictures and to produce output color pictures. Four computer-generated output color separations are combined to give a color image in which small color reflectance differences on the lunar surface are represented by the computer-generated colors independent of the intensity of the light reflected from the lunar surface. Calibration step wedges have been carried through the entire process to provide total system calibration for the removal of film nonlinearities. The computer calculations map the red/green, blue/green combination at each image point onto the chromaticity diagram so that it is represented by a unique color, and then calculates the four color sources used to produce the desired color at this point in the output picture. These same methods can be used to represent other parameters occurring and sensed simultaneously over a spatial region.

BOGNER, R. S.

B21 Development and Testing of a High Cycle Life 30 A-h Sealed AgO–Zn Battery

R. S. Bogner

Technical Memorandum 33-536, May 1, 1972

A two-phase program was initiated to investigate design parameters and new technology for the development of an improved AgO–Zn battery. The basic performance goal was 100 charge/discharge cycles (22 h/2 h) at 50% depth-of-discharge following a 6-mo period of charged stand at room temperature (25 ± 4°C). Phase I, cell evaluation, involved testing 70 cells in five-cell groups. The major design variables were active material ratios, electrolyte concentrations, separator systems, and negative plate shape. Phase I testing showed that cycle life could be improved 10 to 20% by using greater ratios of zinc to silver oxide and higher electrolyte concentrations. Wedge-shaped negatives increased cycle life by nearly 100%. The fibrous-sausage-casing separators proved superior to the RAI 2291 separators for cycle life; however, test results were complicated by the cell-pack tightness, a variable not originally planned to be introduced into the tests.

Phase II battery evaluation, which was initiated before the Phase I results were known completely, involved evaluation of six designs of 19-cell batteries. Phase II testing was done at the Naval Ammunition Depot, Crane, Indiana. Only one battery exceeded 100

cycles following a 9-mo charged stand. That battery, containing fibrous-sausage-casing separators, gave 204 cycles at 50% depth-of-discharge before the first cell failed. Unfortunately, the wedge-shaped negative was not evaluated in Phase II. Phase II and Phase I failures were due to loss of negative plate capacity caused by negative plate erosion.

BOHLIN, R. C.

B22 Mariner 9 Ultraviolet Spectrometer Experiment: Stellar Observations

C. F. Lillie (University of Colorado), R. C. Bohlin (University of Colorado), M. R. Molnar (University of Colorado), C. A. Barth (University of Colorado), and A. L. Lane

Science, Vol. 175, No. 4019, pp. 321–322, January 21, 1972

For abstract, see Lillie, C. F.

BORN, G. H.

B23 Mariner 9 Celestial Mechanics Experiment: Gravity Field and Pole Direction of Mars

J. Lorell, G. H. Born, E. J. Christensen, J. F. Jordan, P. A. Laing, W. Martin, W. L. Sjogren, I. I. Shapiro (Massachusetts Institute of Technology), R. D. Reasenberg (Massachusetts Institute of Technology), and G. L. Slater (Massachusetts Institute of Technology)

Science, Vol. 175, No. 4019, pp. 317–320, January 21, 1972

For abstract, see Lorell, J.

BOSE, T. K.

B24 Cross-Flow Blowing of a Two-Dimensional Stationary Arc

T. K. Bose (Indian Institute of Technology)

AIAA J., Vol. 10, No. 1, pp. 80–86, January 1972

The effect of cross-flow blowing on a two-dimensional stationary arc between a pair of electrodes has been studied theoretically. It is demonstrated in the analysis that the electrons emitted from the cathode undergo collisions with the heavy particles and are deflected in the flow direction by the component of a collisional force associated with the relative difference in flow velocities

between electrons and heavy particles. The resultant motion of the electrons describing the arc is thus caused by a combined action of the collisional force that results from the externally applied electric field. An expression is given which enables computation of the arc shape to be made provided the velocity distribution of the cross-flow and the distribution of the externally applied electric field are prescribed. The analysis has been applied for a case in which an analytical expression for the distribution of the externally applied electric field is available. An electrical discharge between two point electrodes was chosen with a uniform velocity distribution of the cross-flow. Numerical results are presented for the maximum deflection as a function of a blowing parameter. In addition, it is shown that the temperature distribution within the arc is asymmetric.

BOUDREAU, J. E.

B25 Closed-Loop Dynamics of In-Core Thermionic Reactor Systems

C. D. Sawyer and J. E. Boudreau

Technical Memorandum 33-546, May 15, 1972

For abstract, see Sawyer, C. D.

BRERETON, R. G.

B26 A View of the Moon

R. G. Brereton

JPL Quarterly Technical Review, Vol. 2, No. 1, pp. 1–11, April 1972

Apollo information on lunar science is now voluminous, and NASA has recognized the need for a task that would collate and interpret Apollo results and provide a synthesized view of the Moon. The initial conclusions of such a task carried out at JPL are reviewed in this article. In summary, whereas most of the Earth's surface is highly mobile because of dynamic endogenic and exogenic processes, the lunar surface is old and stable and coexists with the ambient environment of space. The Moon is essentially quiet seismically, does not have a heavy solid or liquid core, and has a much cooler internal temperature than Earth. The lunar lithosphere is both old and strong and appears to have been little modified by volcanic or tectonic activity for more than three billion years.

BROKL, S. S.

B27 DSN Progress Report for March–April 1972: Computer Display and Entry Panel

S. S. Brokl

Technical Report 32-1526, Vol. IX, pp. 44–48, June 15, 1972

The computer display and entry panel is a programmable high-speed numerical display and entry device for use with XDS 900-series computers. It contains additional sense-switch and sense-light capability along with a system interrupt. This type of device is expected to find application in troubleshooting Deep Space Instrumentation Facility minicomputers in the network repair facility, in developing minicomputer software, and as a status-display device for the DSN network operations control facility.

BROWN, D. W.

B28 DSN Progress Report for January–February 1972: Third-Order Phase-Locked Loop Perspectives

D. W. Brown

Technical Report 32-1526, Vol. VIII, pp. 103–114, April 15, 1972

Compared with the development of a second-order phase-lock design, the analysis and practical application of a third-order phase-lock design have been sporadic in both the servomechanism and telecommunication fields. The attractiveness of minimal tracking errors resulting from near "perfect" third-order filtering (three true integrators) has been largely offset by undesirable acquisition properties and to some extent by a dearth of analysis of this configuration. A useful approach, both in viewpoint and in design, is to consider the prevalent "imperfect" second-order and third-order configurations for what they are—namely, loops with one integrator augmented by one or two lag time constants, so proportioned with respect to loop gain as to approximate the closed-loop response of true second- and third-order configurations, while manifesting a controlled (but not infinite) improvement in tracking performance over the first-order loop. This article seeks to apply this approach to the existing work in third-order analysis, and to emphasize the principal effects, both positive and negative, of the relative proportioning of loop gain and time constants, with a view toward practical exploitation of the best features of these loop configurations.

BUTMAN, S.

B29 DSN Progress Report for March–April 1972: On a Communications Strategy for Channels With Unknown Capacity

S. Butman

Technical Report 32-1526, Vol. IX, pp. 53–58, June 15, 1972

When the capacity of a channel cannot be determined in advance, or if it can change unpredictably, there is a problem in selecting the rate of transmission. On the one hand, a design for the worst case prevents recovery of large amounts of data when the situation is better than anticipated. On the other hand, a design based on optimistic assumptions is threatened by total failure when the conditions are bad. This article discusses a strategy that covers the in-between range of possibilities, and its implementation on Mariner-type telemetry systems. It is shown that large increases in expected data rate can be obtained at the cost of small reductions in the minimum rate. Final decisions are made on the ground after all the data are received.

CAIN, D. L.

C01 Mariner 9 S-Band Martian Occultation Experiment: Initial Results on the Atmosphere and Topography of Mars

A. J. Kliore, D. L. Cain, G. Fjeldbo, B. L. Seidel, and S. I. Rasool (National Aeronautics and Space Administration)

Science, Vol. 175, No. 4019, pp. 313–317, January 21, 1972

For abstract, see Kliore, A. J.

CAMERON, R. E.

C02 Surface Distribution of Microorganisms in Antarctic Dry-Valley Soils: A Martian Analog

R. E. Cameron, H. P. Conrow, D. R. Gensel, G. H. Lacy, and F. A. Morelli

Antarctic J. U.S., Vol. VI, No. 5, pp. 211–213, September–October 1971

Planners for future soft landings on Mars need to know whether a single soil sample taken near the point of landing is likely to be adequate for analysis and life detection or whether several samples

taken at various locations would be better. A JPL project in the barren dry valleys of Antarctica is helping to resolve that problem and others related to Martian exploration.

Two Antarctic dry valleys, McKelvey Valley and Pearse Valley, were selected for systematic sampling of the surface 2 cm of soil to determine if a sterile soil could be found in a specified area of the dry valleys and to determine the distribution, abundance, and kinds of microorganisms present within a given area. This article presents the results of analyses performed on the soil samples.

CAMPBELL, J. D.

C03 DSN Progress Report for January–February 1972: Antenna Drive System Performance Evaluation Using PN Codes

R. M. Gosline, E. B. Jackson, and J. D. Campbell

Technical Report 32-1526, Vol. VIII, pp. 74–79, April 15, 1972

For abstract, see Gosline, R. M.

CANNON, W. A.

C04 Origin of Planetary Primordial Rare Gas: The Possible Role of Adsorption

F. P. Fanale and W. A. Cannon

Geochim. Cosmochim. Acta, Vol. 36, No. 3, pp. 319–328, March 1972

For abstract, see Fanale, F. P.

CARRAWAY, J. B.

C05 Miniature Biotelemeter Gives Multichannel Wideband Biomedical Data

J. B. Carraway

JPL Quarterly Technical Review, Vol. 2, No. 1, pp. 152–166, April 1972

Doctors and biologists have expressed a need for the capability to monitor vital physiological functions from human and animal subjects unrestrained by wires. JPL has responded under NASA Technology Applications Office sponsorship by developing an advanced device suitable for a wide variety of medical and biological research applications. The design of this miniature, 12-cm^3, 10-channel, wideband (5-kHz/channel), pulse-amplitude-modulation/

frequency-modulation biotelemeter takes advantage of modern device technology (e.g., integrated-circuit operational amplifiers, complementary-symmetry metal oxide semiconductor logic, and solid-state switches) and hybrid packaging techniques. The telemeter is currently being used for monitoring 10 channels of neuron firings from specific regions of the brains in rats implanted with chronic electrodes. Possible follow-on applications include multichannel telemetry of electroencephalograms, electrocardiograms, electromyograms, state functions, and dynamic processes such as blood flow and body chemistry. The design, fabrication, and testing of an engineering-model biotelemeter are described in this article.

CASSON, D.

C06 Solution Properties of Novel Polyelectrolytes

D. Casson and A. Rembaum

Macromolecules, Vol. 5, No. 1, pp. 75–81,
January–February 1972

A series of polyelectrolytes, of different molecular weights, with the unit segment structure

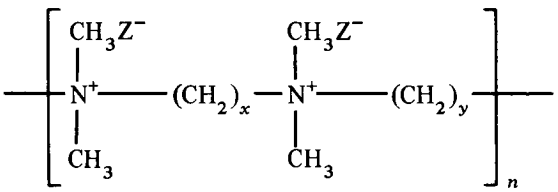

were synthesized through the Menschutkin reaction and are referred to as ionene polymers. The solution properties of a high-charge-density ionene polymer (3,4 Br, $x = 3$, $y = 4$, Z = Br) were compared with those of an ionene polymer in which the positive charges are separated by six CH_2 groups (6,6 Br, $x = 6$, $y = 6$, Z = Br). These polyelectrolytes, when dissolved in aqueous 0.4 *M* KBr, were found to approximate the behavior of conventional polymers. The intrinsic viscosity–molecular weight relationship in aqueous 0.4 *M* KBr was determined for 3,4 Br and 6,6 Br by means of the light-scattering technique and can be expressed by

$$[\eta]_{3,4\ Br} = (2.94 \times 10^{-4})M^{0.61}$$

$$[\eta]_{6,6\ Br} = (6.22 \times 10^{-4})M^{0.58}$$

A viscosity study as a function of concentration of a number of potassium salts in water revealed that the reduced viscosity of a 6,6 Br increases as the anions change in the following order: $CNS^- < I^- < NO_3^- < Br^- < Cl^- < F^-$. This trend is attributed to a

parallel decrease of counterion site binding. In the absence of added salts, the viscosity behavior is adequately represented by the Fuoss equation.

CHADWICK, H. D.

C07 Binary Single-Sideband Phase-Modulated Communication Systems

H. D. Chadwick

IEEE Trans. Inform. Theor., Vol. IT-18, No. 1, pp. 214–215, January 1972

Single-sideband phase modulation, in which a signal is simultaneously phase- and amplitude-modulated by a signal and its Hilbert transform, is shown to be suboptimum for binary signaling in white gaussian noise. An alternative single-sideband technique based on the properties of binary suppressed-carrier phase modulation is proposed and shown to give performance equivalent to the double-sideband version.

CHANEY, W. D.

C08 DSN Progress Report for January–February 1972: DSN Tracking System: Operation With the Mutual Stations

W. D. Chaney and H. E. Nance

Technical Report 32-1526, Vol. VIII, pp. 5–7, April 15, 1972

Two types of 26-m-antenna tracking stations are available to the DSN for spacecraft tracking. Pioneer F will be supported primarily by the Mutual stations (combined DSN and Spaceflight Tracking and Data Network equipment). This article describes in some detail the various functions performed by the Mutual station tracking system and compares the system equipment and functions with those of the standard DSN tracking station. The operational capabilities and interfaces between the modules within the station are presented in a logical sequence, with the final output interfacing with the Ground Communications Facility and the Space Flight Operations Facility.

CHASE, S. C., JR.

C09 Infrared Radiometry Experiment on Mariner 9

S. C. Chase, Jr. (Santa Barbara Research Center),
H. Hatzenbeler (Santa Barbara Research Center),
H. Kieffer (University of California, Los Angeles), E. Miner,

G. Münch (California Institute of Technology), and
G. Neugebauer (California Institute of Technology)

Science, Vol. 175, No. 4019, pp. 308–309,
January 21, 1972

The brightness temperatures at 10 and 20 μm measured by the Mariner 9 infrared radiometer differ substantially from those predicted by the radiometer results of Mariners 6 and 7. The results indicate a significant latitude-dependent contribution of the atmospheric dust to the observed thermal emission.

CHRISTENSEN, E. J.

C10 Mariner 9 Celestial Mechanics Experiment: Gravity Field and Pole Direction of Mars

J. Lorell, G. H. Born, E. J. Christensen, J. F. Jordan,
P. A. Laing, W. Martin, W. L. Sjogren,
I. I. Shapiro (Massachusetts Institute of Technology),
R. D. Reasenberg (Massachusetts Institute of Technology),
and G. L. Slater (Massachusetts Institute of Technology)

Science, Vol. 175, No. 4019, pp. 317–320,
January 21, 1972

For abstract, see Lorell, J.

CLAUSS, R. C.

C11 DSN Progress Report for March–April 1972: Low Noise Receivers: Microwave Maser Development

R. C. Clauss and R. B. Quinn

Technical Report 32-1526, Vol. IX, pp. 128–136,
June 15, 1972

Microwave maser amplifiers have been used by JPL in the DSN for 12 yr. Pump-frequency requirements have been met mainly with reflex klystron oscillators. Other microwave-power sources have been tested for use as maser pump sources. Successful performance tests have been achieved with backward-wave oscillators, crystal-controlled oscillators using solid-state multipliers, impatt oscillators, and an impatt noise generator. Current maser pump source requirements have a frequency range of 12.5 to 45 GHz. Power required is approximately 150 mW. Cost, availability, reliability, frequency and power stability, tunability, and power-requirement considerations have resulted in the use of klystrons as pump sources for all maser amplifiers now operating in the DSN.

COFFIN, R. C.

C12 DSN Progress Report for March–April 1972: Firmware Control of Block IV Ranging Demodulator Assembly

R. C. Coffin

Technical Report 32-1526, Vol. IX, pp. 188–195,
June 15, 1972

The Mark III Data System Development Plan is encouraging engineers designing equipment for use in the DSN to utilize computer control and monitoring. It is becoming apparent that the difficulty of development and the cost of software are prohibitive. A concept called firmware is proposed. Firmware is a design concept which directs the engineer to employ special-purpose digital and/or analog circuitry whenever possible to reduce software or interface requirements. The ranging demodulator assembly (RDA) is being developed under the firmware concept. By employing firmware, the RDA interface and software requirements have been kept to a minimum. The phase calibration of the RDA is achieved with a single switch or one-line command from the computer. Monitoring is handled by the firmware, which supplies one line to the computer indicating the operability of the RDA.

CONRATH, B. J.

C13 Infrared Spectroscopy Experiment on the Mariner 9 Mission: Preliminary Results

R. A. Hanel (Goddard Space Flight Center),
B. J. Conrath (Goddard Space Flight Center),
W. A. Hovis (Goddard Space Flight Center),
V. G. Kunde (Goddard Space Flight Center),
P. D. Lowman (Goddard Space Flight Center),
J. C. Pearl (Goddard Space Flight Center),
C. Prabhakara (Goddard Space Flight Center),
B. Schlachman (Goddard Space Flight Center), and
G. V. Levin (Biospherics Incorporated)

Science, Vol. 175, No. 4019, pp. 305–308,
January 21, 1972

For abstract, see Hanel, R. A.

CONROW, H. P.

C14 Surface Distribution of Microorganisms in Antarctic Dry-Valley Soils: A Martian Analog

R. E. Cameron, H. P. Conrow, D. R. Gensel, G. H. Lacy, and F. A. Morelli

Antarctic J. U.S., Vol. VI, No. 5, pp. 211–213, September–October 1971

For abstract, see Cameron, R. E.

CORK, M. J.

C15 Mariner 9 Propulsion Subsystem Performance During Interplanetary Cruise and Mars Orbit Insertion

M. J. Cork, R. L. French, C. J. Leising, and D. D. Schmit

JPL Quarterly Technical Review, Vol. 2, No. 1, pp. 113–122, April 1972

On November 14, 1971, the Mariner 9 1334-N (300-lbf) thrust rocket engine was fired for just over 15 min to place a man-made satellite into orbit about another planet for the first time. Propulsion subsystem data gathered during the 5-mo interplanetary cruise and the orbit insertion are of significance to future missions of this type. Specific results related to performance predictability; zero-g heat transfer; and nitrogen permeation, diffusion, and solubility values are presented.

COSTOGUE, E. N.

C16 Integration of a Breadboard Power Conditioner With a 20-cm Ion Thruster

T. D. Masek, T. W. Macie, E. N. Costogue, W. J. Muldoon (Hughes Aircraft Company), D. R. Garth (Hughes Aircraft Company), and G. C. Benson (Hughes Aircraft Company)

J. Spacecraft Rockets, Vol. 9, No. 2, pp. 71–78, February 1972

For abstract, see Masek, T. D.

CRAWFORD, W. E.

C17 Digital Canopus Tracker Digital Electronics

W. E. Crawford

Technical Report 32-1559, July 1, 1972

Circuitry has been developed for digital control of the Canopus tracker. A feasibility and demonstration breadboard has been constructed using microelectronic integrated circuits. The breadboard contains the digital circuits necessary for closed-loop electro-optical control of the tracker. Also included in the breadboard is the digital logic necessary for star acquisition, particle rejection, programmable gate selection, cone angle selection, and routing of the digital roll error signal.

CUDDIHY, E. F.

C18 Lifetime Estimates for Sterilizable Silver–Zinc Battery Separators

E. F. Cuddihy, D. E. Walmsley, and J. Moacanin

JPL Quarterly Technical Review, Vol. 2, No. 1, pp. 72–81, April 1972

The lifetime of the current separator membrane in the electrolyte environment of JPL silver–zinc batteries has been estimated at 3 to 5 yr. The separator membranes are crosslinked polyethylene film containing grafted poly(potassium acrylate) (PKA), the latter being the hydrophilic agent which promotes electrolyte ion transport. The lifetime was estimated by monitoring the rate of loss of PKA from the separators, caused by chemical attack of the electrolyte, and relating this loss rate to a known relationship between battery performance and PKA concentration in the separators.

C19 Analysis of the Failure of a Polyester Peripheral Drive Belt on the Mariner Mars 1971 Flight Tape Recorder

E. F. Cuddihy

JPL Quarterly Technical Review, Vol. 2, No. 1, pp. 82–99, April 1972

A polyester peripheral drive belt on the Mariner Mars 1971 flight tape recorder failed when a thin longitudinal strip separated off along one edge. Analysis showed that the most probable cause of failure occurred from flexural fatigue initiating in mechanically weak locations introduced into the belt during fabrication. Also, methyl ethyl ketone (MEK), which is employed as a cleaning solvent during fabrication, was found to cause permanent degradation of engineering properties of polyester and could have contributed to the reduction of the fatigue resistance. This article reviews fatigue properties of the polyester drive belt for the specific operating condition, as well as the sensitivity of polyester to

cleaning solvents and the origin of the mechanically weak locations introduced during fabrication.

C20 Fatigue of Teflon Bladder Materials

E. F. Cuddihy

J. Appl. Polym. Sci., Vol. 15, No. 12, pp. 3101–3108, December 1971

The fatigue properties of Teflon laminates employed in the fabrication of liquid propellant expulsion bladders were studied by cyclically stretching specimens to constant load in order to achieve a correlation of cycles to failure versus the maximum stress amplitude. This approach provides a useful technique for evaluating the resistance of bladder materials to fatigue failure which could be caused by vibration-induced cyclic loadings during ground testing and launch. Further, the data provides for a direct comparison of the relative fatigue properties of Teflon laminates and, in particular for those which were studied, the relative fatigue properties correlated with their ultimate breaking stresses. This observation, which suggests a simple and rapid method for evaluating relative fatigue behavior of candidate Teflon laminates, is discussed along with the effect of delamination on the fatigue properties observed for one laminate.

CURKENDALL, D. W.

C21 DSN Progress Report for January–February 1972: On Modeling Continuous Accelerations as Piecewise Constant Functions

R. K. Russell and D. W. Curkendall

Technical Report 32-1526, Vol. VIII, pp. 45–52, April 15, 1972

For abstract, see Russell, R. K.

CURTRIGHT, J.

C22 DSN Progress Report for January–February 1972: DSN Frequency and Time Scale Change From UTC to IAT or New UTC

J. Curtright

Technical Report 32-1526, Vol. VIII, pp. 127–130, April 15, 1972

By international agreement, the Universal Time, Coordinated (UTC) time scale was changed to parallel that of the atomic (A.1)

scale. The new time scale is called New UTC 1972 or International Atomic Time (IAT). This change in time scale made it necessary to change the frequency and time standards at all Deep Space Instrumentation Facility stations. The existing offset of UTC from A.1 time was removed from the oscillators, and all clocks were retarded approximately 107,600 μsec. This article covers the background material leading to the change, problems dealt with during the planning for it, and the procedures used to implement the change.

DECKER, D. K.

D01 Methods for Utilizing Maximum Power From a Solar Array

D. K. Decker

JPL Quarterly Technical Review, Vol. 2, No. 1, pp. 37–48, April 1972

Ion thrusters are being considered for outer-planet spacecraft propulsion. In a typical mission, the spacecraft primary energy source may be required to deliver as high as 16 kW of power to the thruster system. This power level is quite high compared to system power levels developed in the past. It is therefore very important to utilize the maximum available power from the energy source at all times.

A preliminary study of maximum power utilization methods was performed for an outer-planet spacecraft using an ion thruster propulsion system and a solar array as the primary energy source. The problems which arise from operating the array at or near the maximum power point of its current–voltage characteristic are discussed. Two closed-loop system configurations which use extremum regulators to track the array maximum power point are presented. Also, three open-loop systems are presented that either: (1) measure the maximum power of each array section and compute the total array power, (2) utilize a reference array to predict the characteristics of the solar array, or (3) utilize impedance measurements to predict the maximum power utilization. The advantages and disadvantages of each system are discussed, and recommendations for further development are made.

DIAZ, A. F.

D02 Carbon-to-Metal Chlorine Exchange: IV. Mercuric Salt Promoted Acetolysis of exo-Norbornyl Chloride

J. P. Hardy, A. F. Diaz, and S. Winstein

J. Am. Chem. Soc., Vol. 94, No. 7, pp. 2363–2370, April 5, 1972

For abstract, see Hardy, J. P.

DORMAN, J.

D03 DSN Progress Report for March–April 1972: Overseas 64-m-Diameter Antenna Power Configuration

J. Dorman

Technical Report 32-1526, Vol. IX, pp. 218–226, June 15, 1972

The construction of the two new 64-m-diameter antennas at Deep Space Stations 63 (Madrid) and 43 (Tidbinbilla) required additional power generating equipment at these sites. As the new sites were in close proximity to the existing Deep Space Stations 61 (Madrid) and 42 (Tidbinbilla), the new equipment was designed to integrate with the existing power generating and distribution systems. This integration will enable the new and existing generators to be combined into a single generating system and provide total site power for both 64-m and 26-m antenna station requirements. Studies are being made to determine the economic and technical advantages of using commercial power. If proved favorable, the equipment presently being installed is designed to provide parallel operation of the generating system with commercially produced power.

The new equipment is equipped with automatic generator starting and stopping features and power demand sensing monitors. The monitors automatically start, synchronize, and connect, generators to share load demand equally between running generators as power demand increases. Conversely, if the demand decreases, unnecessary generators are removed from the generating system. This article describes the techniques developed and incorporated into the design of the new generation and distribution equipment and the proposed future development of the power generating systems.

DOWNS, G. S.

D04 Second Decrease in the Period of the Vela Pulsar

P. E. Reichley and G. S. Downs

Nature Phys. Sci., Vol. 234, No. 46, p. 48, November 15, 1971

For abstract, see Reichley, P. E.

EISENBERGER, I.

E01 DSN Progress Report for March–April 1972: An Inventory Policy for the Deep Space Network

I. Eisenberger, F. R. Maiocco, and G. Lorden (California Institute of Technology)

Technical Report 32-1526, Vol. IX, pp. 84–87, June 15, 1972

This article describes a proposed inventory and procurement policy for optimal procedures in ordering and allocating for the DSN network supply depot (NSD). The policy defined differs from conventional inventory stockage and resupply systems in that it takes into consideration the inventory status not only of NSD but also of each of the complex supply facilities.

FANALE, F. P.

F01 Origin of Planetary Primordial Rare Gas: The Possible Role of Adsorption

F. P. Fanale and W. A. Cannon

Geochim. Cosmochim. Acta, Vol. 36, No. 3, pp. 319–328, March 1972

The degree of physical adsorption of Ne, Ar, Kr, and Xe on pulverized samples of the Allende meteorite at 113°K has been measured. The observed pattern of equilibrium enrichment of heavy rare gases over light on the pulverized meteorite surfaces relative to the gas phase is similar to the enrichment pattern (Xe > Kr > Ar ⋙ Ne, He) exhibited by "planetary primordial" rare gas when compared with the composition of solar rare gas. Results indicate that at 113°K a total nebular pressure of from 10^{-2} to 10^{-3} atm would be required to explain the Ar, Kr, and Xe abundances in carbonaceous chondrites with an adsorption mechanism. This pressure estimate is compatible with the range of possible nebular pressures (10^{-2} to 10^{-6} atm), suggested by astrophysical arguments. However, the subsequent mechanism by which initially adsorbed gas might have been transferred into the interiors of grains cannot be identified at present. The hypothesis that the presence of "planetary primordial" Ar, Kr, and Xe in carbonaceous chondrites is due to their adsorption from the gaseous portion of the preplanetary cloud is offered as an alternative to the hypothesis that these gases were incorporated as the result of attainment of solubility equilibrium between dust and gas.

FARMER, C. B.

F02 The Detection and Mapping of Water Vapor in the Martian Atmosphere

C. B. Farmer and D. D. LaPorte

Icarus, Vol. 16, No. 1, pp. 34–46, February 1972

The objectives of the water vapor investigations, to be carried out during the Viking missions, are described in the light of our current knowledge of Martian atmospheric conditions and the diurnal and seasonal variations of the water abundance. A discussion is given of the relative merits of the different experimental approaches which can be adopted for this purpose, followed by a summary of the detection limits achievable in the available spectral regions.

These considerations led to the choice of a spectrometer operating in the 7300-cm^{-1} (1.4-μ) region, with a spectral resolution of approximately 1 cm^{-1} and a surface spatial resolution at periapsis of 3 × 24 km. The design of the spectrometer and the results of laboratory simulation tests which have been carried out to verify the expected instrumental performance are described.

F03 Jupiter: Observation of Deuterated Methane in the Atmosphere

R. Beer, C. B. Farmer, R. H. Norton,
J. V. Martonchik (University of Texas), and
T. G. Barnes (University of Texas)

Science, Vol. 172, No. 4028, pp. 1360–1361,
March 24, 1972

For abstract, see Beer, R.

FERRERA, J. D.

F04 A Mechanism for Three-Axis Control of an Ion Thruster Array

G. S. Perkins, K. G. Johnson, J. D. Ferrera, and
T. D. Masek

J. Spacecraft Rockets, Vol. 9, No. 3, pp. 218–220,
March 1972

For abstract, see Perkins, G. S.

FITZGERALD, D. J.

F05 Ion Thruster Performance Calibration

E. V. Pawlik, R. Goldstein, D. J. Fitzgerald, and R. W. Adams

Preprint 72-475, AIAA Ninth Electric Propulsion Conference, Bethesda, Maryland, April 17–19, 1972

For abstract, see Pawlik, E. V.

FJELDBO, G.

F06 Mariner 9 S-Band Martian Occultation Experiment: Initial Results on the Atmosphere and Topography of Mars

A. J. Kliore, D. L. Cain, G. Fjeldbo, B. L. Seidel, and S. I. Rasool (National Aeronautics and Space Administration)

Science, Vol. 175, No. 4019, pp. 313–317, January 21, 1972

For abstract, see Kliore, A. J.

FORNEY, P. B.

F07 Mariner Mars 1969 Infrared Spectrometer

K. C. Herr (University of California, Berkeley), P. B. Forney (University of California, Berkeley), and G. C. Pimentel (University of California, Berkeley)

Appl. Opt., Vol. 11, No. 3, pp. 493–501, March 1972

For abstract, see Herr, K. C.

FRENCH, R. L.

F08 Mariner 9 Propulsion Subsystem Performance During Interplanetary Cruise and Mars Orbit Insertion

M. J. Cork, R. L. French, C. J. Leising, and D. D. Schmit

JPL Quarterly Technical Review, Vol. 2, No. 1, pp. 113–122, April 1972

For abstract, see Cork, M. J.

FYMAT, A. L.

F09 Polarization Effects in Fourier Spectroscopy: I. Coherency Matrix Representation

A. L. Fymat

Appl. Opt., Vol. 11, No. 1, pp. 160–173, January 1972

A general analytical method using the formalisms of polarization coherency and Jones's matrices is provided for the evaluation of all polarization effects in fourier spectroscopy. The method applies to any incident state of arbitrary (complete, random, or partial) polarization. Inversely, it may also be used for determining the intensity and state of polarization of the source of light. TE- and TM-mode reflectivity and transmissivity for beam splitters and the dependence of these quantities on the incident polarization are obtained. It is demonstrated that three different efficiencies for these optical components must be introduced. Interferometer efficiency expressions for the source beam and the detector beam are also derived and shown to be essentially different from the previous efficiencies. Polarization effects of beam splitters, reflectors, and their composite combinations (interferometers) are investigated in detail. General conditions for complete or restricted polarization compensation are derived. Theoretical signal-to-noise ratio expressions for both the source beam and the detector beam are also obtained; these formulas specifically account for the incident state of polarization, the polarization effects of the interferometer, and make use of the exact expressions for the appropriate interferometer efficiency. In an appendix, a brief comparison is made between some usual representations of the state of wave polarization.

GARRISON, G. W.

G01 Telecommunications System Design for the Mariner Mars 1971 Spacecraft

F. J. Taylor and G. W. Garrison

Technical Memorandum 33-535, May 1, 1972

For abstract, see Taylor, F. J.

GARTH, D. R.

G02 Integration of a Breadboard Power Conditioner With a 20-cm Ion Thruster

T. D. Masek, T. W. Macie, E. N. Costogue,
W. J. Muldoon (Hughes Aircraft Company),

D. R. Garth (Hughes Aircraft Company), and
G. C. Benson (Hughes Aircraft Company)

J. Spacecraft Rockets, Vol. 9, No. 2, pp. 71–78, February 1972

For abstract, see Masek, T. D.

GELLER, M.

G03 The James Wavefunction for the Ground State of H_2^+

M. Geller and O. Ludwig (Villanova University)

Chem. Phys. Lett., Vol. 12, No. 2, p. 403, December 15, 1971

A recent article in *Chem. Phys. Lett.* by Jackson, McEachran, and Cohen on the James wavefunction for the ground state of H_2^+ duplicates and thereby confirms previous calculations by the present authors (published in *J. Chem. Phys.*, 1962).

GENSEL, D. R.

G04 Surface Distribution of Microorganisms in Antarctic Dry-Valley Soils: A Martian Analog

R. E. Cameron, H. P. Conrow, D. R. Gensel,
G. H. Lacy, and F. A. Morelli

Antarctic J. U.S., Vol. VI, No. 5, pp. 211–213, September–October 1971

For abstract, see Cameron, R. E.

GODFREY, J. F.

G05 The Effect of Temperature on the Survival of Microorganisms in a Deep Space Vacuum

C. A. Hagen, J. F. Godfrey, and R. H. Green

Space Life Sci., Vol. 3, No. 2, pp. 108–117, December 1971

For abstract, see Hagen, C. A.

GOLDSTEIN, R.

G06 Ion Thruster Performance Calibration

E. V. Pawlik, R. Goldstein, D. J. Fitzgerald, and
R. W. Adams

Preprint 72-475, AIAA Ninth Electric Propulsion Conference, Bethesda, Maryland, April 17–19, 1972

For abstract, see Pawlik, E. V.

GOLDSTEIN, R. M.

G07 Radar Observations of Mercury

R. M. Goldstein

Astron. J., Vol. 76, No. 10, pp. 1152–1154, December 1971

Radar scattering properties of the planet Mercury at 12.5-cm wavelength are presented. Data from two inferior conjunctions show that backscattering anomalies can be attributed to specific regions on the planetary surface. The rotation period of Mercury is measured to better than 0.4%.

GOODWIN, P. S.

G08 DSN Progress Report for January–February 1972: Helios Mission Support

P. S. Goodwin

Technical Report 32-1526, Vol. VIII, pp. 16–19, April 15, 1972

Project Helios is a cooperative U.S./West German space effort. Two unmanned solar-orbiting spacecraft are planned for launching: the first in mid-1974, and the second in late 1975. These spacecraft will follow a trajectory that brings them closer to the Sun (under 0.3 AU) than any known spacecraft to date. Using specially designed instruments, the Helios spacecraft will enter unexplored regions near the Sun in an attempt to expand mankind's knowledge of how the Sun influences life on Earth.

In addition to the scientific goals, Project Helios presents many challenging technological problems—none the least of which is to design a spacecraft which will endure 16 times the amount of heat from the Sun (at 0.25 AU) than is normally received on Earth. In addition, the spacecraft will reach its closest approach to the Sun (perihelion) only 90 days after launch. These and other facets of this unique mission were described in Volumes II through VI of this series. Volume VII treated the JPL/Tracking and Data System activities during the Sixth Helios Joint Working Group Meeting held at Oberpfaffenhofen, West Germany, October 20 to 27, 1971. This article covers the DSN Helios activities since that date.

G09 **DSN Progress Report for March–April 1972: Helios Mission Support**

P. S. Goodwin

Technical Report 32-1526, Vol. IX, pp. 33–34, June 15, 1972

Project Helios is a joint space endeavor between the United States and West Germany, the objective of which is to place two unmanned spacecraft into heliocentric orbits whose perihelion will be closer to the Sun than any previously or presently planned free-world deep space undertaking. The West German government is designing and fabricating the spacecraft and will conduct mission operations. NASA will provide the launch vehicle, the launch facilities, and the major portion of the tracking. The launch of the first spacecraft is planned for mid-1974 and the second in late-1975. This article deals with the DSN support to Project Helios during March and April 1972.

GOSLINE, R. M.

G10 **DSN Progress Report for January–February 1972: Antenna Drive System Performance Evaluation Using PN Codes**

R. M. Gosline, E. B. Jackson, and J. D. Campbell

Technical Report 32-1526, Vol. VIII, pp. 74–79, April 15, 1972

A maintenance tool for quick and easy evaluation of the performance of an antenna drive system is described and preliminary results are given. The technique uses a pseudo-noise (PN) code as a system input signal and correlates the system output with all possible states of the input pseudo-noise code. The resulting correlation function has the same shape as the system response to an impulse input and can be considered in the same way. A program description, block diagrams, and some system response curves are given.

GOTTLIEB, P.

G11 **Lunar Gravity via Apollo 14 Doppler Radio Tracking**

W. L. Sjogren, P. Gottlieb, P. M. Muller, and W. Wollenhaupt (Manned Spacecraft Center)

Science, Vol. 175, No. 4018, pp. 165-168, January 14, 1972

For abstract, see Sjogren, W. L.

GREEN, R. H.

G12 The Effect of Temperature on the Survival of Microorganisms in a Deep Space Vacuum

C. A. Hagen, J. F. Godfrey, and R. H. Green

Space Life Sci., Vol. 3, No. 2, pp. 108–117, December 1971

For abstract, see Hagen, C. A.

HAGEN, C. A.

H01 The Effect of Temperature on the Survival of Microorganisms in a Deep Space Vacuum

C. A. Hagen, J. F. Godfrey, and R. H. Green

Space Life Sci., Vol. 3, No. 2, pp. 108–117, December 1971

A Space Molecular Sink Research Facility (Molsink) was used to evaluate the ability of microorganisms to survive the vacuum of outer space. This facility could be programmed to simulate flight spacecraft vacuum environments at pressures in the 10^{-10}-torr range and thermal gradients (30 to 60°C) closely associated to surface temperatures of inflight spacecraft.

Initial populations of *Staphylococcus epidermidis* and a *Micrococcus* sp. were reduced approximately 1 log while exposed to -105 and 34°C, and approximately 2 logs while exposed to 59°C for 14 days in the vacuum environment. Spores of *Bacillus subtilis* var. *niger* were less affected by the environment. Initial spore populations were reduced 0.2, 0.3, and 0.8 log during the 14-day vacuum exposure at -124, 34, and 59°C, respectively.

HAINES, E. L.

H02 Precise Coordinate Control in Fission Track Uranium Mapping

E. L. Haines

Nucl. Instr. Methods, Vol. 98, No. 1, pp. 183–184, January 1, 1972

An important problem in fission track uranium mapping is coordinate control; it is hard to relate locations of track concentrations on the detector to the locations of the uranium-rich minerals on the polished section. This article presents a method for precisely locating mineral grains related to uranium concentrations revealed by the track detector. The method uses a congruent transformation of the coordinate system of the detector to the coordinate system of the polished rock section.

HANEL, R. A.

H03 Infrared Spectroscopy Experiment on the Mariner 9 Mission: Preliminary Results

R. A. Hanel (Goddard Space Flight Center),
B. J. Conrath (Goddard Space Flight Center),
W. A. Hovis (Goddard Space Flight Center),
V. G. Kunde (Goddard Space Flight Center),
P. D. Lowman (Goddard Space Flight Center),
J. C. Pearl (Goddard Space Flight Center),
C. Prabhakara (Goddard Space Flight Center),
B. Schlachman (Goddard Space Flight Center), and
G. V. Levin (Biospherics Incorporated)

Science, Vol. 175, No. 4019, pp. 305–308,
January 21, 1972

The Mariner 9 infrared spectroscopy experiment has provided good-quality spectra of many areas of Mars, predominantly in the southern hemisphere. Large portions of the thermal emission spectra are significantly affected by dust with a silicon oxide content approximately corresponding to that of an intermediate igneous rock, thus implying that Mars has undergone substantial geochemical differentiation. Derived temperature profiles indicate a warm daytime upper atmosphere with a strong warming over the south polar cap. Atmospheric water vapor is clearly observed over the south polar area and less strongly over other regions.

HARDY, J. P.

H04 Carbon-to-Metal Chlorine Exchange: IV. Mercuric Salt Promoted Acetolysis of exo-Norbornyl Chloride

J. P. Hardy, A. F. Diaz, and S. Winstein

J. Am. Chem. Soc., Vol. 94, No. 7, pp. 2363–2370,
April 5, 1972

Mercuric salts enhance the rate of acetolysis of *exo*-norbornyl chloride, I-Cl. Rate constants have been measured for solvolysis, k_t, exchange of radiolabeled chlorine between mercuric chloride and I-Cl, k_e, and loss of optical activity, k_α. Relative solvolytic rate constants for mercuric acetate, chloromercuric acetate, and mercuric chloride-promoted reactions at 75°C are 1820, 89, and 1, respectively. Since the rate enhancements are much greater than expected for normal salt effects, the mercuric salts must be intimately involved in the ionization process. For the mercuric chloride-promoted reaction,

$$\frac{k_\alpha}{k_t} = 9.6$$

indicating that some 90% of the ion pairs return to covalent I-Cl in the poorly dissociating acetic acid solvent. The ratio

$$\frac{k_{rac}}{k_e} = \frac{k_\alpha - k_t}{k_e} = 2.0$$

for mercuric chloride can be interpreted in terms of one or more ion-pair intermediates $I^+HgCl_3^-$ of differing structure. In a manner similar to $HgCl_2$, $Hg(OAc)_2$ facilitates C—Cl bond heterolysis, and carries the solvent anion, OAc^-, into intimate contact with the incipient carbonium ion, which makes the chloromercuric diacetate anion a unique "leaving group."

HARSTAD, K. G.

H05 One Dimensional Line Radiative Transfer

K. G. Harstad

Technical Memorandum 33-538, April 1, 1972

Integrations over solid angle and frequency are performed in the expressions for the radiant heat flux and local energy loss of a line in a region of strong variation of the source function in one direction. Approximations are given for the coefficients and kernels in the resulting forms, which involve integrals over the physical coordinate.

HATZENBELER, H.

H06 Infrared Radiometry Experiment on Mariner 9

S. C. Chase, Jr. (Santa Barbara Research Center),
H. Hatzenbeler (Santa Barbara Research Center),
H. Kieffer (University of California, Los Angeles), E. Miner,
G. Münch (California Institute of Technology), and
G. Neugebauer (California Institute of Technology)

Science, Vol. 175, No. 4019, pp. 308–309,
January 21, 1972

For abstract, see Chase, S. C., Jr.

HERR, K. C.

H07 Mariner Mars 1969 Infrared Spectrometer

K. C. Herr (University of California, Berkeley),
P. B. Forney (University of California, Berkeley), and
G. C. Pimentel (University of California, Berkeley)

Appl. Opt., Vol. 11, No. 3, pp. 493–501, March 1972

The infrared spectrometer that recorded spectra of the atmosphere and surface of Mars during the Mariner 6 and 7 flyby missions is described. The instrument continuously scanned the 1.9- to 14.4-μ spectral region at 10 s per scan. Approximately 1% spectral resolution was furnished by two rotating, circular, variable interference filters. The spectral region 1.9–6.0 μ was recorded with a PbSe detector cooled to 175 K by radiation to deep space. The spectral region 3.9–14.4 μ was modulated by a cold (175-K)tuning fork chopper and recorded with a mercury-doped germanium detector cooled to 22 K by a Joule–Thomson two-stage (N_2 and H_2) cryostat. The total weight of the instrument was 17.4 kg (monochromator plus electronics, 11.5 kg; gas delivery system, 5.9 kg), and it consumed 11 W of power.

HERRIN, P. D.

H08 DSN Progress Report for March–April 1972: The Development of a Dual-In-Line Package Microcircuit Card and Card Cage Assembly

P. D. Herrin

Technical Report 32-1526, Vol. IX, pp. 103–114,
June 15, 1972

An improved dual-in-line package microcircuit card and card-cage assembly have been developed. The external dimensions and the basic configuration of a previously-developed card have been essentially maintained. However, the number of microcircuit socket locations has been increased from 106 to 126 by compressing dimensions, and the number of interface plug connections has been raised from 82 to 240 by using a new high-density connector. Also, the physical size of the filtering capacitors has been reduced by selecting a miniaturized version. All wire-wrap terminals have been placed on 2.5-mm (0.100-in.) centers, with the exception of the capacitor terminals, to allow the card to be wired on an automated wire-wrap machine for potential savings of time, effort, and cost.

HIPSHER, H.

H09 Mariner 9 Science Experiments: Preliminary Results

R. H. Steinbacher, A. J. Kliore, J. Lorell, H. Hipsher (National Aeronautics and Space Administration), C. A. Barth (University of Colorado), H. Masursky (U.S. Geological Survey), G. Münch (California Institute of Technology), J. C. Pearl (Goddard Space Flight Center), and B. A. Smith (New Mexico State University)

Science, Vol. 175, No. 4019, pp. 293–294, January 21, 1972

For abstract, see Steinbacher, R. H.

HOBBY, G. L.

H10 The Carbon-Assimilation Experiment: The Viking Mars Lander

N. H. Horowitz, J. S. Hubbard, and G. L. Hobby

Icarus, Vol. 16, No. 1, pp. 147–152, February 1972

For abstract, see Horowitz, N. H.

HOFFMAN, J. K.

H11 Studies on the Frictional Behavior of Magnetic Recording Tapes

S. H. Kalfayan, R. H. Silver, and J. K. Hoffman

JPL Quarterly Technical Review, Vol. 2, No. 1, pp. 100–106, April 1972

For abstract, see Kalfayan, S. H.

HOGGAN, H. R.

H12 DSN Progress Report for March–April 1972: Prototype S- and X-Band Feed System Hardware

M. S. Katow and H. R. Hoggan

Technical Report 32-1526, Vol. IX, pp. 185–187, June 15, 1972

For abstract, see Katow, M. S.

HOLMES, J. K.

H13 Performance of a First-Order Transition Sampling Digital Phase-Locked Loop Using Random-Walk Models

J. K. Holmes

IEEE Trans. Commun., Vol. COM-20, No. 2, pp. 119–131, April 1972

A new mechanization of a first-order all digital phase-locked loop is discussed and analyzed. The purpose of the loop is to provide continuous tracking of the incoming waveform corrupted by the presence of white gaussian noise. Based on a random-walk model, solutions are obtained for the steady-state timing-error variance and mean time to slip a cycle. As a result of the mean first-time-to-slip analysis, a difference equation and its solution are obtained that generalize a previously derived equation. Using a procedure that appears new, an upper bound on the timing-error bias due to a doppler shift of the synchronized waveform is also derived. An example, for which the results presented here are applicable, is considered in some detail.

HOLTZE, R. F.

H14 Properties of Conductive Thick-Film Inks

R. F. Holtze

Technical Memorandum 33-532, April 15, 1972

Ten different conductive inks used in the fabrication of thick-film circuits were evaluated for their physical and handling properties. Viscosity, solid contents, and spectrographic characteristics of the unfired inks were determined. Inks were screened on ceramic substrates and fired for varying times at specified temperatures. Selected substrates were given additional firings to simulate the heat exposure that would be received if thick-film resistors were added to the substrate.

Data are presented covering: (1) printing characteristics, (2) solderability using Sn-63 and a 4% silver solder, (3) leach resistance, (4) solder adhesion, and (5) wire bonding properties. The results obtained using different firing schedules are compared, and the general results obtained for each ink are given. The changes in firing time or the application of a simulated-resistor firing had little effect on the properties of most inks.

HOPPER, D. J.

H15 A Closely Regulated TWT Converter

D. J. Hopper and R. W. Andryczyk (General Electric Company)

IEEE Trans. Aerosp. Electron. Sys., Vol. AES-7, No. 6, pp. 1147–1150 November 1971

The design concept for the traveling wave tube amplifier converter for possible use in the Thermoelectric Outer-Planet Spacecraft (TOPS) is presented. An unusual combination of semiconductors and magnetics was utilized to achieve very stable voltage regulation on a number of separate outputs to satisfy the requirements of a high-power traveling wave tube (TWT), and at the same time operate at an efficiency of better than 90% from a 30-V source. The circuitry consists of an output filter, an auxiliary Jensen oscillator driving a high-reactance transformer to provide current limiting to the heater, a variable time delay, a main Jensen oscillator driving the power transformer with a maximum step-up ratio of 120 to 1, and series transistorized post regulators to provide precise voltage adjustment and low output impedance.

This paper discusses the design of the high-reactance transformer and the high step-up ratio transformer, as well as the high-voltage series regulators that are limited in range and operate at the top of the unregulated output voltage. Test data is presented, and details of current transients caused by charging the filter circuits, input current ripple, and output voltage ripples are considered. The circuit provides better than 0.5% regulation against load change, input voltage change, and over-operating temperature range of from −20 to 80°C, with output ripple voltage of less than 2 V peak-to-peak on top of the 3600-Vdc output. The measured efficiency was typically 87%, and recommendations are included to improve this to in excess of 90%.

HORD, C. W.

H16 Mariner 9 Ultraviolet Spectrometer Experiment: Initial Results

C. A. Barth (University of Colorado), C. W. Hord (University of Colorado), A. I. Stewart (University of Colorado), and A. L. Lane

Science, Vol. 175, No. 4019, pp. 309–312, January 21, 1972

For abstract, see Barth, C. A.

HOROWITZ, N. H.

H17 The Carbon-Assimilation Experiment: The Viking Mars Lander

N. H. Horowitz, J. S. Hubbard, and G. L. Hobby

Icarus, Vol. 16, No. 1, pp. 147–152, February 1972

The carbon-assimilation experiment detects life in soils by measuring the incorporation of carbon from ^{14}CO and $^{14}CO_2$ into organic matter. It is based on the premise that Martian life, if it exists, is carbonaceous and exchanges carbon with the atmosphere, as do all terrestrial organisms. It is especially sensitive for photosynthesizing cells, but it detects heterotrophs also. The experiment has the particular advantage that it can be carried out under essentially Martian conditions of temperature, pressure, atmospheric composition, and water abundance.

HORSEWOOD, J. L.

H18 Basic Parameters for Low Thrust Mission and System Analysis

T. A. Barber, J. L. Horsewood (Analytical Mechanics Associates, Inc.), and H. Meissinger (TRW Systems, Inc.)

Preprint 72-426, AIAA Ninth Electric Propulsion Conference, Bethesda, Maryland, April 17–19, 1972

For abstract, see Barber, T. A.

HOVIS, W. A.

H19 Infrared Spectroscopy Experiment on the Mariner 9 Mission: Preliminary Results

R. A. Hanel (Goddard Space Flight Center),
B. J. Conrath (Goddard Space Flight Center),
W. A. Hovis (Goddard Space Flight Center),
V. G. Kunde (Goddard Space Flight Center),
P. D. Lowman (Goddard Space Flight Center),
J. C. Pearl (Goddard Space Flight Center),
C. Prabhakara (Goddard Space Flight Center),
B. Schlachman (Goddard Space Flight Center), and
G. V. Levin (Biospherics Incorporated)

Science, Vol. 175, No. 4019, pp. 305–308, January 21, 1972

For abstract, see Hanel, R. A.

HUBBARD, J. S.

H20 The Carbon-Assimilation Experiment: The Viking Mars Lander

N. H. Horowitz, J. S. Hubbard, and G. L. Hobby

Icarus, Vol. 16, No. 1, pp. 147–152, February 1972

For abstract, see Horowitz, N. H.

HUNT, G. E.

H21 Formation of Spectral Lines in Planetary Atmospheres: I. Theory for Cloudy Atmospheres; Application to Venus

G. E. Hunt

J. Quant. Spectrosc. Radiat. Transfer, Vol. 12, No. 3, pp. 387–404, March 1972

The theory of the formation of spectral lines in a cloudy planetary atmosphere is studied in detail. It is shown that models based upon homogeneous, isotropically scattering atmospheres cannot be used to reproduce observed spectroscopic features of phase effect and the shape of spectral lines for weak *and* strong bands. The theory must, therefore, be developed using an inhomogeneous (gravitational) model of a planetary atmosphere, accurately incorporating all the physical processes of radiative transfer.

Such a model of the lower Venus atmosphere, consistent with our present knowledge, is constructed. The results discussed in this article demonstrate the effects of the parameters that describe the atmospheric model on the spectroscopic features of spectral line profile and phase effect, at visible and near infrared wavelengths. This information enables us to develop a comprehensive theory of line formation in a Venus atmosphere.

H22 Formation of Spectral Lines in a Planetary Atmosphere: II. Spectroscopic Evidence for the Structure of the Visible Venus Clouds

G. E. Hunt

J. Quant. Spectrosc. Radiat. Transfer, Vol. 12, No. 3, pp. 405–419, March 1972

This article demonstrates that there is spectroscopic evidence for the structure of the visible Venus cloud layers. From physically realistic models of the lower Venus atmosphere, we have shown that only observations of the phase variations of the CO_2 bands in the Venus spectrum can provide the information for a unique identification of the structure of the cloud layers. It is proved that Venus cannot have a single dense cloud layer, but must have two

scattering layers; a thin aerosol layer is situated in the lower stratosphere, overlying a dense cloud deck.

The aerosol plays an important role in the scattering of radiation, so that its identification provides an explanation of the reflecting layer-scattering model controversy for the interpretation of spectra formed in a cloudy planetary atmosphere.

HUTCHISON, R. B.

H23 Astronomical Infrared Spectroscopy With a Connes-Type Interferometer: III. Alpha Orionis, 2600–3450 cm^{-1}

R. Beer, R. B. Hutchison, R. H. Norton, and D. L. Lambert (University of Texas)

Astrophys. J., Vol. 172, No. 1, Pt. 1, pp. 89–115, February 15, 1972

For abstract, see Beer, R.

JACKSON, E. B.

J01 DSN Progress Report for January–February 1972: DSN Research and Technology Support

E. B. Jackson

Technical Report 32-1526, Vol. VIII, pp. 68–73, April 15, 1972

Major activities in support of the DSN research and technology program performed at both the Venus Deep Space Station and the Microwave Test Facility during the last two months are presented. Progress and performance summaries are given in the following areas: pulsar reception, mu ranging from the Mars Deep Space Station, tricone assembly and testing, precision antenna gain measurements on the 26-m antenna weak-source observations of various radio sources, very long baseline interferometry in cooperation with National Radio Astronomy Observatory, dual carrier measurements, noise and intermodulation experiments, clock synchronization transmissions, and various maintenance activities.

J02 DSN Progress Report for January–February 1972: Antenna Drive System Performance Evaluation Using PN Codes

R. M. Gosline, E. B. Jackson, and J. D. Campbell

Technical Report 32-1526, Vol. VIII, pp. 74–79, April 15, 1972

For abstract, see Gosline, R. M.

J03 DSN Progress Report for March–April 1972: DSN Research and Technology Support

E. B. Jackson and R. B. Kolbly

Technical Report 32-1526, Vol. IX, pp. 147–151, June 15, 1972

The activities of the development support group, including the Microwave Test Facility, during the two-month period ending April 15, 1972, are summarized. Activities include operational clock synchronization, precision antenna-gain measurement, weak-source observation, pulsar observation, tricone-support-structure testing, and planetary-radar preparation and execution. Activities at the Microwave Test Facility include special klystron testing and tuning for the Manned Spaceflight Tracking and Data Network, special part fabrication for the tricone support structure, and design and fabrication of the flow panel and crowbar subassemblies for the clock-synchronization transmitting system. Significant maintenance items include replacement of the azimuth drive gear reducer on the 26-m-diameter antenna and modification of the power-distribution system associated with the 100-kW clock synchronization transmitter.

JAFFE, L. D.

J04 Cracking of Lunar Mare Soil

L. D. Jaffe

Nature, Vol. 234, No. 5329, pp. 402–403, December 17, 1971

Some of the early photographs of the disturbed lunar mare soil seemed to suggest that the soil layer consists of a thin, flat, rather rigid crust over a softer substrate. As described in this article, more recent photographs give evidence that the former impression of flatness and crusting is an illusion and that the lunar soil deforms and cracks in the same manner as homogeneous isotropic terrestrial soils of moderate bulk density, having a small amount of cohesion.

JAIVIN, G. I.

J05 Mariner Mars 1971 Scan Platform Pointing Calibration

G. D. Pace, G. I. Jaivin, and R. A. Virzi

JPL Quarterly Technical Review, Vol. 2, No. 1, pp. 49–57, April 1972

For abstract, see Pace, G. D.

JENSEN, W. M.

J06 Development of Boron Epoxy Rocket Motor Chambers

W. M. Jensen, A. C. Knoell, and C. Zweben (Materials Sciences Corporation)

Proceedings of the Twenty-Seventh Annual Technical Conference of the Reinforced Plastics/Composites Institute, Washington, D.C., February 8–11, 1972, sponsored by the Society of the Plastics Industry, Inc., Sect. 17-C, pp. 1–10

A 71-cm-diameter 74-cm-long boron/epoxy composite rocket motor chamber was designed based on the geometric configuration of the JPL Applications Technology Satellite titanium alloy apogee motor chamber. Because analyses showed large stress concentrations in the domes, the configuration was modified using the same basic constraints for openings and attachments. The rocket motor chamber was then fabricated by filament winding with boron/epoxy tape and hydrostatically tested to failure at 264 N/cm^2, 57.2 N/cm^2 above the design value. Two more rocket motor chambers were fabricated with the same basic constraints, but shortened to 57.6 cm for a smaller propellant load. The first of these short chambers failed in proof because of filament winding fabrication difficulties. The second chamber was successfully fabricated and passed the hydrostatic proof test.

JET PROPULSION LABORATORY

J07 Proceedings of the Jupiter Radiation Belt Workshop (Held at the Jet Propulsion Laboratory, Pasadena, California, July 13–15, 1971)

Jet Propulsion Laboratory

Technical Memorandum 33-543, July 1, 1972

Outer-planet mission studies emphasized the need to reduce the uncertainty in Jupiter trapped radiation belt models and the requirement to establish the best models from which spacecraft design requirements should be derived. The best models should be conservative enough that spacecraft designed to the models have an acceptable risk associated with the models, but not so overly

conservative that a large design penalty is required for a small reduction in risk.

Because of the highly specialized nature of this topic, questions could best be addressed by a group of specialists who actually were working in the fields involved. Consequently, the Jupiter Radiation Belt Workshop was sponsored by JPL to provide a forum to review the current state of Jupiter radiation belt knowledge and to recommend a best set of models for the determination of spacecraft design requirements. The 22 formal presentations of the workshop, the conclusions, and some post-workshop models of Jupiter radiation belts are presented in these proceedings, which were edited by A. J. Beck of JPL.

JOHNSON, K. G.

J08 A Mechanism for Three-Axis Control of an Ion Thruster Array

G. S. Perkins, K. G. Johnson, J. D. Ferrera, and T. D. Masek

J. Spacecraft Rockets, Vol. 9, No. 3, pp. 218–220, March 1972

For abstract, see Perkins, G. S.

JORDAN, J. F.

J09 Mariner 9 Celestial Mechanics Experiment: Gravity Field and Pole Direction of Mars

J. Lorell, G. H. Born, E. J. Christensen, J. F. Jordan, P. A. Laing, W. Martin, W. L. Sjogren, I. I. Shapiro (Massachusetts Institute of Technology), R. D. Reasenberg (Massachusetts Institute of Technology), and G. L. Slater (Massachusetts Institute of Technology)

Science, Vol. 175, No. 4019, pp. 317–320, January 21, 1972

For abstract, see Lorell, J.

JUSTISS, J.

J10 DSN Progress Report for January–February 1972: Manufacturing Engineering of Surface Panels for the 64-m Antennas

J. Justiss, W. Kissane, and M. S. Katow

Technical Report 32-1526, Vol. VIII, pp. 89–97, April 15, 1972

The procurement of two 26-m antennas for the overseas deep space stations was authorized with new vendors. These changes engendered new procedures to insure quality manufacturing of the surface panels for maximum RF performance. The new checking procedures are described including the mathematical formulations and functional aspects of the checking fixtures. A computer program was developed to solve for the parameters. Notes on the computing of arc lengths along the parabolic curve are included.

KALFAYAN, S. H.

K01 Studies on the Frictional Behavior of Magnetic Recording Tapes

S. H. Kalfayan, R. H. Silver, and J. K. Hoffman

JPL Quarterly Technical Review, Vol. 2, No. 1, pp. 100–106, April 1972

Magnetic tape recorders exhibit various failure modes. Those ascribable to friction between tape and magnetic head cause phenomena such as seizure (stick) and seizure and release (stick–slip). Methods have been developed at JPL for the measurement of frictional forces acting on the tape while in motion or at rest, as well as the extent of stick–slip. The effects of factors such as temperature, humidity, kind of gaseous atmosphere, and tape speed on the frictional interaction between various tapes and heads have been investigated. The results were instrumental in the selection of a tape for the Mariner Mars 1971 spacecraft. This article discusses recent studies on the stick–slip behavior of tapes, as well as the performance of a metallic tape compared to that of the usual plastic tapes.

KATOW, M. S.

K02 DSN Progress Report for January–February 1972: Manufacturing Engineering of Surface Panels for the 64-m Antennas

J. Justiss, W. Kissane, and M. S. Katow

Technical Report 32-1526, Vol. VIII, pp. 89–97, April 15, 1972

For abstract, see Justiss, J.

K03 **DSN Progress Report for March–April 1972: Prototype S- and X-Band Feed System Hardware**

M. S. Katow and H. R. Hoggan

Technical Report 32-1526, Vol. IX, pp. 185–187, June 15, 1972

The hardware for supporting the prototype S- and X-band feed system on the 64-m-diameter antenna is described. The S-band ellipsoid reflector is supported on flextures which provide for thermal expansion. The X-band-dichroic/S-band-flat reflector assembly consists of a welded assembly of aluminum plates with provisions for mounting the X-band transparent sheet.

KELLY, L. B.

K04 **Tracking and Data System Support for the Mariner Mars 1971 Mission: First Trajectory Correction Maneuver Through Orbit Insertion**

G. P. Textor, L. B. Kelly, and M. Kelly

Technical Memorandum 33-523, Vol. II, June 15, 1972

For abstract, see Textor, G. P.

KELLY, M.

K05 **Tracking and Data System Support for the Mariner Mars 1971 Mission: First Trajectory Correction Maneuver Through Orbit Insertion**

G. P. Textor, L. B. Kelly, and M. Kelly

Technical Memorandum 33-523, Vol. II, June 15, 1972

For abstract, see Textor, G. P.

KIEFFER, H.

K06 **Infrared Radiometry Experiment on Mariner 9**

S. C. Chase, Jr. (Santa Barbara Research Center), H. Hatzenbeler (Santa Barbara Research Center), H. Kieffer (University of California, Los Angeles), E. Miner, G. Münch (California Institute of Technology), and G. Neugebauer (California Institute of Technology)

Science, Vol. 175, No. 4019, pp. 308–309, January 21, 1972

For abstract, see Chase, S. C., Jr.

KIKIN, G. M.

K07 Completely Modular Thermionic Reactor Ion Propulsion System (TRIPS)

M. L. Peelgren, G. M. Kikin, and C. D. Sawyer

Technical Memorandum 33-550, May 15, 1972

For abstract, see Peelgren, M. L.

KISSANE, W.

K08 DSN Progress Report for January–February 1972: Manufacturing Engineering of Surface Panels for the 64-m Antennas

J. Justiss, W. Kissane, and M. S. Katow

Technical Report 32-1526, Vol. VIII, pp. 89–97, April 15, 1972

For abstract, see Justiss, J.

KLIORE, A. J.

K09 Mariner 9 Science Experiments: Preliminary Results

R. H. Steinbacher, A. J. Kliore, J. Lorell, H. Hipsher (National Aeronautics and Space Administration), C. A. Barth (University of Colorado), H. Masursky (U.S. Geological Survey), G. Münch (California Institute of Technology), J. C. Pearl (Goddard Space Flight Center), and B. A. Smith (New Mexico State University)

Science, Vol. 175, No. 4019, pp. 293–294, January 21, 1972

For abstract, see Steinbacher, R. H.

K10 Mariner 9 S-Band Martian Occultation Experiment: Initial Results on the Atmosphere and Topography of Mars

A. J. Kliore, D. L. Cain, G. Fjeldbo, B. L. Seidel, and S. I. Rasool (National Aeronautics and Space Administration)

Science, Vol. 175, No. 4019, pp. 313–317, January 21, 1972

A preliminary analysis of 15 radio occultation measurements taken on the day side of Mars between 40°S and 33°S has revealed that the temperature in the lower 15 to 20 km of the atmosphere of

Mars is essentially isothermal and warmer than expected. This result, which is also confirmed by the increased altitude of the ionization peak of the ionosphere, can possibly be caused by the absorption of solar radiation by fine particles of dust suspended in the lower atmosphere. The measurements also revealed elevation differences of 13 km and a range of surface pressures between 2.9 and 8.3 mbars. The floor of the classical bright area of Hellas was found to be about 6 km below its western rim and 4 km below the mean radius of Mars at that latitude. The region between Mare Sirenum and Solis Lacus was found to be relatively high, lying 5 to 8 km above the mean radius. The maximum electron density in the ionosphere (about 1.5×10^5 electrons per cm^3), which was found to be remarkably constant, was somewhat lower than that observed in 1969 but higher than that observed in 1965.

KNOELL, A. C.

K11 Development of Boron Epoxy Rocket Motor Chambers

W. M. Jensen, A. C. Knoell, and C. Zweben (Materials Sciences Corporation)

Proceedings of the Twenty-Seventh Annual Technical Conference of the Reinforced Plastics/Composites Institute, Washington, D.C., February 8–11, 1972, sponsored by the Society of the Plastics Industry, Inc., Sect. 17-C, pp. 1–10

For abstract, see Jensen, W. M.

KOLBLY, R. B.

K12 DSN Progress Report for March–April 1972: DSN Research and Technology Support

E. B. Jackson and R. B. Kolbly

Technical Report 32-1526, Vol. IX, pp. 147–151, June 15, 1972

For abstract, see Jackson, E. B.

KUNDE, V. G.

K13 Infrared Spectroscopy Experiment on the Mariner 9 Mission: Preliminary Results

R. A. Hanel (Goddard Space Flight Center),
B. J. Conrath (Goddard Space Flight Center),
W. A. Hovis (Goddard Space Flight Center),

V. G. Kunde (Goddard Space Flight Center),
P. D. Lowman (Goddard Space Flight Center),
J. C. Pearl (Goddard Space Flight Center),
C. Prabhakara (Goddard Space Flight Center),
B. Schlachman (Goddard Space Flight Center), and
G. V. Levin (Biospherics Incorporated)

Science, Vol. 175, No. 4019, pp. 305–308,
January 21, 1972

For abstract, see Hanel, R. A.

LACY, G. H.

L01 Surface Distribution of Microorganisms in Antarctic Dry-Valley Soils: A Martian Analog

R. E. Cameron, H. P. Conrow, D. R. Gensel,
G. H. Lacy, and F. A. Morelli

Antarctic J. U.S., Vol. VI, No. 5, pp. 211–213,
September–October 1971

For abstract, see Cameron, R. E.

LAING, P. A.

L02 Mariner 9 Celestial Mechanics Experiment: Gravity Field and Pole Direction of Mars

J. Lorell, G. H. Born, E. J. Christensen, J. F. Jordan,
P. A. Laing, W. Martin, W. L. Sjogren,
I. I. Shapiro (Massachusetts Institute of Technology),
R. D. Reasenberg (Massachusetts Institute of Technology),
and G. L. Slater (Massachusetts Institute of Technology)

Science, Vol. 175, No. 4019, pp. 317–320,
January 21, 1972

For abstract, see Lorell, J.

LAMBERT, D. L.

L03 Astronomical Infrared Spectroscopy With a Connes-Type Interferometer: III. Alpha Orionis, 2600–3450 cm^{-1}

R. Beer, R. B. Hutchison, R. H. Norton, and
D. L. Lambert (University of Texas)

Astrophys. J., Vol. 172, No. 1, Pt. 1, pp. 89–115, February 15, 1972

For abstract, see Beer, R.

LANE, A. L.

L04 Mariner 9 Ultraviolet Spectrometer Experiment: Initial Results

C. A. Barth (University of Colorado), C. W. Hord (University of Colorado), A. I. Stewart (University of Colorado), and A. L. Lane

Science, Vol. 175, No. 4019, pp. 309–312, January 21, 1972

For abstract, see Barth, C. A.

L05 Mariner 9 Ultraviolet Spectrometer Experiment: Stellar Observations

C. F. Lillie (University of Colorado), R. C. Bohlin (University of Colorado), M. R. Molnar (University of Colorado), C. A. Barth (University of Colorado), and A. L. Lane

Science, Vol. 175, No. 4019, pp. 321–322, January 21, 1972

For abstract, see Lillie, C. F.

LANE, F. L.

L06 Investigation of Gold Embrittlement in Connector Solder Joints

F. L. Lane

Technical Memorandum 33-533, April 1, 1972

An investigation was performed to determine to what extent, if any, typical flight connector solder joints may be embrittled by the presence of gold. In addition to mappings of gold content in connector solder joints by an electron microprobe analyzer, metallographic examinations and mechanical tests (thermal shock, vibration, impact, and tensile strength) were also conducted. This memorandum presents a description of the specimens and tests, a discussion of the data, and some conclusions.

LaPORTE, D. D.

L07 The Detection and Mapping of Water Vapor in the Martian Atmosphere

C. B. Farmer and D. D. LaPorte

Icarus, Vol. 16, No. 1, pp. 34–46, February 1972

For abstract, see Farmer, C. B.

LAYLAND, J. W.

L08 DSN Progress Report for March–April 1972: Performance of an Optimum Buffer Management Strategy for sequential Decoding

J. W. Layland

Technical Report 32-1526, Vol. IX, pp. 88–96,
June 15, 1972

Sequential decoding has been found to be an efficient means of communicating at low undetected error rates from deep space probes, but a failure mechanism known as erasure or computational overflow remains a significant problem. The erasure of a block occurs when the decoder has not finished decoding that block at the time that it must be output.

A recent article developed a technique for scheduling the operations of a sequential decoder that has the potential for significant reduction in erasure probability relative to a decoder with the same parameters and using the conventional method of scheduling. Performance results reported previously depend upon the accuracy of an accepted model for the number of computations needed to decode a block of data. This article presents a re-evaluation of decoder performance, using actual sequential decoding data. Results are generally unchanged: a decoder with a 10-block buffer will achieve less than a 10^{-4} erasure probability with the new scheduling technique whenever a similar decoder had achieved less than a 10^{-2} erasure probability in conventional operation.

L09 DSN Progress Report for March–April 1972: Variable Length Short Constraint-Length Convolutional Codes: A Comparison of Maximum Likelihood and Sequential Decoding

J. W. Layland

Technical Report 32-1526, Vol. IX, pp. 97–102,
June 15, 1972

Maximum-likelihood decoding of short-constraint-length convolutional codes is one of the likely candidates for implementing high-

performance telemetry systems for future deep-space missions. It has, in fact, been considered to be the best choice for video missions, providing better performance at the design point of 5×10^{-3} than other systems of comparable complexity. Recent advances in knowledge of sequential decoding have posed the question as to whether sequential decoding might, in fact, be preferable to maximum-likelihood decoding. The answer, developed here in terms of a hypothesized maximum-likelihood decoder built technologically similar to the JPL high-speed multi-mission sequential decoder, is that maximum-likelihood decoding is preferable to sequential decoding at a 5×10^{-3} bit error rate. The reverse is true at 10^{-3} and below.

Two code families of variable constraint length are also developed which permit easy implementation of encoders for this hypothesized maximum-likelihood decoder.

LEAVITT, R. K.

L10 The Least-Squares Process of MEDIA for Computing DRVID Calibration Polynomials

R. K. Leavitt

Technical Memorandum 33-542, May 15, 1972

This document describes and evaluates a process for computing a least-squares polynomial approximation of data points in which the optimum degree of the polynomial is automatically determined. An iterative smoothing technique is used to replace every point with the value taken on by a moving least-squares polynomial computed from a subset of points centered at the point being replaced. The optimum degree of the resulting polynomial approximation is determined by analyzing the finite differences of each successive set of smoothed points. To evaluate the process, this document uses both artificially constructed data and actual Mariner Mars 1971 tracking data.

This process has been incorporated into the Transmission Media Calibration computer program (MEDIA), which calibrates radiometric data to overcome the effects on the tracking signal of charged-particle media. MEDIA was used in support of the Mariner Mars 1971 Project.

LEISING, C. J.

L11 Mariner 9 Propulsion Subsystem Performance During Interplanetary Cruise and Mars Orbit Insertion

M. J. Cork, R. L. French, C. J. Leising, and D. D. Schmit

JPL Quarterly Technical Review, Vol. 2, No. 1, pp. 113–122, April 1972

For abstract, see Cork, M. J.

LESH, J. R.

L12 DSN Progress Report for March–April 1972: Carrier Power Estimation Accuracy

J. R. Lesh

Technical Report 32-1526, Vol. IX, pp. 207–217, June 15, 1972

In this article, estimation theoretic techniques are used to derive expressions for the accuracy of the digital instrumentation subsystem (DIS) and telemetry and command processor (TCP) computer methods of carrier power estimation. Evaluation of these expressions shows that the TCP method is presently far more accurate than the DIS method. A procedure by which the DIS accuracy can be greatly improved is also presented.

LEVIN, G. V.

L13 Infrared Spectroscopy Experiment on the Mariner 9 Mission: Preliminary Results

R. A. Hanel (Goddard Space Flight Center),
B. J. Conrath (Goddard Space Flight Center),
W. A. Hovis (Goddard Space Flight Center),
V. G. Kunde (Goddard Space Flight Center),
P. D. Lowman (Goddard Space Flight Center),
J. C. Pearl (Goddard Space Flight Center),
C. Prabhakara (Goddard Space Flight Center),
B. Schlachman (Goddard Space Flight Center), and
G. V. Levin (Biospherics Incorporated)

Science, Vol. 175, No. 4019, pp. 305–308, January 21, 1972

For abstract, see Hanel, R. A.

LEVITT, B. K.

L14 Interplex: An Analysis of Optimized Power Allocations for Two- and Three-Channel PSK/PM Telecommunications Systems

B. K. Levitt

JPL Quarterly Technical Review, Vol. 2, No. 1, pp. 143–151, April 1972

Under certain conditions, interplex modulation techniques can significantly improve the performance of a multichannel phase-shift-keyed/phase-modulated (PSK/PM) telemetry system by increasing the useful available power relative to that of conventional PSK/PM systems. However, previous efforts to compare the two modulation schemes and provide a measure of this improvement have occasionally fostered the false impression that the total average signal power and the channel modulation indices were common to both systems. In practice, in designing either modulation system for a deep-space telecommunications link, optimal modulation indices are selected to minimize the total average signal power subject to certain minimum requirements on the average telemetry channel and carrier powers. This article illustrates these optimal design concepts for two- and three-channel telemetry modes in the context of the Mariner Venus–Mercury 1973 mission and provides a more realistic measure of the usefulness of interplex. These ideas are then applied as an example to a particular Mariner Venus–Mercury 1973 telemetry mode to demonstrate that interplex can reduce the required total average power by more than 2 dB in some cases.

LILLIE, C. F.

L15 Mariner 9 Ultraviolet Spectrometer Experiment: Stellar Observations

C. F. Lillie (University of Colorado), R. C. Bohlin (University of Colorado), M. R. Molnar (University of Colorado), C. A. Barth (University of Colorado), and A. L. Lane

Science, Vol. 175, No. 4019, pp. 321–322, January 21, 1972

Photoelectric spectra have been obtained for a number of early-type stars in the 1100- to 2000-Å region with the Mariner 9 ultraviolet spectrometer. The resonance lines of H-I, Si-IV, and C-IV are easily identified, as are features due to C-II, C-III, Si-III, Fe-II, and N-IV. The absolute energy distribution derived from the data lie about 20% below those of OAO-2 in the 1200- to 2000-Å region.

LIN, H. S.

L16 Analysis of Morgantown Vehicle Steering Control

H. S. Lin and E. L. Marsh

JPL Quarterly Technical Review, Vol. 2, No. 1, pp. 58–71, April 1972

The proposed Morgantown public transportation system will use a fleet of computer-controlled vehicles operating on a separate dedicated network of roadways called a "guideway." An automatic steering system on each vehicle will enable the traversal of the proposed route of various guideway sections.

This article describes a preliminary study made at JPL to analyze the steering control for the Morgantown vehicles. The primary requirement was to design an automatic steering system that would achieve a smooth ride and simultaneously eliminate the need for excess margin in the guideway width, a significant factor in overall system cost. Front- and rear-wheel steering and front and rear sensing capabilities were assumed in the analysis. The system finally adopted—front- and rear-wheel steering and front sensing—was shown by computer simulations and by Boeing Company vehicle steering experiments to be adequate.

LINNES, K. W.

L17 DSN Progress Report for January–February 1972: Radio Science Support

K. W. Linnes

Technical Report 32-1526, Vol. VIII, pp. 24–28, April 15, 1972

Since 1967, radio scientists have used the DSN 26- and 64-m-diameter antenna stations to investigate pulsars, to study the effect of solar corona on radio signals, and to observe radio emissions from X-ray sources. More recently, very long baseline interferometry (VLBI) techniques have been used for high-resolution studies of quasars. During the reporting period, VLBI observations were made of quasars and also of the Mariner 9 spacecraft. Support was also provided by the 64-m-diameter antenna for the measurement of cosmic background noise.

LORDEN, G.

L18 DSN Progress Report for March–April 1972: An Inventory Policy for the Deep Space Network

I. Eisenberger, F. R. Maiocco, and G. Lorden (California Institute of Technology)

Technical Report 32-1526, Vol. IX, pp. 84–87, June 15, 1972

For abstract, see Eisenberger, I.

LORELL, J.

L19 Mariner 9 Science Experiments: Preliminary Results

R. H. Steinbacher, A. J. Kliore, J. Lorell, H. Hipsher (National Aeronautics and Space Administration), C. A. Barth (University of Colorado), H. Masursky (U.S. Geological Survey), G. Münch (California Institute of Technology), J. C. Pearl (Goddard Space Flight Center), and B. A. Smith (New Mexico State University)

Science, Vol. 175, No. 4019, pp. 293–294, January 21, 1972

For abstract, see Steinbacher, R. H.

L20 Mariner 9 Celestial Mechanics Experiment: Gravity Field and Pole Direction of Mars

J. Lorell, G. H. Born, E. J. Christensen, J. F. Jordan, P. A. Laing, W. Martin, W. L. Sjogren, I. I. Shapiro (Massachusetts Institute of Technology), R. D. Reasenberg (Massachusetts Institute of Technology), and G. L. Slater (Massachusetts Institute of Technology)

Science, Vol. 175, No. 4019, pp. 317–320, January 21, 1972

Analysis of the Mariner 9 radio-tracking data shows that the Martian gravity field is rougher than that of Earth or the Moon, and that the accepted direction of Mars rotation axis is in error by about 0.5 deg. The new value for the pole direction for the epoch 1971.9, referred to the mean equatorial system of 1950.0, is right ascension = 317.3 ± 0.3 deg, declination = 52.6 ± 0.2 deg. The values found for the coefficients of the low-order harmonics of Mars gravity field are as follows:

$$J_2 = (1.96 \pm 0.01) \times 10^{-3}$$

$$C_{22} = -(5 \pm 1) \times 10^{-5}$$

$$S_{22} = (3 \pm 1) \times 10^{-5}$$

where J_2 is referred to an equatorial radius of 3394 km. The value for J_2 is in excellent agreement with the result from Wilkins' analysis of the observations of Phobos. The other two coefficients imply a value of $(2.5 \pm 0.5) \times 10^{-4}$ for the fractional difference in

the principal equatorial moments of inertia; the axis of the minimum moment passes near 105°W.

LOWMAN, P. D.

L21 Infrared Spectroscopy Experiment on the Mariner 9 Mission: Preliminary Results

R. A. Hanel (Goddard Space Flight Center),
B. J. Conrath (Goddard Space Flight Center),
W. A. Hovis (Goddard Space Flight Center),
V. G. Kunde (Goddard Space Flight Center),
P. D. Lowman (Goddard Space Flight Center),
J. C. Pearl (Goddard Space Flight Center),
C. Prabhakara (Goddard Space Flight Center),
B. Schlachman (Goddard Space Flight Center), and
G. V. Levin (Biospherics Incorporated)

Science, Vol. 175, No. 4019, pp. 305–308, January 21, 1972

For abstract, see Hanel, R. A.

LUDWIG, A. C.

L22 Conical-Reflector Antennas

A. C. Ludwig

IEEE Trans. Anten. Prop., Vol. AP-20, No. 2, pp. 146–152, March 1972

The mechanical advantages of a singly curved conical reflector are demonstrated by the experimental test of a furlable 1.83-m conical-Gregorian antenna at 16.33 GHz. The measured gain of 47.5 dB corresponds to a net efficiency of over 57%. A ray-optics analysis of conical-reflector antennas is presented, and data useful in the design of conical antennas is given. The conical-Gregorian antenna, in which a subreflector is used in conjunction with a conventional horn feed, is considered in detail. A physical-optics analysis of the conical-Gregorian antenna is used to investigate diffraction and other effects, and to analytically confirm the high performance of the antenna. It is concluded that conical antennas are a valuable addition to available antenna-design concepts.

LUDWIG, O.

L23 The James Wavefunction for the Ground State of H_2^+

M. Geller and O. Ludwig (Villanova University)

Chem. Phys. Lett., Vol. 12, No. 2, p. 403,
December 15, 1971

For abstract, see Geller, M.

LYTTLETON, R. A.

L24 Does a Continuous Solid Nucleus Exist in Comets?

R. A. Lyttleton

Astrophys. Space Sci., Vol. 15, No. 2, pp. 175–184,
February 1972

The implication of actual cometary observations for the physical nature of comets is briefly reviewed and brings out the complete conflict with observation of the ice-dust solid nucleus model put forward in recent years as representing the fundamental structure of comets. That under increasing solar heat the nucleus develops an expanding atmosphere is inconsistent with the well-established phenomenon that the coma *contracts* with decreasing distance from the Sun. Several comets remaining always beyond Mars have nevertheless been strongly active and produced fine tails. That some comets show at times a star-like point of light is readily explicable on the dust-cloud structure and by no means establishes that a solid nucleus exists. With the nucleus-area corresponding not to a small solid mass but to an optical phenomenon, there would be no reason to expect that it would describe a precise dynamical orbit. On the hypothesis of a nucleus, it is necessary to postulate further some internal jet-propulsion mechanism to account for the orbital deviations.

In planning a space-mission to a comet, and if search for a nucleus is included, it will be of the highest importance for its success to ensure beforehand that the equipment carried will not fail to discover a kilometric-sized body if one is present; otherwise a null result could be interpreted simply as a failure of this part of the mission and not as proving the absence of any nucleus.

MACIE, T. W.

M01 Integration of a Breadboard Power Conditioner With a 20-cm Ion Thruster

T. D. Masek, T. W. Macie, E. N. Costogue,
W. J. Muldoon (Hughes Aircraft Company),
D. R. Garth (Hughes Aircraft Company), and
G. C. Benson (Hughes Aircraft Company)

J. Spacecraft Rockets, Vol. 9, No. 2, pp. 71–78, February 1972

For abstract, see Masek, T. D.

MACLAY, J. E.

M02 DSN Progress Report for March–April 1972: DSN Monitor and DSN Operations Control System Testing

J. E. Maclay

Technical Report 32-1526, Vol. IX, pp. 12–14, June 15, 1972

In preparation for Mariner Mars 1971 support, the DSN Monitor System and Operations Control System were individually tested, after which they provided support for combined system tests. These tests provided valuable test preparation and execution practice.

MAIOCCO, F. R.

M03 DSN Progress Report for March–April 1972: An Inventory Policy for the Deep Space Network

I. Eisenberger, F. R. Maiocco, and G. Lorden (California Institute of Technology)

Technical Report 32-1526, Vol. IX, pp. 84–87, June 15, 1972

For abstract, see Eisenberger, I.

MARGOLIS, J. S.

M04 A Compilation of Laboratory Spectra

J. S. Margolis

Technical Memorandum 33-541, May 15, 1972

This memorandum contains an up-to-date listing of the spectra obtained in the spectroscopy laboratory and a complete description of the experimental conditions.

MARSH, E. L.

M05 Analysis of Morgantown Vehicle Steering Control

H. S. Lin and E. L. Marsh

JPL Quarterly Technical Review, Vol. 2, No. 1, pp. 58–71, April 1972

For abstract, see Lin, H. S.

MARTIN, W.

M06 Mariner 9 Celestial Mechanics Experiment: Gravity Field and Pole Direction of Mars

J. Lorell, G. H. Born, E. J. Christensen, J. F. Jordan, P. A. Laing, W. Martin, W. L. Sjogren, I. I. Shapiro (Massachusetts Institute of Technology), R. D. Reasenberg (Massachusetts Institute of Technology), and G. L. Slater (Massachusetts Institute of Technology)

Science, Vol. 175, No. 4019, pp. 317–320, January 21, 1972

For abstract, see Lorell, J.

MARTONCHIK, J. V.

M07 Jupiter: Observation of Deuterated Methane in the Atmosphere

R. Beer, C. B. Farmer, R. H. Norton, J. V. Martonchik (University of Texas), and T. G. Barnes (University of Texas)

Science, Vol. 172, No. 4028, pp. 1360–1361, March 24, 1972

For abstract, see Beer, R.

MASEK, T. D.

M08 Integration of a Breadboard Power Conditioner With a 20-cm Ion Thruster

T. D. Masek, T. W. Macie, E. N. Costogue, W. J. Muldoon (Hughes Aircraft Company), D. R. Garth (Hughes Aircraft Company), and G. C. Benson (Hughes Aircraft Company)

J. Spacecraft Rockets, Vol. 9, No. 2, pp. 71–78, February 1972

A breadboard of a lightweight 2.5-kW power conditioner was developed and integrated with an oxide ion thruster. The power conditioner was subsequently modified and integrated with a hollow cathode thruster. The problems of integration with each type of thruster are reviewed. Work leading to optimization of the

closed-loop system performance during startup and recycling after thruster arcing is described. Electrical efficiency, weight, reliability, and other critical parameters are evaluated. The integration program has shown that the system satisfies the requirements of solar electric spacecraft.

M09 A Mechanism for Three-Axis Control of an Ion Thruster Array

G. S. Perkins, K. G. Johnson, J. D. Ferrera, and T. D. Masek

J. Spacecraft Rockets, Vol. 9, No. 3, pp. 218–220, March 1972

For abstract, see Perkins, G. S.

MASSIER, P. F.

M10 Partially Ionized Gas Flow and Heat Transfer in the Separation, Reattachment, and Redevelopment Regions Downstream of an Abrupt Circular Channel Expansion

L. H. Back, P. F. Massier, and E. J. Roschke

Trans. ASME, Ser. C: J. Heat Transf., Vol. 94, No. 1, pp. 119–127, February 1972

For abstract, see Back, L. H.

MASURSKY, H.

M11 Mariner 9 Science Experiments: Preliminary Results

R. H. Steinbacher, A. J. Kliore, J. Lorell, H. Hipsher (National Aeronautics and Space Administration), C. A. Barth (University of Colorado), H. Masursky (U.S. Geological Survey), G. Münch (California Institute of Technology), J. C. Pearl (Goddard Space Flight Center), and B. A. Smith (New Mexico State University)

Science, Vol. 175, No. 4019, pp. 293–294, January 21, 1972

For abstract, see Steinbacher, R. H.

M12 Mariner 9 Television Reconnaissance of Mars and Its Satellites: Preliminary Results

H. Masursky, et al.

Science, Vol. 175, No. 4019, pp. 294–305,
January 21, 1972

At orbit insertion on November 14, 1971, the Martian surface was largely obscured by a dust haze with an extinction optical depth that ranged from near unity in the south polar region to probably greater than 2 over most of the planet. The only features clearly visible were the south polar cap, one dark spot in Nix Olympica, and three dark spots in the Tharsis region. During the third week the atmosphere began to clear and surface visibility improved, but contrasts remained a fraction of their normal value. Each of the dark spots that apparently protrude through most of the dust-filled atmosphere has a crater or crater complex in its center. The craters are rimless and have featureless floors that, in the crater complexes, are at different levels. The largest crater within the southernmost spot is approximately 100 km wide. The craters apparently were formed by subsidence and resemble terrestrial calderas. The south polar cap has a regular margin, suggesting very flat topography. Two craters outside the cap have frost on their floors; an apparent crater rim within the cap is frost free, indicating preferential loss of frost from elevated ground. If this is so, then the curvilinear streaks, which were frost covered in 1969 and are now clear of frost, may be low-relief ridges. Closeup pictures of Phobos and Deimos show that Phobos is about 25 ± 5 by 21 ± 1 km and Deimos is about 13.5 ± 2 by 12.0 ± 0.5 km. Both have irregular shapes and are highly cratered, with some craters showing raised rims. The satellites are dark objects with geometric albedos of 0.05.

Contributors to this article include:

U.S. Geological Survey: H. Masursky, R. M. Batson, J. F. McCauley, L. A. Soderblom, R. L. Wildey, M. H. Carr, D. J. Milton, and D. E. Wilhelms

New Mexico State University: B. A. Smith, T. B. Kirby, and J. C. Robinson

University of Washington: C. B. Leovy

Jet Propulsion Laboratory: G. A. Briggs, T. C. Duxbury, and C. H. Acton, Jr.

California Institute of Technology: B. C. Murray, J. A. Cutts, R. P. Sharp, S. Smith, and R. B. Leighton

Cornell University: C. Sagan, J. Veverka, and M. Noland

Stanford University: J. Lederberg and E. Levinthal

Ames Research Center: J. B. Pollack and J. T. Moore, Jr.

IIT Research Institute: W. K. Hartmann

Bellcomm, Inc.: E. N. Shipley

University of Texas: G. de Vaucouleurs

Rand Corporation: M. E. Davies

McCLURE, J. P.

M13 DSN Progress Report for March–April 1972: Madrid-to-JPL 50-kbit/s Wideband Error Statistics

J. P. McClure

Technical Report 32-1526, Vol. IX, pp. 177–184, June 15, 1972

Detailed analysis of the results of wideband data tests conducted at 50 kbit/s in June 1971 between Madrid and the Space Flight Operations Facility confirms the burst nature of the transmission errors. Measured burst length depends critically on the definition of a burst. A typical burst length of 200 bits was determined for the error model and method of measurement employed. During good circuit conditions, the block error rate varies directly with block length; however, this proportionality does not hold during poor circuit conditions. The average number of error bits in an error block holds reasonably constant even as the error rate changes by several orders of magnitude.

McELIECE, R. J.

M14 DSN Progress Report for March–April 1972: A Note on the Griesmer Bound

L. D. Baumert and R. J. McEliece

Technical Report 32-1526, Vol. IX, pp. 49–52, June 15, 1972

For abstract, see Baumert, L. D.

M15 DSN Progress Report for March–April 1972: Hiding and Covering in a Compact Metric Space

R. J. McEliece and E. C. Posner

Technical Report 32-1526, Vol. IX, pp. 59–64, June 15, 1972

This article studies the relationship between games of search in a compact metric space X and the absolute epsilon entropy $I(X)$ of X. The main result is that

$$I(X) = -\log v_L^*,$$

v_L^* being the lower value of a game in X we call "restricted hide and seek."

M16 Hide and Seek, Data Storage, and Entropy

R. J. McEliece and E. C. Posner

Ann. Math. Statist., Vol. 42, No. 5, pp. 1706–1716, October 1971

This article discusses the relationship between games of search and the optimum storage of information. The presentation centers primarily around (1) the case of finite sets, and (2) a generalization to compact metric spaces. The result is a synthesis of the epsilon entropy theory of approximation with the theory of data transmission and compression.

M17 Weights of Irreducible Cyclic Codes

L. D. Baumert and R. J. McEliece

Inform. Control, Vol. 20, No. 2, pp. 158–175, March 1972

For abstract, see Baumert, L. D.

MEISSINGER, H.

M18 Basic Parameters for Low Thrust Mission and System Analysis

T. A. Barber, J. L. Horsewood (Analytical Mechanics Associates, Inc.), and H. Meissinger (TRW Systems, Inc.)

Preprint 72-426, AIAA Ninth Electric Propulsion Conference, Bethesda, Maryland, April 17–19, 1972

For abstract, see Barber, T. A.

MENICHELLI, V. J.

M19 Evaluation of Electroexplosive Devices by Nondestructive Test Techniques and Impulsive Waveform Firings

V. J. Menichelli

Technical Report 32-1556, June 15, 1972

Special requirements of the aerospace industry necessitate more detailed knowledge of the quality and reliability of each electroexplosive device selected for use on spacecraft. Statistical methods

do not practically demonstrate the high reliability needed. To close this gap, nondestructive test techniques and instrumentation for 1-W/1-A no-fire devices have been developed. Several lots of squibs have been evaluated using these techniques and this instrumentation in order to obtain data on the quality and normal behavior of each electroexplosive device without firing or degrading the unit. Performance data were obtained by initiating each electroexplosive device with an impulsive waveform and sensing the initiation characteristics, sensitivity, and output.

M20 Initiation of Insensitive Explosives by Laser Energy

V. J. Menichelli and L. C. Yang

Technical Report 32-1557, June 1, 1972

Instantaneous longitudinal detonations have been observed in confined columns of pentaerythritol tetranitrate (PETN), cyclotrimethylene trinitramine (RDX), and tetryl when these materials were pulsed with light energy from a focused Q-switch ruby laser. The laser energy ranged from 0.5 to 4.2 J, with a pulse width of 25 ns. Enhancement of the ignition mechanism is hypothesized when a 100-nm (1000-Å) thick aluminum film is vacuum-deposited on the explosive side of the window. Upon irradiation from the laser, a shock is generated at the aluminum–explosive interface. Steady-state detonations can be reached in less than 0.5 μs, with less than 10% variation in detonation velocity for PETN and RDX.

M21 Nondestructive Testing of Insensitive Electroexplosive Devices by Transient Techniques

L. A. Rosenthal (Rutgers University) and V. J. Menichelli

Mater. Eval., Vol. XXX, No. 1, pp. 13–19, January 1972

For abstract, see Rosenthal, L. A.

MINER, E.

M22 Infrared Radiometry Experiment on Mariner 9

S. C. Chase, Jr. (Santa Barbara Research Center),
H. Hatzenbeler (Santa Barbara Research Center),
H. Kieffer (University of California, Los Angeles), E. Miner,
G. Münch (California Institute of Technology), and
G. Neugebauer (California Institute of Technology)

Science, Vol. 175, No. 4019, pp. 308–309,
January 21, 1972

For abstract, see Chase, S. C., Jr.

MOACANIN, J.

M23 Lifetime Estimates for Sterilizable Silver–Zinc Battery Separators

E. F. Cuddihy, D. E. Walmsley, and J. Moacanin

JPL Quarterly Technical Review, Vol. 2, No. 1, pp. 72–81, April 1972

For abstract, see Cuddihy, E. F.

MOLNAR, M. R.

M24 Mariner 9 Ultraviolet Spectrometer Experiment: Stellar Observations

C. F. Lillie (University of Colorado), R. C. Bohlin (University of Colorado), M. R. Molnar (University of Colorado), C. A. Barth (University of Colorado), and A. L. Lane

Science, Vol. 175, No. 4019, pp. 321–322, January 21, 1972

For abstract, see Lillie, C. F.

MONDT, J. F.

M25 Thermionic Reactor Electric Propulsion System Requirements

J. F. Mondt, C. D. Sawyer, and R. W. Schaupp (Ames Research Center)

Technical Memorandum 33-549, June 1, 1972

Mission analysis, system analysis, and mission engineering studies have been conducted to find a single nuclear-electric propulsion (NEP) system that would be applicable for a broad range of unmanned outer-planet missions. The NEP system studied uses an in-core nuclear thermionic reactor as the electric power source and mercury bombardment ion engines for propulsion. Many requirements imposed on the NEP system by the mission were determined in the process of trying to find a single NEP system for many missions. The NEP system requirements are preliminary in nature and subject to small changes with further iterations between these types of studies and the technology program. It was determined that other applications for in-core thermionic reactors must also be considered in determining specific reactor requirements. It is concluded that a single thermionic reactor NEP system could be useful for a broad range of unmanned outer-planet missions. The thermionic reactor NEP system should have: (1) a power level in the 70- to 120-kWe range, (2) a system specific

weight of approximately 30 kg/kWe, and (3) a full power output capability of 20,000 hr.

MORELLI, F. A.

M26 Surface Distribution of Microorganisms in Antarctic Dry-Valley Soils: A Martian Analog

R. E. Cameron, H. P. Conrow, D. R. Gensel, G. H. Lacy, and F. A. Morelli

Antarctic J. U.S., Vol. VI, No. 5, pp. 211–213, September–October 1971

For abstract, see Cameron, R. E.

MORGAN, C. L.

M27 DSN Progress Report for January–February 1972: Integration of the DSN Sequence of Events Generator

C. L. Morgan

Technical Report 32-1526, Vol. VIII, pp. 125–126, April 15, 1972

This article reviews the concept, function, implementation, and operational status of the DSN sequence-of-events generator. The supporting software resides in an IBM 360/75 as a part of the real-time mission support software system. The program title is "Sequence-of-Events Generator."

MOYNIHAN, P. I.

M28 Minimum Impulse Tests of 0.45-N Liquid Hydrazine Catalytic Thrusters

P. I. Moynihan

JPL Quarterly Technical Review, Vol. 2, No. 1, pp. 107–112, April 1972

Many studies have identified the need for high-performance, low-total-impulse chemical thrusters for attitude-propulsion applications on spacecraft with limit cycle attitude control. Specifically, studies for outer-planet spacecraft have identified a need for thrusters with a steady-state thrust of 1.3×10^{-1} to 4.5×10^{-1} N (0.03 to 0.1 lbf) and a pulsed "impulse bit" of 4.5×10^{-4} to 4.5×10^{-3} N-s (10^{-4} to 10^{-3} lbf-s). No data on small catalytic thrusters with this capability have heretofore been available. Therefore, in support of an attitude-control tradeoff study performed under the

Thermoelectric Outer-Planet Spacecraft Project, an exploratory test series was conducted on three types of 0.45-N (0.1-lbf) liquid hydrazine thrusters to ascertain the minimum impulse bit capability for this class of engine. This article describes this test series and discusses the results. The testing was performed at 21 and 145°C (70 and 300°F) while maintaining nominal 0.45-N (0.1-lbf) upstream conditions. Valve on-times as low as 0.008 s were applied. Impulse bits as low as 1.0×10^{-3} and 2.6×10^{-3} N-s (2.3×10^{-4} and 5.7×10^{-4} lbf-s) were observed for thruster temperatures of 21 and 145°C (70 and 300°F), respectively.

MUDGWAY, D. J.

M29 DSN Progress Report for January–February 1972: Viking Mission Support

D. J. Mudgway

Technical Report 32-1526, Vol. VIII, pp. 20–23, April 15, 1972

Until recently, the DSN configuration intended for support of the Viking 1975 mission included the Space Flight Operations Facility with its central processing system, mission support areas, and Simulation Center. In response to the NASA Headquarters directive of October 1, 1971, the Project/DSN interface was changed, deleting the Space Flight Operations Facility from the scope of DSN responsibility. As a consequence, many existing understandings between the DSN and the Project must now be renegotiated, with a resulting impact on schedules, documentation, and resources.

This article identifies areas where rework is necessary and describes progress toward defining the new DSN configuration for Viking and reestablishing a mutually acceptable interface between the project and the DSN.

MULDOON, W. J.

M30 Integration of a Breadboard Power Conditioner With a 20-cm Ion Thruster

T. D. Masek, T. W. Macie, E. N. Costogue,
W. J. Muldoon (Hughes Aircraft Company),
D. R. Garth (Hughes Aircraft Company), and
G. C. Benson (Hughes Aircraft Company)

J. Spacecraft Rockets, Vol. 9, No. 2, pp. 71–78, February 1972

For abstract, see Masek, T. D.

MULHALL, B. D.

M31 DSN Progress Report for March–April 1972: Navigation Demonstrations With the Mariner Venus–Mercury 1973 Spacecraft Requiring X-Band Receiving Capability at a Second DSN Station

B. D. Mulhall

Technical Report 32-1526, Vol. IX, pp. 38–43, June 15, 1972

The opportunities to demonstrate two-station tracking with radio metric doppler and range data calibrated for charged particles by the X- and S-band technique during the Mariner Venus–Mercury 1973 mission are described together with the rationale for undertaking and experiments. The errors which corrupt two-station tracking for single and dual frequency operation are also described.

MULLER, P. M.

M32 Lunar Gravity via Apollo 14 Doppler Radio Tracking

W. L. Sjogren, P. Gottlieb, P. M. Muller, and W. Wollenhaupt (Manned Spacecraft Center)

Science, Vol. 175, No. 4018, pp. 165–168, January 14, 1972

For abstract, see Sjogren, W. L.

MÜNCH, G.

M33 Mariner 9 Science Experiments: Preliminary Results

R. H. Steinbacher, A. J. Kliore, J. Lorell, H. Hipsher (National Aeronautics and Space Administration), C. A. Barth (University of Colorado), H. Masursky (U.S. Geological Survey), G. Münch (California Institute of Technology), J. C. Pearl (Goddard Space Flight Center), and B. A. Smith (New Mexico State University)

Science, Vol. 175, No. 4019, pp. 293–294, January 21, 1972

For abstract, see Steinbacher, R. H.

M34 Infrared Radiometry Experiment on Mariner 9

S. C. Chase, Jr. (Santa Barbara Research Center), H. Hatzenbeler (Santa Barbara Research Center), H. Kieffer (University of California, Los Angeles), E. Miner, G. Münch (California Institute of Technology), and G. Neugebauer (California Institute of Technology)

Science, Vol. 175, No. 4019, pp. 308–309, January 21, 1972

For abstract, see Chase, S. C., Jr.

MYKKELTVEIT, J.

M35 DSN Progress Report for March–April 1972: A Note on Kerdock Codes

J. Mykkeltveit (California Institute of Technology)

Technical Report 32-1526, Vol. IX, pp. 82–83, June 15, 1972

The performance of an important class of low-rate nonlinear binary codes recently discovered by A. M. Kerdock is superior to that of linear codes with the same parameters. Before these codes can be put to practical use, several questions must be answered. This article considers one of the questions. It shows that the nonlinear Kerdock codes are systematic; i.e., they have distinguishable information and check positions.

NAKAMURA, Y.

N01 Solid Propulsion Advanced Concepts

Y. Nakamura and J. I. Shafer

Technical Memorandum 33-534, May 1, 1972

In this study, the feasibility and application of a solid propulsion powered spacecraft concept to implement high-energy missions independent of multiplanetary swingby opportunities are assessed, and recommendations are offered for future work. An upper-stage, solid propulsion launch vehicle augmentation system was selected as the baseline configuration in view of the established program goals of low cost and high reliability.

During the study, a new high-mass-fraction solid motor staging design, the conesphere motor concept, was conceived, and its anticipated performance predictions further enhanced the candidacy of the solid propulsion baseline configuration. A class of missions of increasing scientific interest was identified, and the

attendant launch energy thresholds for alternate approaches were determined. Spacecraft and propulsion system data that characterize mission performance capabilities were generated to serve as the basis for subsequent tradeoff studies. A cost-effectiveness model was used for the preliminary feasibility assessment to provide a meaningful comparative effectiveness measure of the various candidate designs. The results substantiated the feasibility of the powered spacecraft concept when used in conjunction with several intermediate-sized launch vehicles, as well as the existence of energy margins by which to exploit the attainment of extended mission capabilities. Additionally, in growth option applications, the employment of advanced propulsion systems and alternate spacecraft approaches appears promising.

NANCE, H. E.

N02 DSN Progress Report for January–February 1972: DSN Tracking System: Operation With the Mutual Stations

W. D. Chaney and H. E. Nance

Technical Report 32-1526, Vol. VIII, pp. 5–7, April 15, 1972

For abstract, see Chaney, W. D.

NEUGEBAUER, G.

N03 Infrared Radiometry Experiment on Mariner 9

S. C. Chase, Jr. (Santa Barbara Research Center),
H. Hatzenbeler (Santa Barbara Research Center),
H. Kieffer (University of California, Los Angeles), E. Miner,
G. Münch (California Institute of Technology), and
G. Neugebauer (California Institute of Technology)

Science, Vol. 175, No. 4019, pp. 308–309,
January 21, 1972

For abstract, see Chase, S. C., Jr.

NORTON, R. H.

N04 Astronomical Infrared Spectroscopy With a Connes-Type Interferometer: III. Alpha Orionis, 2600–3450 cm^{-1}

R. Beer, R. B. Hutchison, R. H. Norton, and
D. L. Lambert (University of Texas)

Astrophys. J., Vol. 172, No. 1, Pt. 1, pp. 89–115, February 15, 1972

For abstract, see Beer, R.

N05 Jupiter: Observation of Deuterated Methane in the Atmosphere

R. Beer, C. B. Farmer, R. H. Norton, J. V. Martonchik (University of Texas), and T. G. Barnes (University of Texas)

Science, Vol. 172, No. 4028, pp. 1360–1361, March 24, 1972

For abstract, see Beer, R.

OAKLEY, E. C.

001 DSN Progress Report for January–February 1972: SOFTWARE: A General-Purpose External Function for PDP-11 BASIC

E. C. Oakley

Technical Report 32-1526, Vol. VIII, pp. 80–88, April 15, 1972

This article describes a new tool to dramatically simplify the test and software development phases in computer-controllable subsystems for the DSN. This tool does not add to the endless computer language proliferation, but instead adds dimension to a well-established, high-level, moderately sophisticated language to enable simplified control of minicomputer peripherals. Some of its versatility is demonstrated by programs used to aid its own implementation in hardware exercisers.

OLIVER, R. E.

002 Furlable Spacecraft Antenna Development: An Interim Report

R. E. Oliver and A. H. Wilson

Technical Memorandum 33-537, April 15, 1972

Activities at JPL directed toward the development of large furlable spacecraft antennas using conical main reflectors are described. Two basic antenna configurations which utilize conical main reflectors have been conceived at JPL and are under development. In the conical-Gregorian configuration each ray experiences two reflections in traveling from the feed center to the aperture plane. In the Quadreflex configuration, each ray experiences four reflections, one at each of two subreflector surfaces and two at the main conical reflector surface.

The RF gain measurements obtained from the 1.83-m (6-ft) and 0.762-m (30-in.) models of the conical-Gregorian and Quadreflex concepts, respectively, were sufficiently encouraging to warrant further development of the concepts.

ONDRASIK, V. J.

003 DSN Progress Report for January–February 1972: The Translation of the Tropospheric Zenith Range Effect From a Radiosonde Balloon Site to a Tracking Station

K. L. Thuleen and V. J. Ondrasik

Technical Report 32-1526, Vol. VIII, pp. 39–44, April 15, 1972

For abstract, see Thuleen, K. L.

OTOSHI, T. Y.

004 A Study of Microwave Leakage Through Perforated Flat Plates

T. Y. Otoshi

IEEE Trans. Microwave Theor. Techniq., Vol. MTT-20, No. 3, pp. 235–236, March 1972

A simple formula useful for predicting leakage through a circular hole array in a metallic flat plate is presented. A correction is given for plate thickness. The formula is applicable to arrays having either a 60-deg (staggered) or 90-deg (square) hole pattern, but is restricted to the case of (1) an obliquely incident plane wave with the E field polarized normal to the plane of incidence, and (2) large transmission loss. When theoretical values were compared to experimental data obtained on test samples having transmission losses greater than 20 dB, the agreement between theory and experiment was typically better than 1 dB at S-band and 2 dB at X-band.

PACE, G. D.

P01 Mariner Mars 1971 Scan Platform Pointing Calibration

G. D. Pace, G. I. Jaivin, and R. A. Virzi

JPL Quarterly Technical Review, Vol. 2, No. 1, pp. 49–57, April 1972

Accurate calibration is required to meet the pointing accuracy requirements of science instruments mounted on a spacecraft scan platform. Calibration methods used on previous missions required

excessive system-test time and did not achieve the desired accuracy. Therefore, a new technique was devised for the Mariner Mars 1971 mission wherein both ground and in-flight calibrations were performed. A more analytical approach was used for ground calibration, and in-flight calibration was performed using narrow-angle television pictures of stars. The results were outstanding, indicating the potential of this technique for future missions when imaging experiments are flown. The Mariner Mars 1971 calibration technique and results are summarized in this article.

PALUKA, J. R.

P02 DSN Progress Report for January–February 1972: 100-kW X-Band Transmitter for FTS

J. R. Paluka

Technical Report 32-1526, Vol. VIII, pp. 98–102, April 15, 1972

During the month of July 1971 a 100-kW X-band transmitter was installed on the Venus Deep Space Station 9-m antenna. This transmitter replaces the experimental 25-kW transmitter formerly used at this station to transmit timing signals via the Moon to five other tracking stations in the DSN. Primary results of this change are an improved signal-to-noise ratio, higher reliability, and a change from the experimental frequency of 8.450 GHz to the operational frequency of 7.1495 GHz.

PAWLIK, E. V.

P03 Ion Thruster Performance Calibration

E. V. Pawlik, R. Goldstein, D. J. Fitzgerald, and R. W. Adams

Preprint 72-475, AIAA Ninth Electric Propulsion Conference, Bethesda, Maryland, April 17–19, 1972

The calibration of a typical 20-cm-diameter ion thruster was examined to determine performance penalties that must be assessed in projecting measured performance into a space environment. Four specific areas were investigated. These include (1) double ion content of the beam, (2) back ingestion from the vacuum facility, (3) beam spreading, and (4) propellant flow rate measurements. The double ion content was measured and found to be as high as 5.5% at an arc voltage of 35 V. Back ingestion was observed to become significant above tank pressures of 6×10^{-6} torr. Beam spreading reduced effective thrust on the order of 2.5%.

PEARL, J. C.

P04 Mariner 9 Science Experiments: Preliminary Results

R. H. Steinbacher, A. J. Kliore, J. Lorell, H. Hipsher (National Aeronautics and Space Administration), C. A. Barth (University of Colorado), H. Masursky (U.S. Geological Survey), G. Münch (California Institute of Technology), J. C. Pearl (Goddard Space Flight Center), and B. A. Smith (New Mexico State University)

Science, Vol. 175, No. 4019, pp. 293–294, January 21, 1972

For abstract, see Steinbacher, R. H.

P05 Infrared Spectroscopy Experiment on the Mariner 9 Mission: Preliminary Results

R. A. Hanel (Goddard Space Flight Center), B. J. Conrath (Goddard Space Flight Center), W. A. Hovis (Goddard Space Flight Center), V. G. Kunde (Goddard Space Flight Center), P. D. Lowman (Goddard Space Flight Center), J. C. Pearl (Goddard Space Flight Center), C. Prabhakara (Goddard Space Flight Center), B. Schlachman (Goddard Space Flight Center), and G. V. Levin (Biospherics Incorporated)

Science, Vol. 175, No. 4019, pp. 305–308, January 21, 1972

For abstract, see Hanel, R. A.

PEELGREN, M. L.

P06 Completely Modular Thermionic Reactor Ion Propulsion System (TRIPS)

M. L. Peelgren, G. M. Kikin, and C. D. Sawyer

Technical Memorandum 33-550, May 15, 1972

The nuclear-reactor-powered ion-propulsion system described is an advanced, completely modularized system which lends itself to development of prototype and/or flight type components without the need for complete system tests until late in the development program. This modularity is achieved in all of the subsystems and components of the electric propulsion system, including: (1) the thermionic fuel elements, (2) the heat-rejection subsystem (heat pipes), (3) the power-conditioning modules, and (4) the ion thrus-

ters. Both flashlight- and external-fuel in-core thermionic reactors are considered as the power source.

The thermionic fuel elements would be useful over a range of reactor power levels. Electrically heated acceptance testing of fuel elements in their flight configuration is possible for the external-fuel case. Nuclear-heated testing by sampling methods could be used for acceptance testing of flashlight-fuel elements. The use of heat pipes for cooling the collectors and transporting heat to the radiator allows early prototype or flight configuration of testing of a small module of the heat-rejection subsystem as opposed to full scale liquid-metal pumps and radiators in a large vacuum chamber. The power conditioner is arranged in modules with passive cooling which allows complete prototype testing. The ion engines are typically matched with one or more power-conditioner modules and are the same size for any power level propulsion system of interest.

PERKINS, G. S.

P07 A Mechanism for Three-Axis Control of an Ion Thruster Array

G. S. Perkins, K. G. Johnson, J. D. Ferrera, and T. D. Masek

J. Spacecraft Rockets, Vol. 9, No. 3, pp. 218–220, March 1972

The JPL solar–electric propulsion system technology hardware program (SEPST III) is directed toward developing the SEP technology required for several advanced missions. The SEP system has two principal functions: (1) to convert solar energy into spacecraft acceleration and (2) to provide control torques for spacecraft attitude control. The first function is performed by use of power conditioners, a thruster, a controller for power management and failure detection, and, if needed for reliability, a thruster power-conditioner switching matrix. The second function is performed by the thrust vector control (TVC) subsystem. This paper describes the mechanical portion of the TVC subsystem under development in the SEPST III program.

PERLMAN, M.

P08 An Organization of a Digital Subsystem for Generating Spacecraft Timing and Control Signals

M. Perlman

Technical Memorandum 33-539, May 15, 1972

A modulo-M counter (of clock pulses) is decomposed into parallel modulo-m_i counters, where each m_i is a prime power divisor of M. Each m_i is a cascade of α_i identical modulo-p_i counters, where

$$m_i = p_i^{\alpha_i}$$

The modulo-p_i counters are feedback shift registers which cycle through p_i distinct states. By this organization, every possible nontrivial data-frame subperiod (in terms of clock-pulse intervals) and delayed subperiod may be derived.

The number of clock pulses required to bring all (or a subset of all) modulo-p_i counters to a state or count designated for each counter is determined by the Chinese Remainder Theorem. This corresponds to the solution of simultaneous congruences over relatively prime moduli.

PHILLIPS, W. M.

P09 Some Observations on Uranium Carbide Alloy/Tungsten Compatibility

W. M. Phillips

Technical Memorandum 33-547, May 15, 1972

Chemical compatibility tests between pure tungsten and thoriated tungsten were run at 1800°C for up to 3300 h with uranium carbide alloys. Alloying with zirconium carbide appeared to widen the homogeneity range of uranium carbide, making additional carbon available for reaction with the tungsten. Reaction layers were formed both by vapor phase reaction and by physical contact, producing UWC_2 and/or W_2C, depending upon the phases present in the starting fuel alloy. Formation of UWC_2 results in slow growth of the reaction layer with time, while W_2C formation results in rapid growth of the reaction layer, allowing equilibrium to be reached in less than 2500 h at 1800°C. The presence of a thermal gradient had no effect on the reactions observed nor did the presence of thoria in the tungsten clad.

PIMENTEL, G. C.

P10 Mariner Mars 1969 Infrared Spectrometer

K. C. Herr (University of California, Berkeley),
P. B. Forney (University of California, Berkeley), and
G. C. Pimentel (University of California, Berkeley)

Appl. Opt., Vol. 11, No. 3, pp. 493–501, March 1972

For abstract, see Herr, K. C.

POSNER, E. C.

P11 DSN Progress Report for March–April 1972: Hiding and Covering in a Compact Metric Space

R. J. McEliece and E. C. Posner

Technical Report 32-1526, Vol. IX, pp. 59–64, June 15, 1972

For abstract, see McEliece, R. J.

P12 Hide and Seek, Data Storage, and Entropy

R. J. McEliece and E. C. Posner

Ann. Math. Statist., Vol. 42, No. 5, pp. 1706–1716, October 1971

For abstract, see McEliece, R. J.

P13 Epsilon Entropy and Data Compression

E. C. Posner and E. R. Rodemich

Ann. Math. Statist., Vol. 42, No. 6, pp. 2079–2125, December 1971

This article discusses efficient data transmission, or "data compression," from the standpoint of the theory of epsilon entropy. The notion of the entropy of a "data source" is defined. This quantity gives a precise measure of the amount of channel capacity necessary to describe a data source to within a given fidelity, epsilon, with probability 1, when each separate "experiment" must be transmitted without storage from experiment to experiment. Also defined is the absolute epsilon entropy of a source, which is the amount of capacity needed when storage of experiments is allowed before transmission. The absolute epsilon entropy is shown to be equal to Shannon's rate distortion function evaluated for zero distortion, when suitable identifications are made. The main result is that the absolute epsilon entropy and the epsilon entropy have ratio close to one if either is large. Thus, very little can be saved by storing the results of independent experiments before transmission.

POTTER, P. D.

P14 DSN Progress Report for January–February 1972: S- and X-Band Feed System

P. D. Potter

Technical Report 32-1526, Vol. VIII, pp. 53–60, April 15, 1972

To support the Mariner 1973 X-band experiment, it will be necessary to implement a dual-frequency microwave feed system for the Mars Deep Space Station 64-m antenna. This system must be capable of simultaneous low noise reception at S- and X-bands and high power transmission at S-band. To fulfill this requirement, a particularly attractive approach, the reflex feed system, is being implemented. The system makes simultaneous use of both an X-band feedcone and an S-band feedcone. By a system of two reflectors, one of which is dichroic, the effective S-band phase center is translated from its normal position in the S-band feedhorn to a new point which very nearly coincides with the X-band feedhorn phase center. Thus, during simultaneous S- and X-band operation, the antenna subreflector optics are aligned with the X-band feedcone position. This article describes the analytical techniques used to design and analyze the feed system, as well as preliminary results from scale model tests.

P15 DSN Progress Report for March–April 1972: S- and X-Band RF Feed System

P. D. Potter

Technical Report 32-1526, Vol. IX, pp. 141–146, June 15, 1972

In support of the Mariner Venus–Mercury 1973 X-band experiment, it is necessary to implement a dual-frequency microwave feed system for the DSS 14 64-m-diameter antenna. To fulfill this requirement, a particularly attractive approach, the reflex feed system, is being implemented. The reflex feed configuration and the analytical techniques used for its analysis were described in a previous report. This article describes the calculated gain performance of the system at S-band and discusses the heating of the reflex-feed dichroic reflector caused by high-power S-band transmission.

POULSON, P. L.

P16 Operating Executive for the DSIF Tracking Subsystem Software

P. L. Poulson

JPL Quarterly Technical Review, Vol. 2, No. 1, pp. 135–142, April 1972

The advanced engineering model of the Deep Space Instrumentation Facility tracking subsystem is currently being developed. The subsystem will provide effective and reliable tracking and data acquisition support for the complex planetary and interplanetary spaceflight missions planned for the 1970 decade. The nucleus of the subsystem is a Honeywell H832 digital computer. This article describes the design and capabilities of the real-time operating executive software being developed for this subsystem.

PRABHAKARA, C.

P17 Infrared Spectroscopy Experiment on the Mariner 9 Mission: Preliminary Results

R. A. Hanel (Goddard Space Flight Center),
B. J. Conrath (Goddard Space Flight Center),
W. A. Hovis (Goddard Space Flight Center),
V. G. Kunde (Goddard Space Flight Center),
P. D. Lowman (Goddard Space Flight Center),
J. C. Pearl (Goddard Space Flight Center),
C. Prabhakara (Goddard Space Flight Center),
B. Schlachman (Goddard Space Flight Center), and
G. V. Levin (Biospherics Incorporated)

Science, Vol. 175, No. 4019, pp. 305–308, January 21, 1972

For abstract, see Hanel, R. A.

QUINN, R. B.

Q01 DSN Progress Report for March–April 1972: Low Noise Receivers: Microwave Maser Development

R. C. Clauss and R. B. Quinn

Technical Report 32-1526, Vol. IX, pp. 128–136, June 15, 1972

For abstract, see Clauss, R. C.

RAKUNAS, R. R.

R01 DSN Progress Report for March–April 1972: DSN Command System Tests

R. R. Rakunas and A. Schulze

Technical Report 32-1526, Vol. IX, pp. 15–17, June 15, 1972

The DSN Command System is continually updated to support successive flight projects. Tests are scheduled as each new model of Space Flight Operations Facility/Deep Space Instrumentation Facility Command System software is delivered. The test philosophy and results for the Mark III era are described.

RASOOL, S. I.

R02 Mariner 9 S-Band Martian Occultation Experiment: Initial Results on the Atmosphere and Topography of Mars

A. J. Kliore, D. L. Cain, G. Fjeldbo, B. L. Seidel, and S. I. Rasool (National Aeronautics and Space Administration)

Science, Vol. 175, No. 4019, pp. 313–317, January 21, 1972

For abstract, see Kliore, A. J.

RAZOUK, R.

R03 Surface Tension of Propellants

R. Razouk

JPL Quarterly Technical Review, Vol. 2, No. 1, pp. 123–134, April 1972

The design and successful performance of the surface-tension-type propellant management systems for spacecraft require knowledge of propellant surface tension and contact angle values and of the behavior of these parameters under various conditions of temperature, pressure, gravitational forces, and aging. The work reported in this article is concerned with the measurement of surface tension. An apparatus is described for determining the surface tension of propellants by measuring the maximum bubble pressure using two capillaries of different bores. The innovation is the use of a pressure transducer coupled to a bridge supply and a strip chart recorder for registering the development of the pressure difference as the bubble is formed and released. This enables the measurements to be made under controlled atmospheres and the equipment to be remotely operated. Preliminary experiments were done on propellant-grade hydrazine, monomethylhydrazine, and purified hydrazine at temperatures between 275.4 and 353.2 K. Straight-line expressions and logarithmic expressions reproduce equally well the variation of surface tension with temperature.

Contaminated hydrazine, pre-exposed to coupons of 6Al–4V titanium alloy for long periods, gives slightly higher values of surface tension.

REASENBERG, R. D.

R04 Mariner 9 Celestial Mechanics Experiment: Gravity Field and Pole Direction of Mars

J. Lorell, G. H. Born, E. J. Christensen, J. F. Jordan, P. A. Laing, W. Martin, W. L. Sjogren, I. I. Shapiro (Massachusetts Institute of Technology), R. D. Reasenberg (Massachusetts Institute of Technology), and G. L. Slater (Massachusetts Institute of Technology)

Science, Vol. 175, No. 4019, pp. 317–320, January 21, 1972

For abstract, see Lorell, J.

REICHLEY, P. E.

R05 Second Decrease in the Period of the Vela Pulsar

P. E. Reichley and G. S. Downs

Nature Phys. Sci., Vol. 234, No. 46, p. 48, November 15, 1971

This article discusses a second discontinuity in period of the Vela Pulsar which occurred between August 21 and September 4, 1971. A preliminary analysis of the data shows that the period decreased by 179 ns and that the rate of change of period increased. A definitive analysis of the discontinuity will have to await more data because of the normally irregular behavior of the period.

REID, M. S.

R06 DSN Progress Report for January–February 1972: Improved RF Calibration Techniques: System Operating Noise Temperature Calibrations

M. S. Reid

Technical Report 32-1526, Vol. VIII, pp. 61–67, April 15, 1972

System operating noise temperatures and other calibration data of the S-band research operational cone at the Venus Deep Space Station and the tricone system at the Mars Deep Space Station are reported for the period October 1, 1971 through January 31, 1972.

During this reporting period, the tricone system consisted of the polarization diversity S-band (PDS) cone, the S-band megawatt transmit (SMT) cone, and the multifrequency X- and K-band (MXK) cone. S-band calibration data for various configuration modes of the PDS and SMT cones as well as X-band calibration data for the MXK cone are reported.

REIER, M.

R07 The Response of Covered Silicon Detectors to Monoenergetic Gamma Rays

M. Reier

Nucl. Sci. Eng., Vol. 47, No. 4, pp. 409-414, April 1972

Measurements have been made of the efficiency in detecting gamma rays of a 0.3-mm-, 3-mm-, and 5-mm-thick silicon detector covered with different absorbers. Calibrated sources over the range from 279 keV to 2.75 MeV were used. The need for the absorbers to obtain meaningful results and their contribution to the response of the detectors at electron biases from 50 to 200 keV are discussed in detail. It is shown that the results are virtually independent of the atomic number of the absorber. In addition, the role of the absorber in increasing the efficiency with increasing photon energy for low bias settings is demonstrated for the 0.3-mm crystal. Qualitative explanations are given for the shapes of all curves of efficiency versus energy at each bias.

REMBAUM, A.

R08 Solution Properties of Novel Polyelectrolytes

D. Casson and A. Rembaum

Macromolecules, Vol. 5, No. 1, pp. 75-81, January-February 1972

For abstract, see Casson, D.

RENZETTI, N. A.

R09 DSN Progress Report for January-February 1972: DSN Functions and Facilities

N. A. Renzetti

Technical Report 32-1526, Vol. VIII, pp. 1-4, April 15, 1972

The Deep Space Network (DSN), established by the NASA Office of Tracking and Data Acquisition and under the system manage-

ment and technical direction of JPL, is designed for two-way communications with unmanned spacecraft traveling approximately 16,000 km (10,000 mi) from earth to planetary distances. The objectives, functions, and organization of the DSN are summarized, and its three facilities—the Deep Space Instrumentation Facility, the Ground Communications Facility, and the Space Flight Operations Facility—are described.

R10 DSN Progress Report for March–April 1972: DSN Functions and Facilities

N. A. Renzetti

Technical Report 32-1526, Vol. IX, pp. 1–4, June 15, 1972

The DSN, established by the NASA Office of Tracking and Data Acquisition and under the system management and technical direction of JPL, is designed for two-way communications with unmanned spacecraft traveling approximately 16,000 km (10,000 mi) from Earth to planetary distances. The objectives, functions, and organization of the DSN are summarized, and its three facilities—the Deep Space Instrumentation Facility, the Ground Communications Facility, and the Space Flight Operations Facility—are described.

RODEMICH, E. R.

R11 Epsilon Entropy and Data Compression

E. C. Posner and E. R. Rodemich

Ann. Math. Statist., Vol. 42, No. 6, pp. 2079–2125, December 1971

For abstract, see Posner, E. C.

ROSCHKE, E. J.

R12 Partially Ionized Gas Flow and Heat Transfer in the Separation, Reattachment, and Redevelopment Regions Downstream of an Abrupt Circular Channel Expansion

L. H. Back, P. F. Massier, and E. J. Roschke

Trans. ASME, Ser. C: J. Heat Transf., Vol. 94, No. 1, pp. 119–127, February 1972

For abstract, see Back, L. H.

ROSENTHAL, L. A.

R13 Nondestructive Testing of Insensitive Electroexplosive Devices by Transient Techniques

L. A. Rosenthal (Rutgers University) and V. J. Menichelli

Mater. Eval., Vol. XXX, No. 1, pp. 13–19, January 1972

By pulsing an electroexplosive device with a safe level constant current and examining the resistance variation of the bridgewire, it is possible to explore the electrothermal behavior of the bridgewire-explosive interface. The bridgewire, acting as a resistance thermometer, provides a signal which describes the average wire temperature and the heat sinking to the explosive and enclosure. This article describes equipment and observations specific to nondestructive testing of 1-W/1-A no fire devices.

RUSSELL, R. K.

R14 DSN Progress Report for January–February 1972: On Modeling Continuous Accelerations as Piecewise Constant Functions

R. K. Russell and D. W. Curkendall

Technical Report 32-1526, Vol. VIII, pp. 45–52, April 15, 1972

Random, non-gravitational forces acting on the spacecraft in an unpredictable manner have long been identified as a major limitation in using DSN radio data to deduce the state of the spacecraft and predict its subsequent motion. An important aspect of properly handling the non-gravitational forces is determining when their presence affects the data to an extent and in a manner that cannot be modeled accurately within the limitations of the batch filtering orbit determination procedures. This is relevant in its own right but is also important in regard to the proper configuration of the operational sequential filters.

The design of these filters is such that the data is segregated into a series of batches. Between batches, stochastic elements are assumed to enter, and any or all of the parameters subject to solution can change at that time. Within any one batch, however, every parameter is assumed constant, and, within that batch, the data is treated exactly as it is treated in the classical least squares problem. In the limit as batch size reduces to a single data point, this machinery becomes identical to the point sequential filter widely discussed in the literature. To reduce the computational complexity of the operational sequential filters, however, it is desirable to keep the batch sizes as large as possible. Determining this bound

in the presence of what is viewed as a continuously varying force model becomes the focus of this article.

SATO, T.

S01 Transformation of Received Signal Polarization Angle to the Plane of the Ecliptic

C. T. Stelzried, T. Sato, and A. Abreu

J. Spacecraft Rockets, Vol. 9, No. 2, pp. 69–70, February 1972

For abstract, see Stelzried, C. T.

SAWYER, C. D.

S02 Closed-Loop Dynamics of In-Core Thermionic Reactor Systems

C. D. Sawyer and J. E. Boudreau

Technical Memorandum 33-546, May 15, 1972

Using a point model of an in-core thermionic converter, alternative schemes for providing closed-loop reactor control were investigated. It was found that schemes based on variable-gain power regulation buffers which use the reactor current as the control variable provide complete protection from thermionic burnout and also provide a virtually constant voltage to the user. A side benefit is that the emitter-temperature transients are small; even for a complete electric load drop, the emitter temperature transient is less than 100°K. The current-regulation scheme was selected for further study with a distributed-parameter model which was developed to account for variations in thermionic and heat transfer properties along the length of a cylindrical converter. It was found that, even though the emitter-temperature range is about 200°K along the converter length, the dynamic properties are unchanged when using the current-control scheme.

S03 Thermionic Reactor Electric Propulsion System Requirements

J. F. Mondt, C. D. Sawyer, and R. W. Schaupp (Ames Research Center)

Technical Memorandum 33-549, June 1, 1972

For abstract, see Mondt, J. F.

S04 Completely Modular Thermionic Reactor Ion Propulsion System (TRIPS)

M. L. Peelgren, G. M. Kikin, and C. D. Sawyer

Technical Memorandum 33-550, May 15, 1972

For abstract, see Peelgren, M. L.

SCHAUPP, R. W.

S05 Thermionic Reactor Electric Propulsion System Requirements

J. F. Mondt, C. D. Sawyer, and R. W. Schaupp (Ames Research Center)

Technical Memorandum 33-549, June 1, 1972

For abstract, see Mondt, J. F.

SCHLACHMAN, B.

S06 Infrared Spectroscopy Experiment on the Mariner 9 Mission: Preliminary Results

R. A. Hanel (Goddard Space Flight Center),
B. J. Conrath (Goddard Space Flight Center),
W. A. Hovis (Goddard Space Flight Center),
V. G. Kunde (Goddard Space Flight Center),
P. D. Lowman (Goddard Space Flight Center),
J. C. Pearl (Goddard Space Flight Center),
C. Prabhakara (Goddard Space Flight Center),
B. Schlachman (Goddard Space Flight Center), and
G. V. Levin (Biospherics Incorporated)

Science, Vol. 175, No. 4019, pp. 305–308, January 21, 1972

For abstract, see Hanel, R. A.

SCHMIT, D. D.

S07 Mariner 9 Propulsion Subsystem Performance During Interplanetary Cruise and Mars Orbit Insertion

M. J. Cork, R. L. French, C. J. Leising, and D. D. Schmit

JPL Quarterly Technical Review, Vol. 2, No. 1, pp. 113–122, April 1972

For abstract, see Cork, M. J.

SCHULZE, A.

S08 DSN Progress Report for March–April 1972: DSN Command System Tests

R. R. Rakunas and A. Schulze

Technical Report 32-1526, Vol. IX, pp. 15–17, June 15, 1972

For abstract, see Rakunas, R. R.

SEIDEL, B. L.

S09 Mariner 9 S-Band Martian Occultation Experiment: Initial Results on the Atmosphere and Topography of Mars

A. J. Kliore, D. L. Cain, G. Fjeldbo, B. L. Seidel, and S. I. Rasool (National Aeronautics and Space Administration)

Science, Vol. 175, No. 4019, pp. 313–317, January 21, 1972

For abstract, see Kliore, A. J.

SHAFER, J. I.

S10 Solid Propulsion Advanced Concepts

Y. Nakamura and J. I. Shafer

Technical Memorandum 33-534, May 1, 1972

For abstract, see Nakamura, Y.

SHAPIRO, I. I.

S11 Mariner 9 Celestial Mechanics Experiment: Gravity Field and Pole Direction of Mars

J. Lorell, G. H. Born, E. J. Christensen, J. F. Jordan, P. A. Laing, W. Martin, W. L. Sjogren, I. I. Shapiro (Massachusetts Institute of Technology), R. D. Reasenberg (Massachusetts Institute of Technology), and G. L. Slater (Massachusetts Institute of Technology)

Science, Vol. 175, No. 4019, pp. 317–320, January 21, 1972

For abstract, see Lorell, J.

SHIMADA, K.

S12 Out-of-Core Evaluations of Uranium Nitride-Fueled Converters

K. Shimada

Technical Memorandum 33-545, May 1, 1972

Two uranium–nitride-fueled converters were tested parametrically for their initial characterization and are currently being life-tested out of core. In this memorandum, the test method being employed for the parametric and diagnostic measurements during the life tests and the test results are presented. One converter, with a rhenium emitter, had an initial output power density of 6.9 W/cm^2 at the blackbody emitter temperature, T_E, of 1900°K. The power density remained unchanged for the first 1000 h of the life test at T_E = 1900°K but it degraded nearly 50% during the following 1000 h. The electrode work function measurements indicated that the uranium fuel was diffusing out of the emitter clad of 0.635-mm thickness. The other converter, with a tungsten emitter, had an initial output power density of 2.2 W/cm^2 at T_E = 1900°K. The power density increased exponentially to 3.6 W/cm^2 during the 3500 h of the life test. The rate of improvement increased thereafter and the power density was 3.9 W/cm^2 at 4300 h. The power density suddenly degraded within 20 h to practically zero output at 4735 h.

S13 Probe Measurements of Cesium Plasma in a Simulated Thermionic Energy Converter

K. Shimada

Technical Memorandum 33-551, May 15, 1972

Cesium-filled thermionic energy converters are being considered as candidate electrical energy sources in future spacecraft requiring tens to hundreds of kilowatts of electric power. The high operating temperatures necessary for a large specific power and high efficiency inevitably impose stringent constraints on the converter fabrication to achieve the desired reliability of the power system. The converter physics for reducing operating temperatures and cesium plasma losses are being studied to achieve high reliability without sacrificing the power performance of the converters. Various cesium parameters that affect the converter performance are: (1) electron temperatures, (2) plasma ion densities, and (3) electric potential profiles. These were investigated using a Langmuir probe in a simulated converter. The parameters were measured in different cesium discharge modes.

SIEGMETH, A. J.

S14 DSN Progress Report for January–February 1972: Pioneer Mission Support

A. J. Siegmeth

Technical Report 32-1526, Vol. VIII, pp. 8–15, April 15, 1972

The previous articles on the Jupiter-bound Pioneer F and G mission support delineated the mission description and the functional planning activities of the Tracking and Data System. Beginning with the current article, an account will be given of the actual management organization and engineering planning activities which were essential to assure effective scientific data return and spacecraft control.

S15 DSN Progress Report for March–April 1972: Pioneer Mission Support

A. J. Siegmeth

Technical Report 32-1526, Vol. IX, pp. 18–32, June 15, 1972

This article reviews the status of the second-generation Pioneer missions, Pioneers 6, 7, 8, and 9; and the prelaunch and launch support of Pioneer 10, which is the first member of the third generation, whose destinations are Jupiter and beyond. This mission was identified in previous reports as Pioneer F: it was renamed Pioneer 10 after its successful launch. The planning activities for the second mission of the third generation, Pioneer G, and a summary on the fourth-generation Pioneers planned for the exploration of Venus are also presented.

SILVER, R. H.

S16 Studies on the Frictional Behavior of Magnetic Recording Tapes

S. H. Kalfayan, R. H. Silver, and J. K. Hoffman

JPL Quarterly Technical Review, Vol. 2, No. 1, pp. 100–106, April 1972

For abstract, see Kalfayan, S. H.

SIMON, H. S.

S17 DSN Progress Report for March–April 1972: Mariner Mars 1971/Pioneer 10 Multi-Mission Level Modeling Runs Using the SFOF Mark IIIA Central Processing System Model

H. S. Simon

Technical Report 32-1526, Vol. IX, pp. 162–176, June 15, 1972

Simulation models are currently being used for Space Flight Operations Facility (SFOF) development at JPL. This article documents the results of a series of modeling runs made during January and February 1972. The model contained a majority of the SFOF Mark IIIA central processing system capabilities required to support simultaneously the orbital phase of the Mariner Mars 1971 mission and the early cruise phase of the Pioneer 10 mission.

SIMON, M. K.

S18 On the Selection of an Optimum Design Point for Phase-Coherent Receivers Employing Bandpass Limiters

M. K. Simon

IEEE Trans. Commun., Vol. COM-20, No. 2, pp. 210–214, April 1972

In the design of phase-coherent receivers employing bandpass limiters, it is customary to specify system performance relative to its value at a fixed design point. For a given design point, it is well known that an optimum tradeoff can be found between the power allocated to the carrier and sideband signals. This paper describes an attempt to further improve the performance of such coherent carrier systems by optimizing the design point based upon a given practical optimization criterion. The single-channel system is treated in detail and a brief discussion is given on how to extend the optimization technique to a two-channel system.

SIMON, W.

S19 Plume Backscatter Measurements Using Quartz Crystal Microbalances in JPL Molsink (Molecular Sink)

W. Simon

Technical Memorandum 33-540, May 15, 1972

Recent tests in the JPL Molsink facility have provided the first quantitative evidence of gas flows in the far upstream region of small nozzles with large boundary layer flow. Gas-mass fluxes were

measured using quartz-crystal microbalances. Both nitrogen and carbon dioxide were used as test gases. Gas deposition rates on the order of 100 monolayers per min were detected 13 in. upstream from the nozzle exit plane. It is significant to note that the crystals detected gases considerably beyond the Prandtl-Meyer turning angle. Tests are being continued using improved cryogenic, quartz-crystal systems and additional types of gases. The data from these tests will be essential in the formulation of scaling laws and analytical prediction methods for viscous plume behavior.

SJOGREN, W. L.

S20 Lunar Gravity via Apollo 14 Doppler Radio Tracking

W. L. Sjogren, P. Gottlieb, P. M. Muller, and
W. Wollenhaupt (Manned Spacecraft Center)

Science, Vol. 175, No. 4018, pp. 165-168,
January 14, 1972

Gravity measurements at high resolution were obtained over a 100-km band from 70 to -70 deg of longitude during the orbits of low periapsis altitude (approximately 16 km). The line-of-sight accelerations are plotted on Aeronautical Chart and Information Center mercator charts (scale 1:1,000,000) as contours at 10-mgal intervals. Direct correlations between gravity variations and surface features are easily determined. Theophilus, Hipparchus, and Ptolemaeus are negative features, whereas Mare Nectaris is a large positive region. The acceleration profiles over Mare Nectaris are suggestive of a broad disk near the surface rather than a deeply buried spherical body. These data are in good agreement with the short arc of Apollo 12 lunar module descent data.

S21 Mariner 9 Celestial Mechanics Experiment: Gravity Field and Pole Direction of Mars

J. Lorell, G. H. Born, E. J. Christensen, J. F. Jordan,
P. A. Laing, W. Martin, W. L. Sjogren,
I. I. Shapiro (Massachusetts Institute of Technology),
R. D. Reasenberg (Massachusetts Institute of Technology),
and G. L. Slater (Massachusetts Institute of Technology)

Science, Vol. 175, No. 4019, pp. 317-320,
January 21, 1972

For abstract, see Lorell, J.

SLATER, G. L.

S22 Mariner 9 Celestial Mechanics Experiment: Gravity Field and Pole Direction of Mars

J. Lorell, G. H. Born, E. J. Christensen, J. F. Jordan, P. A. Laing, W. Martin, W. L. Sjogren, I. I. Shapiro (Massachusetts Institute of Technology), R. D. Reasenberg (Massachusetts Institute of Technology), and G. L. Slater (Massachusetts Institute of Technology)

Science, Vol. 175, No. 4019, pp. 317–320, January 21, 1972

For abstract, see Lorell, J.

SLEKYS, A.

S23 DSN Progress Report for March–April 1972: Predetection Recording and Dropouts

A. Slekys

Technical Report 32-1526, Vol. IX, pp. 115–118, June 15, 1972

Predetection recording of spacecraft telemetry data allows possible future analysis of data records in the event of failures of transmitted signals. Dropouts occurring in the playback process necessarily cause loss of information and, more importantly, loss of time synchronization with the remaining data. The object of this study is to show that, with proper digital handling of a timing signal initially recorded along with telemetry data, using a device incorporating a proposed digital dropout detector, time synchronization can be maintained throughout dropouts of lengths less than 100 ms, within some small probability of error. Uses extend to recording of planetary-entry low-rate and very-long-baseline interferometry data and, in particular, to planetary radio-occultation information, which is already recorded with a timing signal on the same tape track.

SMITH, B. A.

S24 Mariner 9 Science Experiments: Preliminary Results

R. H. Steinbacher, A. J. Kliore, J. Lorell, H. Hipsher (National Aeronautics and Space Administration), C. A. Barth (University of Colorado), H. Masursky (U.S. Geological Survey), G. Münch (California Institute of Technology), J. C. Pearl (Goddard Space Flight Center), and B. A. Smith (New Mexico State University)

Science, Vol. 175, No. 4019, pp. 293–294, January 21, 1972

For abstract, see Steinbacher, R. H.

SMITH, R. H.

S25 DSN Progress Report for March–April 1972: 10-W S-Band Amplifier

R. H. Smith

Technical Report 32-1526, Vol. IX, pp. 196–200, June 15, 1972

A more powerful S-band amplifier was needed to drive the high-power transmitters of the DSN. Two types of 10-W solid-state amplifiers with 23-dB gain, operating at 2115 MHz for the DSN 400-kW transmitter and 2388 MHz for the 450-kW R&D transmitter, were developed.

SRIDHAR, R.

S26 Approximate Nonlinear Filters and Deterministic Filter Gains

A. K. Bejczy and R. Sridhar (University of California, Los Angeles)

Trans. ASME, Ser. G: J. Dynam. Sys., Meas., Contr., Vol. 94, No. 1, pp. 57–63, March 1972

For abstract, see Bejczy, A. K.

STEINBACHER, R. H.

S27 Mariner 9 Science Experiments: Preliminary Results

R. H. Steinbacher, A. J. Kliore, J. Lorell, H. Hipsher (National Aeronautics and Space Administration), C. A. Barth (University of Colorado), H. Masursky (U.S. Geological Survey), G. Münch (California Institute of Technology), J. C. Pearl (Goddard Space Flight Center), and B. A. Smith (New Mexico State University)

Science, Vol. 175, No. 4019, pp. 293–294, January 21, 1972

To form the science payload for the Mariner 9 spacecraft, NASA selected six experiments: television, infrared spectroscopy, infrared radiometry, ultraviolet spectrometer, S-band occultation, and celestial mechanics. This article presents a brief summary of results

from these experiments, obtained during the first 30 days after orbit insertion.

STELZRIED, C. T.

S28 Transformation of Received Signal Polarization Angle to the Plane of the Ecliptic

C. T. Stelzried, T. Sato, and A. Abreu

J. Spacecraft Rockets, Vol. 9, No. 2, pp. 69–70, February 1972

The solar occultation of the Pioneer 6 spacecraft in November 1968 provided the first opportunity to measure the polarization rotation of a continuous-wave signal in the solar corona. The received signal polarization angle measured with the JPL 64-m Mars Deep Space Station azimuth–elevation mount antenna was transformed to the plane of the ecliptic. The derivation of the equations required for this transformation is presented.

S29 Operating Noise-Temperature Calibrations of Low-Noise Receiving Systems

C. T. Stelzried

Microwave J., Vol. 14, No. 6, pp. 41–46, 48, June 1971

A technique has been developed for calibrating the operating noise-temperature of low-noise Earth station receiving systems. The technique, which consists of switching the maser input between the antenna and a microwave ambient termination, has been used on several antenna/cone configurations for the JPL/NASA Deep Space Communications System. Extensive operational measurement data are presented for the period July 1966 to March 1968. The details of the calibration technique, error analysis, and programming are presented. For a receiving system with 30-K total operating noise temperature, the total probable error (dispersion and bias) is approximately 0.30 K.

STEWART, A. I.

S30 Mariner 9 Ultraviolet Spectrometer Experiment: Initial Results

C. A. Barth (University of Colorado), C. W. Hord (University of Colorado), A. I. Stewart (University of Colorado), and A. L. Lane

Science, Vol. 175, No. 4019, pp. 309–312, January 21, 1972

For abstract, see Barth, C. A.

TAHERZADEH, M.

T01 Neutron Radiation Characteristics of Plutonium Dioxide Fuel

M. Taherzadeh

Technical Report 32-1555, June 1, 1972

The major sources of neutrons from plutonium-dioxide nuclear fuel are considered in detail. These sources include spontaneous fission of several Pu isotopes, (α,n) reactions with low Z impurities in the fuel, and (α,n) reactions with ^{18}O. For spontaneous fission neutrons, a neutron emission rate of $(1.95 \pm 0.07) \times 10^3$ n/s/g PuO_2 is obtained.

The neutron yield from (α,n) reactions with oxygen is calculated by integrating the reaction rate equation over all α-particle energies and all center-of-mass angles. The results indicate a neutron emission rate of $(1.14 \pm 0.26) \times 10^4$ n/s/g PuO_2.

The neutron yield from (α,n) reactions with low Z impurities in the fuel is presented in tabular form for one part per million of each impurity. The total neutron yield due to the combined effects of all the impurities depends upon the fractional weight concentration of each impurity. The total neutron flux emitted from a particular fuel geometry is estimated by adding the neutron yield due to the induced fission to that of the other neutron sources.

TAUSWORTHE, R. C.

T02 Convergence of Oscillator Spectral Estimators for Counted-Frequency Measurements

R. C. Tausworthe

IEEE Trans. Commun., Vol. COM-20, No. 2, pp. 214–217, April 1972

A common intermediary connecting frequency-noise calibration or testing of an oscillator to useful applications is the spectral density of the frequency-deviating process. In attempting to turn test data into predicts of performance characteristics, one is naturally led to estimation of statistical values by sample-mean and sample-variance techniques. However, sample means and sample variances themselves are statistical quantities that do not necessarily converge (in the mean-square sense) to actual ensemble-average means

and variances, except perhaps for excessively large sample sizes. This is especially true for the flicker noise component of oscillators. This article shows, for the various types of noises found in oscillators, how sample averages converge (or do not converge) to their statistical counterparts. The convergence rate is shown to be the same for all oscillators of a given spectral type.

TAYLOR, F. J.

T03 Telecommunications System Design for the Mariner Mars 1971 Spacecraft

F. J. Taylor and G. W. Garrison

Technical Memorandum 33-535, May 1, 1972

The configuration of the Mariner Mars 1971 spacecraft telecommunications system is detailed, with particular attention to modifications performed to accommodate the orbital mission. This memorandum describes the analysis and planning prior to launch. Results of major analyses and tests are summarized.

TEXTOR, G. P.

T04 DSN Progress Report for March–April 1972: Mariner Mars 1971 Mission Support

G. P. Textor

Technical Report 32-1526, Vol. IX, pp. 35–37, June 15, 1972

On Feburary 12, 1972, Mariner 9 completed its 180th revolution about the planet Mars and its 90th day of scientific data gathering from orbit. This marked the end of the nominal mission, which was to obtain data from orbit for a minimum of 90 days, and marked the beginning of the extended mission. This article presents the objectives, constraints, profile, and present DSN coverage plan for the Mariner Mars 1971 extended mission.

T05 Tracking and Data System Support for the Mariner Mars 1971 Mission: First Trajectory Correction Maneuver Through Orbit Insertion

G. P. Textor, L. B. Kelly, and M. Kelly

Technical Memorandum 33-523, Vol. II, June 15, 1972

This document describes the Tracking and Data System (TDS) activities in support of the Mariner Mars 1971 Project from the first trajectory correction maneuver on June 4, 1971, through

cruise and orbit insertion on November 14, 1971. Included are presentations of the changes and updates to the TDS requirements, plan, and configuration plus detailed information on TDS flight support performance evaluation and pre-orbital testing and training during this report period.

With the loss of Mariner 8 at launch, a few changes to the Mariner Mars 1971 requirements, plan, and configuration were necessitated. Mariner 9 is now assuming the mission plan of Mariner 8, including the TV mapping cycles and a 12-hr orbital period.

A second trajectory correction maneuver was not required because of the accuracy of the first maneuver. All testing and training for orbital operations were completed satisfactorily and on schedule. The orbit insertion was accomplished with excellent results.

THOMAS, J. B.

T06 DSN Progress Report for January–February 1972: An Analysis of Long Baseline Radio Interferometry, Part II

J. B. Thomas

Technical Report 32-1526, Vol. VIII, pp. 29–38, April 15, 1972

This article continues the analysis of the cross-correlation procedure used in long baseline radio interferometry begun in Technical Report 32-1526, Vol. VII, pp. 37–50. It is assumed that the radio signal is generated by a very distant, completely incoherent, extended source. For both digital and analog recording systems, the normalized cross-correlation function is derived in terms of noise temperature, fringe visibility, and bandpass overlap. For very strong point sources and accurate model delays, it is shown that the digital cross-correlation function becomes a sawtooth time function whose extrema and zero crossings agree with the sinusoidal cross-correlation function produced by an analog system. For weak sources, such as those common to most very long baseline interferometry measurements, the digital cross-correlation function is identical to the normalized analog cross-correlation function, except for a loss of $2/\pi$ in amplitude.

General signal/noise (SNR) expressions are derived for both the digital and the analog cross-correlation functions. For a very strong point source, the SNR in a digital system can be infinitely better than that in an analog system at time points of maximum correlation. However, at points of weak correlation, the digital SNR is $2/\pi$ smaller than the analog value. In the case of small correlated amplitude, the digital system produces an SNR that is uniformly $2/\pi$ worse than the analog system ratio.

THOMAS, J. R.

T07 Mariner Venus–Mercury 1973 Mission Solar Proton Environment: Fluence and Dose

J. R. Thomas (The Boeing Company)

JPL Quarterly Technical Review, Vol. 2, No. 1, pp. 12–28, April 1972

The solar proton environment for the Mariner Venus–Mercury 1973 mission may be the most severe yet encountered in space missions, because the trajectory by Mercury will bring the spacecraft significantly closer to the Sun than any previous spacecraft. This study presents a derivation of proton fluence over the duration of the mission in terms of a relatively constant low-energy component, the solar wind, and a probabilistic high-energy component from discrete solar events. An updated correlation of yearly energetic proton fluence with yearly average Sunspot number is presented. This correlation and Sunspot cycle forecasts for the period of the mission (late-1973 through early-1975) form the basis for the high-energy proton fluence estimates with various confidence levels. Uncertainties in the probability estimates and in calculation of the scaling with distance from the Sun are discussed. Selection of a particular 95-percentile model as the design constraint is recommended, along with reasons for not using the worst-case model. Interior fluences are calculated and expressed in terms expected to be useful for spacecraft design.

THULEEN, K. L.

T08 DSN Progress Report for January–February 1972: The Translation of the Tropospheric Zenith Range Effect From a Radiosonde Balloon Site to a Tracking Station

K. L. Thuleen and V. J. Ondrasik

Technical Report 32-1526, Vol. VIII, pp. 39–44, April 15, 1972

The temporal behavior of the wet tropospheric zenith range effect, $\Delta\rho_z(w)$, over the radiosonde balloon sites at Edwards Air Force Base and Yucca Flats, Nevada, is compared. The $\Delta\rho_z(w)$ over the balloon site may be translated to a nearby tracking station for use in performing tropospheric navigational error analysis studies and for developing models, incorporating seasonal variations, to be used for the tropospheric calibration of radio metric data. The daily variations in $\Delta\rho_z(w)$ appear to prohibit the use of radiosonde balloon data for the daily calibration of radio metric data.

VIRZI, R. A.

V01 Mariner Mars 1971 Scan Platform Pointing Calibration

G. D. Pace, G. I. Jaivin, and R. A. Virzi

JPL Quarterly Technical Review, Vol. 2, No. 1, pp. 49–57, April 1972

For abstract, see Pace, G. D.

VOLKOFF, J. J.

V02 DSN Progress Report for March–April 1972: Photon Noise Generation of Cathode-Ray Tube Display Systems

J. J. Volkoff

Technical Report 32-1526, Vol. IX, pp. 152–161, June 15, 1972

The mean-square fluctuation components associated with the various luminous fluxes of ambient and generated light emitted from a cathode-ray tube (CRT) system are derived and combined to represent the photon-noise component. A rationale for the criteria required for the discernment of noisy shades of gray as displayed by CRT systems is developed. The criteria are applied to an actual CRT system and are verified with experimental results.

WALMSLEY, D. E.

W01 Lifetime Estimates for Sterilizable Silver–Zinc Battery Separators

E. F. Cuddihy, D. E. Walmsley, and J. Moacanin

JPL Quarterly Technical Review, Vol. 2, No. 1, pp. 72–81, April 1972

For abstract, see Cuddihy, E. F.

WICK, M. R.

W02 DSN Progress Report for January–February 1972: DSN Programmed Oscillator Development

M. R. Wick

Technical Report 32-1526, Vol. VIII, pp. 115–124, April 15, 1972

This article describes the development of a programmed oscillator utilizing a Dana Laboratory Digiphase synthesizer Model 7010-

S-179. A brief description of the synthesizer characteristics and the technique for digital control is given. With this synthesizer, the programmed oscillator has the capability of being controlled at rates and ranges required for tracking outer-planet probes while providing the resolution and stability required for narrow-loop bandwidth receivers.

WILLIAMS, H. E.

W03 Analysis of a Laterally Loaded Ring With a Hinged Cross Section

H. E. Williams (Harvey Mudd College)

AIAA Preprint 72-355, AIAA (American Institute of Aeronautics and Astronautics)/ASME (American Society of Mechanical Engineers)/SAE (Society of Automotive Engineers) Thirteenth Structures, Structural Dynamics, and Materials Conference, San Antonio, Texas, April 10–12, 1972

A ring assembly constructed by lacing together three elements into a basic channel cross section is analyzed. The ring is supported at three equidistant points and loaded by a uniform distribution of radial and transverse loads. Bulkheads may be introduced at discrete cross sections to prevent distortion. The purpose of this analysis is to determine the behavior of the deflection as the number and location of the bulkheads and the degree of rigidity of the supports are varied.

The method of analysis is an application of the Principle of Virtual Work within the framework of small displacement theory. Numerical results are presented for the geometrical parameters of a model. An important result is the observation that bulkheads have virtually no effect on the deflections of the web.

WILSON, A. H.

W04 Furlable Spacecraft Antenna Development: An Interim Report

R. E. Oliver and A. H. Wilson

Technical Memorandum 33-537, April 15, 1972

For abstract, see Oliver, R. E.

WINSTEIN, S.

W05 Carbon-to-Metal Chlorine Exchange: IV. Mercuric Salt Promoted Acetolysis of exo-Norbornyl Chloride

J. P. Hardy, A. F. Diaz, and S. Winstein

J. Am. Chem. Soc., Vol. 94, No. 7, pp. 2363–2370, April 5, 1972

For abstract, see Hardy, J. P.

WOLLENHAUPT, W.

W06 Lunar Gravity via Apollo 14 Doppler Radio Tracking

W. L. Sjogren, P. Gottlieb, P. M. Muller, and W. Wollenhaupt (Manned Spacecraft Center)

Science, Vol. 175, No. 4018, pp. 165–168, January 14, 1972

For abstract, see Sjogren, W. L.

YANG, J.-N.

Y01 Simulation of Random Envelope Processes

J.-N. Yang

J. Sound Vibr., Vol. 21, No. 1, pp. 73–85, March 1972

Efficient and practical methods of simulating stationary and nonstationary random envelope processes are presented. The stationary envelope processes are simulated by using the fast Fourier transform while the nonstationary envelope processes are simulated as the square root of the sum of a series of cosine functions and a series of sine functions with random phase angles. Typical applications of the envelope simulation are the simulations of peaks and troughs which play an important role in the analyses of the first excursion probability, fatigue and crack propagation. In particular, applications to the crack propagation under random loadings are demonstrated in detail.

Y02 Statistical Distribution of Spacecraft Maximum Structural Response

J.-N. Yang

J. Spacecraft Rockets, Vol. 9, No. 1, pp. 57–59, January 1972

This article presents a direct statistical analysis of spacecraft maximum response under conditions of nonstationary random excitations resulting from booster engine shutdown and describes the resultant spacecraft structural reliability. It is found that the Gumbel Type I asymptotic distribution of maximum values provides a reasonably good statistical model for spacecraft maximum responses. This approach makes it possible to perform the reliability-based optimum design of spacecraft structures.

YANG, L. C.

Y03 Initiation of Insensitive Explosives by Laser Energy

V. J. Menichelli and L. C. Yang

Technical Report 32-1557, June 1, 1972

For abstract, see Menichelli, V. J.

YOUNG, A. T.

Y04 Observing Venus Near the Sun

A. T. Young and L. D. G. Young

Sky Telesc., Vol. 43, No. 3, pp. 140–144, March 1972

Daytime astronomical observing is very difficult within a few degrees of the Sun. If any direct sunlight falls inside the telescope tube or on the objective, it can ruin the seeing and image contrast. This article discusses the problems, special requirements, hints, and optimum conditions for near-Sun observation of Venus.

YOUNG, L. D. G.

Y05 Comments on Accurate Formula for Gaseous Transmittance in the Infrared

L. D. G. Young

Appl. Opt., Vol. 11, No. 1, pp. 202–203, January 1972

This article discusses the accuracy of data previously published for gaseous transmittance in the infrared. The choice of input data, rather than the method of calculation, is questioned.

Y06 Relative Intensity Calculations for Nitrous Oxide

L. D. G. Young

J. Quant. Spectrosc. Radiat. Transfer, Vol. 12, No. 3, pp. 307–322, March 1972

A tabulation of calculated rotational line intensities, relative to the integrated intensity of a vibration–rotation band, is given for Σ–Σ, Π–Σ, Σ–Π, Π–Π, and Δ–Π transitions of $^{14}N^{16}O_2$. These calculations were made for a temperature of 250°K (typical for the Earth's atmosphere) and for 300°K (representative of laboratory conditions). A summary of band-intensity measurements is also given.

Y07 Observing Venus Near the Sun

A. T. Young and L. D. G. Young

Sky Telesc., Vol. 43, No. 3, pp. 140–144, March 1972

For abstract, see Young, A. T.

ZOHAR, S.

Z01 DSN Progress Report for March–April 1972: New Hardware Realizations of Non-Recursive Digital Filters

S. Zohar

Technical Report 32-1526, Vol. IX, pp. 65–81, June 15, 1972

Analysis of the bit-level operations involved in the convolution realizing a non-recursive digital filter leads to hardware designs of digital filters based on the operation of counting. Two distinct designs are outlined: The first is capable of very high speed, but is rather expensive. The second is quite slow, but has the advantages of low cost and high flexibility. The basic designs considered utilize fixed-point representation for the data and filter coefficients. Variants which allow floating-point representation of the coefficients are also described.

ZWEBEN, C.

Z02 Development of Boron Epoxy Rocket Motor Chambers

W. M. Jensen, A. C. Knoell, and C. Zweben (Materials Sciences Corporation)

Proceedings of the Twenty-Seventh Annual Technical Conference of the Reinforced Plastics/Composites Institute, Washington, D.C., February 8–11, 1972, sponsored by the Society of the Plastics Industry, Inc., Sect. 17-C, pp. 1–10

For abstract, see Jensen, W. M.

Subject Index

Subject Categories

Subjects

Publication Index

Technical Reports

Number	Entry
32-1555	T01
32-1556	M19
32-1557	M20
32-1558	B17
32-1559	C17

DSN Progress Reports for January–April 1972 (Technical Report 32-1526, Vols. VIII and IX)

JPL Technical Section	Entry
331 Communications Systems Research	A04
	A05
	B09
	B27
	B29
	E01
	H08
	L08
	L09
	M15
	M35
	S23
	Z01
332 DSIF Engineering	D03
	J10

Technical Memorandums

JPL Quarterly Technical Review, Vol. 2, No. 1

Open Literature Reporting

AIAA Guidance, Control and Flight Mechanics Conference, Hempstead, New York, August 16–18, 1971 **Entry**

AIAA J. **Entry**

AIAA Ninth Electric Propulsion Conference, Bethesda, Maryland, April 17–19, 1972 **Entry**

AIAA/ASME/SAE Thirteenth Structures, Structural Dynamics, and Materials Conference, San Antonio, Texas, April 10–12, 1972 **Entry**

Ann. Math. Statist. **Entry**

Antarctic J. U.S. **Entry**

Appl. Opt. **Entry**

NASA — JPL — Coml., L.A., Calif.